

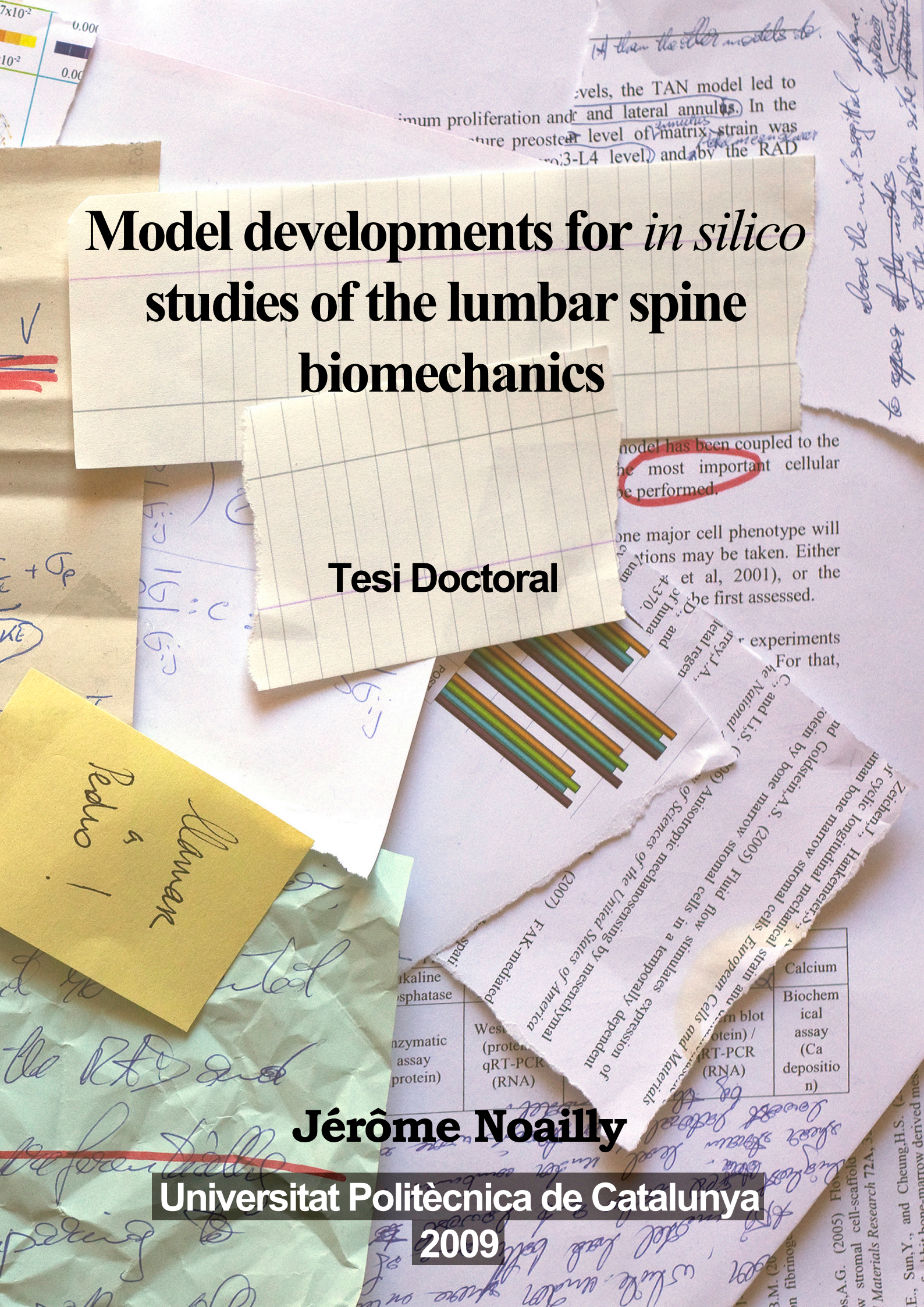
Model developments for *in silico* studies of the lumbar spine biomechanics

Tesi Doctoral

Jérôme Noailly

Universitat Politècnica de Catalunya

2009



Chapter3

*"El subtil mirall discret que ens encén la mirada
és el no-res que sempre descobrim."*

(Miquel Martí i Pol)

Chapter 3

**DEVELOPMENT OF A NEW L3-L5 LUMBAR
SPINE FINITE ELEMENT BI-SEGMENT MODEL
INFLUENCE OF THE GEOMETRY ON TISSUE STRESS
DISTRIBUTIONS AND CONSEQUENCE ON VALIDATION**

A.	Introduction	117
B.	Development of a new model.....	119
I.	Vertebral bodies and intervertebral discs.....	119
II.	Pedicles and spinal canal.....	120
III.	Processes	120
IV.	Ligaments.....	121
V.	Discussion on the quantitative geometry	123
a.	Vertebral body linear dimensions.....	123
b.	Spinal canal and pedicles linear dimensions	124
c.	Inter-process distances and processes lengths.....	124
d.	Angular dimensions.....	125
e.	Conclusion.....	125
C.	Models comparison	131
I.	Method	131
II.	Results.....	133
a.	Flexion.....	133
1)	Supraspinous ligament removal	134
2)	Interspinous ligament removal	134
3)	Intertransverse ligament removal	135
4)	Capsular ligament removal.....	135
5)	Ligamentum flavum removal	136
6)	Bony posterior elements removal.....	137
7)	Posterior longitudinal ligament removal	138
8)	Anterior longitudinal ligament removal	138
9)	Nucleus pulposus removal.....	139
b.	Extension	146
1)	Capsular ligament removal.....	146
2)	Bony posterior elements removal.....	147
3)	Posterior longitudinal ligament removal	148
4)	Anterior longitudinal ligament removal	149
5)	Nucleus pulposus removal.....	149
c.	Lateral bending.....	156
1)	Intertransverse ligament removal	156
2)	Capsular ligament removal.....	157
3)	Ligamentum flavum removal	158
4)	Bony posterior elements removal.....	159
5)	Posterior longitudinal ligament removal	159
6)	Nucleus pulposus removal.....	160

d.	Axial rotation.....	168
1)	Capsular ligament removal.....	168
2)	Ligamentum flavum removal.....	169
3)	Bony posterior elements removal.....	170
4)	Posterior longitudinal ligament removal.....	171
5)	Nucleus pulposus removal.....	171
e.	Intact models.....	179
III.	Discussion.....	180
a.	Supraspinous and interspinous ligaments.....	180
b.	Intertransverse ligament.....	181
c.	Capsular ligament.....	182
d.	Ligamentum flavum.....	184
e.	Bony posterior elements.....	185
f.	Posterior longitudinal ligament.....	186
g.	Anterior longitudinal ligament.....	187
h.	Nucleus pulposus.....	188
i.	Intact models.....	189
IV.	Conclusion.....	190

A. Introduction

In spine biomechanics, finite element modelling is an approximation of a mechanical system that can be divided into four groups: the geometrical, numerical, mechanical constitutive laws, and boundary conditions parts. The geometrical approximation involves the level of description of the tissues that constitute the structure, and the accuracy of the individual shapes drawn for these tissues. This usually depends on the different methods used to take up the geometry of the structure that has to be modelled. The combination of Computed Tomography (CT) scans and X-ray imaging with magnetic resonance imaging, histology and anatomical information from the medical literature is essential to minimize the geometrical uncertainties. The numerical approximation is basically faced by the element technology, the mesh refinement, and the criteria of convergence. Obviously, mesh refinement interacts with the geometrical approximation, since it defines how the discretization will fit to the original digitized curves. The mechanical approximation is also in interaction with the numerical part, since coherence has to be maintained between the user inputs and the selected methods of computation. However, the main source of mechanical errors may come from the material constitutive equations and the determination of their parameters. Since tissue material properties have to be determined experimentally, various aspects such as type and magnitude of the applied loads, the testing rate, and the hydration of the sample, will influence the choice of a suitable mechanical description for the modelled tissue. In the case of composite materials, the mechanical approximation will interact with the geometrical approximation, given that the level of refinement of the tissue structure description will decide in part if a homogenization of the material mechanical description will be done or if a structural mechanical law can be used. Finally, the last aspect of the mechanical approximation is related to the simulation of suitable boundary conditions; if the aim is to reproduce a controlled experimental protocol, then boundary conditions modelling may not represent any limitations. However, if the aim is to represent an *in vivo* mechanical environment, many unknowns like the muscle activation factors, the influence of the adjacent ligamentous structures on the balance between load and displacement control have to be approximated.

Therefore, one of the great difficulties during the creation of a finite element model is the estimation of the acceptability of all the performed approximations through a process of validation. This is the only way to confer to the model some predicting power that should allow extrapolating the simulated experimentally visible data to new data exclusively accessible through numerical modelling. Spine segments *in vitro* testing can be used for model validation, provided that the testing conditions follow a specific protocol (Adams, 1995). Many of the published finite element lumbar spine models were not validated (Langrana *et al.*, 1991; Lavaste *et al.*, 1992; Kong *et al.*, 1998; Kim, 2000; Eberlein *et al.*, 2004; Noailly *et al.*, 2005) and for most of the validated or partially validated ones, validation was performed through a simple comparison of the computed ranges of motions and/or disc bulge with experimental results (Goel *et al.*, 1995a; Chen *et al.*, 2008; Natarajan and Andersson, 1999; Natarajan *et al.*, 1999; Zander *et al.*, 2001; Goel *et al.*, 2005). When in some studies the numerical results did not match with the *in vitro* data, the material properties were adjusted to the experimental stiffness, ranges of motion or intradiscal disc pressure changes (Shirazi-

Adl, 1994; Smit, 1996; Meakin and Hukins, 2001; Eberlein *et al.*, 2001; Sham *et al.*, 2005). These direct comparisons, including model fitting, may lead to a level of validation that is satisfactory depending on what is expected from the model. However, if the numerical study does not match exactly to the validated system, predictions may be erroneous. A given range of motions results from multiple interactions between ligaments, intervertebral disc and facets that are load dependent (Adams *et al.*, 1980; Tencer *et al.*, 1982). For example, the use of range of motion as only validating data might be insufficient to describe a whole segment biomechanical behaviour. Validations based on experimental intradiscal pressure changes may be questionable, since the standard deviations found in the literature are so large that the comparison is more qualitative than quantitative (Zander *et al.*, 2001). A clear illustration of validation problem appears in the finite element study of Wang *et al.* (Wang *et al.*, 1997) whose results under static conditions are compared to the a priori validated Shirazi-Adl's model (Shirazi-Adl *et al.*, 1986). While the ranges of motion and the annulus fibres maximum stress are similar, the facet contact forces diverge greatly. It shows that the load path is different in both models. In fact, when the number of variables usually introduced in such validation protocols is too small compared to the multiple interactions between the spinal components, various modelling possibilities may correspond to a given range of motion and intervertebral disc stress states. Therefore, as stated by Viceconti *et al.* (Viceconti *et al.*, 2005), the number of independent parameters in the model should be lower than the order of the experimental information. In most cases this condition can not be fulfilled, and therefore, the sensitivity of the model should be investigated in order to determine the most critical parameters.

Since the material properties are usually taken from some reference finite element studies published in the literature (Shirazi-Adl *et al.*, 1986; Ueno and Liu, 1987; Sharma *et al.*, 1995; Eberlein *et al.*, 2001), the greatest differences between the distinct lumbar spine models come mainly from the different geometrical approximations. Robin *et al.* (Robin *et al.*, 1994) modelled the influence of vertebrae and intervertebral discs linear dimensions on the ranges of motion and found that the parameters that affect the intervertebral disc height were the most important ones. They also investigated the effect of the zygapophysial joint facets orientation and concluded that the change in load transfer should be further examined. In their study on the effect of intervertebral disc geometrical changes, Natarajan *et al.* (Natarajan and Andersson, 1999) found a load case dependent correlation between disc geometry, annulus fibre stresses and facet contact forces. However, the role of the ligaments was not investigated. Dupont *et al.* (Dupont *et al.*, 2002) performed the same type of work including facet joint gap and facet angle variation, and concluded that ligament stresses were mainly influenced by disc height. Nonetheless, these studies aimed to investigate specifically the influence of single components and no conclusions were drawn about the possible consequences of the geometrical diversity on model validation.

The objective of the present Chapter was to examine the interaction between geometry and load transfer in order to show that, even if the geometry is not a determining factor from the point of view of the resulting ROM, it may affect considerably the relative role of the different model components. Comparing a pre-existing validated model (Smit, 1996) with a newly built one with similar material

properties, it is hypothesised that both models are able to predict similar motions and may be validated by comparison of in vitro segment motion data.

B. Development of a new model

In order to bring a response to the effect of the geometrical approximation, a new model was created through a reconstruction of geometrically accurate vertebrae and a revision of the intervertebral discs, cortex thicknesses, and ligaments and zygapophysial articular cartilages geometries. L3 and L5 were entirely remodelled, while for L4, only the posterior bony elements were modified. All the changes were guided by the determination of relative dimensions and shapes with respect to the pre-existing L4 model, X-ray observations, literature data, and measurements on a natural bone spine obtained from Sawbones®.

I. Vertebral bodies and intervertebral discs

The width and depths of the L3 and L5 vertebral bodies were modified from upper bony endplates measurements; the new dimensions remained proportional to L4 with proportionality ratios computed from the mean quantitative geometrical data given by Panjabi et al (Panjabi *et al.*, 1992). The characteristic wedge shape of the lumbar vertebrae (Amonoo-Kuofi, 1991; Rauschnig, 1991) was represented through slight modifications of the transversal orientations of the bony endplates in accordance to sagittal plane X-rays. The L4-L5 intervertebral disc resulted ventrally 10% higher than the L3-L4 one, which corresponds well with reported literature quantitative data (Frobin *et al.*, 1997). In the L3 vertebra model, a slight posterior concave shape was introduced in the transversal plane (Peitgen *et al.*, 1998; Rao, 1994). This concavity affected the L3-L4 intervertebral disc, making thinner the posterior annulus and inducing a more posterior position of the nucleus pulposus in accordance to common anatomical descriptions (Rao, 1994; White III and Panjabi, 1990). The final volume occupied by the L3-L4 nucleus pulposus was about 42% of the total disc volume which was within the range of 30-50% reported in the literature (White III and Panjabi, 1990). The L4-L5 nucleus pulposus was shifted to a more posterior location by a third of the distance between the centre and the posterior rim of the disc (Rao, 1994; Bogduk, 1997; White III and Panjabi, 1990). Finally, the thickness variations in the cortex of the vertebral bodies were modelled from reported quantitative data (Silva *et al.*, 1994; Ritzel *et al.*, 1998; Edwards *et al.*, 2001) (Fig. 3.1a,b).

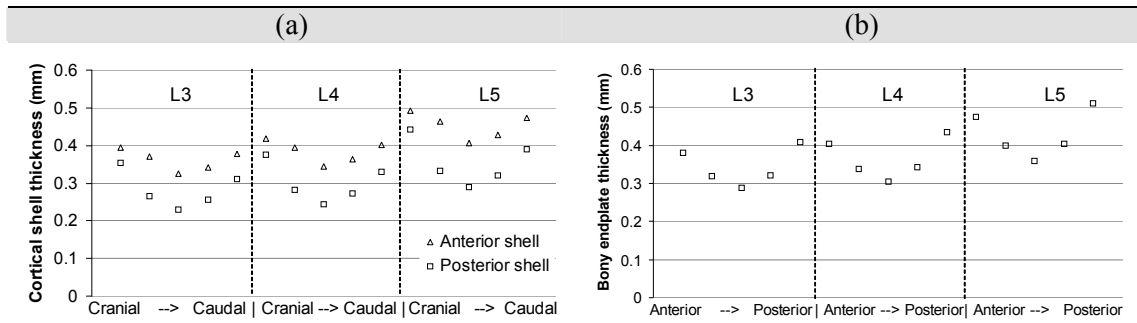


Figure 3.1: Thickness profiles used to model the vertebral cortex. a) Cortical shell. b) Bony endplate.

II. Pedicles and spinal canal

The morphological data of Panjabi et al (Panjabi *et al.*, 1992) were also used to correct the cross section and the orientation of the L3 and L5 pedicles with respect to the sagittal plane. The pedicles of L5 were given an oblique posterior and lateral course from the postero-lateral aspect of the vertebra, which is one of the specific anatomical characteristics of this vertebra (Rauschnig, 1991). The cross section changes introduced a decrease in the spinal canal sagittal diameter and an increase in the transverse diameter from L3 to L5, as indicated in the anatomical description performed by Rauschnig (Rauschnig, 1991). The vertebral bodies and pedicles geometrical updates made the vertebral foramen becoming more triangular from L3 to L5 which agreed with the literature (Rao, 1994).

III. Processes

The spinous process length was kept proportional to the vertebral body depth and was modified by using the ratio between the depths of the vertebra (mark (1) in Fig. 3.2a) and the distance from the centre of the upper endplate to the postero-inferior extremity of the process (mark (2) in Fig. 3.2a) (Panjabi *et al.*, 1992). In a similar way, the length of the transverse processes was calculated with the ratio between the width of the vertebra (mark (3) in Fig. 3.2b) and the distance between the extremities of the processes (mark (4) in Fig. 3.2b). The thicknesses and heights of both transverse and spinous processes were redefined from our own measurements on natural bone (Fig. 3.3c) and the inclinations of the transverse processes with respect to the transversal plane were modified in order to make them running slightly upwards (Rauschnig, 1991). The superior articular processes were reoriented to a more frontal position and the depths of the superior facets were increased (Tulsi and Hermanis, 1993). The inter-facet distances, as well as the inferior articular processes sagittal orientation were estimated from the corrected L4 articular processes and quantitative data from Panjabi et al (Panjabi *et al.*, 1993). The resulting synovial joint central and ventral gaps were respectively about 2 mm and 4 mm, which corresponded well to the reported literature

(Bogduk, 1997; Lewin *et al.*, 1962; Tanno *et al.*, 2004). On this new facet articular basis, the cartilage layers of both superior and inferior facets could be increased to about 1 mm at the centre in order to fill the gap (Lewin *et al.*, 1962).

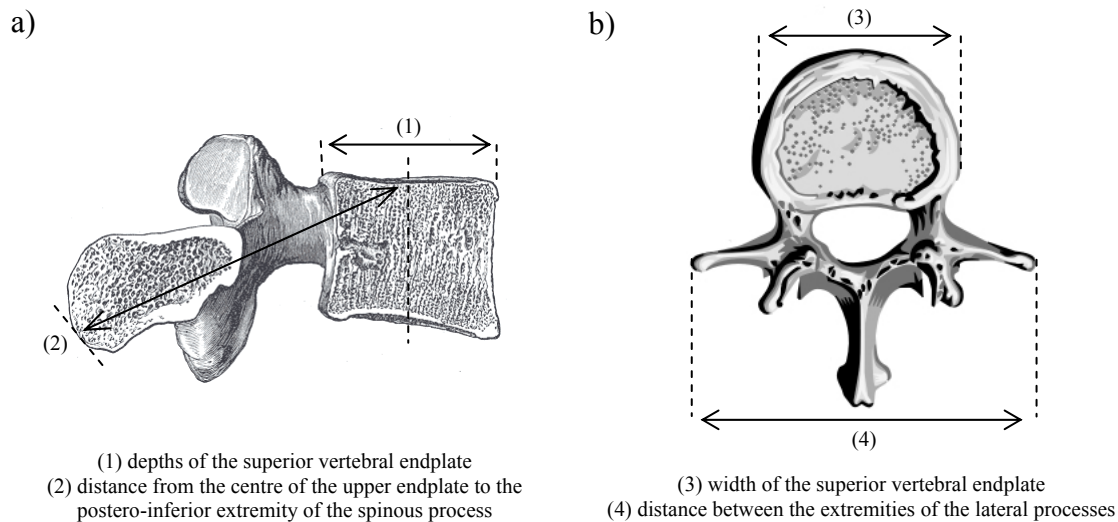


Figure 3.2: Measurements used to correct the geometry of the L4 lateral and spinous processes.

IV. Ligaments

All the geometrical changes previously cited are illustrated in Figure 3.3. As in the model described in Chapter 2, the ligaments were modelled by representing the action lines of the main resisting fibres with unidirectional elements (Fig. 3.3a,e). However, in the new model developed here, the number of elements and the attachment points that defined a ligament were modified according to anatomical data (Rissanen, 1960; Tkaczuk, 1968; Bogduk, 1997; Hayman *et al.*, 2000c; Hayman *et al.*, 2000b; Hayman *et al.*, 2000a; Yahia and Garzon, 1993; Panjabi *et al.*, 1991) in order to obtain a more distributed and realistic mechanical action (Fig. 3.3e, 3.4).

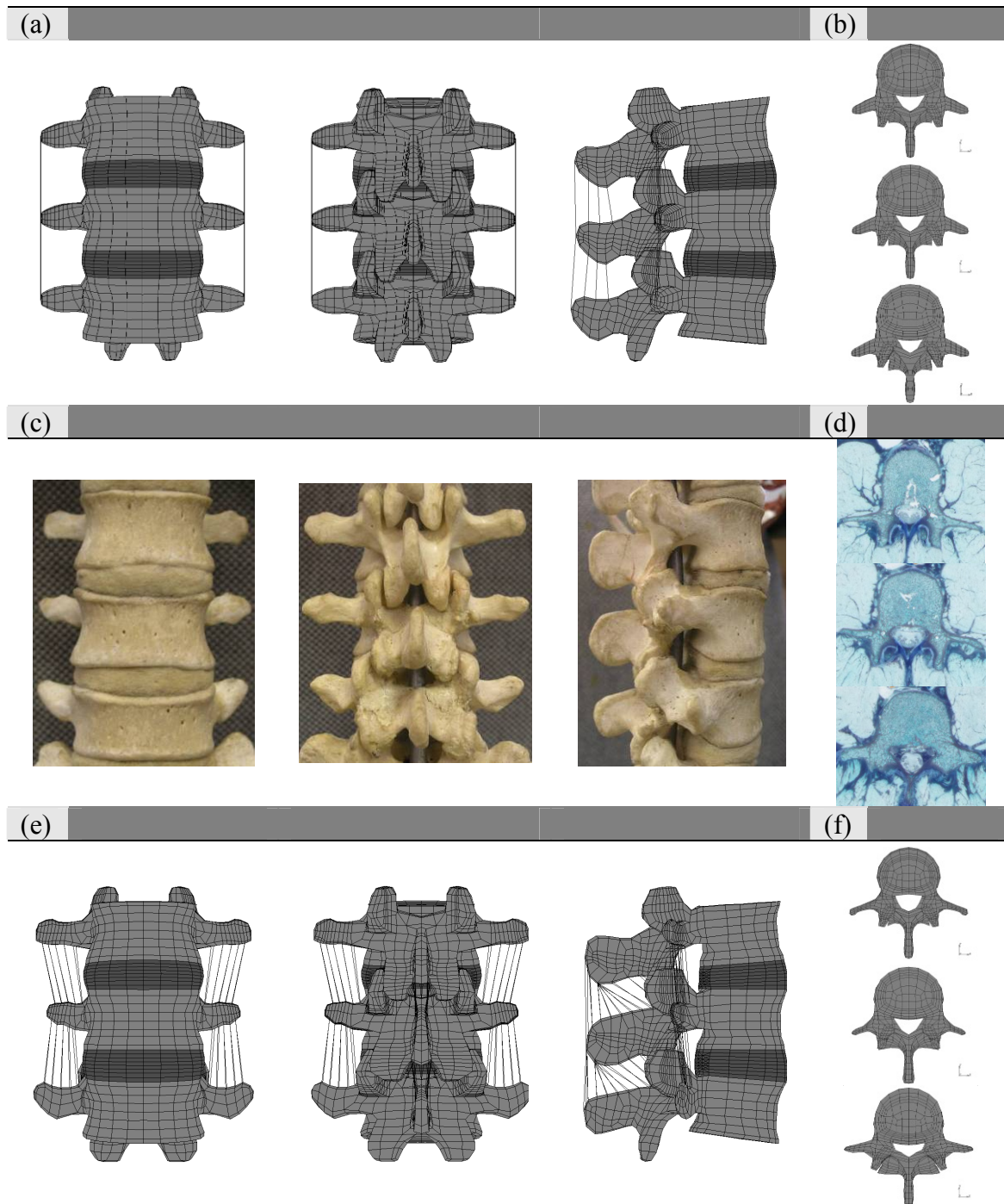


Figure 3.3: Frontal and sagittal views of the L3-L5 lumbar spine bi-segment and cranial view of the individual vertebrae that form the bi-segment. a) Old geometry, b) L3, L4 and L5 vertebrae of the old geometry, c) Natural bone, d) L3, L4 and L5 natural vertebrae, e) New geometry, f) L3, L4 and L5 vertebrae of the new geometry.

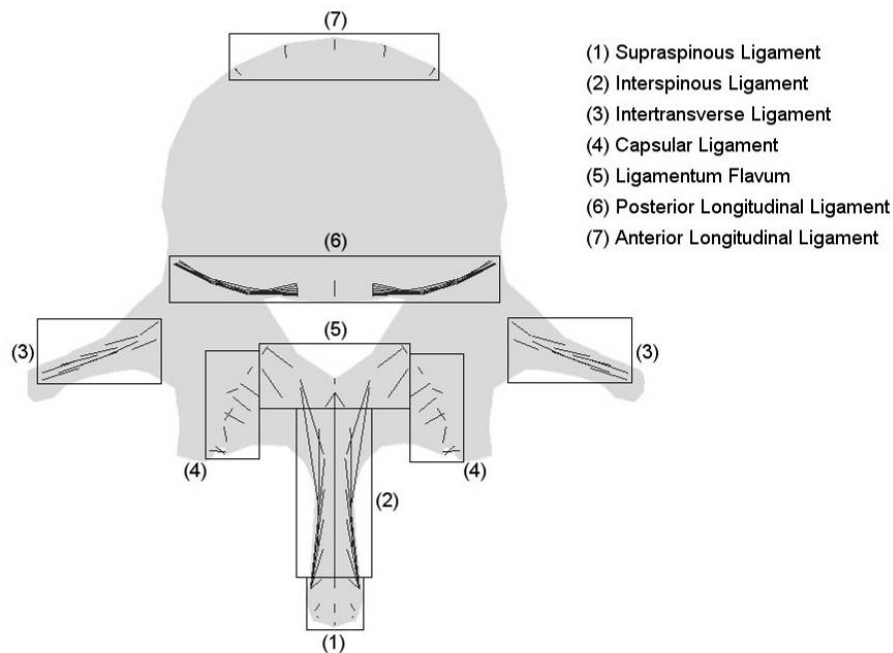


Figure 3.4: Coronal view showing the distribution of the ligament truss elements between L3 and L4.

V. Discussion on the quantitative geometry

Figures from 3.5a to 3.6 compare quantitatively the dimensions obtained after the model geometrical update with measurements on natural healthy vertebrae from different morphological studies.

a. Vertebral body linear dimensions

In a general manner, the vertebral body linear dimensions are in good accordance with the literature data (Fig. 3.5a). The unique parameter that was found out of the collected data range is the upper depth (EPDu) of the L4 vertebra. Nonetheless, the dimensions of this vertebra came directly from the original CT scan acquired by Smit (Smit, 1996) and it made no sense to modify them. The adjustment of the vertebral cortex thickness that followed the modification of the general vertebral body lengths influenced somewhat the final results. Thereby, while Panjabi et al (Panjabi *et al.*, 1992) did not reported significant variations between L4 and L5 (although L5 tended to be slightly smaller), the transversal dimensions of the modelled vertebra (EPDu,l, EPWu,l) generally increased continuously from L3 to L5. For the upper bony endplates (EPDu, EPWu), this was in accordance with the data reported by Scoles et al (Scoles *et al.*, 1988) and Ericksen (Ericksen, 1976). The fact that the new transversal dimensions of the model were guided by the upper bony endplate led to some discrepancies with the data of Panjabi et al (Panjabi *et al.*, 1992) with respect to the lower bony endplate length

(EPD1) and width (EPW1). The authors reported that the largest lower endplates were found for the L3 vertebra in accordance with the need to resist to the horizontal shear forces that are larger at the most frontal point of the lordosis curvature. In the model, this was not represented, however, from L3 to L5, the inferior endplate depths follow the trend found by Krag et al (Krag *et al.*, 1988). Berry et al (Berry *et al.*, 1987) also reported L3 endplates smaller than L4. For the L3 and L4 inferior endplate widths, model dimensions resulted in accordance with Panjabi et al (Panjabi *et al.*, 1992) and from L4 to L5, the trend was that described by Berry et al (Berry *et al.*, 1987).

b. Spinal canal and pedicles linear dimensions

The width of the spinal canal (SCW) increased from L3 to L5 and corresponded generally well with the values from the literature (Fig. 3.5b). The depth (SCD) was out of range for L4. However, as for the depth of the upper L4 endplate, this dimension came directly from the original CT scan. While the data from the literature generally reported an increasing depth from L3 to L5, the model presented an inversed trend principally due to the posterior concavity introduced in the L3 vertebral body. From L4 to L5, the depth diminution was about 0.3mm, and was due to the difference in the posterior cortical shell thickness and to the mesh changes when the orientations of the pedicles were modified in L5. Nevertheless, as stated in Section B.II, the decrease in depth of the spinal canal from L1 to L5 was qualitatively documented (Rauschnig, 1991). The larger pedicle height (PDH) in L4 than in L3 was in accordance with the measurements of Panjabi et al (Panjabi *et al.*, 1992), while the slightly lower height of the L5 pedicles compared to L4 corresponded rather to the data of Zindrick et al (Zindrick *et al.*, 1987). In fact the cross section of the pedicles was corrected principally through the modification of their width (PDW) in order to match with the spinal canal width.

c. Inter-process distances and processes lengths

Some inter-process distances, as the distance between the tips of the transverse processes (TPW) of L3 and the distances between the inferior articular facets (IFWi) of L3 and L4 diverged somewhat from the literature data range (Fig. 3.5c). The length between the transverse processes of L4 came directly from the original CT scan, and the inferior inter-facet distances were computed from the ratio between the superior and inferior facets of the same zygapophysial joint with values obtained from Panjabi et al (Panjabi *et al.*, 1993). The distance between the superior facets (IFWu) was directly fitted to Panjabi et al (Panjabi *et al.*, 1993). Hence, a coherent joint geometry with a reasonable articular gap could be ensured (Section B.III). Note that the number of available quantitative data for comparison with the model dimensions was fairly limited.

d. Angular dimensions

All the angular data for endplate orientation (Epltu, Epltl) were below the literature data range (Fig. 3.5d). Nonetheless, the values reported by Panjabi et al (Panjabi *et al.*, 1992) were tried out and led to very inclined endplates and distorted intervertebral disc space that was in appearance far from the information provided by in-sagittal plane radiographs. The angle change was then qualitatively performed from the radiograph observations and as shown in Figure 3.5a, this led to anterior and posterior heights of the vertebrae (VBHa, VBHb) that were in good accordance with the quantitative literature. Pedicles sagittal and transversal orientation (PDls, PDlt) were generally within the range of collected quantitative data and from L3 to L5, the angle changes followed the tendencies reported by Panjabi et al (Panjabi *et al.*, 1992). Because facet depth and orientation are related (Chap. 1), both data were taken from a common study (Section B.III). Therefore, the superior facet orientation with respect to the sagittal plane (Ss) was adjusted to the data of Tulsi and Hermanis (Tulsi and Hermanis, 1993) and the inferior facet angle was modified in order to keep the same relation between superior and inferior facet orientations as calculated from Panjabi et al (Panjabi *et al.*, 1993). This explains, as for the inter-facet distances why the inferior facet sagittal orientation (Si) is systematically out of range (Fig. 3.5d). No data were given in Figure 3.5d for the L3 superior facets and L5 inferior facets, since these articular surfaces do not participate to the bi-segment motion and their respective orientations were not modified.

e. Conclusion

Most of the 60 different dimensions that were checked in the model were within the range of values offered by the selected literature. Nonetheless, many features such as spinal canal sizes, pedicle sizes, pedicle orientation, inter-facet distances, facets orientation, endplate transversal orientation and intervertebral disc height, etc... were linked together and could not be independently fitted to the reported measurements. Moreover, most of the dimensions of the pre-existing L4 came directly from the original CT scan and were not modified even if they were not in accordance with the literature. This resulted in 13 dimensional values that were out of the reported quantitative data range. For that reason, the qualitative evaluation of the specific morphological characteristics that appeared in the lumbar spine bi-segment model through the geometrical update was highly important (Sections B.I-IV).

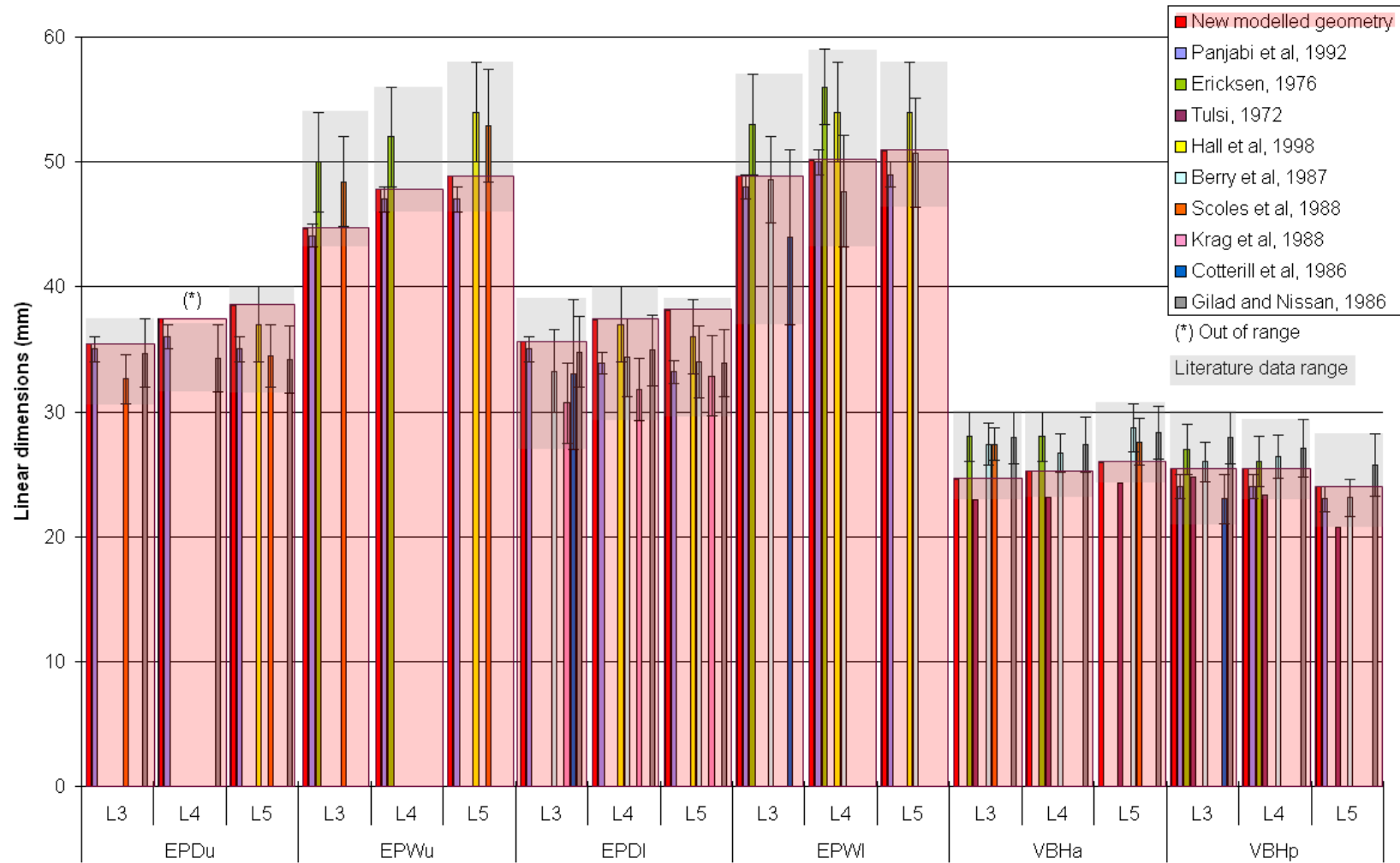


Figure 3.5a: Comparison of the model vertebral body linear dimensions with quantitative morphological data from the literature. Significances of the abbreviations are given in Fig. 3.6a,b.

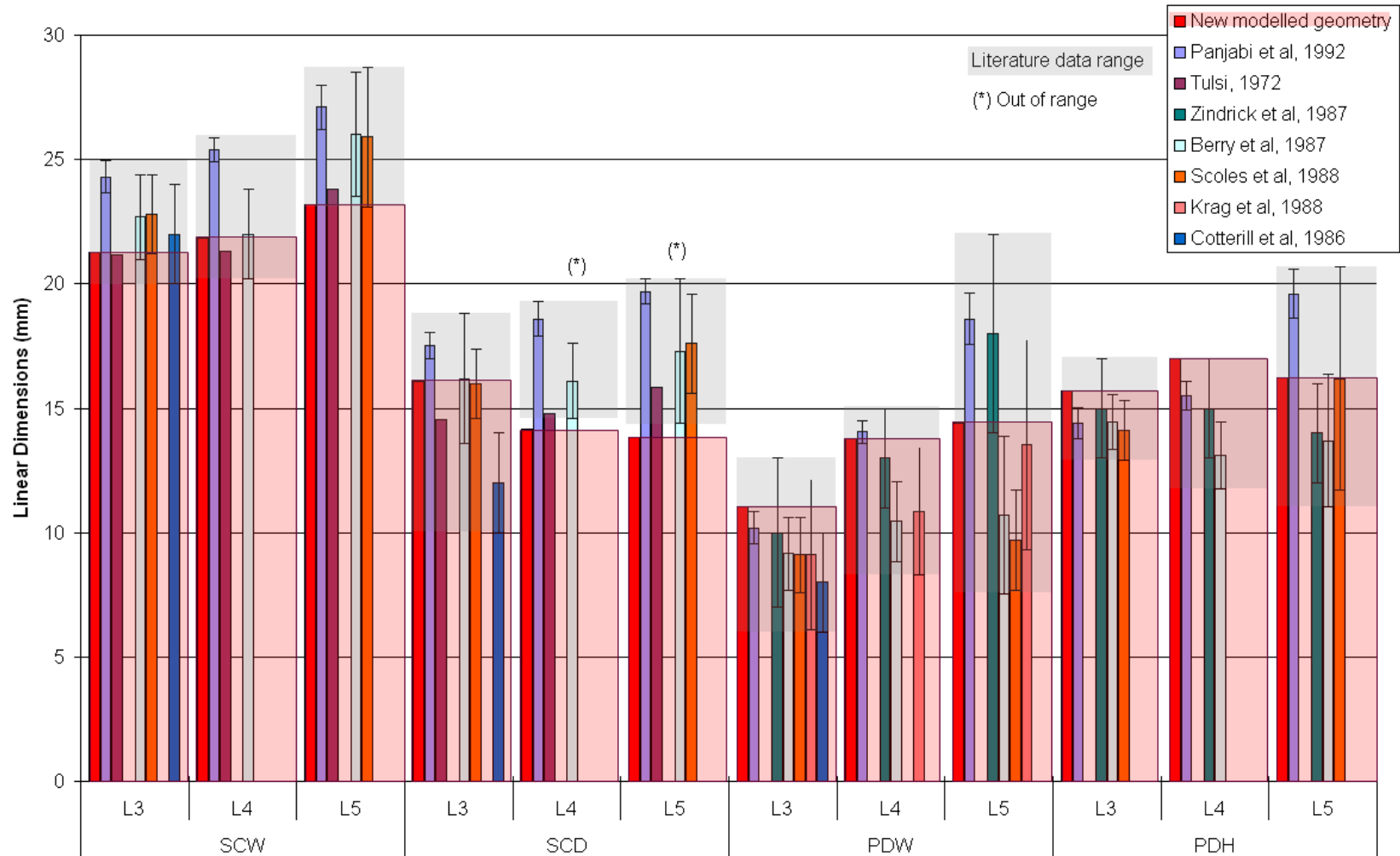


Figure 3.5b: Comparison of the model spinal canal and pedicles dimensions with quantitative morphological data from the literature. Significances of the abbreviations are given in Fig. 3.6d.

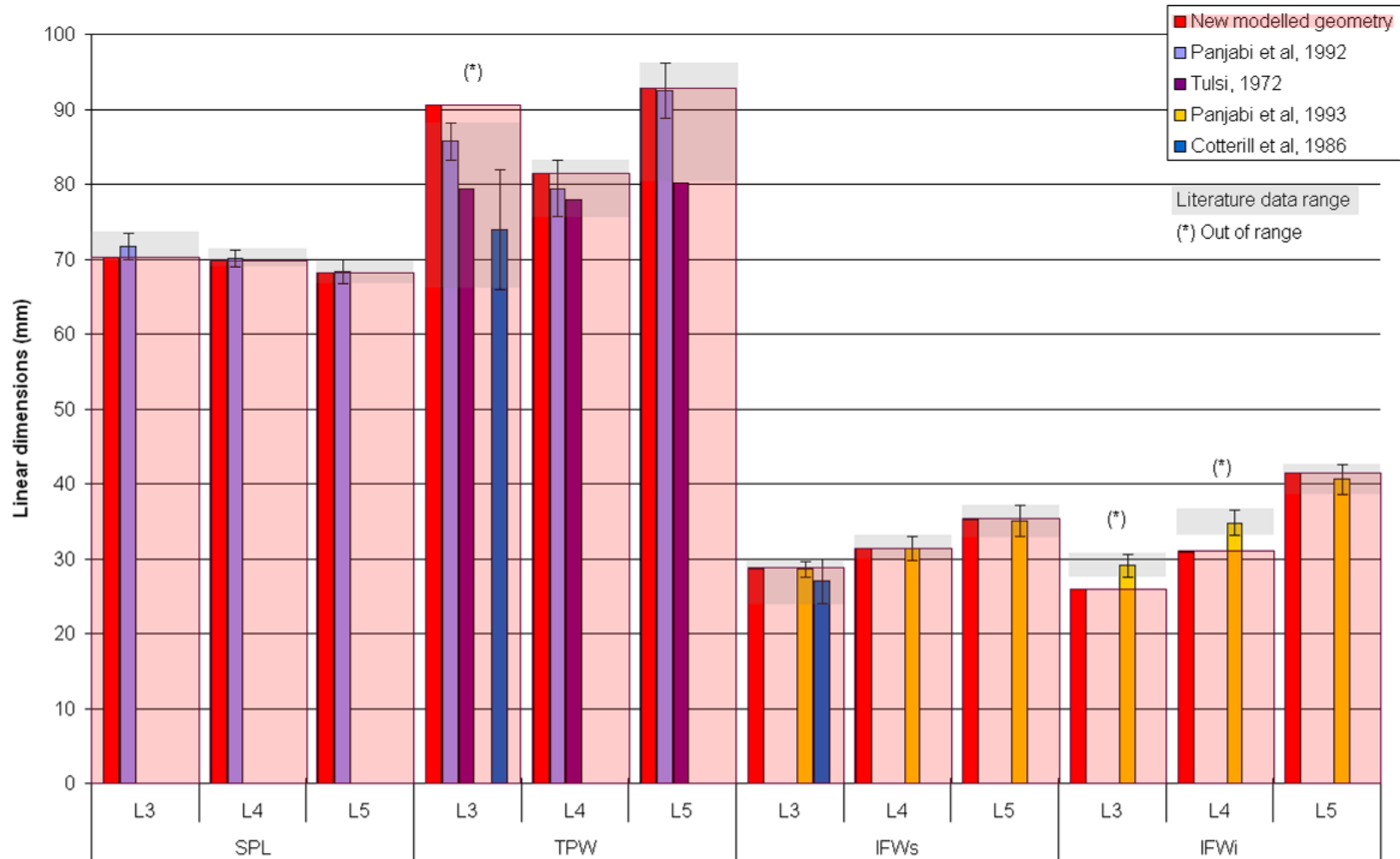


Figure 3.5c: Comparison of the distances between the different bony posterior elements of the model with quantitative morphological data from the literature. Significances of the abbreviations are given in Fig. 3.6a,b,e.

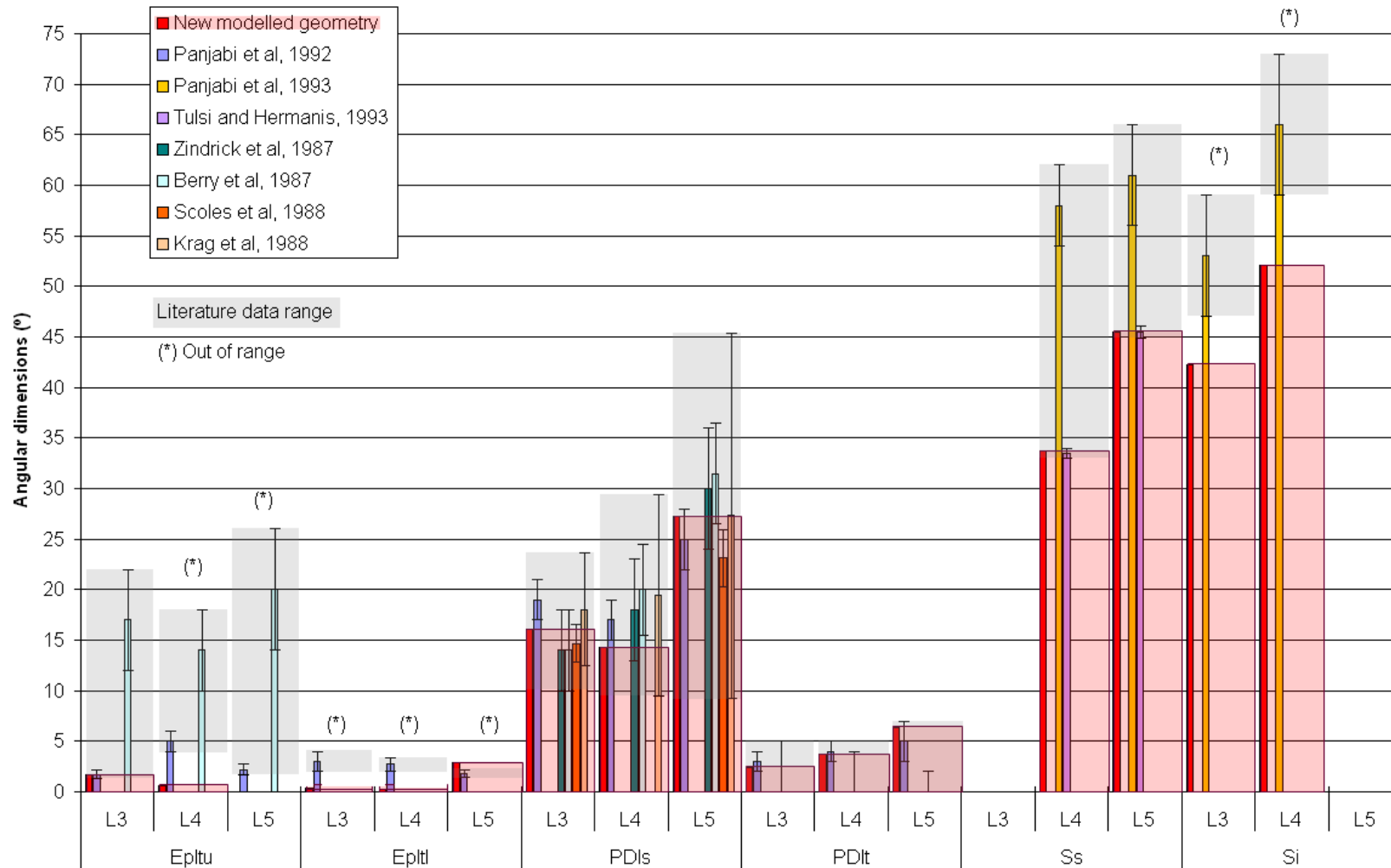


Figure 3.5d: Comparison of the model vertebrae angular dimensions with quantitative morphological data from the literature. Significances of the abbreviations are given in Fig. 24b,c,d,f. The value of Si is the same angle as represented in Fig. 3.6e applied to the inferior articular processes.

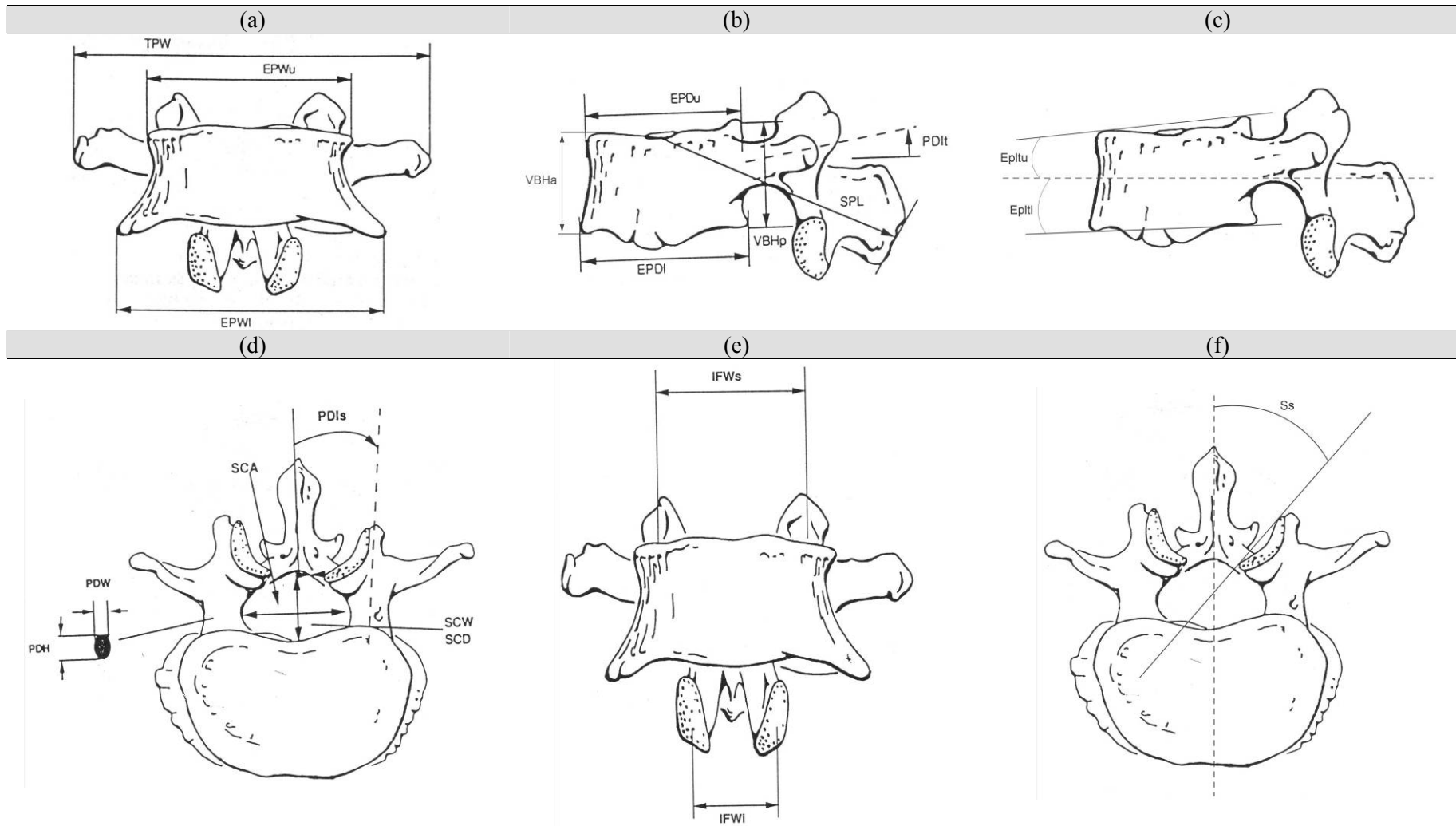


Figure 3.6: Linear and angular geometrical parameters used in Figures 3.5a,b,c,d (adapted from (Panjabi et al., 1992)). a),e) Frontal view, b),c) Sagittal views, d),f) Cranial views.

C. Models comparison

I. Method

Both load magnitude and type of boundary conditions were defined according to a Spine Tester (WISI) developed at the Institut für Unfallchirurgische Forschung und Biomechanik (UFB - Ulm Universität, Ulm, Germany) (Wilke *et al.*, 1994) (Fig. 3.7). Experimental ranges of motion measured with this system were used in order to compare the models. Hence, according to the testing protocol, for both the old and the new geometry, 7.5N.m axial, sagittal and frontal rotational moments were applied on the top of L3 and the lower half of L5 was fixed in all directions. Pure moments were applied on the mesh of the model as described in Chapter 2. For each motion, successive removals of ligaments and cartilages were made to determine the influence of the spinal components (Table 3.1). Note that in this context, 7.5N was the maximum tested moment magnitude ensuring that no failure will occur in the reduced segments (Heuer *et al.*, 2007b). Ranges of motion, facet contact forces, ligament and intervertebral disc stresses were computed and the relative differences between the incomplete geometries and their respective intact versions (old and new) were analysed:

$$\text{relative difference} = \frac{|\text{incomplete geometry value} - \text{complete geometry value}|}{\text{complete geometry value}} \quad (3.1)$$

In order to avoid confusion in the results presented in the following sections, it is interesting to note from Equation (3.1) that the change of relative difference, calculated between two successive component resections, has not any direct relation with the relative numerical gain or loss of the studied value. Since the variations are always reported to a common initial state, the sign and magnitude of the difference of relative differences between two resections only indicate if the values progress toward or away from those of the defined initial state.

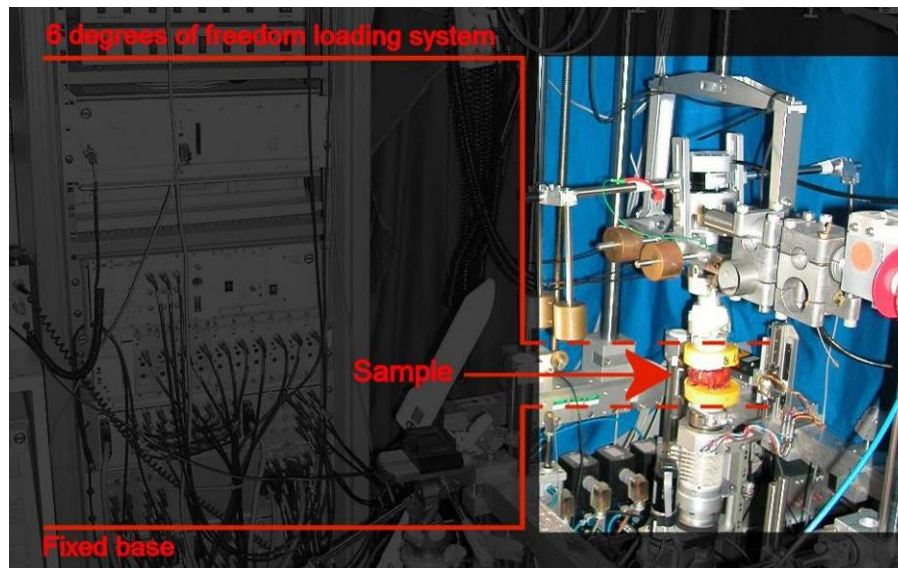

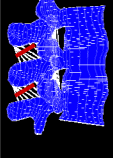
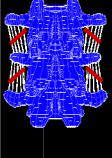
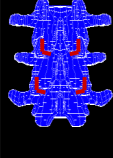
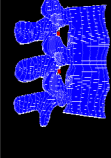
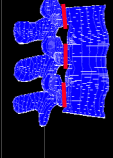
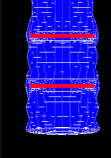
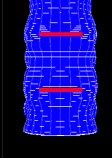
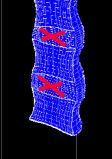


Figure 3.7: Spine tester used at the Institut für Unfallchirurgische Forschung und Biomechanik – Universität Ulm, Ulm, Germany (Wilke et al., 1994).

Table 3.1: Description of the successive resections of spinal components performed on the models.

Model	woSSL	woISL	woITL	woCL	woLF	woBPE	woPLL	woALL	woNP
Removed component	Supraspinous ligament	Interspinous ligament	Intertransverse ligament	Capsular ligament	Ligamentum Flavum	Bony posterior elements	Posterior longitudinal ligament	Anterior longitudinal ligament	Nucleus pulposus
									

In both models, the mesh was refined in order to obtain optimal contact detections at the zygapophysial joints (Fig. 3.8a,b) and smooth deformed curves both at the annulus and nucleus outlines (Fig. 3.8c,d). Moreover, in the new geometry, the cortex was subdivided in two layers in the thickness direction, in order to obtain a finer load distribution at the vertebral body peripheries. The type and number of elements used for both geometries are presented in Table 3.2. The material properties remained the same as those used for the old model (Table 2.1). Pre-processing, processing and post-processing were performed with MSC Marc Mentat 2005r2 under large displacements and large strains.

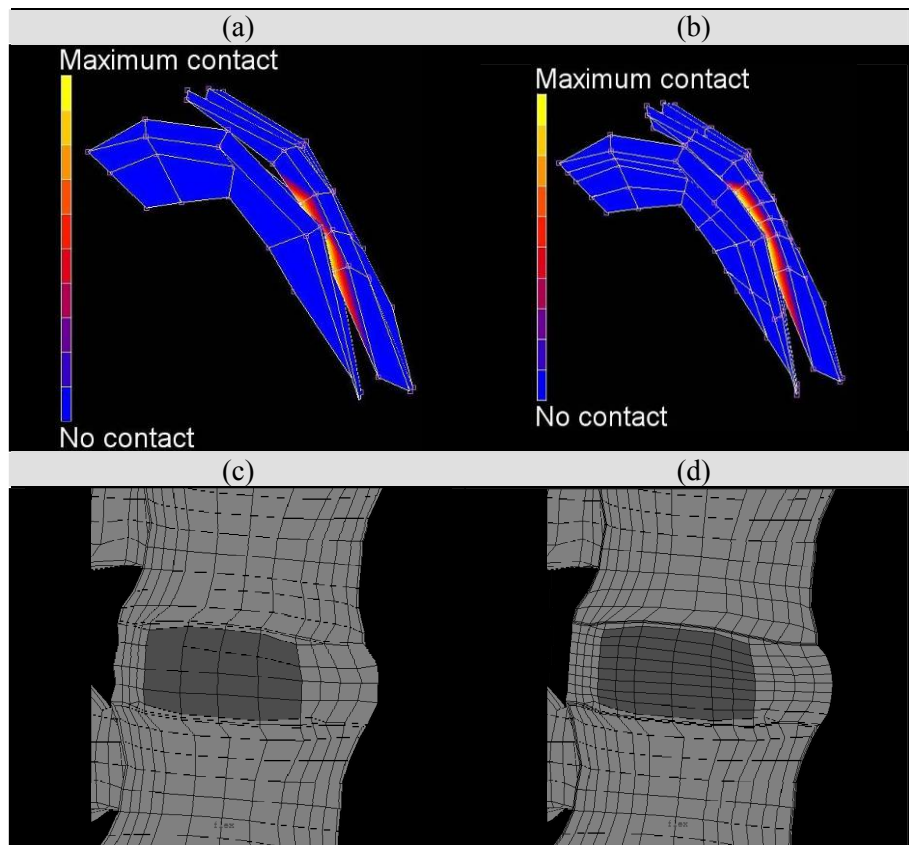


Figure 3.8: Effects of mesh refinement. a),b) Cranial view of the right cartilage facet layers mid-transversal plane under 7.5Nm left axial rotation before and after mesh refinement. c),d) Sagittal cut of the anterior part of the L4-L5 level L3-L5 lumbar spine bi-segment model under 7.5Nm flexion before and after mesh refinement.

Table 3.2: Numbers and types of elements used for the modelling of the old and new geometries.

	8 nodes isoparametric hexaedral elements	9 nodes isoparametric Hermann elements	8 nodes Rebar elements	2 nodes three dimensional truss elements
Old geometry	8492	2016	1280	130
New geometry	9812	2016	1280	402

II. Results

a. Flexion

All the numerical results about the biomechanical effect of the successive removals on both models are reported in Figures from 3.9 to 3.13 at the end of the section. Nonetheless, each of the subsection concerning a specific removal contains a Table that qualitatively summarises the major effects of the current component suppression (Tables 3.3 – 3.8).

1) Supraspinous ligament removal

In flexion, the supraspinous ligament (SSL) removal had no effect on the old geometry; however in the new geometry, the L4-L5 segment became slightly stiffer (Fig. 3.9a). As shown by the relative differences (Fig. 3.9b), the increase did not overcome 4%, and it was almost inexistent at the L3-L4 level. Nonetheless, contact forces results indicated that the absence of SSL nearly doubles the role of contact in the L3-L4 segment of the new geometry (Fig. 3.10). The L4-L5 range of motion (ROM) decrease associated with the SSL suppression also induced lower anterior ligaments stresses with a change of up to 9% for the posterior longitudinal ligament (PLL) (Fig. 3.11). The L4-L5 ligamentum flavum (LF) stress was lowered of a similar amount, and the intertransverse ligament (ITL) stress decreased about twice more (Fig. 3.12). Nonetheless, the interspinous ligament (ISL) and capsular ligaments (CL) became more tensed, respectively at the L4-L5 and L3-L4 levels. In the intervertebral disc annulus fibrosus, while the fibres of the L3-L4 level were not affected by the SSL removal, those of the L4-L5 level were relaxed to about 7% of their initial stress state (Fig. 3.13). As shown in Figure 3.12a, in the intact models, SSL was only stressed in the new geometry and its suppression had not any influence on the old geometry (Fig. 3.9b, 3.12b, 3.13b).

Table 3.3: Qualitative representation of the maximum effect of the supraspinous ligament suppression on the different studied mechanical criteria under flexion.

Model	Range of motion		Facet contact force		Anterior ligament stress		Posterior ligament stress		Annulus fibrosus stress	
	L3-L4	L4-L5	L3-L4	L4-L5	L3-L4	L4-L5	L3-L4	L4-L5	L3-L4	L4-L5
Old geometry	-	-	-	-	-	-	-	-	-	-
New geometry	-	~	III	-	~ (PLL)	I (PLL)	~ (CL)	II (ITL)	~ (ANT)	I

-: Relative difference < 2% | ~: Relative difference ≤ 5% | I: Relative difference < 10% | II: Relative difference < 50% | III: Relative difference < 100%.

2) Interspinous ligament removal

The further suppression of the ISL increased the rotations at the L4-L5 level of both geometries and while in the old geometry, the anterior ligament and the AF fibre stresses increased beyond their original values (Fig. 3.11a, 3.13a), in the new geometry, the L4-L5 segment returned to a similar value as in its intact version (Fig. 3.9a). This was translated by a decrease of the relative differences of the ligaments and annulus stresses at this level (Fig. 3.11b, 3.12b, 3.13b). At the L3-L4 level, the absence of ISL induced a loss of contact in both geometries (Fig. 3.10a), the new geometry being more than twice more sensitive than the old one.

Table 3.4: Qualitative representation of the maximum effect of the interspinous ligament suppression on the different studied mechanical criteria under flexion.

Model	Range of motion		Facet contact force		Anterior ligament stress		Posterior ligament stress		Annulus fibrosus stress	
	L3-L4	L4-L5	L3-L4	L4-L5	L3-L4	L4-L5	L3-L4	L4-L5	L3-L4	L4-L5
Old geometry	-	I	I	-	~ (PLL)	II (PLL)	II (ITL)	III (ITL)	~	II (LAT)
New geometry	-	*	II*	-	*	*	II (LF)	II (ITL)	~*	I*

-: Relative difference < 2% | ~: Relative difference ≤ 5% | I: Relative difference < 10% | II: Relative difference < 50% | III: Relative difference < 100%.

Uppercase * indicates that a relative difference decrease occurred with respect to the previous component suppression.

3) Intertransverse ligament removal

After ITL was taken away, the L4-L5 ROM of both models increased slightly (Fig. 3.9a). While the anterior longitudinal ligament (ALL) stress did not change significantly, the PLL stress of the new geometry was increased of about 8% (Fig. 3.11b) and the LF stress was increased of about 12% (Fig. 3.12b). In the AF, and for both geometries, the lateral fibre stresses rose to values corresponding to relative differences about 5% greater than for the previous resection (Fig. 3.13).

Table 3.5: Qualitative representation of the maximum effect of the intertransverse ligament suppression on the different studied mechanical criteria under flexion.

Model	Range of motion		Facet contact force		Anterior ligament stress		Posterior ligament stress		Annulus fibrosus stress	
	L3-L4	L4-L5	L3-L4	L4-L5	L3-L4	L4-L5	L3-L4	L4-L5	L3-L4	L4-L5
Old geometry	-	I	I ^o	-	~ (PLL)	II (PLL)	~ (CL)	II (CL)	~	II (LAT)
New geometry	-	~	II ^o	-	~ (PLL)	I (PLL)	II (LF)	II (LF)	*	II (LAT)

-: Relative difference < 2% | ~: Relative difference ≤ 5% | I: Relative difference < 10% | II: Relative difference < 50%

Uppercase * indicates that a relative difference decrease occurred with respect to the previous component suppression. Uppercase ^o indicates that no significant change occurred with respect to the previous component suppression (relative difference change ≤ 5%).

4) Capsular ligament removal

As shown in Fig. 3.9b, among all the removed components, CL had the largest effect on the L3-L4 segment of both geometries. The new geometry was nonetheless about two-folds more affected. In the new and old models, the ligament suppression induced a large ROM increase (Fig. 3.9a). However, while the L3-L4 contact forces also rose in the new geometry, they vanish completely in the old one (Fig. 3.10a). The new geometry L3-L4 LF, PLL, and AF fibres stresses increased significantly (Fig. 3.11 – 3.13) with relative differences ranging between about 450% (Fig. 3.12b) and 1200%

(Fig. 3.11b). For both models, the posterior AF fibres were the most affected ones. In the old geometry, the ligaments were not as sensitive to CL removal as in the new geometry, and the LF and PLL stress changes remained between about 5 and 10 times lower (Fig. 3.11b,3.12b). At the L4-L5 level, the suppression of CL induced a loss of ROM that was proportionally larger for the new geometry than for the old one (Fig. 3.9). Such decrease combined with the L3-L4 ROM increase that simultaneously occurred, made that both the L3-L4 and the L4-L5 segments acquired similar flexibilities. The loss of mobility at the L4-L5 level also resulted in less stress in the corresponding annulus fibres (Fig. 3.13) and of the anterior ligament (Fig. 3.11). In the old geometry, the LF returned to its original stress state (Fig. 3.12).

Table 3.6: Qualitative representation of the maximum effect of the capsular ligament suppression on the different studied mechanical criteria under flexion.

Model	Range of motion		Facet contact force		Anterior ligament stress		Posterior ligament stress		Annulus fibrosus stress	
	L3-L4	L4-L5	L3-L4	L4-L5	L3-L4	L4-L5	L3-L4	L4-L5	L3-L4	L4-L5
Old geometry	III	-*	IV	-	V (PLL)	I* (ALL) -II (PLL)	II (LF)	-* (LF)	IV (POST)	I* (ANT) -II (PLAT)
New geometry	IV	I	VI	-	VI (PLL)	II (ALL)	V (LF)	II (LF)	VI (POST)	II (ANT)

-.: Relative difference < 2% | ~: Relative difference ≤ 5% | I: Relative difference < 10% | II: Relative difference < 50% | III: Relative difference < 100% | IV: Relative difference < 200% | V: Relative difference < 500% | VI: Relative difference ≥ 500%
 Uppercase * indicates that a relative difference decrease occurred with respect to the previous component suppression.

Symbols in red cells represent the maximum relative difference change induced by the removal when change occurs in a component different from that associated to the maximum relative difference value.

5) Ligamentum flavum removal

After CL suppression, the successive removal of LF induced one of the most important further increases of ROM (relative difference increase of about 18%) in the L3-L4 segment of the new geometry (Fig. 3.9) and this change induced a complete lost of the L3-L4 facet contact (Fig. 3.10a). Neither the new geometry L4-L5 level nor the old geometry seemed to be significantly affected (Fig. 3.9b). The new geometry L3-L4 ALL and PLL stresses were significantly increased (Fig. 3.11a). At the L4-L5 level, almost no changes were computed in the ALL. However, a stress increase of about 6% contributed to restore partly the PLL tensile state to the value that had been predicted before CL removal (Fig. 3.11b). The AF fibres of the new geometry were also the most affected ones with posterior stress increases up to more than 100% (Fig. 3.13). The anterior fibres resulted only 10% more tensed and the relative differences rose progressively toward the posterior area. At the L4-L5 level, the changes in the new geometry did not overcome 5% (Fig. 3.13b). Nonetheless, while the anterior and lateral AF fibres stresses tended to decrease, the posterior fibres became slightly more tensed (Fig. 3.13a). In the old geometry, the AF fibres stresses were increased at all locations (Fig. 3.13a). However, the changes were never higher than 9% (Fig. 3.13b).

Table 3.7: Qualitative representation of the maximum effect of the ligamentum flavum suppression on the different studied mechanical criteria under flexion.

Model	Range of motion		Facet contact force		Anterior ligament stress		Annulus fibrosus stress	
	L3-L4	L4-L5	L3-L4	L4-L5	L3-L4	L4-L5	L3-L4	L4-L5
Old geometry	III ^o	~	IV ^o	-	V (PLL)	II (PLL)	IV (POST)	II (LAT)
New geometry	IV	I*	VI*	-	VI ⁺ (PLL)	II (ALL) -I (PLL)	VI ⁺ (POST)	II (ANT) -I (LAT)

-: Relative difference < 2% | ~: Relative difference ≤ 5% | I: Relative difference < 10% | II: Relative difference < 50% | III: Relative difference < 100% | IV: Relative difference < 200% | V: Relative difference < 500% | VI: Relative difference ≥ 500%
 Uppercase * indicates that a relative difference decrease occurred with respect to the previous component suppression. Uppercase ^o indicates that no significant change occurred with respect to the previous component suppression (relative difference change ≤ 5%).
 Uppercase ⁺ indicates further relative difference increases ≥ 100% for pre-existing values ≥ 500%.

Symbols in red cells represent the maximum relative difference change induced by the removal when change occurs in a component different from that associated to the maximum relative difference value.

6) Bony posterior elements removal

As shown in Figure 3.9, the ROM changes induced by the bony posterior elements (BPE) were not significant. However, and while no contact had been predicted before the suppression of the BPE (Fig. 3.10a) the PLL stresses tended to decrease for both models (Fig. 3.11). The maximum stress decrease corresponded to a relative difference about 20% lower than before the bony elements suppression, and it was computed for the new geometry L3-L4 PLL (Fig. 3.11b). At the L4-L5 level, both geometries were similarly affected with relative difference changes of about 12%. In the AF, the lateral stresses were generally increased with a maximum at the L3-L4 level of the new geometry, where a percentage of about 35 % larger with respect to the previous configuration (LF removal) was predicted (Fig. 3.13). In the new geometry, the L3-L4 postero-lateral AF area was also more loaded, although the associated relative difference change did not overcome 10%. At the L4-L5 level, the old geometry lateral AF fibres were the most affected with a relative differences increase of about 14%.

Table 3.8: Qualitative representation of the maximum effect of bony posterior elements suppression on the different studied mechanical criteria under flexion.

Model	Range of motion		Anterior ligament stress		Annulus fibrosus stress	
	L3-L4	L4-L5	L3-L4	L4-L5	L3-L4	L4-L5
Old geometry	III ^o	~ ^o	V* (PLL)	I ^o (ALL) -II (PLL)	IV ^o (POST) +II (LAT)	II (LAT)
New geometry	IV ^o	I ^o	VI* (PLL)	II ^o (ALL) -II (PLL)	VI* (POST) +II (LAT)	II ^o (ANT) +I (LAT)

-: Relative difference < 2% | ~: Relative difference ≤ 5% | I: Relative difference < 10% | II: Relative difference < 50% | III: Relative difference < 100% | IV: Relative difference < 200% | V: Relative difference < 500% | VI: Relative difference ≥ 500%
 Uppercase * indicates that a relative difference decrease occurred with respect to the previous component suppression. Uppercase ^o indicates that no significant change occurred with respect to the previous component suppression (relative difference change ≤ 5%).

Symbols in red cells represent the maximum relative difference change induced by the removal when change occurs in a component different from that associated to the maximum relative difference value.

7) Posterior longitudinal ligament removal

PLL removal allowed the L4-L5 level of both geometries recovering the flexibility that was lost after the suppression of CL (Fig. 3.9). With respectively 16% and 26% of relative difference changes associated to mobility increases, the L3-L4 and L4-L5 levels of the old geometry appeared to be more sensitive than those of the new geometry where the ROMs were not significantly increased (Fig. 3.9b). At the L3-L4 level, the ALL tensile stresses were lowered in both geometries, although the new geometry was two fold more affected with relative differences about 20% inferior (Fig. 3.11). At the L4-L5 level, the old geometry resulted more sensitive to PLL suppression, and the ALL tensile stress decrease involved a relative difference change of about 20% against 6% in the new geometry (Fig. 3.11b). In the AF, and in both models, except at the old geometry L4-L5 level, the anterior AF fibres resulted less tensed after the PLL was taken away. All the fibres from other locations became more stressed, with a relative difference increase peak of about 120% in the old geometry L3-L4 posterior fibres (Fig. 3.13b). The following greatest changes were predicted in the postero-lateral area of the new geometry AF ($\approx 70\%$), and in the old geometry AF lateral area ($\approx 50\%$).

Table 3.9: Qualitative representation of the maximum effect of posterior longitudinal ligament suppression on the different studied mechanical criteria under flexion.

Model	Range of motion		Anterior ligament stress		Annulus fibrosus stress	
	L3-L4	L4-L5	L3-L4	L4-L5	L3-L4	L4-L5
Old geometry	III	II	II* (ALL)	II (ALL)	V (PLAT) +II (LAT)	IV (LAT)
New geometry	IV°	I°	III* (ALL)	II° (ALL)	VI (POST) +II (PLAT)	II (LAT)

-: Relative difference < 2% | ~: Relative difference $\leq 5\%$ | I: Relative difference < 10% | II: Relative difference < 50% | III: Relative difference < 100% | IV: Relative difference < 200% | V: Relative difference < 500% | VI: Relative difference $\geq 500\%$
 Uppercase * indicates that a relative difference decrease occurred with respect to the previous component suppression. Uppercase ° indicates that no significant change occurred with respect to the previous component suppression (relative difference change $\leq 5\%$).
 Symbols in red cells represent the maximum relative difference change induced by the removal when change occurs in a component different from that associated to the maximum relative difference value.

8) Anterior longitudinal ligament removal

Whatever the considered model, the suppression of ALL did not induce any significant change in the ROMs (Fig. 3.9). In the AF, only the anterior fibres of the new geometry were affected, becoming up to 57 % more stressed at the L3-L5 level when compared to the intact model (Fig. 3.13). The L4-L5 level was less sensitive with about 17% of relative difference increase (Fig. 3.13b).

Table 3.10: Qualitative representation of the maximum effect of anterior longitudinal ligament suppression on the different studied mechanical criteria under flexion.

Model	Range of motion		Annulus fibrosus stress	
	L3-L4	L4-L5	L3-L4	L4-L5
Old geometry	III ^o	II ^o	V ^o (PLAT)	IV ^o (LAT)
New geometry	IV ^o	I ^o	VI ^o (POST)	II ^o (LAT) -II (ANT)

-: Relative difference < 2% | ~: Relative difference ≤ 5% | I: Relative difference < 10% | II: Relative difference < 50% | III: Relative difference < 100% | IV: Relative difference < 200% | V: Relative difference < 500% | VI: Relative difference ≥ 500%
Uppercase ^o indicates that no significant change occurred with respect to the previous component suppression (relative difference change ≤ 5%).

Symbols in red cells represent the maximum relative difference change induced by the removal when change occurs in a component different from that associated to the maximum relative difference value.

9) Nucleus pulposus removal

Without nucleus pulposus (NP), the ROM became greater in both models (Fig. 3.9a). The L3-L4 level of the new geometry was more than twice sensitive than the L4-L5 level and than the old geometry (Fig. 3.9b). With about 25% of rotation increase with respect to the intact configuration, the NP was after the CL suppression the component that had the largest influence on the models flexibility. As shown by Fig. 3.13, in both models, the AF fibre stresses were reduced in both models and at any location.

Table 3.11: Qualitative representation of the maximum effect of nucleus pulposus suppression on the different studied mechanical criteria under flexion.

Model	Range of motion		Annulus fibrosus stress	
	L3-L4	L4-L5	L3-L4	L4-L5
Old geometry	III	II	V* (PLAT)	III* (LAT)
New geometry	IV	II	VI* (POST) - IV (ANT)	II (ANT)

-: Relative difference < 2% | ~: Relative difference ≤ 5% | I: Relative difference < 10% | II: Relative difference < 50% | III: Relative difference < 100% | IV: Relative difference < 200% | V: Relative difference < 500% | VI: Relative difference ≥ 500%
Uppercase * indicates that a relative difference decrease occurred with respect to the previous component suppression.

When both models have the same symbol affected to the same component, the cell with dashed lines indicates the most affected geometry. No dashed lines were drawn when both geometries were similarly affected.

Symbols in red cells represent the maximum relative difference change induced by the removal when change occurs in a component different from that associated to the maximum relative difference value.

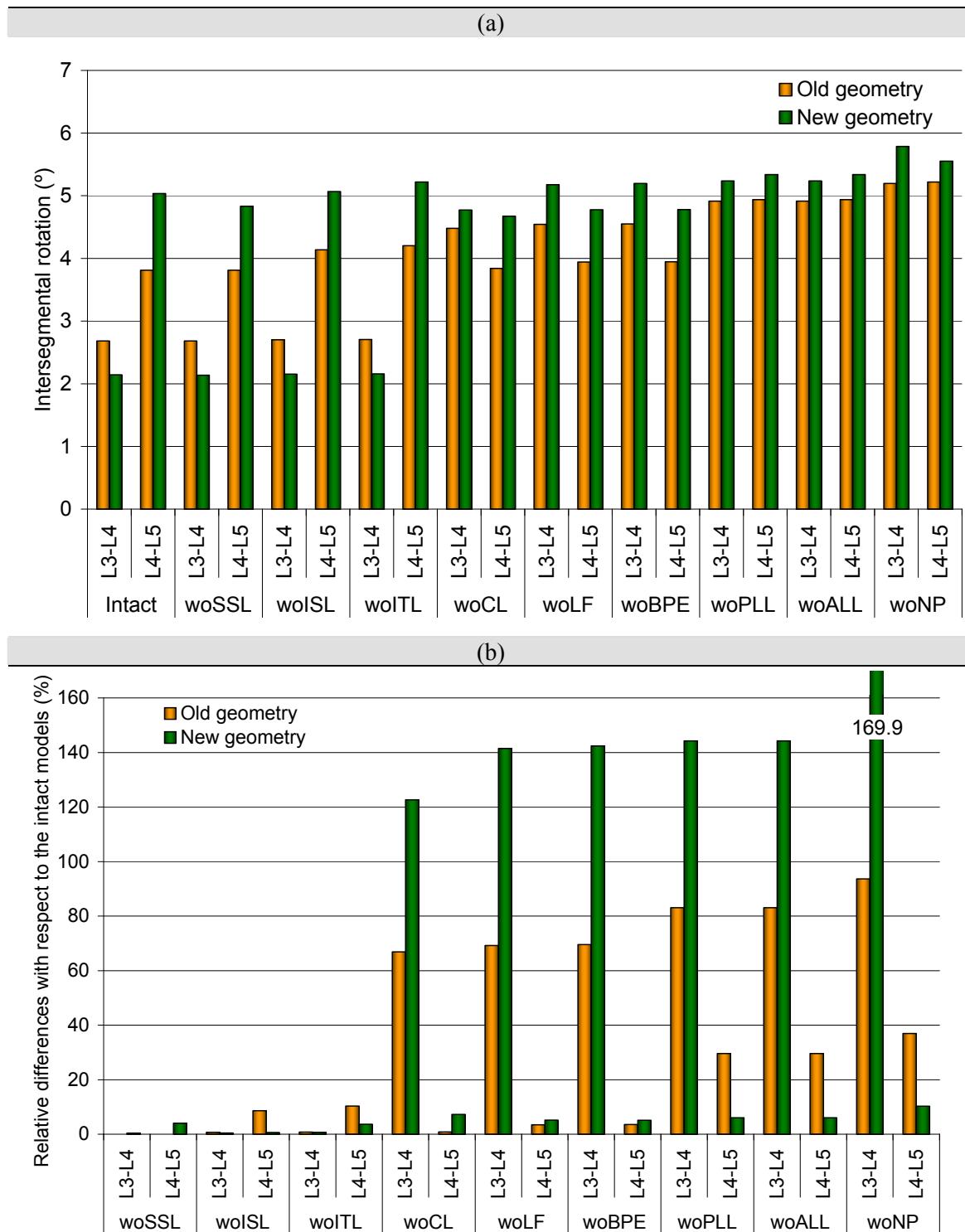


Figure 3.9: Ranges of motions in sagittal flexion at 7.5N.m; a) Absolute values for the intact version of each geometry and after each component resection; b) Relative differences with respect to the intact version of each geometry induced after each of the successive resections.

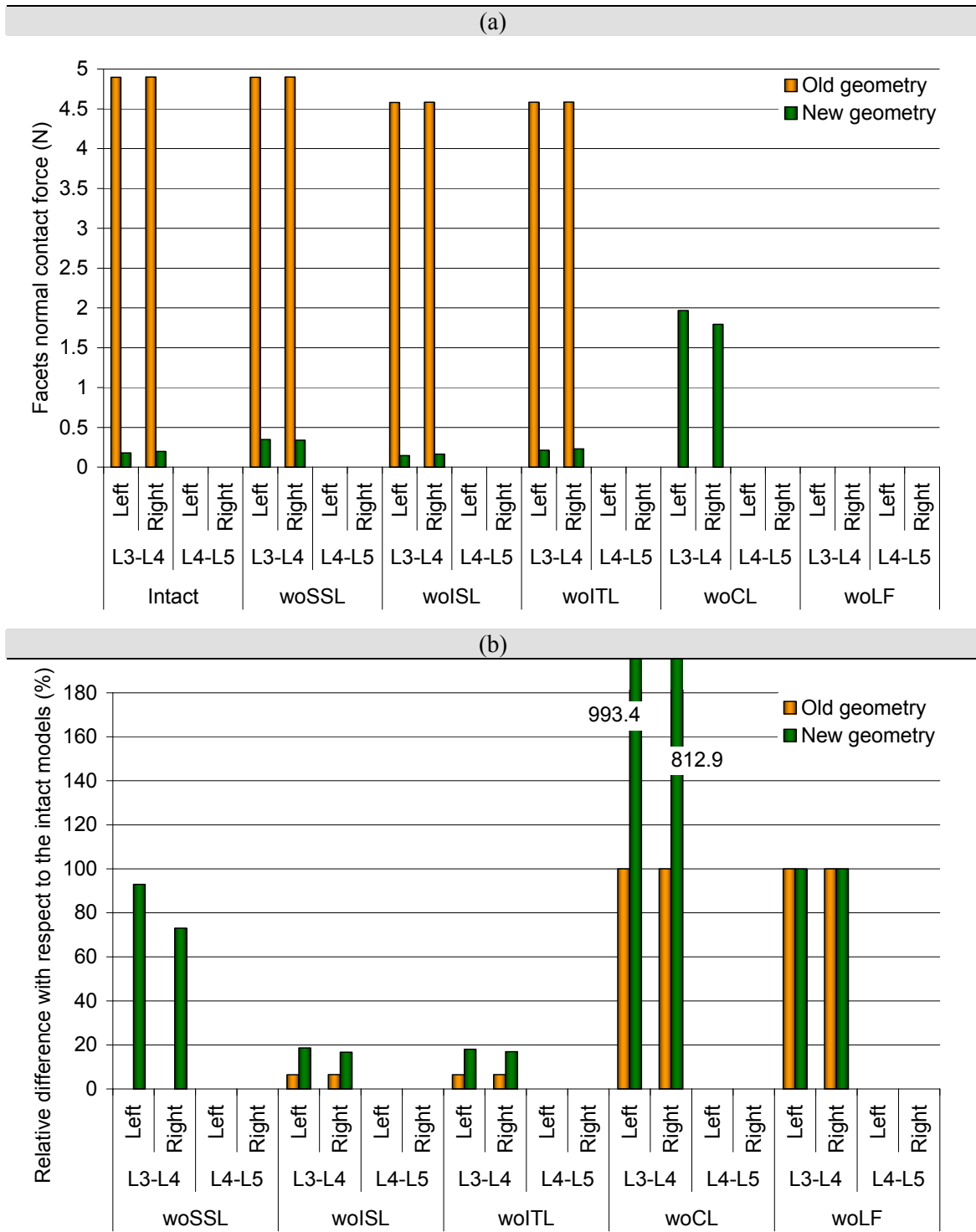


Figure 3.10: Normal facet contact forces under sagittal flexion at 7.5N.m. a) Absolute values for the intact version of each geometry and after each component resection. b) Relative differences with respect to the intact version of each geometry induced after each of the successive resections.

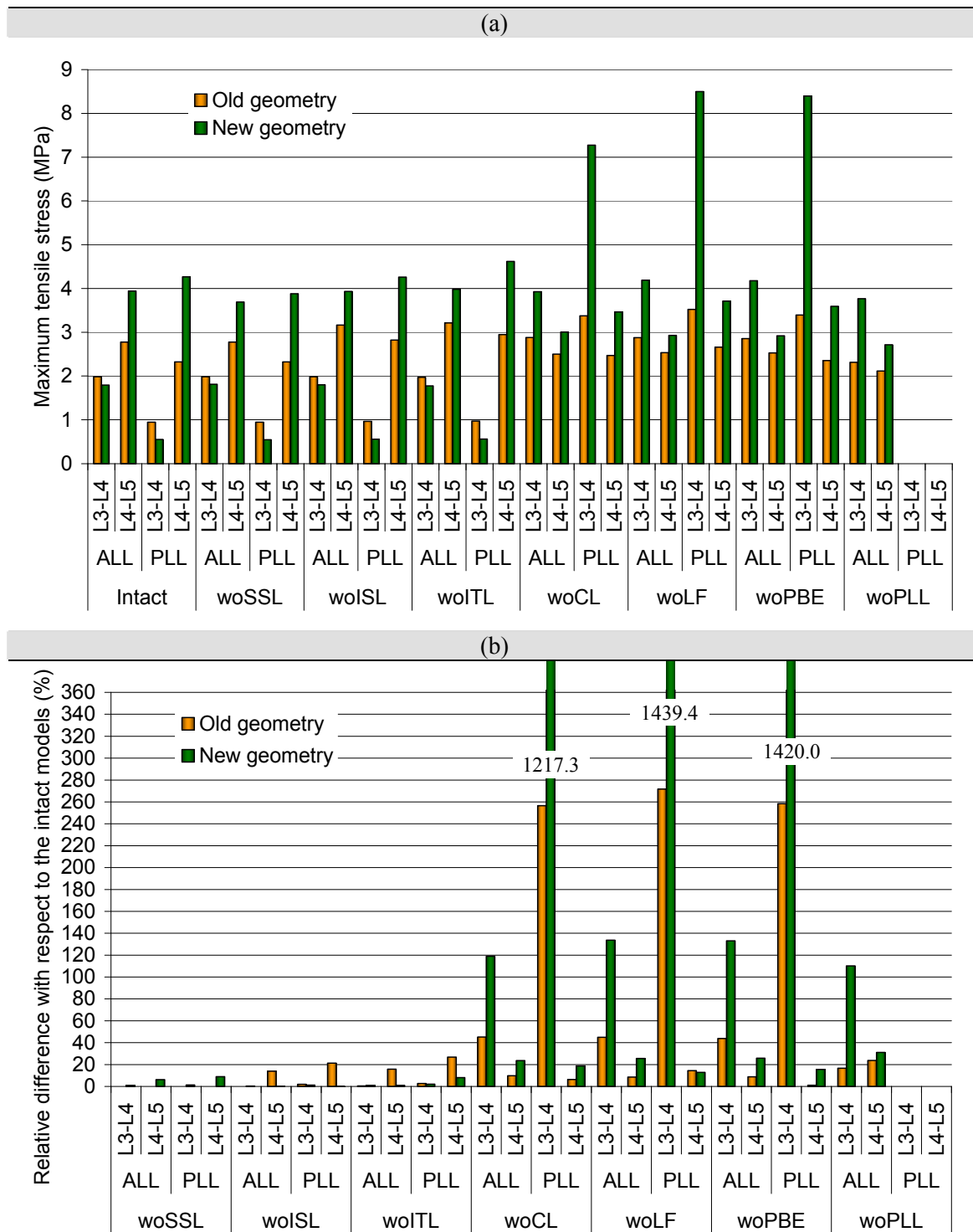


Figure 3.11: Anterior ligaments tensile stresses under sagittal flexion at 7.5N.m. a) Absolute values for the intact version of each geometry and after each component resection. b) Relative differences with respect to the intact version of each geometry induced after each of the successive resections.

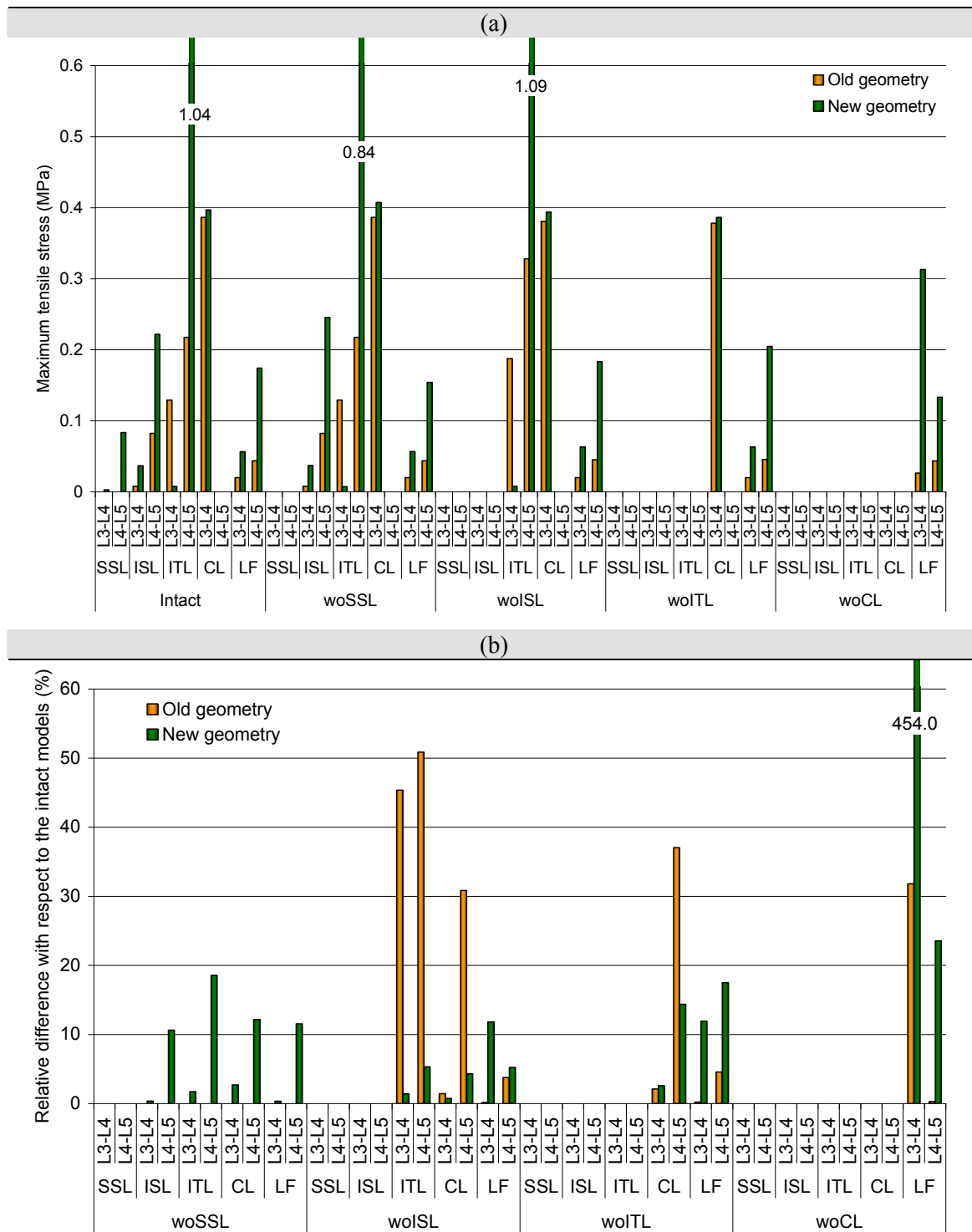


Figure 3.12: Posterior ligaments tensile stresses under sagittal flexion at 7.5N.m. a) Absolute values for the intact version of each geometry and after each component resection. b) Relative differences with respect to the intact version of each geometry induced after each of the successive resections.

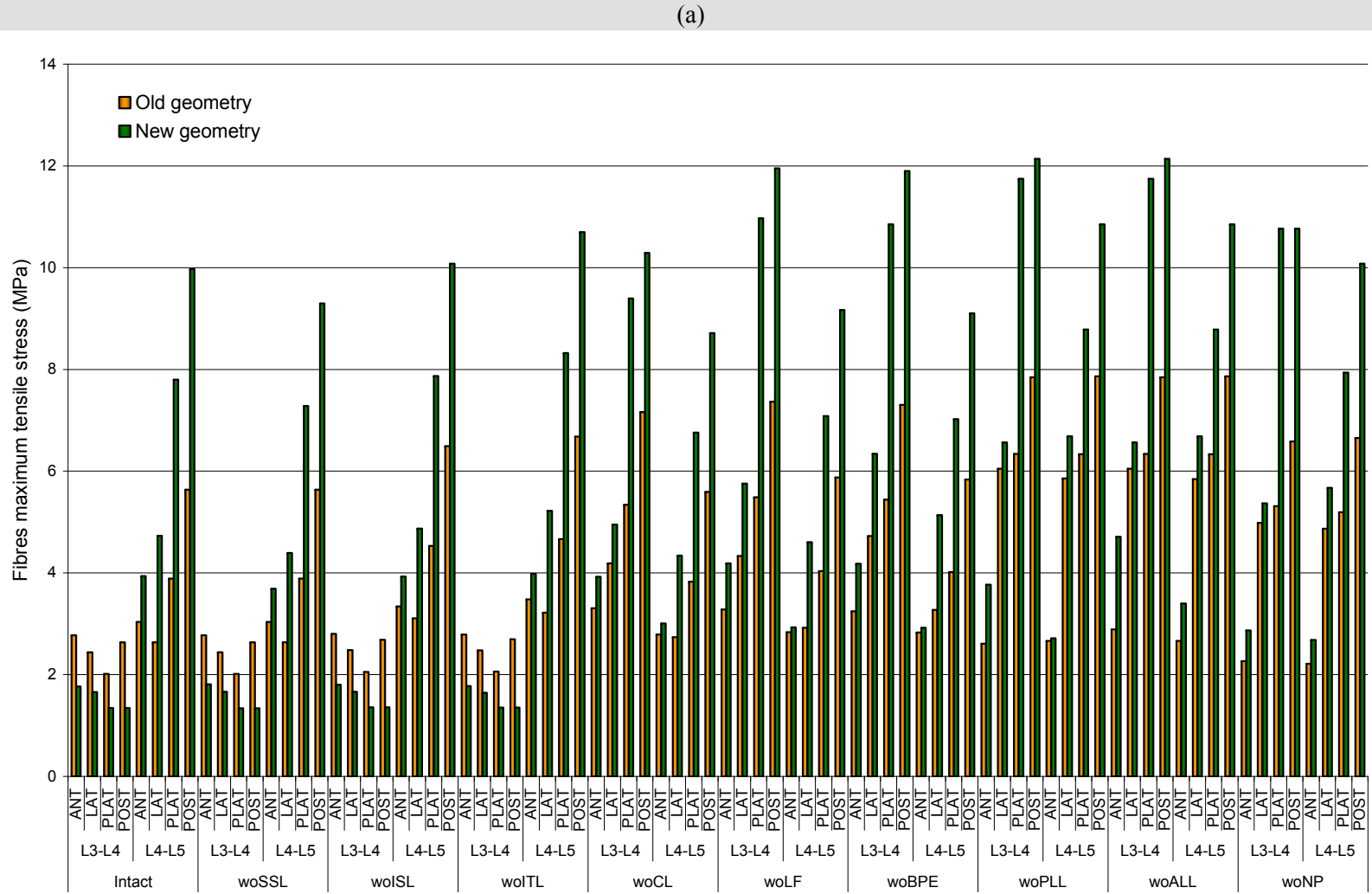


Figure 3.13a: Annulus fibrosus fibres tensile stresses under sagittal flexion at 7.5N.m. – Absolute values for the intact version of each geometry and after each component resection.

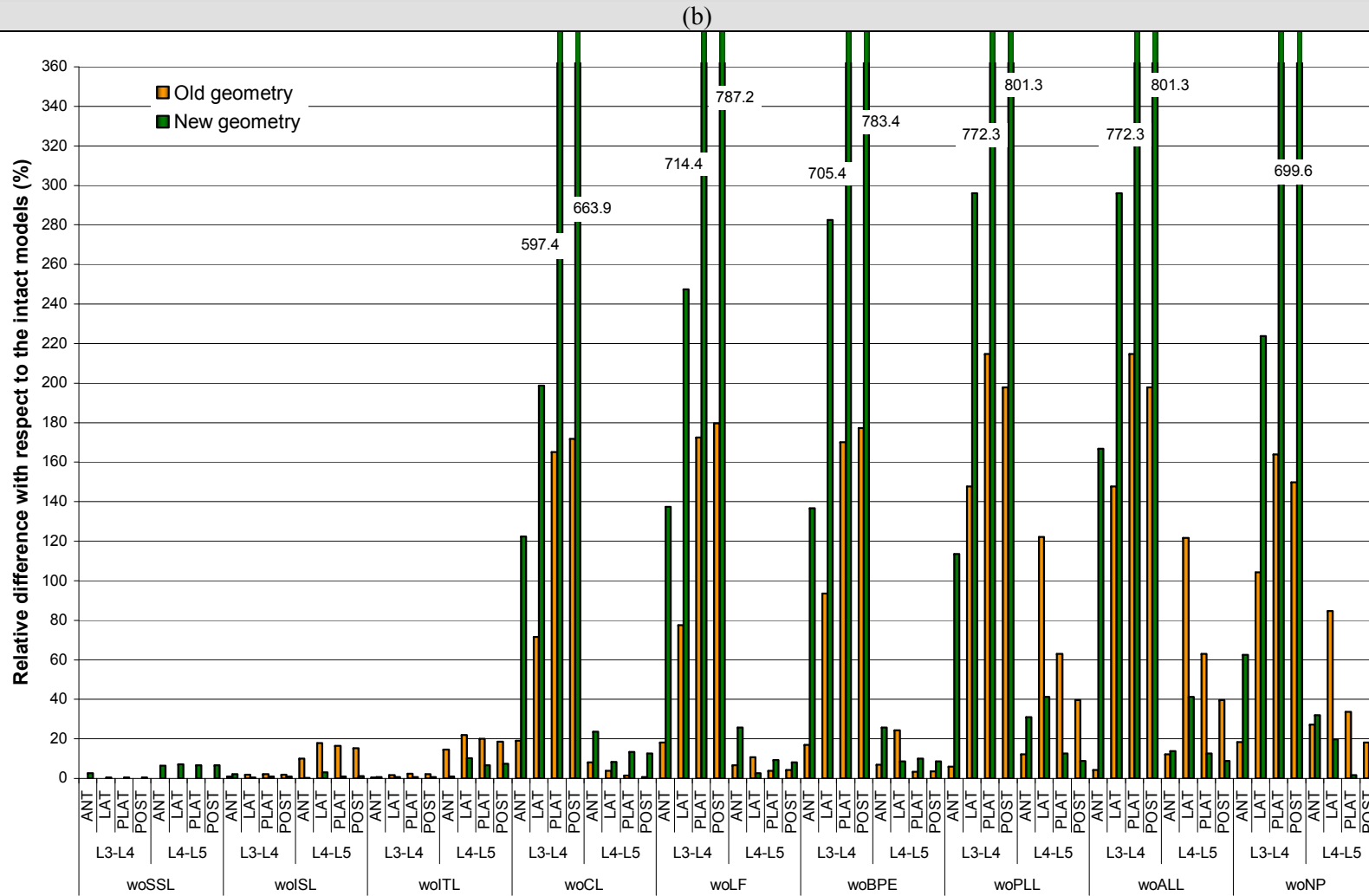


Figure 3.13b: Annulus fibrosus fibres tensile stresses under sagittal flexion at 7.5N.m. – Relative differences with respect to the intact version of each geometry induced after each of the successive resections.

b. Extension

All the numerical results about the biomechanical effect of the successive removals on both models are reported in Figures from 3.14 to 3.17 at the end of the section. As expected, in extension, neither the SSL, nor the ISL, nor the ITL nor the LF had any significant influence on the ranges of motion (Fig. 3.14). Nonetheless, ISL suppression contributed to slightly lower the right L3-L4 contact of the new geometry (Fig. 3.15).

The subsequent resections had more significant effects and are described below. Each of the following subsection concerning a specific removal contains a Table that qualitatively resumes the major effects of the current component suppression (Tables 3.12 – 3.16).

1) Capsular ligament removal

The effect of CL removal was similar to the results in flexion with a softening of L3-L4 and a stiffening of L4-L5. However, in the case of extension, both geometries were similarly affected and the differences between them did not overcome 4% (Fig. 3.14b). For both models, until the CL was removed, the L3-L4 contact remained lower than the L4-L5 one and the differences between both levels were more pronounced in the new geometry (Fig. 3.15a). After CL was taken away, the L4-L5 contact was generally considerably reduced and at the L3-L4 level, while the facet contact increased in the new geometry, it decreased in the old one. The relative differences (Fig. 3.15b) clearly showed that the new geometry was most affected by the absence of CL; the L3-L4 contact changes were nearly 10 times greater than those computed in the old geometry, and the L4-L5 contact changes were about 13% greater than those of the old geometry. At the L3-L4 level, the anterior ligaments resulted significantly more stresses and at the L4-L5 level, the ALL and PLL tensile stresses were lowered for both geometries (Fig. 3.16a). The changes induced in the ALL were almost similar in the two models. Nonetheless, with a relative difference raise of about 4200% due to a stress increase, the PLL of the old geometry was particularly sensitive to CL removal (Fig. 3.16b). In the annulus fibrosus, the ligament suppression made the L3-L4 fibres stresses to rise, while the L4-L5 fibres became less tensed (Fig. 3.17a). For both geometries the largest stress increase took place in the anterior annulus. Nonetheless, the greatest differences between the models were predicted in the L3-L4 posterior AF, where the old geometry was nearly twice more affected than the new geometry (Fig. 3.17b). At the L4-L5 level, the old geometry posterior AF fibres showed also more sensitivity, but the highest difference with the new geometry was only about 10%.

Table 3.12: Qualitative representation of the maximum effect of the capsular ligament suppression on the different studied mechanical criteria under extension.

Model	Range of motion		Facet contact force		Anterior ligament stress		Annulus fibrosus stress	
	L3-L4	L4-L5	L3-L4	L4-L5	L3-L4	L4-L5	L3-L4	L4-L5
Old geometry	III	II	I	II	VI (PLL)	II (PLL)	VI (POST)	II (PLAT)
New geometry	III	I	III	II	V (PLL)	II (PLL)	VI (POST)	II (LAT)

-: Relative difference < 2% | ~: Relative difference ≤ 5% | I: Relative difference < 10% | II: Relative difference < 50% | III: Relative difference < 100% | IV: Relative difference < 200% | V: Relative difference < 500% | VI: Relative difference ≥ 500%

When both models have the same symbol affected to the same component, the cell with dashed lines indicates the most affected geometry. No dashed lines were drawn when both geometries were similarly affected.

2) Bony posterior elements removal

The suppression of the BPE influenced equally both geometries at both levels by increasing slightly the motions (about 3% of relative difference change), see Figure 3.14. At the L3-L4 level, the absence of the BPE tended to reduce the old geometry ALL tensile stress with a relative difference decrease of about 15%, while in the new geometry, the ligament was not affected (Fig. 3.16). For the PLL, the trend was inverted and the relative difference associated to the ligament stress in the new geometry was reduced of about 10%, at the same time as the stress in the old geometry was increased (Fig. 3.16a). Note that the old geometry L3-L4 PLL had an initial very low stress level, and any stress increase with respect to this initial state induced large relative difference changes (Fig. 3.16b). At the L4-L5 level, the stresses of ALL and PLL tended to increase for both geometries and the maximum computed differences were nearly 10%. As shown by Figure 3.17, the new geometry AF fibres were only noteworthy affected in the lateral AF, with a stress increase at the L3-L4 level, and a stress decrease at the L4-L5 level, each corresponding to about 12% of relative difference change. Old geometry fibre stresses rose considerably in the postero-lateral and posterior L3-L4 AF, and as in the new geometry, they became lower in the lateral L4-L5 AF with a similar sensitivity.

Table 3.13: Qualitative representation of the maximum effect of the bony posterior elements suppression on the different studied mechanical criteria under extension.

Model	Range of motion		Anterior ligament stress		Annulus fibrosus stress	
	L3-L4	L4-L5	L3-L4	L4-L5	L3-L4	L4-L5
Old geometry	III	II*	VI ⁺ (PLL)	II (PLL)	VI ⁺ (POST)	II° (POST) -II (PLAT)
New geometry	III	I*	V* (PLL)	II* (PLL)	VI (POST) +II (LAT)	II (LAT)

-: Relative difference < 2% | ~: Relative difference ≤ 5% | I: Relative difference < 10% | II: Relative difference < 50% | III: Relative difference < 100% | IV: Relative difference < 200% | V: Relative difference < 500% | VI: Relative difference ≥ 500%
 Uppercase ° indicates that a relative difference decrease occurred with respect to the previous component suppression. Uppercase * indicates that no significant change occurred with respect to the previous component suppression (relative difference change ≤ 5%). Uppercase + indicates further relative difference increases ≥ 100% for pre-existing values ≥ 500%.

Symbols in red cells represent the maximum relative difference change induced by the removal when change occurs in a component different from that associated to the maximum relative difference value.

3) Posterior longitudinal ligament removal

PLL removal had almost no effect on the models ROM and ALL stresses (Fig. 3.14,3.16). However, while the tensile stresses of the old geometry L3-L4 anterior annulus fibres were further lowered, the new geometry postero-lateral L3-L4 AF fibre stresses and the posterior L3-L4 AF fibre stresses of both geometries were increased (Fig. 3.17a). In the old geometry, the L3-L4 posterior AF fibres stress decrease compensated the augmentation provoked by the previous BPE suppression (Fig. 3.17b). At the L4-L5 level, the old geometry anterior and posterior AF, as well as the new geometry lateral AF were also affected and the changes contribute to restore the intact annulus fibres stress, which was traduced by a relative difference decrease of 10% minimum. In the new geometry posterior annulus, the stresses were further increased.

Table 3.14: Qualitative representation of the maximum effect of the posterior longitudinal ligament suppression on the different studied mechanical criteria under extension.

Model	Range of motion		Anterior ligament stress		Annulus fibrosus stress	
	L3-L4	L4-L5	L3-L4	L4-L5	L3-L4	L4-L5
Old geometry	III°	II°	III° (ALL)	II° (ALL)	VI* (POST) +V (PLAT)	II° (POST)
New geometry	III°	I°	IV* (ALL)	II° (ALL)	VI (POST)	II (POST)

-: Relative difference < 2% | ~: Relative difference ≤ 5% | I: Relative difference < 10% | II: Relative difference < 50% | III: Relative difference < 100% | IV: Relative difference < 200% | V: Relative difference < 500% | VI: Relative difference ≥ 500%
 Uppercase ° indicates that no significant change occurred with respect to the previous component suppression (relative difference change ≤ 5%).

When both models have the same symbol affected to the same component, the cell with dashed lines indicates the most affected geometry. No dashed lines were drawn when both geometries were similarly affected.

Symbols in red cells represent the maximum relative difference change induced by the removal when change occurs in a component different from that associated to the maximum relative difference value.

4) Anterior longitudinal ligament removal

ROM changes appeared again after ALL removal (Fig. 3.14a). At the L3-L4 level, both geometries were similarly affected and at the L4-L5 level, the old geometry resulted about four-fold more sensitive than the new one (Fig. 3.14b). Nonetheless, while in the old geometry, a motion restoration was experienced, in the new one, the segmental mobility was further increased with relative difference changes of up to 7% (Fig. 3.14). In the intervertebral disc, except in the old geometry anterior L3-L4 AF, and in the L4-L5 posterior AF of both models, the annulus fibre stresses changes contributed to restore partly the initial AF stress state (Fig. 3.17b). The old geometry was most affected with relative differences changes of up to 225% in the L3-L4 AF. At the new geometry anterior AF, no changes were predicted, neither at the L3-L4 level, nor at the L4-L5 one.

Table 3.15: Qualitative representation of the maximum effect of the anterior longitudinal ligament suppression on the different studied mechanical criteria under extension.

Model	Range of motion		Annulus fibrosus stress	
	L3-L4	L4-L5	L3-L4	L4-L5
Old geometry	III	*	VI* (POST)	II (POST)
New geometry	III	I°	VI* (POST)	II (POST)

-: Relative difference < 2% | ~: Relative difference ≤ 5% | I: Relative difference < 10% | II: Relative difference < 50% | III: Relative difference < 100% | IV: Relative difference < 200% | V: Relative difference < 500% | VI: Relative difference ≥ 500%
 Uppercase ° indicates that a relative difference decrease occurred with respect to the previous component suppression. Uppercase * indicates that no significant change occurred with respect to the previous component suppression (relative difference change ≤ 5%).
 When both models have the same symbol affected to the same component, the cell with dashed lines indicates the most affected geometry. No dashed lines were drawn when both geometries were similarly affected.

5) Nucleus pulposus removal

The absence of NP induced greater ROM at both levels of both models (Fig. 3.14a). Nevertheless, at the L4-L5 level, the new geometry resulted more affected than the old one (Fig. 3.14b). As shown by Fig. 3.17a, at the L3-L4 level, the AF fibre stresses tended to decrease, except for the new geometry lateral and postero-lateral locations. The postero-lateral AF was where the most significant stress increase took place (Fig. 3.17b). Due to the high stress increase that occurred in the L3-L4 old geometry posterior annulus after CL removal, this latter AF area was the most affected with a large stress decrease (Fig. 3.17). At the L4-L5 level, the lateral AF fibre stresses were slightly increased and at the other locations, there was a general tensile stress decrease (Fig. 3.17a). Except in the anterior AF for both models and in the old geometry postero-lateral fibres, the L4-L5 changes corresponded to a partial restoration of the AF fibres stresses (Fig. 3.17b).

Table 3.16: Qualitative representation of the maximum effect of the nucleus pulposus suppression on the different studied mechanical criteria under extension.

Model	Range of motion		Annulus fibrosus stress	
	L3-L4	L4-L5	L3-L4	L4-L5
Old geometry	III	I	V* (POST)	III (POST)
New geometry	III	II	V (PLAT)	III (POST)

-: Relative difference < 2% | ~: Relative difference ≤ 5% | I: Relative difference < 10% | II: Relative difference < 50% | III: Relative difference < 100% | IV: Relative difference < 200% | V: Relative difference < 500%

Uppercase * indicates that a relative difference decrease occurred with respect to the previous component suppression.

When both models have the same symbol affected to the same component, the cell with dashed lines indicates the most affected geometry. No dashed lines were drawn when both geometries were similarly affected.

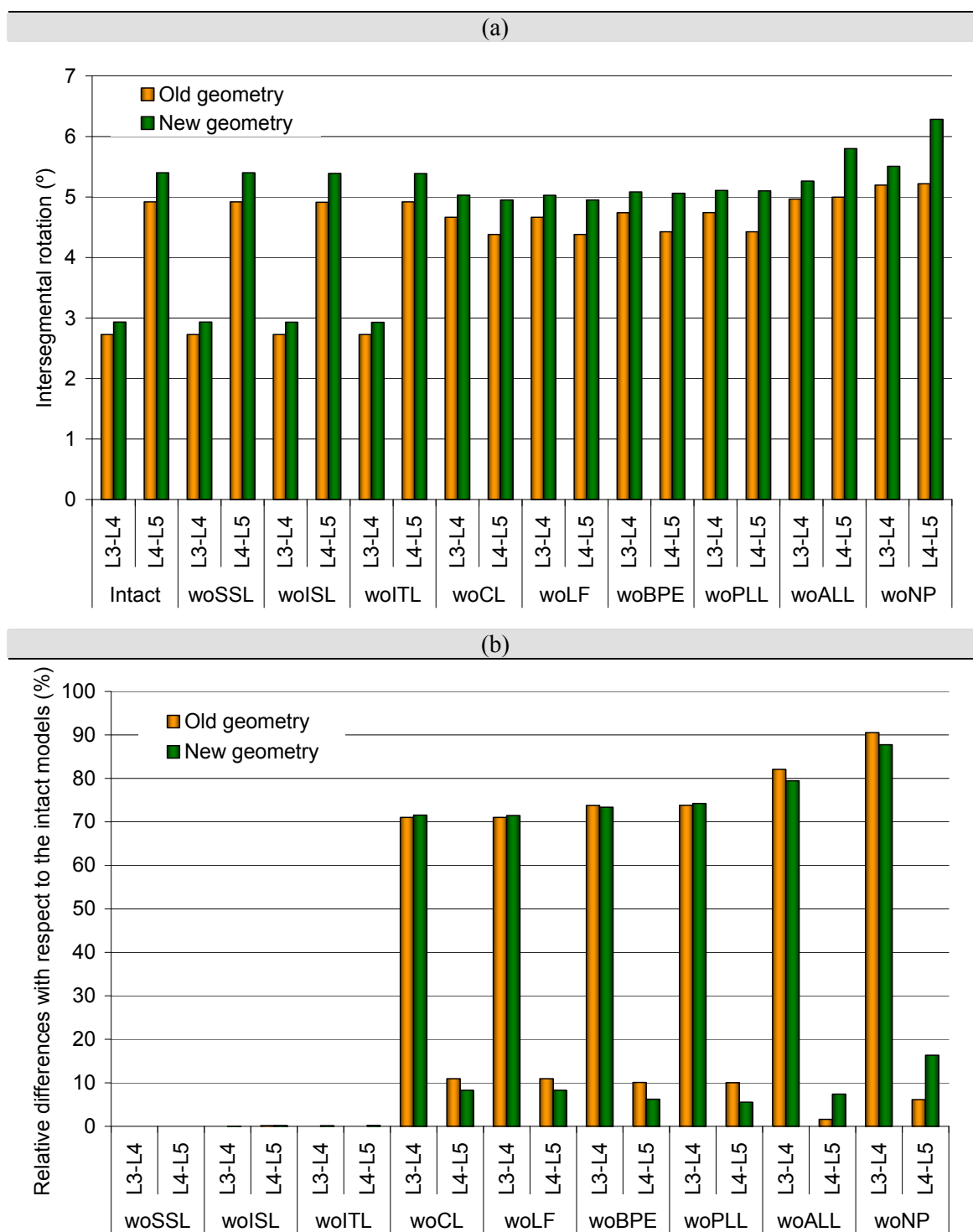


Figure 3.14: Ranges of motions in sagittal extension at 7.5N.m; a) Absolute values for the intact version of each geometry and after each component resection. b) Relative differences with respect to the intact version of each geometry induced after each of the successive resections.

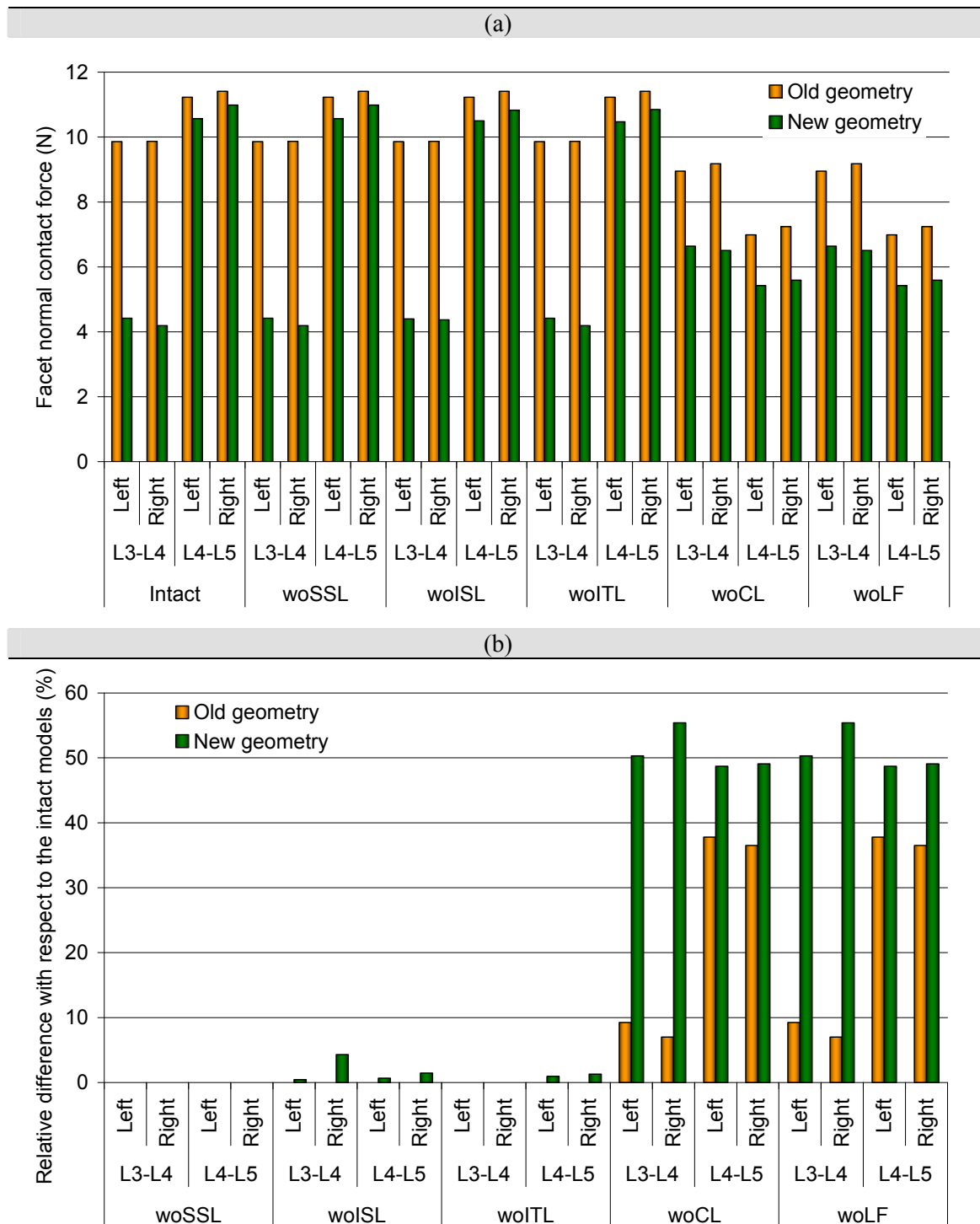


Figure 3.15: Normal facet contact forces under sagittal extension at 7.5N.m. a) Absolute values for the intact version of each geometry and after each component resection. b) Relative differences with respect to the intact version of each geometry induced after each of the successive resections.

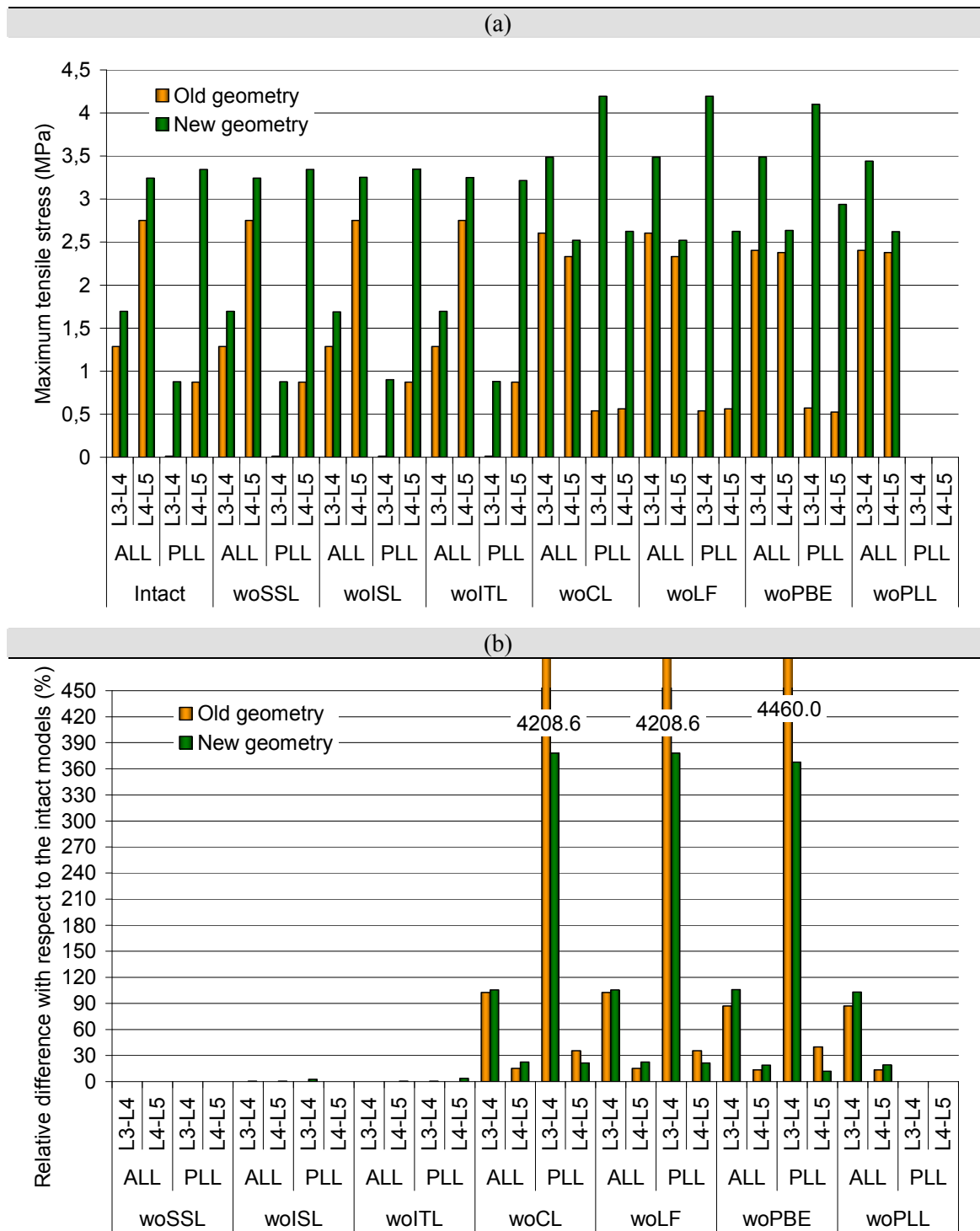


Figure 3.16: Anterior ligaments tensile stresses under sagittal extension at 7.5N.m. a) Absolute values for the intact version of each geometry and after each component resection. b) Relative differences with respect to the intact version of each geometry induced after each of the successive resections.

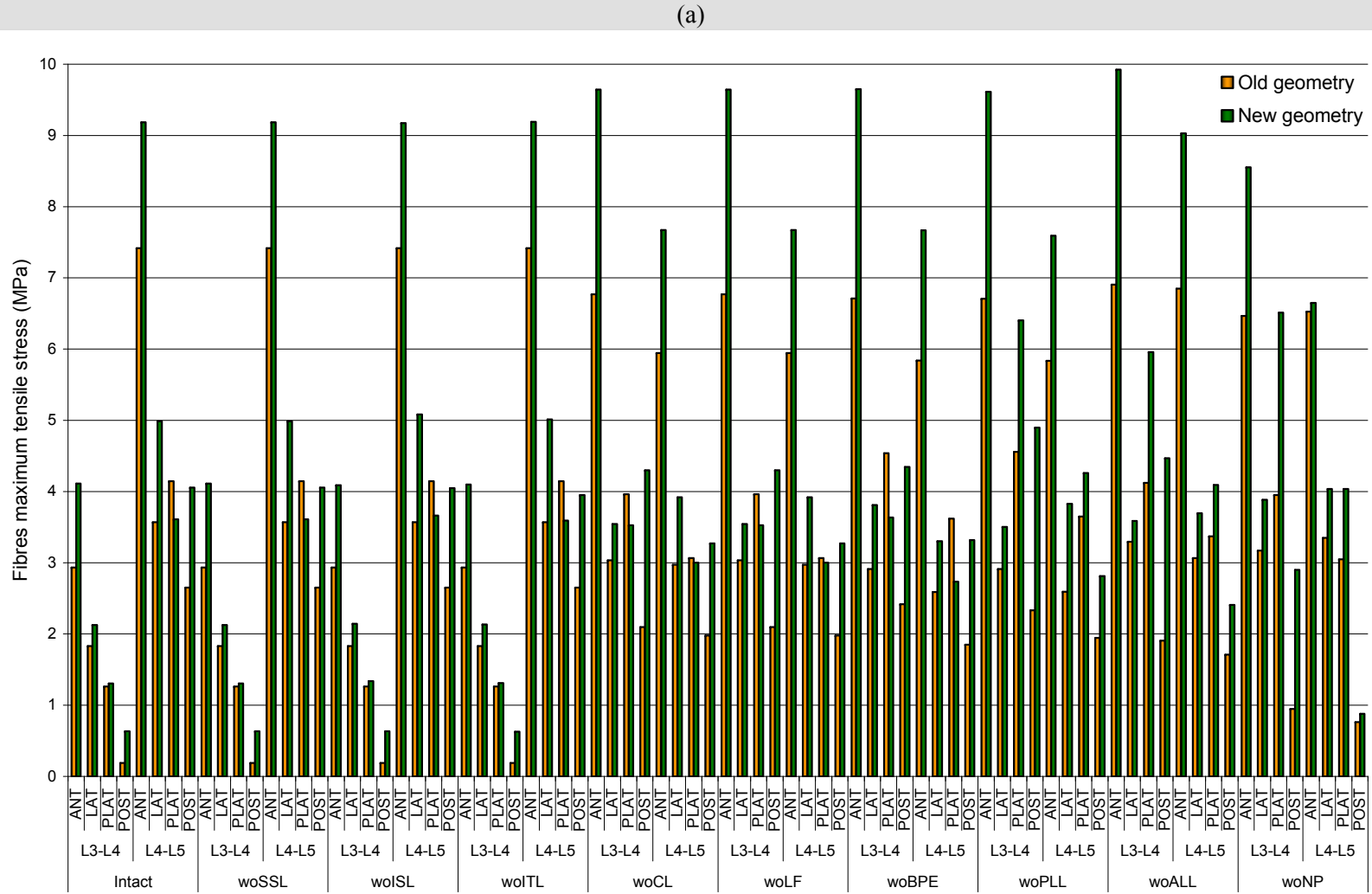


Figure 3.17a: Annulus fibrosus fibres tensile stresses under sagittal extension at 7.5N.m. – Absolute values for the intact version of each geometry and after each component resection.

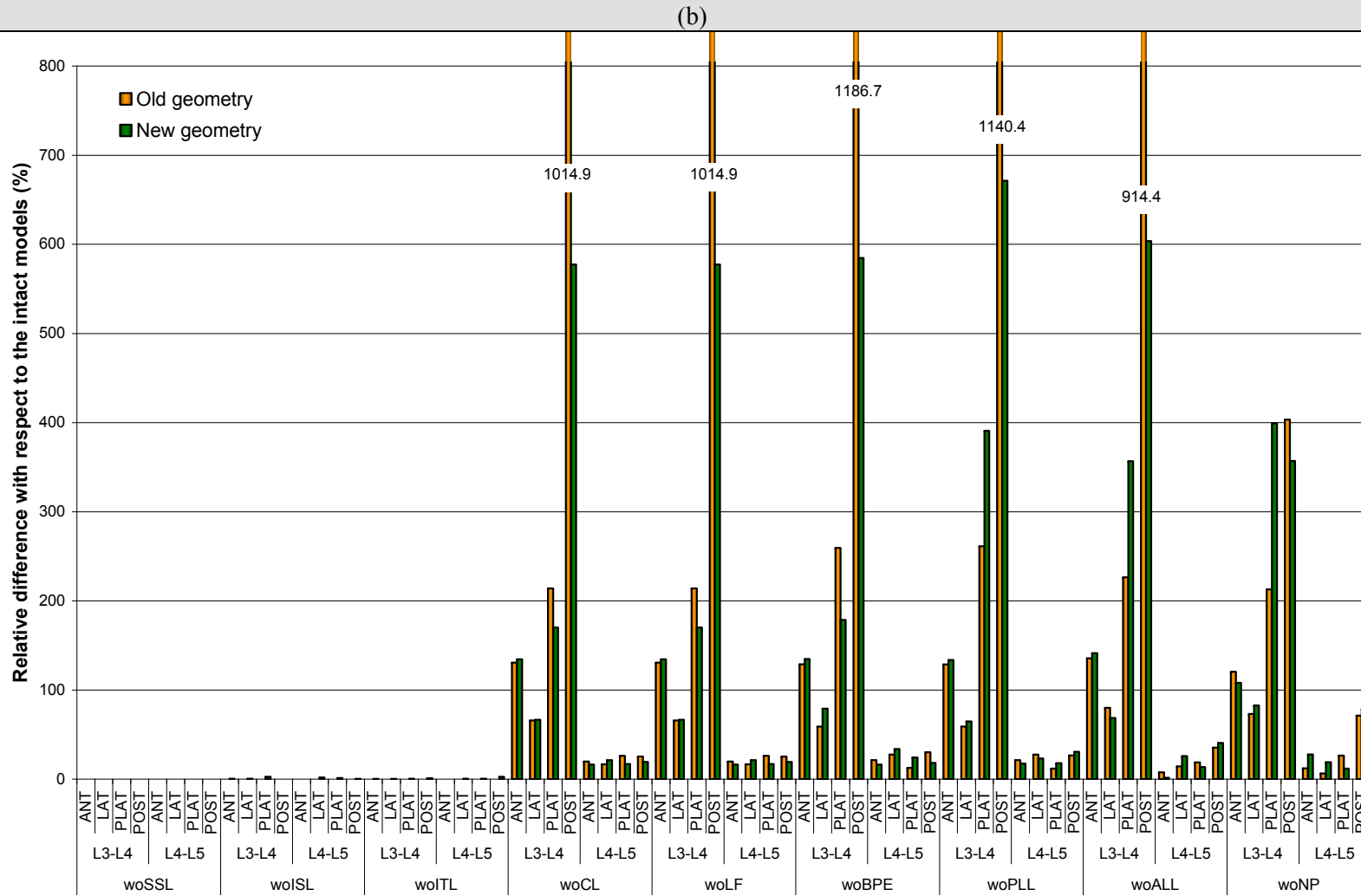


Figure 3.17b: Annulus fibrosus fibres tensile stresses under sagittal extension at 7.5N.m. – Relative differences with respect to the intact version of each geometry induced after each of the successive resections.

c. Lateral bending

The results shown in lateral bending were averaged from the simulations under right and left rotations. By this way, a global behaviour under lateral bending can be studied without multiplying the number of results because of the AF asymmetry with respect to the sagittal plane. From Figures 3.18, 3.19 and 3.20, neither the ROM, nor the facet contact forces, nor the anterior ligaments seemed affected by SSL or ISL removal. Figure 3.21 shows that although a relative difference of about 45% was computed for the new geometry CL after SSL was taken away, no absolute posterior ligament stresses were noteworthy changed and such result may come from the very low tractions predicted for the L4-L5 CL (order of magnitude of 10^{-7} MPa). Without ISL, the L3-L4 new geometry CL became slightly more tensed, but the relative difference did not overcome 5%. The effects of the further resections are presented in detail in the following subsections and their major outcomes are qualitatively summarized from Tables 3.17 to 3.19

1) Intertransverse ligament removal

As shown by Fig. 3.18, although ITL suppression had low effect on the L3-L4 segments, both geometries became softer at the L4-L5 level. However, the influence of the ligament was limited, since the maximum induced relative difference was about 10% in the new geometry, which was nearly two-fold more sensitive than the old one (Fig. 3.18b). In the direction of rotation (referred as “rotation side” in the text), the L3-L4 facet contact normal forces were lowered for both geometries, and while the L4-L5 contact tended to increase in the new geometry, it also decreased in the old one (Fig. 3.19a). At the L3-L4 level, the old geometry appeared more sensitive to ITL removal and the situation was reversed for the L4-L5 level (Fig. 3.19b). In the direction opposite to rotation (referred as “anti rotation side” in the text), no contact was predicted for the new geometry, and the old geometry contact tended to increase at the L3-L4 level and to decrease at the L4-L5 level (Fig. 3.19a). While the anterior ligaments of the old geometry were only few affected by the ITL resection, the new geometry L4-L5 ALL experienced a relative stresses increase with a relative difference change of about 17%. Whatever the model, the alterations predicted in the PLL were less than 4% (Fig. 3.20). CL and LF remained fairly low stressed (Fig. 3.21a), even after ITL has been taken away. Nonetheless, some notable changes were computed in these ligaments (Fig. 3.21b) and the old geometry L3-L4 CL stress associated relative difference increased about 15%, while the new geometry corresponding ligament was partially relaxed. As predicted when SSL was removed, the high relative differences calculated for the CL at the L4-L5 level were not relevant because of the ligament initial low stress value. Nonetheless, at this level, the LF became more stressed with up to 26% and 17% of relative difference changes, respectively in the old and the new geometry. The AF fibres also began to be more stretched (Fig. 3.22a) and the major changes took place in the anterior and postero-lateral L4-L5 annulus for the new geometry, in the L4-L5 lateral annulus for the old geometry and in the L4-L5 posterior annulus for both models (Fig.

3.22b). At these locations, the new geometry was generally nearly twice more affected than the old one.

Table 3.17: Qualitative representation of the maximum effect of the intertransverse ligament suppression on the different studied mechanical criteria under lateral bending.

Model	Range of motion		Facet contact force		Anterior ligament stress		Posterior ligament stress		Annulus fibrosus stress	
	L3-L4	L4-L5	L3-L4	L4-L5	L3-L4	L4-L5	L3-L4	L4-L5	L3-L4	L4-L5
Old geometry	~	I	II (RS)†	I (ARS)†	~ (ALL)	~ (ALL)	II (CL)	III (CL)	~ (LAT)	II (POST)
New geometry	-	I	I (RS)†	I (RS)†	~ (PLL)	II (ALL)	~ (CL)	II (CL)	~ (POST)	II (POST)

-: Relative difference < 2% | ~: Relative difference ≤ 5% | I: Relative difference < 10% | II: Relative difference < 50% | III: Relative difference < 100%

When both models have the same symbol affected to the same component, the cell with dashed lines indicates the most affected geometry. No dashed lines were drawn when both geometries were similarly affected.

† RS: Rotation Side - ARS: Anti Rotation Side

2) Capsular ligament removal

The suppression of CL led to a global increase of the L3-L4 ROM (Fig. 3.18a). Before the ligament was taken away, the old geometry L3-L4 segment was slightly softer than that of the new geometry and the situation became reversed after the resection. At the L4-L5 level, some stiffening was predicted for both geometries, and while in the old model, both levels had a similar mobility, the L4-L5 segment of the new geometry remained softer than the L3-L4 one. Figure 3.18b shows that the new geometry was much more sensitive at the L3-L4 level and at the L4-L5 level, both geometries were likewise affected. At the L3-L4 zygapophysial joint and to the rotation side, the contact was highly lowered for both geometries and almost vanished (Fig. 3.19a). To the anti-rotation side, while the L3-L4 facets contact was partially lost in the old geometry, contact appeared in the new geometry. At the L4-L5 level, the contact was generally lowered in the old geometry, and in the new one, it was somewhat increased to the rotation side. The relative differences (Fig. 3.19b) pointed out that to the rotation side the influence that had the CL removal at the L3-L4 level was slightly larger in the new geometry. At the L4-L5 level, the old model resulted about 10% more affected. To the anti rotation side, the apparition of L3-L4 contact in the new geometry, made this latter to be more sensitive. For both geometries, the L3-L4 ALL tensile stresses were consistently increased with relative difference changes of up to 20%, while the L4-L5 ALL became somewhat less stretched (Fig. 3.20). At both levels, the new geometry resulted considerably more affected than the old one (Fig. 3.20b). Although PLL stresses tended to increase in the L3-L4 segments and to decrease at the L4-L5 levels of both geometries, the ligament was almost not affected. At the L3-L4 level, the CL suppression made the LF tensile stresses to increase, and in the new geometry, they were nearly doubled (Fig. 3.21). At the L4-L5 level, while the old geometry LF tended to relax, that of the new geometry became more stretched with a relative difference increase of about 10% (Fig. 3.21b). In the L3-L4 intervertebral disc,

the AF fibre stresses increased for both geometries all around the fibrous cartilage, and on the contrary, at the L4-L5 level, AF fibres became generally less stressed (Fig. 3.22a). The L3-L4 old geometry AF was most affected, especially at the posterior area (Fig. 3.22b). At the L4-L5 level, the AF fibres stresses were in general partially restored.

Table 3.18: Qualitative representation of the maximum effect of the capsular ligament suppression on the different studied mechanical criteria under lateral bending.

Model	Range of motion		Facet contact force		Anterior ligament stress		Posterior ligament stress		Annulus fibrosus stress	
	L3-L4	L4-L5	L3-L4	L4-L5	L3-L4	L4-L5	L3-L4	L4-L5	L3-L4	L4-L5
Old geometry	II	~*	III (RS)†	II (ARS)†	II (ALL)	*	II (LF)	II* (LF)	II (POST)	II* (POST)
New geometry	II	I*	IV (ARS)†	I (RS)†	II (ALL)	II* (ALL)	II (LF)	II (LF)	II (POST)	II* (POST)

-: Relative difference < 2% | ~: Relative difference ≤ 5% | I: Relative difference < 10% | II: Relative difference < 50% | III: Relative difference < 100% | IV: Relative difference < 200%
 Uppercase * indicates that a relative difference decrease occurred with respect to the previous component suppression.
 When both models have the same symbol affected to the same component, the cell with dashed lines indicates the most affected geometry. No dashed lines were drawn when both geometries were similarly affected.
 † RS: Rotation Side - ARS: Anti Rotation Side

3) Ligamentum flavum removal

No ROM changes were predicted with LF resection (Fig. 3.18), and the maximum contact forces change was computed for the L4-L5 contact of the old geometry to the anti rotation side, where a force contact decrease made the relative differences to increase of about 8% (Fig. 3.19). Whatever the considered geometry, neither the ALL nor the L4-L5 PLL appeared noteworthy affected (Fig. 3.20). In the old geometry, the L3-L4 PLL tensile stresses decreased with a relative difference change of about 7% and in the new geometry, the L3-L4 PLL tended to recover somewhat of its original stress state (Fig. 3.20b). The AF fibre stresses were not greatly affected by the LF removal and the greatest relative difference changes corresponded to stress increases and were found to be about 5% in the L3-L4 old geometry posterior AF and in the L4-L5 new geometry posterior AF (Fig. 3.22).

Table 3.19: Qualitative representation of the maximum effect of the ligamentum flavum suppression on the different studied mechanical criteria under lateral bending.

Model	Range of motion		Facet contact force		Anterior ligament stress		Annulus fibrosus stress	
	L3-L4	L4-L5	L3-L4	L4-L5	L3-L4	L4-L5	L3-L4	L4-L5
Old geometry	II°	~°	III° (RS)†	II (ARS)†	II (PLL)	-°	II (POST)	II (POST)
New geometry	II°	I°	IV° (ARS)†	I° (RS)†	II° (ALL)	II° (ALL)	II (POST)	II (POST)

-: Relative difference < 2% | ~: Relative difference ≤ 5% | I: Relative difference < 10% | II: Relative difference < 50% | III: Relative difference < 100% | IV: Relative difference < 200%
 Uppercase ° indicates that no significant change occurred with respect to the previous component suppression (relative difference change ≤ 5%).

When both models have the same symbol affected to the same component, the cell with dashed lines indicates the most affected geometry. No dashed lines were drawn when both geometries were similarly affected.

† RS: Rotation Side - ARS: Anti Rotation Side

4) Bony posterior elements removal

Without BPE, the old geometry ROM had a slight tendency to increase at the L3-L4 level (Fig. 3.18). However, the only meaningful change occurred in the old geometry L3-L4 PLL, where the relative differences became about 15% greater due to a ligament tensile stress increase (Fig. 3.20). The AF fibre stress variations associated to the BPE removal were generally low and never overcame 10% in terms of relative differences change (Fig. 3.22b). The maximum differences were calculated for the old geometry.

Table 3.20: Qualitative representation of the maximum effect of the bony posterior elements suppression on the different studied mechanical criteria under lateral bending.

Model	Range of motion		Anterior ligament stress		Annulus fibrosus stress	
	L3-L4	L4-L5	L3-L4	L4-L5	L3-L4	L4-L5
Old geometry	II°	~°	II (PLL)	-°	II (POST) -I (ANT)	II (LAT)
New geometry	II°	I°	II° (ALL)	II° (ALL)	II° (POST)	II° (POST)

-: Relative difference < 2% | ~: Relative difference ≤ 5% | I: Relative difference < 10% | II: Relative difference < 50%
 Uppercase ° indicates that no significant change occurred with respect to the previous component suppression (relative difference change ≤ 5%).

When both models have the same symbol affected to the same component, the cell with dashed lines indicates the most affected geometry. No dashed lines were drawn when both geometries were similarly affected.

Symbols in red cells represent the maximum relative difference change induced by the removal when change occurs in a component different from that associated to the maximum relative difference value.

5) Posterior longitudinal ligament removal

The mobility of both geometries was fairly insensitive to the suppression of PLL (Fig. 3.18). The new geometry L3-L4 ALL tensile stresses were slightly increased, and

with a relative difference change of about 4%, this ligament was the most affected (Fig. 3.20b) one. In the intervertebral disc, the relative difference variations were limited and as for the BPE resection, the maximum values were about 10% and were computed for the L4-L5 posterior AF of the old geometry (Fig. 3.22b). For the lateral L3-L4 AF of the new geometry, a relative difference reduction of 9% was predicted. These two latter changes were respectively associated to a stress increase and stress decrease (Fig. 3.22a).

Table 3.21: Qualitative representation of the maximum effect of the posterior longitudinal ligament suppression on the different studied mechanical criteria under lateral bending.

Model	Range of motion		Anterior ligament stress		Annulus fibrosus stress	
	L3-L4	L4-L5	L3-L4	L4-L5	L3-L4	L4-L5
Old geometry	II°	~°	II° (ALL)	~	II° (POST)	II (POST)
New geometry	II°	I°	II (ALL)	II° (ALL)	II (POST) -I (LAT)	II° (POST)

-: Relative difference < 2% | ~: Relative difference ≤ 5% | I: Relative difference < 10% | II: Relative difference < 50%
 Uppercase ° indicates that no significant change occurred with respect to the previous component suppression (relative difference change ≤ 5%).

When both models have the same symbol affected to the same component, the cell with dashed lines indicates the most affected geometry. No dashed lines were drawn when both geometries were similarly affected.

Symbols in red cells represent the maximum relative difference change induced by the removal when change occurs in a component different from that associated to the maximum relative difference value.

6) Nucleus pulposus removal

As shown by Figures 3.18 and 3.22, the effects of ALL removal on the segmental ROM and AF fibre stresses were quite meaningless. Nonetheless, the subsequent NP suppression was responsible for both ROM and AF fibres stress increases. ROM increase took place in both geometries, but with relative difference changes of 15% at each level, the new geometry appeared slightly more sensitive than the old one (Fig. 3.18b). Except at the postero-lateral locations, all the AF tensile stresses were increased (Fig. 3.22a). The greatest changes were predicted in the posterior annuli and with a relative difference variation of about 50%, they were more than twice greater in the old geometry than in the new one (Fig. 3.22b).

Table 3.22: Qualitative representation of the maximum effect of the nucleus pulposus suppression on the different studied mechanical criteria under lateral bending.

Model	Range of motion		Annulus fibrosus stress	
	L3-L4	L4-L5	L3-L4	L4-L5
Old geometry	II	II	III (POST)	III (POST)
New geometry	II	II	II (POST)	II (POST)
			+II (LAT)	+II (ANT)

-: Relative difference < 2% | ~: Relative difference ≤ 5% | I: Relative difference < 10% | II: Relative difference < 50% | III: Relative difference < 100%

When both models have the same symbol affected to the same component, the cell with dashed lines indicates the most affected geometry. No dashed lines were drawn when both geometries were similarly affected.

Symbols in red cells represent the maximum relative difference change induced by the removal when change occurs in a component different from that associated to the maximum relative difference value.

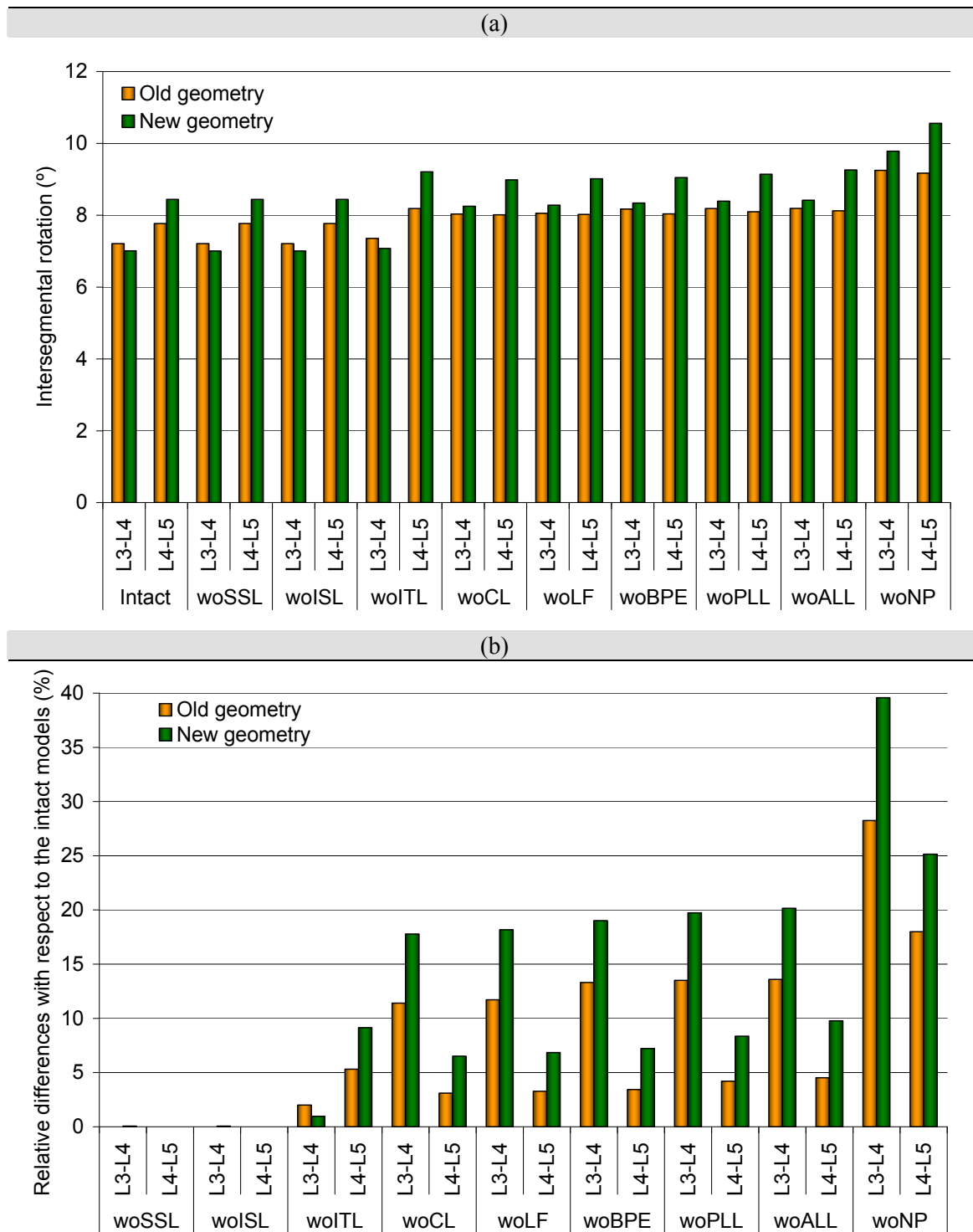


Figure 3.18: Average ranges of motions due to lateral bending at 7.5N.m; a) Absolute values for the intact version of each geometry and after each component resection. b) Relative differences with respect to the intact version of each geometry induced after each of the successive resections.

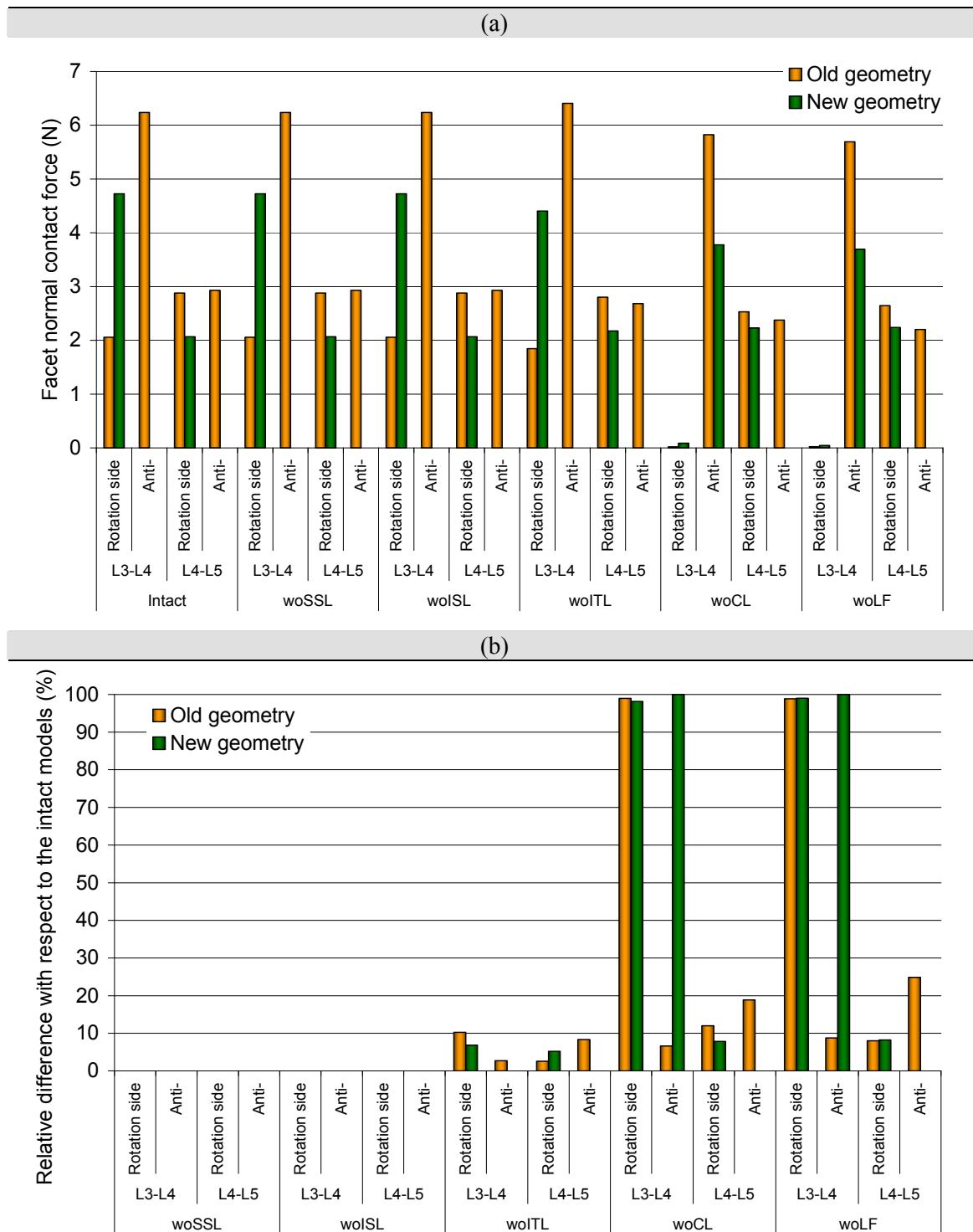


Figure 3.19: Mean normal facet contact forces under lateral bending at 7.5N.m. a) Absolute values for the intact version of each geometry and after each component resection. b) Relative differences with respect to the intact version of each geometry induced after each of the successive resections.

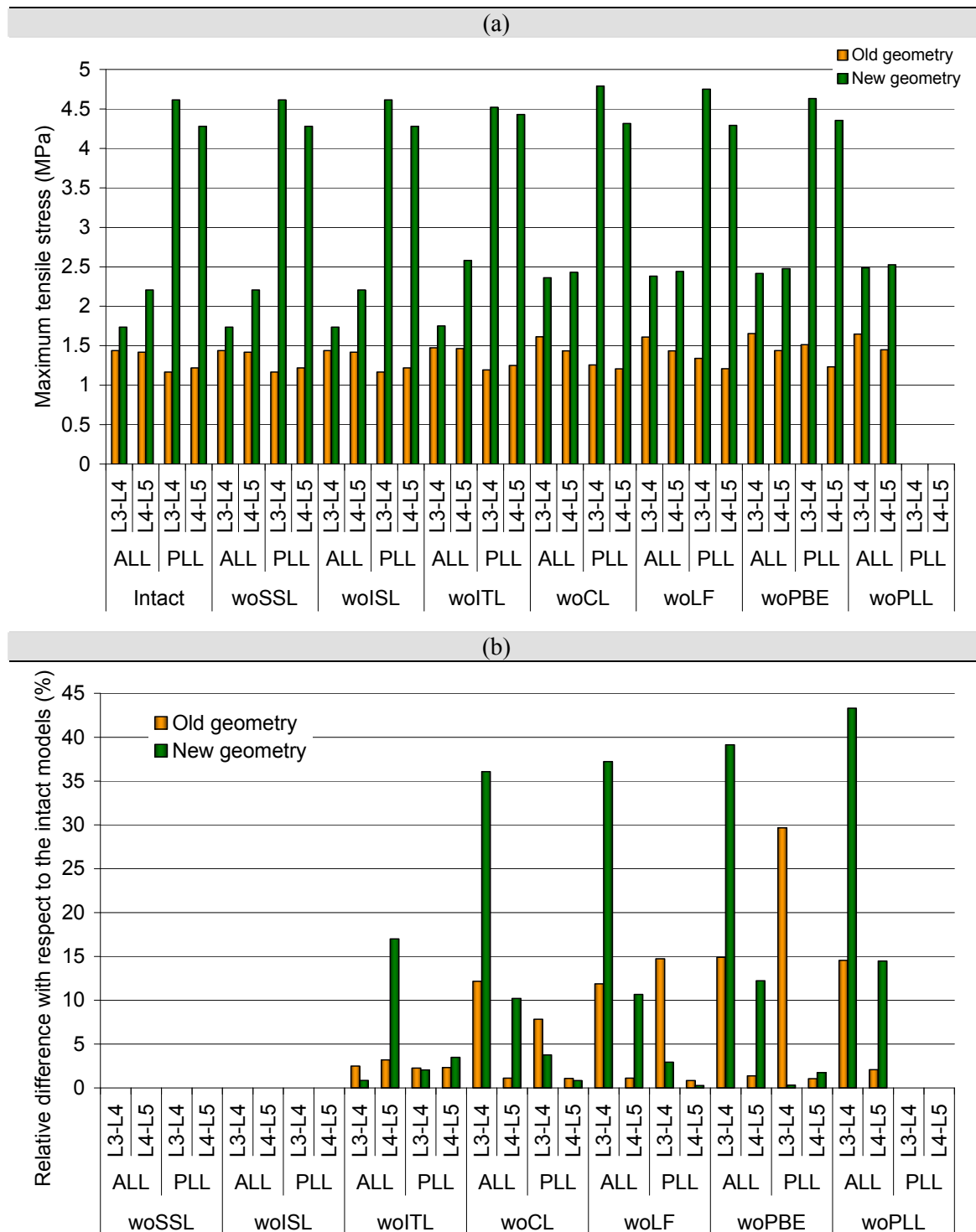


Figure 3.20: Anterior ligaments average tensile stresses under lateral bending at 7.5N. a) Absolute values for the intact version of each geometry and after each component resection. b) Relative differences with respect to the intact version of each geometry induced after each of the successive resections.

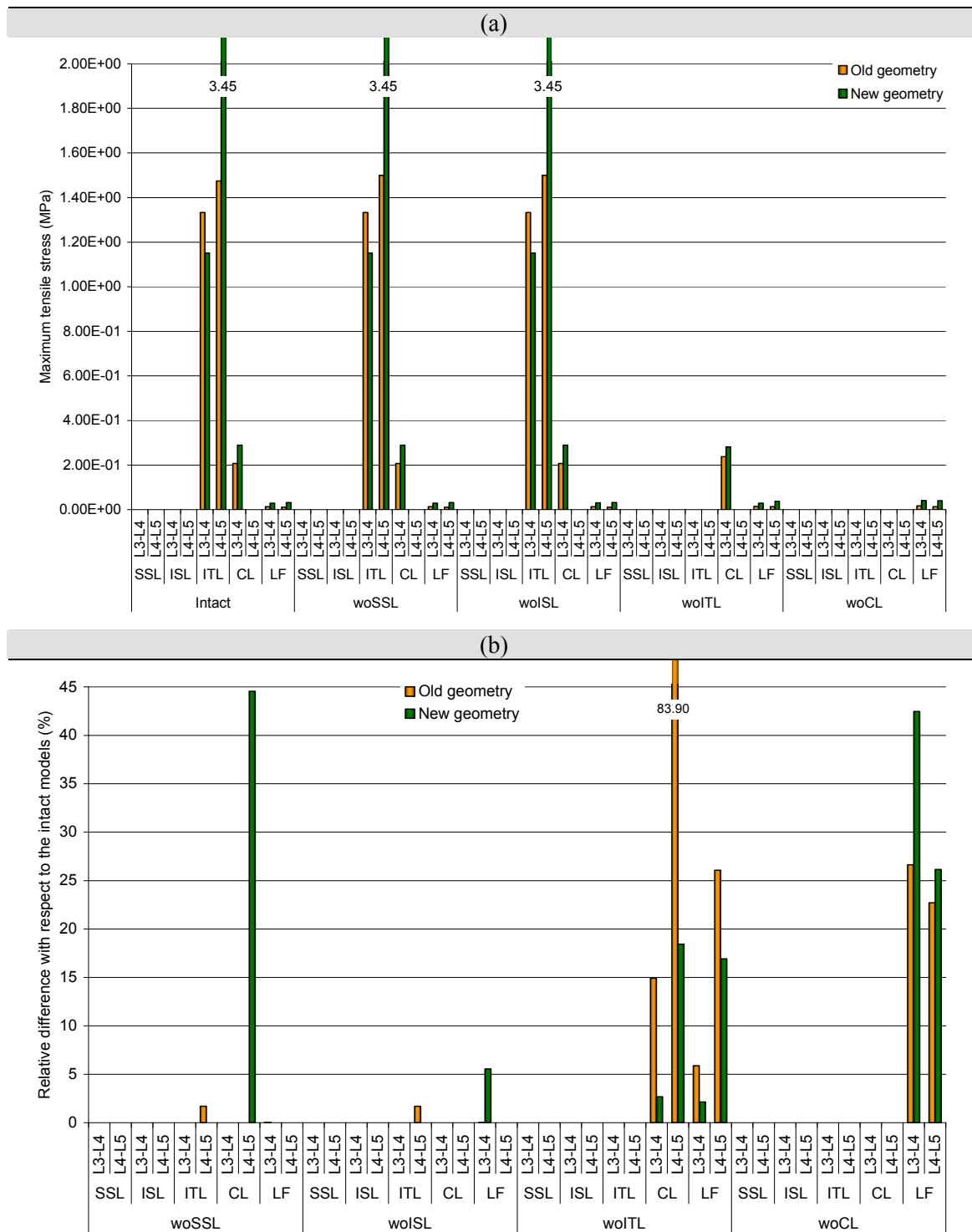


Figure 3.21: Posterior ligaments average tensile stresses under lateral bending at 7.5N.m. a) Absolute values for the intact version of each geometry and after each component resection. b) Relative differences with respect to the intact version of each geometry induced after each of the successive resections.

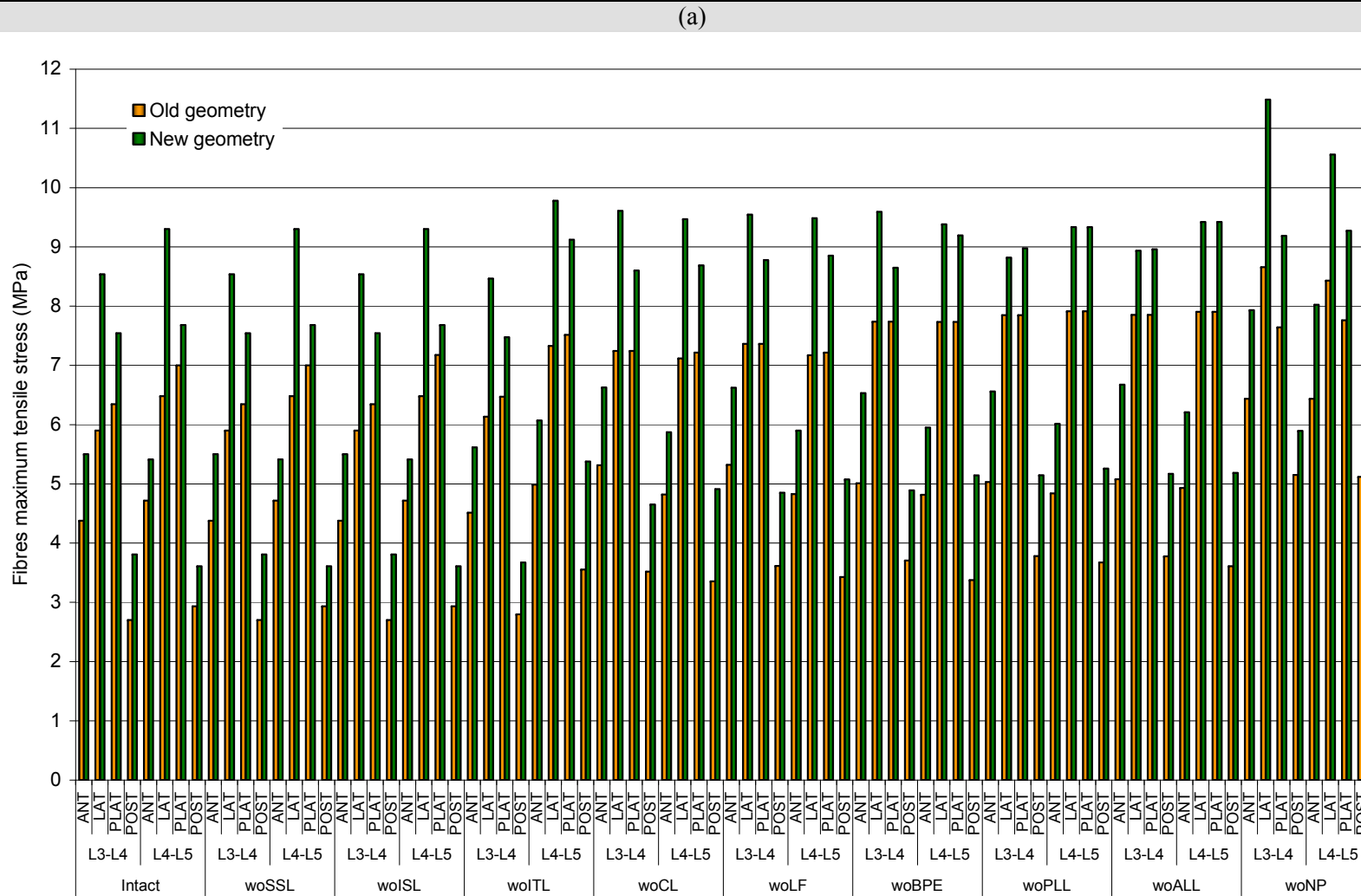


Figure 3.22a: Annulus fibrosus fibres average tensile stresses under lateral bending at 7.5N.m. – Absolute values for the intact version of each geometry and after each component resection.

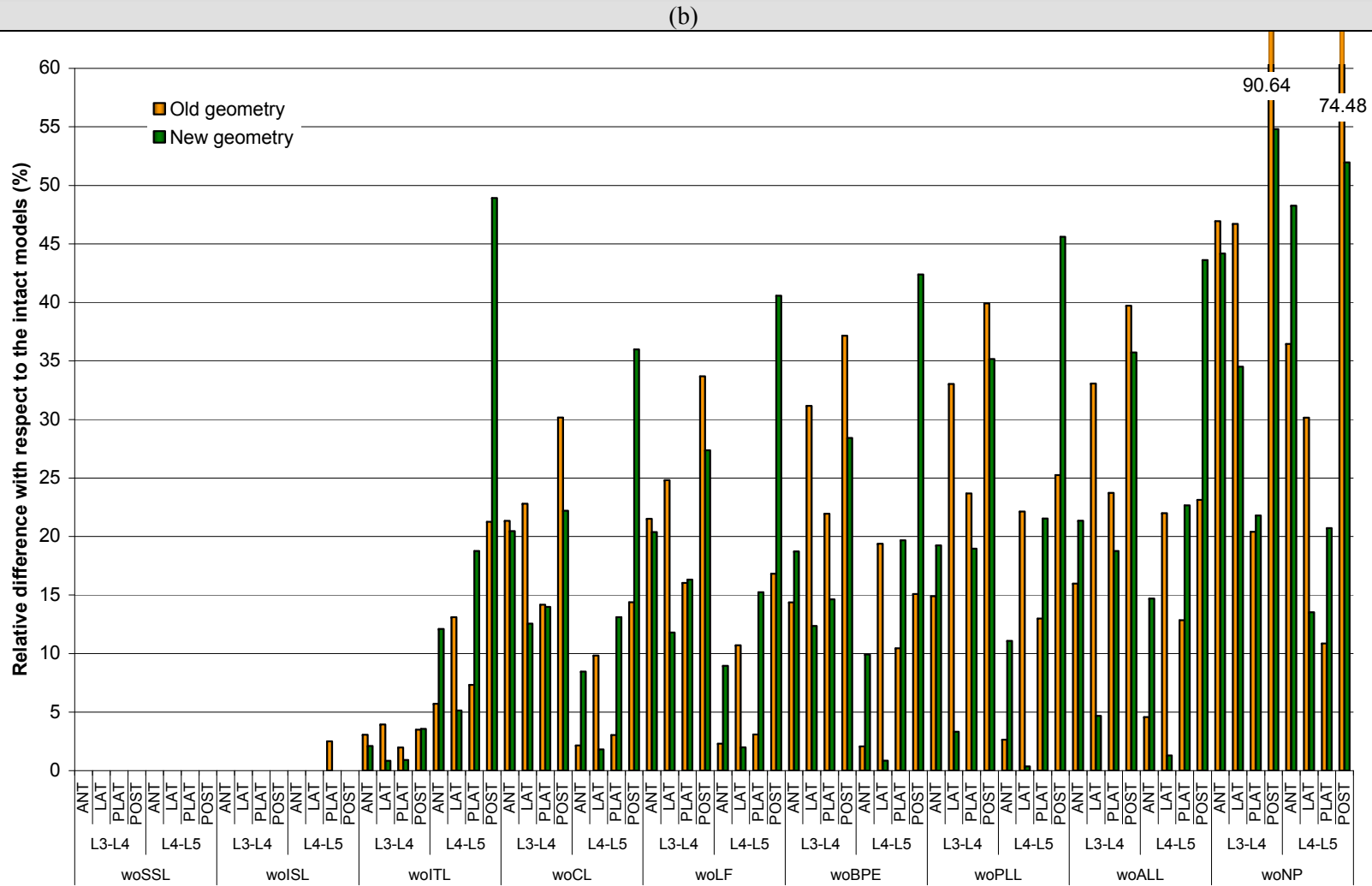


Figure 3.22b: Annulus fibrosus fibres average tensile stresses under lateral bending at 7.5N.m. – Relative differences with respect to the intact version of each geometry induced after each of the successive resections.

d. Axial rotation

As in the case of lateral bending, the results presented in axial rotation were averaged from the left and right motions in order to avoid the influence of the sagittal asymmetric distribution of the modelled AF collagen fibres. Under this condition, Fig. 3.23 shows that before CL removal, none of the successive ligament suppressions modified the mobility of the models motion segments. The new geometry contact forces to the anti-rotation side were only slightly affected with a relative loss of contact of less than 5% after the ISL removal (Fig. 3.24). As shown in Fig. 3.25, as obtained for the ROM, the anterior ligaments stresses did not change until CL was suppressed. ITL begun to be significantly affected after ISL was taken away. However, its initial stress values were so low ($\approx 1.10^{-4}$ MPa), that even if the computed relative differences rose up to 30%, the effect could not be considered as significant (Fig. 3.26). In the new geometry, LF tensile stresses were increased of about 14% at the L3-L4 level, and about 10% at the L4-L5 level. In the old geometry, the changes were only about 7% at the L4-L5 level. In the AF, neither SSL, nor ISL, nor ITL suppressions had any remarkable effect on the fibre stress state (Fig. 3.27). More details are given in the following subsections about the resection of CL and the further components. The major effects of each removal are qualitatively summarised from Table 3.23 to Table 3.27.

1) Capsular ligament removal

CL removal contributed to increase significantly the L3-L4 rotations for both geometries, but the new one resulted about 8% more sensitive to the ligament resection (Fig. 3.23). At the L4-L5 level, the rotations also tended to rise, but the associated relative differences were fairly low (Fig. 3.23b). To the anti rotation side, while the contact normal forces were increased for both models at the L3-L4 level, at the L4-L5 level, they only tended to increase in the new geometry. In the old model, lower contact forces were predicted (Fig. 3.24a). At both levels, the old geometry was more sensitive than the new one and the relative differences for the L3-L4 segment rose up to about 19% (Fig. 3.24b). Nonetheless, in the L4-L5 segment, the maximum changes did not overcome 4.5%. The L3-L4 ALL tensile stresses were substantially increased in both models and in the new geometry, the L4-L5 PLL was also largely affected (Fig. 3.25a). At the L4-L5 level, while the old and new geometry ALL became less tensed, PLL stresses increased. As shown in Figure 3.25b, the changes computed in the L4-L5 ALL were rather insignificant, and for all other ligaments and levels, the new geometry was the most affected one (the major relative increment of tensile stress being about 71% in the L3-L4 PLL). Without CL, a clear stress increase took place in all the LF (Fig. 3.26a). Due to the low absolute LF stresses that were predicted, the relative differences computed for the L3-L4 level reached high numerical values, especially for the new geometry, where the calculated relative stress increase was about 480% (Fig. 3.26b). For the old geometry, it was around 140%. At the L4-L5 level, the sensitivity was similar for both models but once again, not significant. In the L3-L4 segment, AF fibres were in general largely affected with great increments of tensile stress, especially in the lateral and postero-lateral locations (Fig. 3.27). Except in the postero-lateral area, all the fibres were more influenced in the new geometry (Fig. 3.27b). In the postero-lateral AF, the stress increase in the old geometry was the highest one and rose up to about 130%.

In the posterior annulus, while the relative differences ascended up to about 35% in the new geometry, they were about 11% in the old one. In the L4-L5 AF, no significant fibres stress variations were predicted.

Table 3.23: Qualitative representation of the maximum effect of the capsular ligament suppression on the different studied mechanical criteria under axial rotation.

Model	Range of motion		Facet contact force		Anterior ligament stress		Posterior ligament stress		Annulus fibrosus stress	
	L3-L4	L4-L5	L3-L4	L4-L5	L3-L4	L4-L5	L3-L4	L4-L5	L3-L4	L4-L5
Old geometry	II	-	II (ARS)†	~ (ARS)†	II (PLL)	I (PLL)	IV (LF)	II (LF)	IV (PLAT)	-
New geometry	II	~	II (ARS)†	~ (ARS)†	III (PLL)	II (PLL)	V (LF)	II (LF)	III (PLAT)	~

-: Relative difference < 2% | ~: Relative difference ≤ 5% | I: Relative difference < 10% | II: Relative difference < 50% | III: Relative difference < 100% | IV: Relative difference < 200% | V: Relative difference < 500%

When both models have the same symbol affected to the same component, the cell with dashed lines indicates the most affected geometry. No dashed lines were drawn when both geometries were similarly affected.

† RS: Rotation Side - ARS: Anti Rotation Side

2) Ligamentum flavum removal

As shown in Figure 3.23b, the further resection of LF did no seem to affect the ROM, (relative difference changes about 1%). The facet contact forces were also hardly affected. However losses of contact associated with relative difference decreases of about 7% and 8% were predicted respectively in the old and in the new geometry (Fig. 3.24). In the anterior ligaments, the greatest changes were computed for the L3-L4 PLL, and in both models, they corresponded to a relative difference variation of about 9% (Fig. 3.25b). Nonetheless, while for the new geometry this change was due to a stress decrease, in the old geometry it corresponded to a stress increase (Fig. 3.25a). In the AF, the largest predicted effect was a relative difference increase of less than 8% related to a tensile stress level somewhat higher in the old geometry posterior AF fibres (Fig. 3.27).

Table 3.24: Qualitative representation of the maximum effect of the ligamentum flavum suppression on the different studied mechanical criteria under axial rotation.

Model	Range of motion		Facet contact force		Anterior ligament stress		Annulus fibrosus stress	
	L3-L4	L4-L5	L3-L4	L4-L5	L3-L4	L4-L5	L3-L4	L4-L5
Old geometry	II°	-	II* (ARS)†	~ (ARS)†	II (PLL)	I° (PLL)	IV° (PLAT)	~
New geometry	II°	~	~* (ARS)†	I (ARS)†	III* (PLL)	II° (PLL)	III° (PLAT) -I (ANT)	I (POST)

-: Relative difference < 2% | ~: Relative difference ≤ 5% | I: Relative difference < 10% | II: Relative difference < 50% | III: Relative difference < 100% | IV: Relative difference < 200%

Uppercase * indicates that a relative difference decrease occurred with respect to the previous component suppression. Uppercase ° indicates that no significant change occurred with respect to the previous component suppression (relative difference change ≤ 5%).

When both models have the same symbol affected to the same component, the cell with dashed lines indicates the most affected geometry. No dashed lines were drawn when both geometries were similarly affected.

Symbols in red cells represent the maximum relative difference change induced by the removal when change occurs in a component different from that associated to the maximum relative difference value.

† RS: Rotation Side - ARS: Anti Rotation Side

3) Bony posterior elements removal

After the BPE were removed, in both models and at both levels the ROM increased nearly twice and the old geometry was softer than the new one (Fig. 3.23a). Moreover, the relative difference results indicated that the old geometry was between 20% and 30% more sensitive than the new one (Fig. 3.23b). The anterior ligament tensile stresses were also dramatically increased by the posterior bony components resection and old geometry ligament stresses slightly overcame those of the new geometry (Fig. 3.25a). The PLL were the most influenced components and especially in the old geometry, where the relative differences rose up to about 1800% at the L3-L4 level and 1260% at the L4-L5 level (Fig. 3.25b). The values for the new geometry were only about one tenth of these ones. In the L3-L4 segment, the ALL of the new geometry was about two-folds more sensitive than that of the old geometry, and at the L4-L5 level, the ligament was similarly affected in both geometries with relative difference increases of about 12%. The BPE were the constituents whose absence most affected the AF fibres inducing high incremental stretches (Fig. 3.27). The greatest changes took place in the posterior fibres, and at the L3-L4 level, the relative difference variations were about 570% and 530% respectively in the old and in the new geometry (Fig. 3.27b). In the L4-L5 segment, all AF areas and especially the posterior location, showed more sensitivity in the old geometry than in the new one.

Table 3.25: Qualitative representation of the maximum effect of the posterior bony elements suppression on the different studied mechanical criteria under axial rotation.

Model	Range of motion		Anterior ligament stress		Annulus fibrosus stress	
	L3-L4	L4-L5	L3-L4	L4-L5	L3-L4	L4-L5
Old geometry	IV	III	VI (PLL)	VI (PLL)	VI (POST)	V (POST)
New geometry	IV	III	V (PLL)	III (PLL)	VI (POST)	V (POST)

-: Relative difference < 2% | ~: Relative difference ≤ 5% | I: Relative difference < 10% | II: Relative difference < 50% | III: Relative difference < 100% | IV: Relative difference < 200% | V: Relative difference < 500% | VI: Relative difference ≥ 500%
 When both models have the same symbol affected to the same component, the cell with dashed lines indicates the most affected geometry. No dashed lines were drawn when both geometries were similarly affected.

4) Posterior longitudinal ligament removal

PLL resection does not seem to influence the mobility of the models (Fig. 3.23) nor the stress state of the ALL (Fig. 3.25). However, in the AF, as expected, the posterior fibre stresses were increased (Fig. 3.27a). With relative difference changes of about 100% and 60% respectively at the L3-L4 and L4-L5 levels, the new geometry exhibited more than twice sensitivity when compared to the old model (Fig. 3.27b). The anterior fibres were hardly affected and only the AF postero-lateral locations of the new geometry became significantly more stressed, although the effect was less than in the posterior areas.

Table 3.26: Qualitative representation of the maximum effect of the posterior longitudinal ligament suppression on the different studied mechanical criteria under axial rotation.

Model	Range of motion		Anterior ligament stress		Annulus fibrosus stress	
	L3-L4	L4-L5	L3-L4	L4-L5	L3-L4	L4-L5
Old geometry	IV°	III°	II° (ALL)	II (ALL)	VI (POST)	V (POST)
New geometry	IV°	III°	II° (ALL)	II (ALL)	VI+ (POST)	V (POST)

-: Relative difference < 2% | ~: Relative difference ≤ 5% | I: Relative difference < 10% | II: Relative difference < 50% | III: Relative difference < 100% | IV: Relative difference < 200% | V: Relative difference < 500% | VI: Relative difference ≥ 500%
 Uppercase ° indicates that no significant change occurred with respect to the previous component suppression (relative difference change ≤ 5%). Uppercase + indicates further relative difference increases ≥ 100% for pre-existing values ≥ 500%.
 When both models have the same symbol affected to the same component, the cell with dashed lines indicates the most affected geometry. No dashed lines were drawn when both geometries were similarly affected.

5) Nucleus pulposus removal

As shown in Figures 3.23 and 3.27, successive removal of ALL had roughly no effect, neither on the models mean axial rotation ROM, nor on the AF fibres stresses. However, without NP, the ROM rose substantially in both geometries and at both levels (Fig. 3.23a). At the L4-L5 level, the new geometry was more sensitive than the old one, with a ROM relative difference change after NP resection about 20% greater than in the old geometry (Fig. 3.23b). In both geometries, AF fibre stresses were increased,

especially in the postero-lateral area of the L3-L4 level (Fig. 3.27a). At the L4-L5 level, old geometry postero-lateral and posterior fibres were both similarly affected, while in the new geometry, postero-lateral fibres were more influenced than the posterior ones (Fig. 3.27b). Nevertheless, highest fibre stress relative difference changes did not differ more than 10% in both models, and maximum relative difference changes from the previous ALL removal were found in the L3-L4 lateral and postero-lateral AF fibres.

Table 3.27: Qualitative representation of the maximum effect of the nucleus pulposus suppression on the different studied mechanical criteria under axial rotation.

Model	Range of motion		Annulus fibrosus stress	
	L3-L4	L4-L5	L3-L4	L4-L5
Old geometry	V	IV	VI (POST)	V (POST)
			+IV (PLAT)	
New geometry	V	IV	VI (POST)	V (POST)
			+IV (PLAT)	+III (PLAT)

-: Relative difference < 2% | ~: Relative difference ≤ 5% | I: Relative difference < 10% | II: Relative difference < 50% | III: Relative difference < 100% | IV: Relative difference < 200% | V: Relative difference < 500% | VI: Relative difference ≥ 500%

When both models have the same symbol affected to the same component, the cell with dashed lines indicates the most affected geometry. No dashed lines were drawn when both geometries were similarly affected.

Symbols in red cells represent the maximum relative difference change induced by the removal when change occurs in a component different from that associated to the maximum relative difference value.

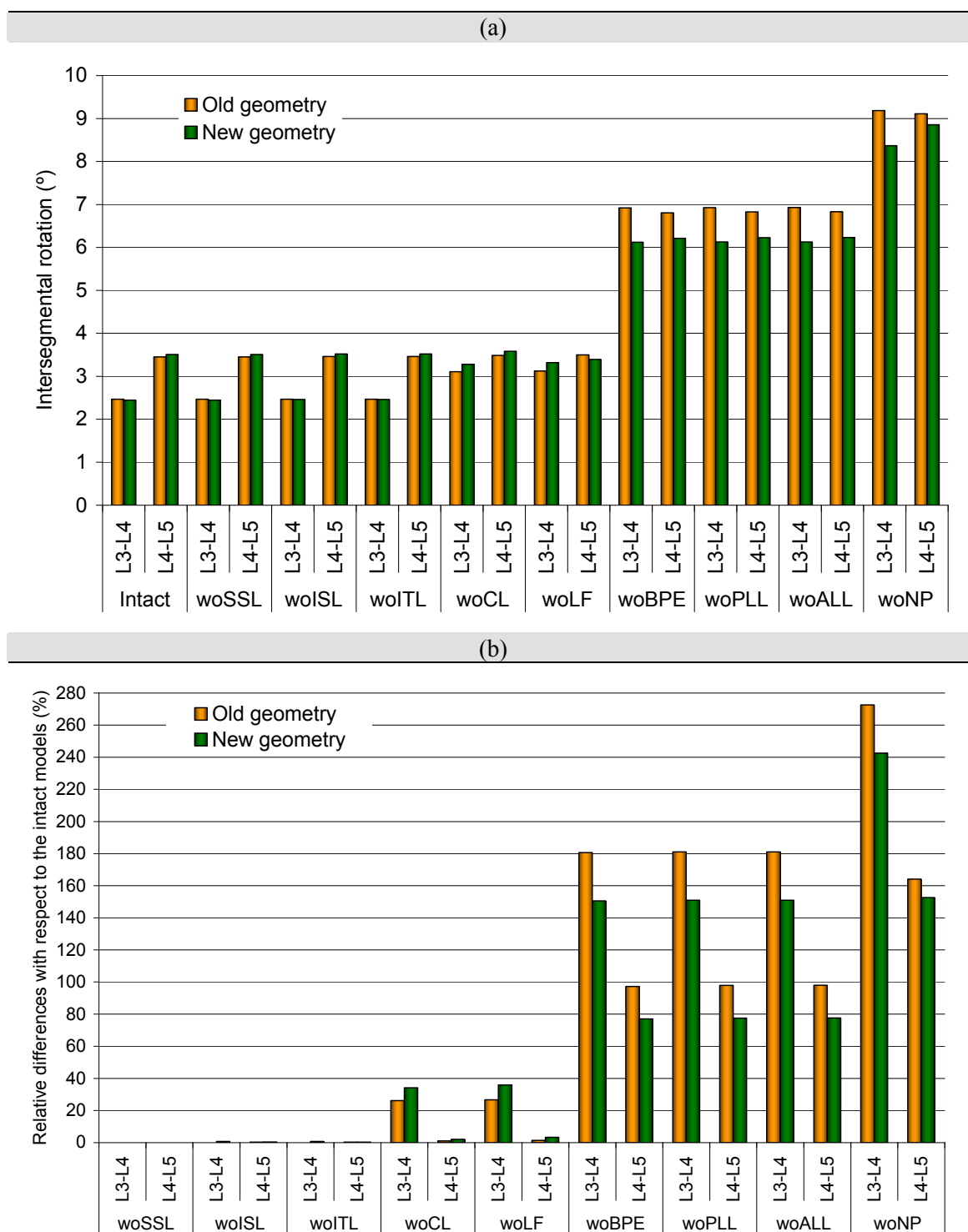


Figure 3.23: Average ranges of motions under axial rotation at 7.5N.m; a) Absolute values for the intact version of each geometry and after each component resection. b) Relative differences with respect to the intact version of each geometry induced after each of the successive resections.

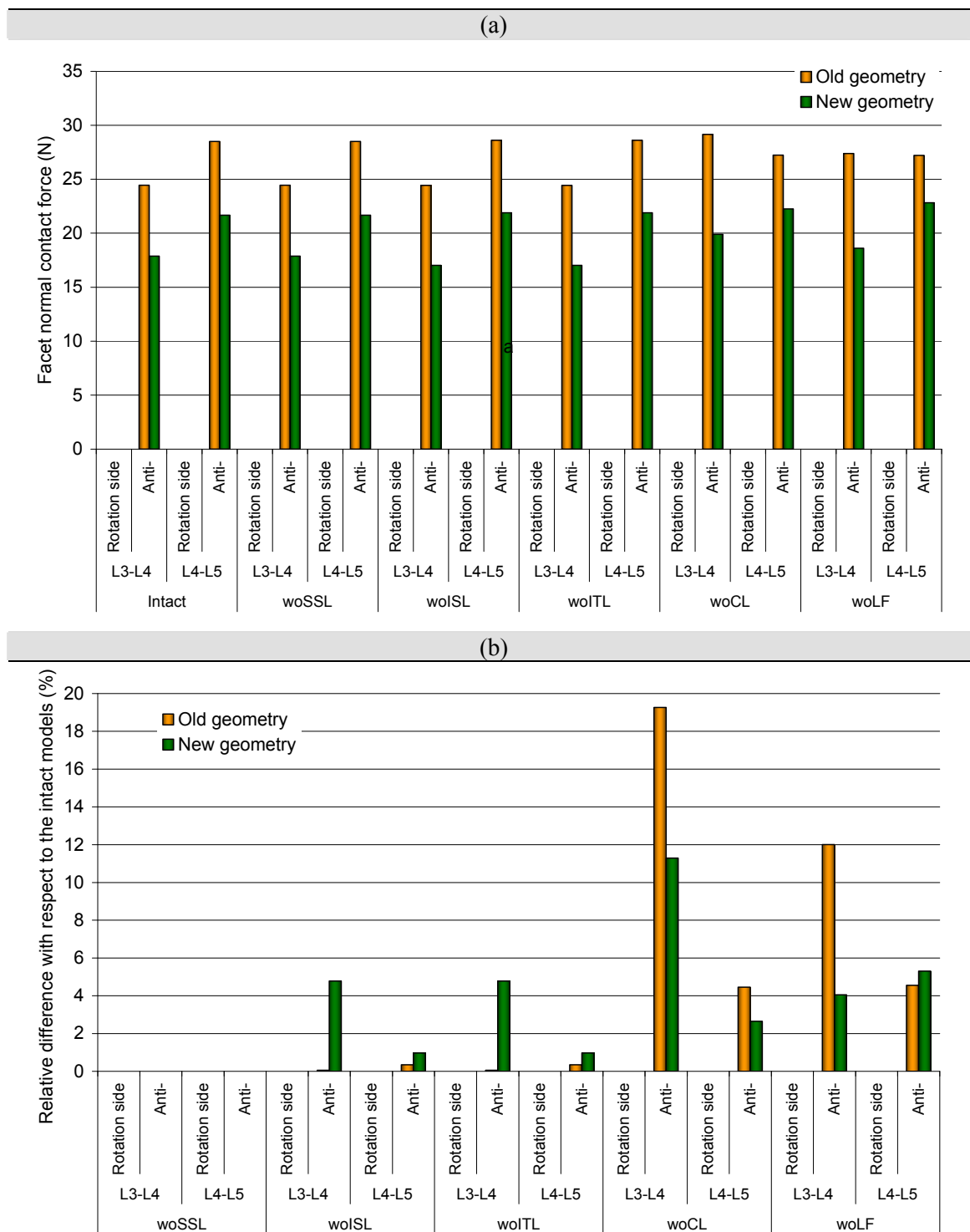


Figure 3.24: Mean normal contact forces on facets under axial rotation at 7.5N.m. a) Absolute values for the intact version of each geometry and after each component resection. b) Relative differences with respect to the intact version of each geometry induced after each of the successive resections.

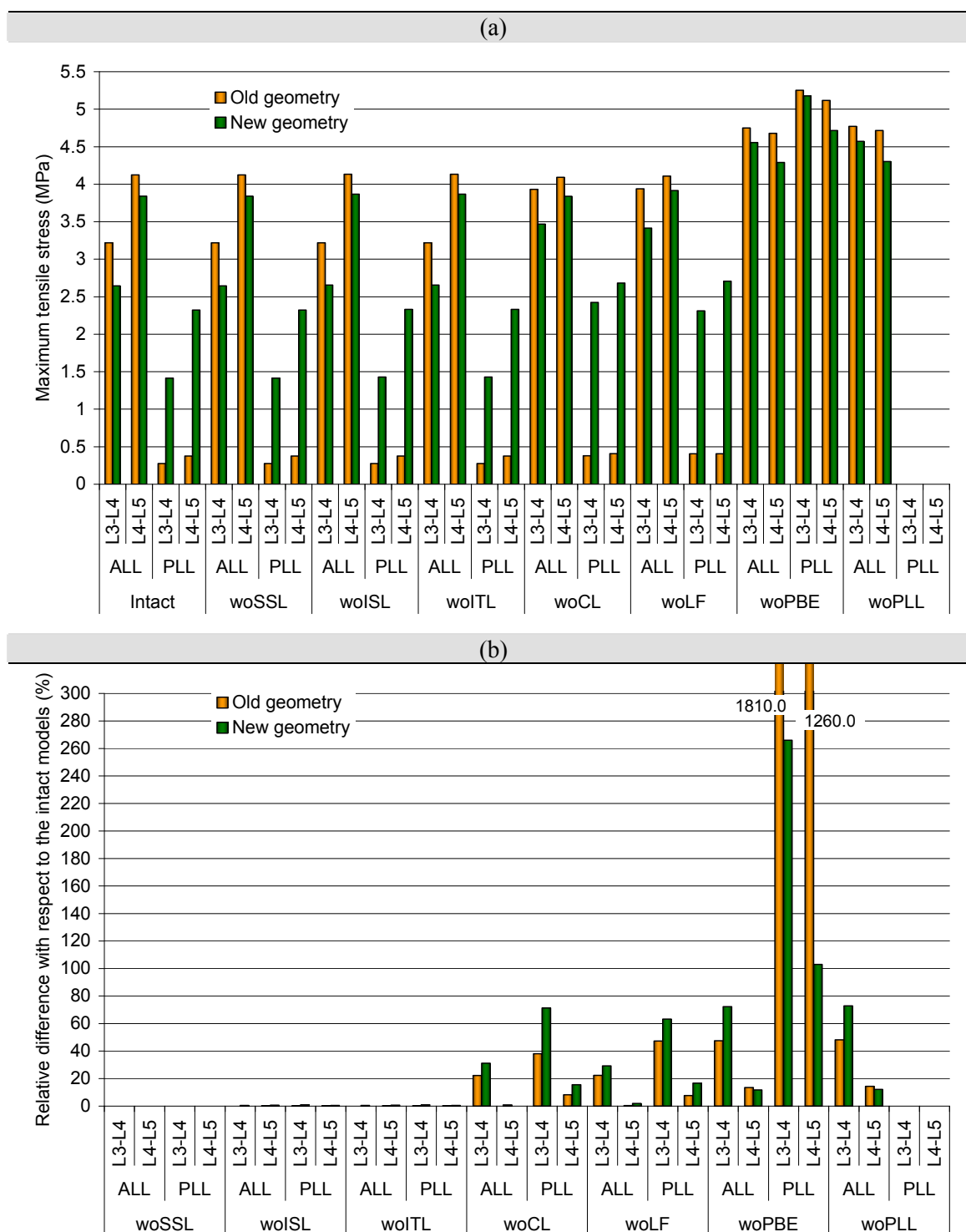


Figure 3.25: Average tensile stresses of the anterior ligaments under axial rotation at 7.5N.m. a) Absolute values for the intact version of each geometry and after each component resection. b) Relative differences with respect to the intact version of each geometry induced after each of the successive resections.

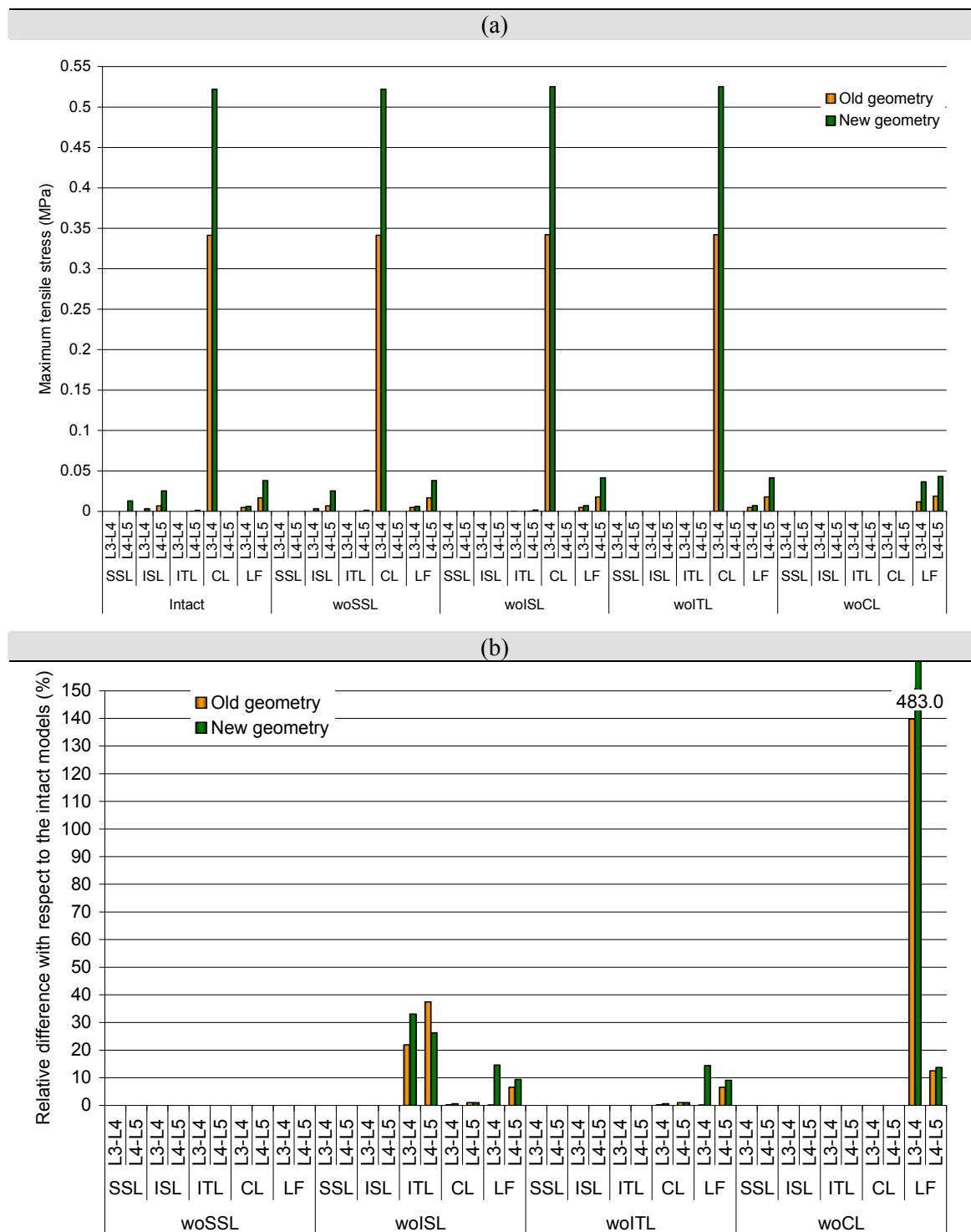


Figure 3.26: Average tensile stresses of the posterior ligaments under axial rotation at 7.5N.m.
 a) Absolute values for the intact version of each geometry and after each component resection.
 b) Relative differences with respect to the intact version of each geometry induced after each of the successive resections.

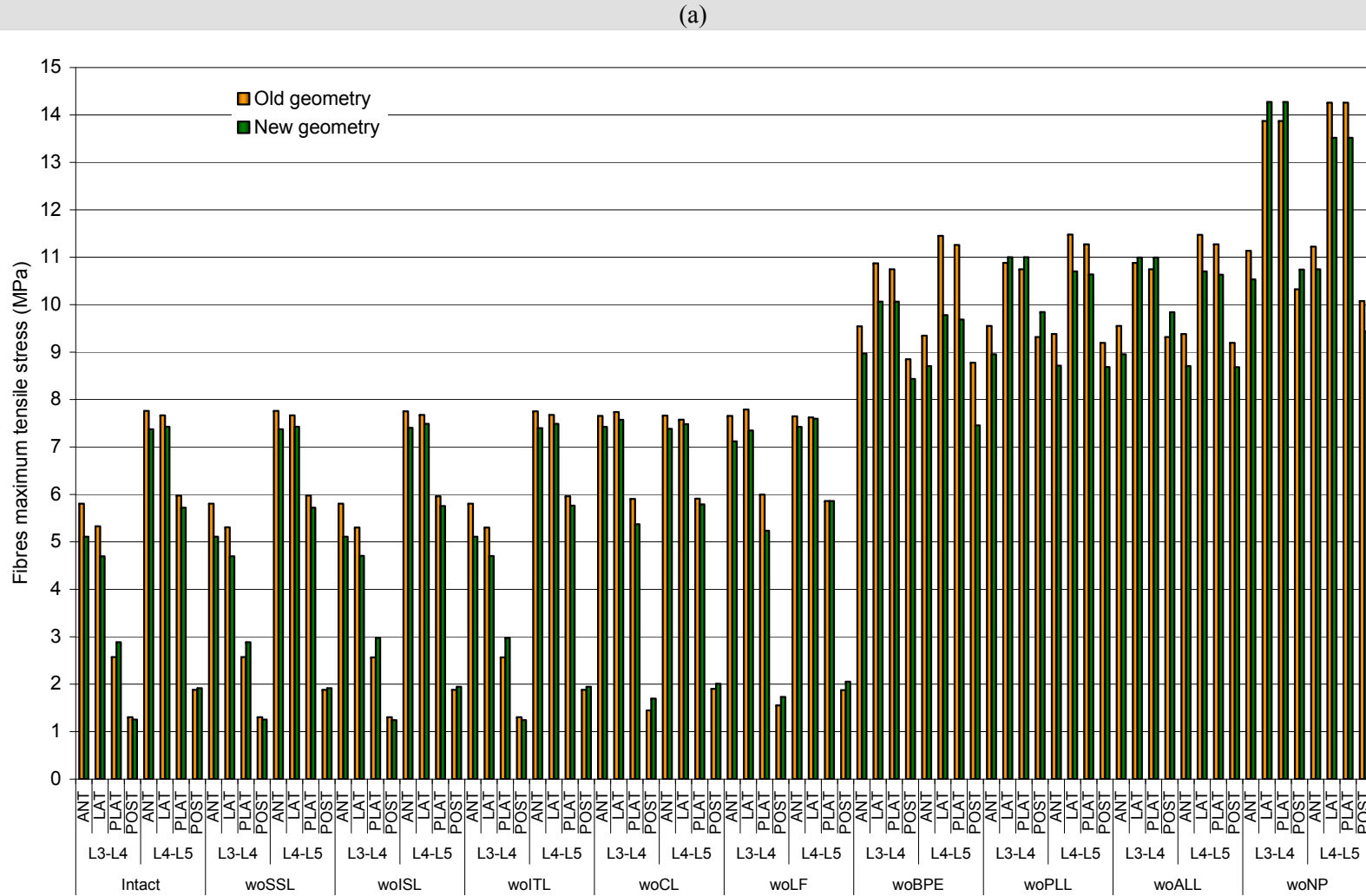


Figure 3.27a: Average tensile stresses of the annulus fibrosus fibres under axial rotation at 7.5N.m. – Absolute values for the intact version of each geometry and after each component resection.

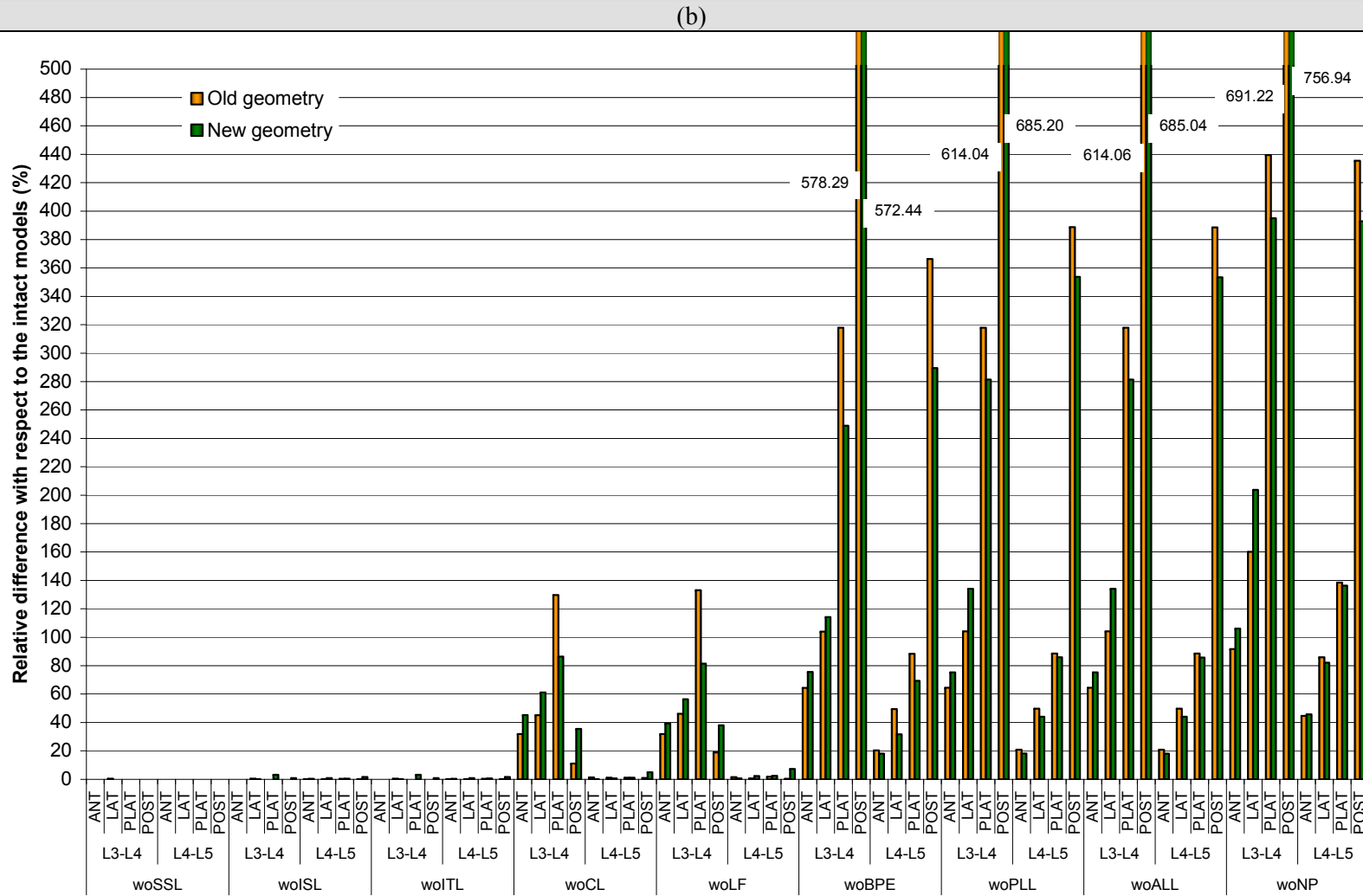


Figure 3.27b: Average tensile stresses of the annulus fibrosus fibres under axial rotation at 7.5N.m. – Relative differences with respect to the intact version of each geometry induced after each of the successive resections.

e. Intact models

Under flexion, while the L3-L4 segment appeared slightly softer in the old geometry than in the new one, at the L4-L5 level, the situation was reversed and the new geometry was significantly softer (Fig. 3.9a). In the new geometry, the load supported by the facet cartilage was nearly inexistent (Fig. 3.10a), and at the L3-L4 level, the anterior ligaments were slightly less stretched than in the old model, while at the L4-L5 level, they were substantially more stressed (Fig. 3.11a). Except for the L3-L4 ITL, although the stresses predicted in the posterior ligaments were limited, they were generally higher in the new geometry, independently on the considered segment (Fig. 3.12a). In the AF, the same scheme as for anterior ligaments was predicted, and the fibre stresses were alternatively greater in the old and new geometry, respectively at the L3-L4 and L4-L5 level.

In extension, the new geometry was always between 6% and 10% more flexible than the old one (Fig. 3.14a). Whatever the motion segment, the facet contact forces were always larger in the old geometry (Fig. 3.15a). Nevertheless, while at the L3-L4 level, they were more than twice higher, at the L4-L5 level, the differences between the results given by both models were less than 10%. The anterior ligaments were also more stressed in the new geometry (Fig. 3.16a), so did the AF fibres, except the L4-L5 postero-lateral ones, that participated more in the old geometry (Fig. 3.17a).

Under lateral bending, as in flexion, the old geometry L3-L4 segment showed somewhat more flexibility, whereas at the L4-L5 level, the new geometry was softer than the old one (Fig. 3.18a). At the L3-L4 level, the new geometry did not offer any contact to the anti-rotation side (Fig. 3.19a), whereas its rotation side normal contact forces were greater than in the old geometry. At the L4-L5 level, the old geometry rotation side contact overcame that of the new geometry. In both motion segments, the anterior ligaments of the new model exhibited higher stress levels, especially at the L4-L5 level (Fig. 3.20a). Dorsally except the L3-L4 ITL, all the posterior ligaments were more stretched in the new geometry (Fig. 3.21a). In the intervertebral disc, the AF fibres were also generally more loaded in the new geometry (Fig. 3.22a).

Under axial rotation, no significant differences were predicted between the respective ROM of both models (Fig. 3.23a). Nonetheless, the facets contacts were much higher in the old geometry than in the new one (Fig. 3.24a). At both levels, while the old geometry ALL offer a greater resistance to the motion, than the new geometry corresponding ligament, the situation was reversed for the PLL (Fig. 3.25a). The CL were also more stressed in the new model (Fig. 3.26a), and finally, the old geometry AF fibres tended to be somewhat more loaded than those of the new geometry (Fig. 3.27a).

Finally, the comparison of the ROM predicted by both geometries with cadaveric data shows that in general both models compared well with the experimental values (Fig. 3.28) and were always within the experimental error. Even though, The ROM predicted at the L3-L4 level of the new geometry in flexion-extension was about 32% lower than the experimental mean rotation. For the rest of the load-cases, the maximum

difference with respect to the experimental data was given by the L3-L4 segment of the old geometry which was about 27% stiffer under lateral bending.

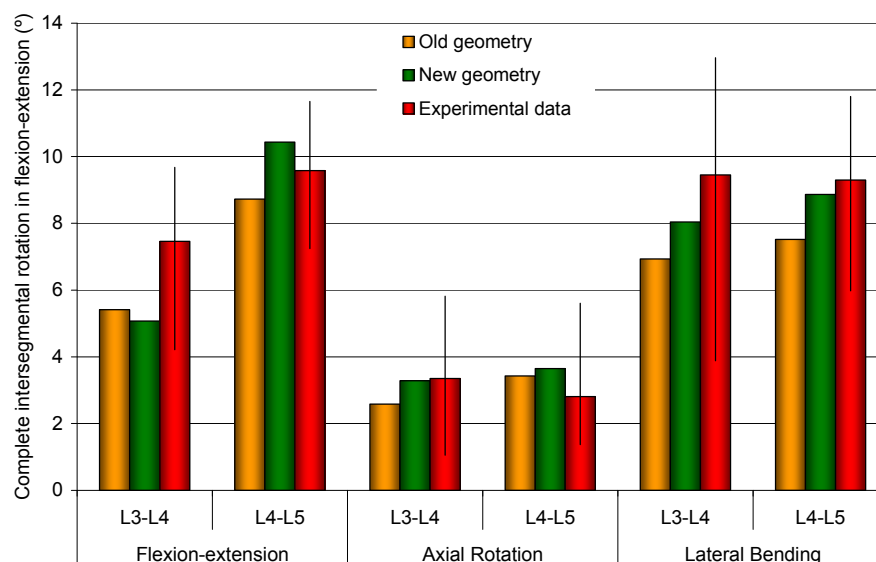


Figure 3.28: Comparison of the predicted ranges of motion with experimental *in vitro* motions for 7.5N.m pure moments.

III. Discussion

a. Supraspinous and interspinous ligaments

The larger spinous processes and the higher anterior L4-L5 intervertebral disc made that the SSL of the new geometry could be activated under the applied 7.5N.m flexion momentum. This allowed identifying several differences on the posterior load path of both geometries and the first difference was put in evidence after the ligament resection, when the new geometry L4-L5 ROM was curiously decreased and the L3-L4 contact force increased. In the new geometry, the fibres of the ISL were oblique with a supero-posterior infero-anterior course. After SSL removal, the ISL was no more shielded by its posterior neighbour and its oblique central and ventral parts became more tensed. Then, the ligament could preserve some stability by compensating a part of the loss of vertical resistance with a larger tendency to reduce the transversal translations that may move away the adjacent vertebrae from each other. Moreover, while the relative differences were just about 4% for the ROM, they were about 90% for the facet joint contact and between 9% and 7% for the PLL. Hence, it seems that the lack of SSL is mostly assumed by the facet joints in an attempt to stabilize the incomplete spine structure, and to impede the anterior components to be greatly affected by possible posterior damages. The great contact loss that occurred in the new geometry after ISL suppression is a logic consequence that fits well to this interpretation. The reorientation of the posterior components reacting force after SSL removal could not be

predicted in the old geometry since the SSL was not activated and the ISL fibres are fully vertical. This contributed to make the ISL removal more traumatic for the old geometry AF fibres. In extension, the action of the oblique fibres of the new geometry ISL was also put in evidence by the slight contact loss after the ligament was removed.

Unfortunately, the real mechanical role of the ISL could not be experimentally documented, since in most of the *in vitro* stepwise reductions of the spinal structure, the SSL and the ISL or even all the posterior ligaments were considered together (Twomey and Taylor, 1983; Adams *et al.*, 1980; Tencer *et al.*, 1982). Heuer *et al.* (Heuer *et al.*, 2007b; Heuer *et al.*, 2007a) cut separately these ligaments under 7.5N.m flexion in L4-L5 functional units and they found after SSL removal a tendency of the intradiscal pressure to decrease (Heuer *et al.*, 2007a). Nonetheless, the results were not statistically relevant and at the contrary to the present predictions, their ROM tended to increase slightly (Heuer *et al.*, 2007a). Such discrepancy is not very surprising; the ROM reduction found in the new geometry without SSL only concerns the L4-L5 level and since the current study is based on a bi-segment, the effective boundary conditions present at each level are roughly different from those applied on a single level, even if the applied loads are similar.

b. Intertransverse ligament

In the new geometry, since it blended with the CL, the LF had larger lateral extensions. That is the reason why under flexion, this ligament was influenced by the absence of ITL and the consequent slight loss of stability within the frontal plane induced by the asymmetric annulus fibres distribution. This was clearly illustrated under axial rotation when, in the new geometry, the oblique ISL was taken away and induced a slight loss of contact. This loss of contact diminished the lateral stabilization provided by the facets and contributed to increase the tensions within the LF. Under flexion, the interaction between the new geometry LF and the intervertebral disc after ITL removal is even more significant in the L4-L5 segment. It is certainly due to the influence of the intervertebral disc height that, in the new geometry, was greater at this level. Moreover, since in the new geometry the different lateral processes have not the same orientation with respect to the sagittal plane as they do in the old geometry, the ITL may be more directly aligned with the force vectors that L3 exerts on the lower vertebrae and its effect may be reinforced.

The results obtained in lateral bending without ITL also show the effect of the higher intervertebral disc in the new geometry. Although changes were low at the L3-L4 level because in the old geometry the ligament resisting force is concentrated at the tip of the transverse process, the model ROM resulted more sensitive to the lack of ITL. On the contrary, at the L4-L5 level the new geometry ITL had a greater role, probably because of the more flexible intervertebral joint and of the more frontal facet that does not offer resistance to the anti-rotation side. The latter unilateral contact may also be due to the axial rotation coupled motions linked to the action of the zygapophysial joints. In both models, the coupled rotation occurs in the same direction as the principal rotation. Therefore, while it tends to reduce the contact to the rotation side, it is likely to

increase it to the anti rotation side. In the new geometry, the coupled motion is twice lower than in the old model and probably insufficient in order to favour the anti rotation side contact. Moreover, without ITL, the coupled motion tended to increase in the old geometry and to decrease in the new model. The changes were the most pronounced at the L4-L5 level of the new geometry, where the coupled motions almost disappeared and even tended to reverse, which would contribute to explain the fact that the new geometry L4-L5 rotation side contact increased with ITL removal, while the old geometry contact decreased with less sensitivity. The broader new geometry L4-L5 ALL was able to recover stresses after ITL was taken away and more generally, the lateral actions of the new geometry L4-L5 anterior ligaments might be linked to the reduction of the coupled rotation. This is in good accordance with the relocation of loads to the anterior and postero-lateral areas of the L4-L5 AF, two-fold more important in the new geometry.

c. Capsular ligament

Under sagittal rotations, CL removal had the greatest effect among all the different spinal ligaments resections. Such prediction is in good accordance with the reported experiments that also studied successive resections (Adams *et al.*, 1980; Twomey and Taylor, 1983). The experiments of Heuer et al (Heuer *et al.*, 2007b) showed a great effect of the CL suppression on the sagittal translations, but not on the vertical translations, which would have led to a limited sensitivity of their specimen rotations under flexion and to statistically non significant extension rotation changes (Heuer *et al.*, 2007a). Tencer et al (Tencer *et al.*, 1982) who removed in separate experiments both facets with or without the ligament group SSL, ISL, ITL, and LF, in single level specimens, came to the conclusion that facet capsules should play an important role in limiting flexion. However, in extension, they could not identify any important load bearing role of the facets until the intervertebral disc was damaged. Although this conclusion agrees with that of Heuer et al (Heuer *et al.*, 2007a), it may also come from the fact that they artificially raised the intradiscal pressure to an *in vivo* value, which does not correspond to the normal condition of a ligamentous specimen whose muscles were dissected. In the present simulations, while the ligament suppression was associated to a softening effect at the L3-L4 level of both geometries, the computed L3-L4 facet contact predictions were opposed in the new and in the old model. It may indicate that in the old geometry, the motion restriction would be principally due to the interaction ligament-facet contact, and in the new geometry, this would be due mostly to the ligament itself.

In flexion, when the in-sagittal plane vertical and transversal resistances offered by the L3-L4 CL are compared in both geometries, it appears that in the new geometry zygapophysial joints, the horizontal restriction is relatively greater than the vertical restriction. Hence, the more horizontal action of the new geometry L3-L4 CL makes the inferior facets to have some preference for the vertical displacements along the superior facets, and it may contribute to explain the low L3-L4 contact forces computed before CL removal. This mechanism would be in good agreement with the structural looseness found at its superior and inferior margins, and with the fact that these locations are

richer in elastic fibres (Chap 1). On the contrary, in the old geometry, the higher relative vertical resistance of CL would contribute to press the L3-L4 zygapophysial joint contact surfaces together. In the new geometry, because of the frontal orientation of the superior facets, the contact apparition that took place impedes the anterior translation; it explains why the remaining ligaments and posterior AF fibres that under flexion use to act in the axial direction were more affected in the new geometry than in the old one by the absence of CL. At the L4-L5 level, after the ligament suppression, the vertical and horizontal translations were not large enough and no contact was predicted. In fact, in both geometries and without CL, the large increase in rotation of L3 induced a two-fold increase of the posterior shear force that acts on L4, impeding its anterior translation and its rotation with respect to L5. Such mechanism makes the effect of the L4-L5 components after CL suppression difficult to predict. Nonetheless, the introduced boundary conditions were necessary in order to compare the model predictions with the experimental results.

Under extension, the differences between both geometries without CL were principally shown by the study of contact forces. In the old geometry, the higher in-sagittal plane vertical resistance loss, together with the L3-L4 contact fading that occurred after CL was taken away, induced an increased compressive force on the posterior AF. In the old geometry, this compressive force was more than 50% greater than in the new geometry, leading to a posterior disc bulge augment about 27% larger. This may explain why the PLL and the posterior AF became more affected in the old model. At the L4-L5 level, for the same grounds as in flexion, a global motion reduction and a general components relaxation were predicted. Both for flexion and extension, the action of the new geometry CL within the sagittal plane agreed well with the experimental results of Heuer et al (Heuer *et al.*, 2007a), who found that once CL was removed the horizontal translations increased much more than the vertical ones.

Under lateral bending and after CL resection, the L4-L5 stiffening effect that comes from the shear force exerted by L3 was also predicted; nonetheless probably because of largest frontal dimensions of the lumbar vertebrae in the transversal plane, the effect was fairly weak. Hence, since in the old geometry, the only difference between both levels came from the ligaments, it explains why once CL removed, the functional units of the bi-segment tended to behave similarly. In the new geometry, the higher L4-L5 intervertebral disc allows maintaining the compliance of the corresponding segment. Together with that, the lateral extensions of the LF would explain why at the L4-L5 level, this ligament became more stretched in the new geometry, while it tended to relax in the old one. At the L3-L4 level, the increasing coupled axial rotation without joint capsules is likely to explain the contact decrease that occurred to the rotation side, as well as the apparition of anti rotation side contact in the new geometry where the coupled rotation is higher and change most. Reminding that under sagittal rotations, the CL might favour facet contact in the old geometry and limit it in the new geometry, if the process is assumed to be similar under lateral bending, it would justify the loss of anti rotation side predicted in the old geometry. Since the coupled rotation increase was more than twenty times higher in the new geometry, the supposed role of this motion is in agreement with the fact that the new model L3-L4 zygapophysial joint contact was to some extent more sensitive to the CL resection than the old model posterior joint. At the L4-L5 level, the effect of the coupled

axial motion might be compensated by the in-frontal plane horizontal shear force exerted by L3. As found after ITL removal, the increased width of the new geometry ALL may be responsible for the larger sensitivity of this ligament under lateral bending. Although in both models PLLs were generally little affected by CL removal, in the old geometry and at the L3-L4 level, the ligament tended to be more influenced due to the smaller shielding provided by the LF. This was confirmed by the fact that in the old geometry, the LF suffered lesser changes than in the new geometry after CL was removed. The larger lateral and posterior L3-L4 AF fibre stress increase that occurred in the old geometry may also come in part from the less protecting LF. Overall, it is also probably a consequence of the general loss of contact that took place at the L3-L4 level while the motion increased.

At the L3-L4 level, more frontal superior articular facets present in the new geometry made that the axial rotation ROM after CL removal was largely more increased than in the old geometry. Nonetheless, and for the same reason, the old geometry facet contact normal forces were more sensitive to the ligament resection. At the L4-L5 level, while the old geometry ROM remained almost the same with a slight tendency to increase, the facet contact in this model was somewhat reduced. In fact, due to the contact, a small coupled flexion motion occurs in conjunction with the main axial rotation movement and, in the old geometry this motion was nearly two-fold that of the new model. Given the role of the CL described under sagittal flexion, the coupled motion may be in part responsible of the contact loss. The presence of a slight flexion movement is in good agreement with the stress raise predicted in the PLL and LF of both geometries. The maximum LF relative stress increase was larger at the new geometry L3-L4 segment, where the coupled flexion was also the greatest. Due to the oblique fibres of its lateral extensions, the PLL of the new geometry was the most affected at both levels. The highest rotation changes that took place at the L3-L4 level of the new geometry occurred together with the highest AF fibre stress changes. However, at the postero-lateral location the lateral extensions of the PLL contributed to limit the AF stress increase.

d. Ligamentum flavum

At L3-L4 level, the next component that limited flexion in the new geometry was the LF, while this ligament had not any effect in the old geometry. In fact, in this latter model, after CL the next component removal that significantly contributed to increase the motion was the PLL. In the old geometry, the reaction force of the PLL is more vertical and less distributed than in the new geometry where the lateral oblique extensions of the ligament were modelled. Thus, the action of the old geometry LF in flexion may be shielded by the strong PLL. This is confirmed by the low load transfers that occurred toward the old geometry L3-L4 PLL before CL removal, and by the low sensitivity of this ligament to the following resections. In the new geometry, the role of the LF in resisting flexion even at low amounts of ROM agrees well with the reported literature (Adams *et al.*, 1980; Twomey and Taylor, 1983; Heuer *et al.*, 2007b). Since LF was the last posterior ligament that offered resistance to axial displacements, the L3-L4 new geometry facet contact disappeared completely and the anterior components

became fairly more stressed. In the old geometry, the stress transfer to the anterior components is quite limited, in accordance to the hypothesis that the vertical PLL already assumes most of the axial resistance.

Since the lateral bending rotational motions were not affected, the slight L4-L5 anti rotation side contact decrease that occurred in the old geometry after LF removal may come from a translation problem only. In fact, while in the new geometry, the lateral shear exerted by L3 becomes more important and seems to compensate the transversal and axial translation increases, in the old geometry, the shear force remains almost the same before and after LF removal. The different behaviour of the new geometry may come from its higher L4-L5 disc and from the larger influence that had its LF due to the ligament larger lateral extensions. All these changes, as well as the discussed contact decrease are fairly low but contribute to describe the differences in components actions between both geometries, in accordance to the interpretations performed above.

As for lateral bending, the changes predicted under axial rotation due to LF removal are minor. Nonetheless, the slight contact loss that occurred in both geometries after the LF removal is accompanied by an increased of coupled flexion, which is in good agreement with the hypothesis that the coupled motion may influence the results in each model. In both models, when LF is taken away, the transversal plane lateral translations of the L3-L4 intervertebral disc tend to be contrary to the rotation side; in the old geometry, the PLL stress is not affected by this phenomena, since the ligament tends to be more affected by the axial translations that come from the coupled flexion; nonetheless, the lateral extensions of the new geometry PLL tend to relax, which explains the obtained predictions and insists on the influence of the ligament geometry.

e. Bony posterior elements

Whatever the spine level and the geometry, the BPE did not affect significantly the ROM in flexion. At low degrees of motion, this result agrees well with the experimental study of Schultz et al, (Schultz *et al.*, 1979) who tested 41 healthy segments. Heuer et al (Heuer *et al.*, 2007b), with 8 specimens, did find a significant increase in flexion ROM after the posterior ligaments and the vertebral arch were cut. Tencer et al (Tencer *et al.*, 1982) also found that similar resection affected the flexion motion, but in their case the difference with the present predictions may be explained the larger amount of torque they applied (11.2N.m). After LF resection, in the new geometry, the final results of the computation showed that there was no contact anymore. Nonetheless, in the old geometry, L3-L4 contact was detected at the beginning of the calculation, and in the new geometry, contact occurred during the solving of intermediate increments, which probably affected the anterior components stress state. In any case, this contact should have affected the equilibrium path, exaggerating the axial translations and limiting the anterior transversal ones, which is in good accordance with the PLL stress decrease and the AF lateral fibre stress increase that were predicted once the facets were removed and contact detection could not interfere anymore in the calculation. These results might be the consequence of a

computational artefact, and must be carefully interpreted in terms of load transfer in the models.

In extension, the relaxation of the L3-L4 ALL in the old geometry after the BPE removal may indicate that the instantaneous centre of rotation was shifted toward the anterior part of the segment, which is in accordance with the L3-L4 PLL stress increase that concurrently occurred and with the findings of Heuer et al (Heuer *et al.*, 2007a) who experimentally measured forward shifts of the upper vertebra lower bounds after the vertebral arch removal in a L4-L5 functional unit. In the new geometry, the fact that the L3-L4 PLL stresses increase and only the lateral L3-L4 AF fibres were further stretched after the BPE were taken away, indicate that the more frontal L4 superior facets had a greater capability to limit the anterior shear exerted by L3 on the L3-L4 intervertebral disc. This disc became then more influent after the facets removal than in the old geometry. At the L4-L5 level, the lateral AF fibre stress decrease may be the result of the action of L3 that would limit the L4 translations associated to the rotation.

In the old geometry, under lateral bending, after the further resection of the BPE, the PLL ligament keeps on being further stretched, while in the new geometry no changes took place; this difference is certainly due to the fact that the lateral extensions of the new geometry PLL already contributed to stabilize the segment before this last component removal. The fact that in absence of facets, the main motion remains almost unchanged, confirms the role of the coupled motion in the contact that was predicted before the resection.

The fact that under axial rotation, the BPE removal affects more the old geometry ROM than the new geometry mobility agrees with the common functional anatomy descriptions that state that the most sagittal contact facets provide major resistance to axial rotation (Bogduk, 1997). The consequence is that most of the remaining models components were more affected in the old geometry than in the new one. Because of its larger width, the new geometry L3-L4 ALL showed a larger sensitivity than the old geometry corresponding ligament. At the L4-L5 level, the difference of disc height between both geometries contributes to smooth the effect of the ligament geometry, so that the ALL were similarly affected.

f. Posterior longitudinal ligament

Under flexion, the stiffening effect that appeared just after CL removal vanished after the suppression of the PLL, allowing more deformations in the L4-L5 intervertebral discs of both geometries. At the L3-L4 level, the axially oriented old geometry PLL contributed greatly to resist the motion and its suppression had therefore a large effect on the augmentation of the ROM and on the posterior AF fibres stresses. In agreement to the experiments of Heuer et al (Heuer *et al.*, 2007b), the ALL stress reductions that occurred in both models were probably due to an anterior shift of the segmental instantaneous centre of rotation and at the L3-L4 level; it was consequently more pronounced in the new geometry, due to the thinner and less resisting posterior annulus fibrosus. At the L4-L5 level, the relaxation was major in the old geometry ALL,

because due to its smaller width, the ligament resistance is more concentrated on the anterior aspect of the disc and is therefore more sensitive to the variations of disc bulge. Curiously, the old geometry anterior AF fibres were not less stressed; this was caused by the lower height of the disc, which made the disc to remain more constrained than the higher new geometry L4-L5 intervertebral disc. The lesser deformability of the thin old geometry L4-L5 disc was also illustrated by the larger relative stress increase, predicted in the old geometry lateral AF area as a result of the ROM and translations changes. The remarkable influence that had the PLL removal on the L3-L4 new geometry postero-lateral area may come from the fact that the lateral extensions of the PLL contributed to protect strongly this area where the annulus thickness tended to decrease toward the posterior zone.

In both geometries, under extension, the PLL removal contributed to reduce the AF posterior stresses, while the anterior AF was not affected in the new geometry and was relaxed in the old one. It seems then that without posterior components, most of the resistance came from the posterior bulk compression of the disc and not from the axially stretched anterior part. This hypothesis goes in the same direction as the experimental based interpretations of Tencer et al. (Tencer *et al.*, 1982). The fact that in the old geometry, the anterior annulus further relaxes may come from the axial mono orientation of the PLL, and from the fact that the ligament resistance is concentrated in a narrow posterior band, having more influence than the new geometry PLL on the instantaneous centre of rotation placement within the mid sagittal plane. In the new geometry, the stabilizing effect of the lateral oblique extensions of the PLL is shown through the postero lateral AF fibre stress decrease. At the L4-L5 level, due to the same reason and also because of the thinner AF in the role of the PLL appeared to be more important in the new geometry than in the old one.

Once more, under lateral bending, the axial fibres of the old geometry PLL contributed to make the ligament more influent with respect to the posterior AF stress state. Because of the lateral shear exerted by L3, the same rotation angle as the L3-L4 segment involves larger axial translations within the L4-L5 segment, which gives to the PLL more influence at this level. In the new geometry, it appeared that the L3-L4 PLL crisscross lateral fibres contributed to induce a slight axial coupled rotation motion, which would explain the predicted lateral AF fibre stress decrease after the ligament was removed. Axial rotation offered a clear illustration that the new geometry PLL lateral crisscross fibres play a great role in stabilizing the thin posterior AF of the lower lumbar spine intervertebral discs.

g. Anterior longitudinal ligament

Under flexion, because of the thinner posterior annulus, the in-sagittal plane deformability of the new geometry is larger than that of the old geometry, and the ALL removal affects greatly the anterior AF fibres. The effect is even more important at the L3-L4 level, where the anterior annulus thickness was not increased.

At the L4-L5 level, in extension, the ALL suppression induced less constrains on the segment mobility, and the blocking effect due to the anterior shear exerted by L3 disappeared, so that in both models, the segments recovered their mobility according to the remaining components. In the old geometry, since both the L3-L4 and L4-L5 levels are geometrically and mechanically equals, they acquired the same flexibility, while in the new geometry, the higher L4-L5 intervertebral disc allowed larger motions at the corresponding level. Nonetheless, the narrower and shorter ALL of the old model made that the ligament removal had more incidence than in the new geometry to the point of view of ROM (L4-L5 level) and AF fibres stress.

h. Nucleus pulposus

When submitted to sagittal moments, at the L3-L4 level, the new geometry was more sensitive to the absence of NP than at the L4-L5 level because the thinner posterior annulus was induced by the modelling of a posterior concavity and not by a posterior shift of the nucleus. Therefore, under flexion, the nucleus had a greater supporting action. The fact that the AF fibre stresses were reduced independently on the considered geometry is in good agreement with the expected stabilizing role of the nucleus pulposus hydrostatic pressure that “blows” the non degenerated intervertebral disc and stretches its peripheral fibrous cartilage fibres (Fennell *et al.*, 1996; Bogduk, 1997).

At the L4-L5 level under extension, because in the new geometry the NP had been shifted toward the posterior part of the disc, it acted as a better support for the posterior vertical negative translations associated to the motion. This explains why NP removal affected more than twice the new geometry than the old one and this is in agreement with some existing interpretations that state that the posterior trabecular bone vertical orientation is due to a direct transmission of compressive loads between the lumbar vertebrae and intervertebral discs (Smit, 1996). The lateral AF fibre stress increases that occurred in both models level may come from the anterior shear deformation of the intervertebral disc. This is supported by the experimental upwards and forwards displacement of the moving vertebrae centre point detected by Heuer *et al.* (Heuer *et al.*, 2007a) after all ligaments, vertebral arch and NP were removed. Given the oblique orientation of the AF fibres, this shear tended to reduce the intervertebral space, increasing the compression of the nucleus pulposus and the pressure it exercises on the AF wall. Hence, when the nucleus is removed, even if the AF deforms more and experiences an increased axial shear, there is also a relaxation that comes from the suppressed radial intradiscal pressure. In the old geometry and at both levels, the anterior shear was greater than in the new geometry, and the shear load exerted on the L3-L4 intervertebral disc was greater than that exerted on the L4-L5 disc. This explains under extension, why the old geometry L4-L5 lateral fibres were slightly stressed, while those of the L3-L4 level tended to became less loaded. In the new geometry, the thinner posterior AF made the axial shear to be more influent than the intradiscal pressure relaxation, and the lateral AF stresses increased at both levels.

Under flexion, the lateral AF fibre stress increase was not predicted; in the new geometry. It may be explained by the minimization of the axial shear provided by greater supports from the anterior L3-L4 and L4-L5 AF. The lordose of the modelled L3-L5 bi-segments may also favour more the anterior shear that accompanies extension than the posterior shear that accompanies flexion. As found experimentally by Heuer et al (Heuer *et al.*, 2007b), while for intact geometries, the ROM in flexion differ from those in extension, after all the successive removals, the sagittal mobility becomes symmetric for the negative and positive applied torques.

Unlike under sagittal motions, the NP removal under lateral bending induced high stress increases within the AF. In fact, the transversal plane elliptic shape of the lumbar intervertebral discs makes that the AF is loaded on much smaller areas than with sagittal rotations, leading to high lateral local stresses and a greater influence of the axial shear that exerts on the anterior and posterior areas. On one hand, as in the new geometry, the NP was more posterior, its effect on the lateral part of the AF was slightly larger than in the old geometry, according to the fact that the major width of the vertebrae is located in the posterior mid part of the lumbar vertebrae horizontal cross section. On the other hand, before NP removal, the thin new geometry posterior AF had to support larger loads than the old geometry AF corresponding area. Therefore, the AF resulted more affected.

In accordance to the process described above for the sagittal extension, under axial rotation, the AF oblique fibres tend to put the NP under compression, which contribute to lock the motion. This is the reason why after NP suppression, the axial rotation ROM raised greatly for both geometries, leading to higher AF fibre stresses. Note that, compared to sagittal and frontal rotational motions, the large effect of nucleus pulposus removal on axial rotation motions was already experimentally highlighted (Cannella *et al.*, 2008). The higher L4-L5 intervertebral disc of the new geometry was logically more sensitive to the absence of NP. The abrupt change in the AF shape between the postero-lateral and the lateral area, together with the less round shape of the AF posterior and postero-lateral zones made the postero-lateral fibres of both models being particularly sensitive to the increasing loading. Moreover, at the L4-L5 level, the thinner postero-lateral AF contributed to affect even more the new geometry.

i. Intact models

Under flexion, from the effect that CL removal had on the geometries, it can be deduced that this ligament is mainly responsible for the lower ROM and for the anterior components stresses computed in the new geometry at the L3-L4 level. At the L4-L5 level, the influence of the intervertebral disc height was probably larger, which may explain that the situation was reversed in the two models. The predominant influence of the intervertebral disc height, even when the dimension change does not exceed 10% is in good agreement with earlier finite element studies (Robin *et al.*, 1994; Natarajan and Andersson, 1999). The contact predictions obtained with the new geometry are in better agreement with Shirazi-Adl (Shirazi-Adl, 1991) simulations where below 7° of sagittal flexion, facet forces were found to be nearly inexistent. As discussed previously, in the

case of SSL removal, the largest action of the SSL and ISL in the new geometry may come directly from the changes in the in the spinous processes dimensions at the L3-L4 level. Once again, at the L4-L5 level, the effect is reinforced by the higher intervertebral disc.

According to the interpretations of the experimental work of Tencer et al (Tencer *et al.*, 1982), the posterior part of the intervertebral disc may play a predominant role in resisting the extension motion. That would corroborate the hypothesis that the thinner new geometry AF is directly involved in the larger motions and anterior stresses computed in the new geometry under extension. The action of the CL previously described in both geometries would be responsible for the larger load transfer that takes place through the facets in the old geometry. At the L4-L5 level, the low differences between contacts in both models may come from the compensation brought by the new geometry higher intervertebral disc, but also from the anterior shear exerted on L4 that the new geometry more frontal facets are more able to limit. The lower L4-L5 posterolateral AF fibre stress predicted in the new geometry would be the result of the action of the PLL lateral extensions.

Under lateral bending, probably due to the restriction offered by the CL (as shown by the effect of its removal), the new model L3-L4 segment resists somewhat more to the motion than the old geometry one. Nonetheless, as stated when the role of the ITL was discussed under lateral bending, the larger coupled rotation in the old geometry limits the rotation side contact and increases the anti-rotation side one. As in flexion, at the L4-L5 level, the effect of the intervertebral disc was stronger and the new geometry became softer than the old one. The lateral extensions of the new geometry anterior ligaments made the ligaments to bear a larger part of the applied load, and the larger mean load transfer through the intervertebral disc is certainly linked to the more frontal facets of the new geometry.

Under axial rotation, the more sagittal facets of the old geometry resist more the motion and make the load transfer by facet contact being greater than in the new geometry, where the most resisting components seems to be the CL and the PLL. Thanks to its lateral oblique fibres, the new geometry PLL helps considerably to limit the rotations, as shown by the comparable results on the AF fibre stresses obtained in both models.

IV. Conclusion

From all these results, it appears that the new geometry seems to behave in a way closer to the reported experimental *in vitro* findings than the old geometry. Moreover, the configuration defined for the updated ligaments and facets allowed the computation of more distributed load transfers. Nonetheless, although both models have respective biomechanical behaviour noteworthy different in terms of load transfer, their predicted rotations compare well with experimental ROM. Ligament fibres orientation and distribution, intervertebral disc height, nucleus pulposus position, and facet joint orientation, are parameters that all generate specific interactions within each model.

Therefore, no real conclusions can be drawn about the better validity of one of the built models. Hence, a validation through a comparison of the computed global behaviours with experimental results does not guarantee the relevance of predictions that are not directly linked to the measurable data.

In the case of the intervertebral disc, it has been shown that the nucleus pulposus hydrostatic pressure depends on the proteoglycan content (Urban and McMullin, 1985) and is therefore load dependent (Taylor *et al.*, 2000). It can be deduced that if the load transfer is affected by the geometrical characteristics of the tissues, a strong interaction may exist between mechanical properties and geometry. The simulated moments were rather low and because of the non linearity of the ligament mechanical behaviour, the influence of their configuration may be considerable for higher load cases. This shows the additional implication of introducing non linear material properties. Moreover, depending on the load case and the considered geometry different zones of the annulus fibrosus were involved in providing the main resistance to the applied load. Given the high diversity of the human annulus fibres anisotropy that were described in the literature (Galante, 1967; Cassidy *et al.*, 1989; Eberlein *et al.*, 2001), each configuration of the fibro-cartilage may be adapted to the particular morphology of the studied spine or group of spines, as well as to the *in vivo* loading history of the subjects.

Although the new geometry was built from the old one, the approach used for the modelling of both morphologies was totally different and resulted in two individual geometrical models. This particularity was essential in order to point out that the geometry has a larger influence on the lumbar spine models load transfers than on their global observable behaviours. Therefore, this work underlined the importance of using experimental validation protocols that identify the relative biomechanical roles of the spinal tissues instead of describing only absolute global behaviours. Such studies may lead to an adaptation of the material properties in terms of constitutive equations, anisotropy and parameters.

Chapter4

*" Négligeant l'autoroute,
je préfère les voies secondaires,
toutes entières parsemées de doutes,
qui fleuriront au printemps (je l'espère)."*

(Belle du Berry, Paris Combo)

Chapter 4

- THE ANNULUS FIBROSUS FUNCTIONAL ANISOTROPY - EFFECT OF THE COLLAGEN NETWORK ORGANISATION LEVEL ON LUMBAR SPINE BIOMECHANICS

A.	Introduction	198
B.	Materials and methods.....	201
I.	Finite element modelling.....	201
a.	Geometry	201
b.	Material properties.....	205
1)	Annulus Fibrosus.....	205
2)	Nucleus pulposus.....	207
3)	Articular facet cartilage	210
c.	Boundary conditions.....	212
II.	Model verification.....	213
III.	Stabilizing capacity of annulus collagen bundles	215
a.	The Radial Stress Distribution parameter.....	215
b.	The Radial Mean Stress parameter.....	215
c.	The Fibre Contribution Quality parameter	215
C.	Results	217
I.	Intradiscal pressure.....	217
II.	Intersegmental motions & facet contact forces.....	219
a.	Intersegmental motions.....	219
1)	Axial compression (reduced model).....	219
2)	Rotational motions.....	220
b.	Facet contact forces	222
1)	Axial compression (reduced model).....	222
2)	Rotational motions.....	223
III.	Annulus stress distribution and fibre contribution quality	225
a.	Flexion.....	225
1)	Radial Mean Stress (RMS) and Radial Stress Distribution (RSD)	225
2)	Fibre Contribution Quality (FCQ).....	228
b.	Extension	228
1)	Radial Mean Stress (RMS) and Radial Stress Distribution (RSD)	228
2)	Fibre Contribution Quality (FCQ).....	231
c.	Axial compression (reduced model).....	231
1)	Radial Mean Stress (RMS) and Radial Stress Distribution (RSD)	231
2)	Fibre Contribution Quality (FCQ).....	233
d.	Spinal erector-like loading	233
1)	Radial Mean Stress (RMS) and Radial Stress Distribution (RSD)	233
2)	Fibre Contribution Quality (FCQ).....	236
e.	Axial rotation.....	236
1)	Radial Mean Stress (RMS) and Radial Stress Distribution (RSD)	236
2)	Fibre Contribution Quality (FCQ).....	239

f.	Lateral bending	239
1)	Radial Mean Stress (RMS) and Radial Stress Distribution (RSD)	239
2)	Fibre Contribution Quality (FCQ)	242
IV.	Annulus matrix shear strain	242
a.	Flexion	242
b.	Extension	246
c.	Axial compression (reduced model)	249
d.	Spinal erector-like loading	252
e.	Lateral bending	255
f.	Axial rotation	258
D.	Discussion	261
I.	Model verification	261
a.	Nucleus pulposus constitutive behaviour	261
b.	Intersegmental rotations	261
1)	7.5N.m rotational moments	261
2)	10N.m rotational moments	263
II.	Annulus fibre-induced anisotropy	263
a.	Intersegmental rotations	263
b.	Intervertebral disc biomechanics	265
1)	Axial compression (reduced model)	265
(i)	General mechanisms and anterior annulus response	265
(ii)	Lateral annulus	265
(iii)	Postero-lateral annulus	266
(iv)	Posterior annulus	267
2)	Sagittal flexion	268
(i)	Anterior annulus	268
(ii)	Lateral annulus	268
(iii)	Postero-lateral and posterior annulus	269
3)	Sagittal extension	270
(i)	Anterior annulus	270
(ii)	Lateral annulus	271
(iii)	Postero-lateral annulus	272
(iv)	Posterior annulus	273
4)	Spinal erector-like loading	274
(i)	Anterior annulus	274
(ii)	Lateral annulus	275
(iii)	Postero-lateral and posterior annuli	276
5)	Lateral bending	278
(i)	Anterior annulus	278
(ii)	Lateral annulus	278
(iii)	Postero-lateral annulus	279
(iv)	Posterior annulus	280
6)	Axial rotation	281
(i)	Anterior annulus	281
(ii)	Lateral annulus	284
(iii)	Postero-lateral annulus	286

(iv) Posterior annulus	288
c. Zygapophysial joint contacts	289
1) Sagittal Flexion.....	289
2) Sagittal extension.....	290
(i) 10 N.m	290
(ii) 7.5 N.m	290
3) Axial compression and spinal erector-like loading	291
4) Lateral bending.....	292
5) Axial rotation.....	292
III. Summary and perspectives.....	294
E. Outcomes	307
I. Modelling remodelling?	307
II. Improving models	309

A. Introduction

As described in Chapter 1, the annulus fibrosus is an organised network of collagen fibres embedded into a ground substance matrix principally constituted of water and proteoglycans. In Chapter 3, it has been shown that the different regions of the lumbar spine annulus fibrosus may react distinctly depending on the simulated boundary conditions and the specific geometry of the model. Within each of these regions, collagen is distributed into concentric layers, where each layer has preferential orientations (Humzah and Soames, 1988; Marchand and Ahmed, 1990). As shown by the calculations performed in Chapter 2, the main resistance offered by the annulus comes from the collagen fibres that stabilize the articulation as they stretch in response to the matrix deformations. Under axial compressive loading, the nucleus pulposus transversally expands, presses on the annulus wall, and also directly affects the stretching level of its fibres. Annulus collagen bundles have therefore a key role in transmitting the loads induced by any kind of intervertebral disc deformation to the adjacent vertebrae, and it is hypothesized that the annulus fibre-induced anisotropy has a great influence on the general intervertebral disc and spine biomechanics.

Two levels of collagen organisation were identified in human lumbar annuli fibrosi. The first organisational level is given by the changes of direction from layer to layer that are quasi-symmetric with respect to the intervertebral disc axial axis and make the collagen network to follow a criss-cross pattern along the annulus thickness. This anisotropy level seems almost universal in the human lumbar intervertebral disc and is qualitatively independent from the considered annulus region. The second level of annulus fibre organisation corresponds to the tangential or radial variations of the absolute angle that the criss-crossed collagen bundles make with the local axes of their respective layers (Fig. 4.1). At this point, various orientation gradients were described in the literature. Marchand and Ahmed (Marchand and Ahmed, 1990) did not find any significant changes in the crossed fibres orientation. Cassidy et al (Cassidy *et al.*, 1989) could observe that the angle with the intervertebral disc axial direction was 30% lower for the inner annulus fibres than for the outer annulus fibres. Elliot and Setton (Elliot and Setton, 2000; Elliot and Setton, 2001) considered this latter configuration and built an anisotropic mechanical model for the annulus. They could subsequently obtain good comparisons of the model predictions with experimental data and gave credit to the particular annulus organisation described by Cassidy et al (Cassidy *et al.*, 1989). However, by photographing dissected human annulus fibrosus layers and using standard image analyses, Eberlein et al (Eberlein *et al.*, 2001) did not find any significant angle variations in the radial direction. Instead, they reported a diminution, by a factor of two, of the angle between fibres and the axial direction of their layer, from the anterior to the posterior annulus. None of the above cited studies reported degenerated intervertebral discs. Moreover, although ageing induced significant changes in the total amount of intervertebral disc collagen and in the relative amounts of collagen I to collagen II (Brickley-Parson and Glimcher, 1984), no specific correlation between age and collagen orientation gradients could be found (Cassidy *et al.*, 1989). Sex dependence was neither reported. Actually, Humzah and Soames (Humzah and Soames, 1988) proposed that a functional relation exists between the longitudinal axes of the annulus cells and the collagen fibres orientations. This idea was largely supported by different cell

morphologies found throughout the annulus (Bruehlmann *et al.*, 2002), and strongly suggests that mechanical loading, annulus matrix strains, and collagen orientation are intimately linked together.

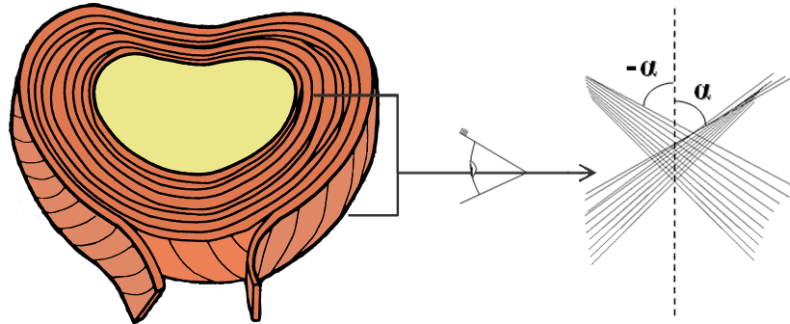


Figure 4.1: Schematic view of the two fibre-induced anisotropy levels found in the human lumbar annulus fibrosus. Left: universal layer-to-layer criss-cross pattern. Right: particular regional variations of the absolute angle (α) between the mono-oriented fibres layers and the annulus anatomical axes.

Through a multi-scale finite element study of the mechanical interaction between annulus fibrosus cells and matrix, Baer *et al.* (Baer *et al.*, 2003) concluded that annulus cell geometries result most likely from an adaptation that minimizes the strains produced by tissue loading. In this context, the biomechanical origin of annular cells and collagen bundles alignment (Bruehlmann *et al.*, 2002) appears undeniable. Understanding how the orientation of the annulus fibres is linked to spine external loading and morphology is then mandatory to explain the functional stabilization provided by particular annulus anisotropy levels. Unfortunately, the reduced geometry used by Baer *et al.* (Baer *et al.*, 2003) did not allow a thorough study of the functional mechanical boundary conditions that apply on the annulus fibrosus. In some lumbar spine finite element studies interpretations of fibre stress/strains predictions, proposed to be clinically relevant, were reported (Schmidt *et al.*, 2007c; Natarajan *et al.*, 2008; Schmidt *et al.*, 2007b). However, results were obtained with modelled annulus configurations, arbitrarily chosen from the literature. This raises the question whether such choices would not lead to erroneous conclusions or misinterpretations of the functional biomechanics of the annulus in particular spine segment geometries. In fact, increasing control on the annulus structural description would allow refining substantially the predicting power of spine numerical studies through a better assessment of the load transfer from the intervertebral disc to the surrounding bones and to the other passive soft tissues contributing to limit the motions. While bone morphology can be easily assessed with three-dimensional reconstructions from Computed Tomography (CT) scans, a quantitative study of the whole annulus internal organization of natural specimens requires accurate techniques of dissection and/or imaging. Assuming that the normal spine is partly contingent on a mechanically induced turnover of its skeletal components, and to some extent, of its soft tissues, a reciprocal adaptation between the vertebral morphology and the annulus fibrosus collagen network should take place over time to optimize stability. Identifying the influence of the annulus anisotropy on its stabilizing capability would then allow optimizing the

modelling of the annulus fibrosus composite structure in the context of lumbar spine geometries acquired from particular CT scans. Such approach is a natural continuation of Chapter 3 in the sense that the objective is to simulate a coherent biomechanical role of the intervertebral disc in the context of a specific modelled geometry.

Such results might be conditioned by the accuracy of the predictions of load transfer between the annulus and the surrounding tissues, in a first instance, the nucleus pulposus should be matter of particular attention (Chapter 2). For the calculations of the previous chapters, nucleus pulposus material properties were not directly extracted from experimental data on spinal tissues. The hyperelastic used Mooney-Rivlin formulation (Table 2.2) was initially reported by Smit (Smit, 1996) who established a numerical correspondence with the isotropic linear formulation of Goel et al (Goel *et al.*, 1995a) to obtain a non-linear elastic and incompressible formulation. This aimed to represent better than a simple Hooke's law, a behaviour controlled by the swelled state of the tissue and by the proteoglycan electrostatic repulsions. Together with the assumption of incompressibility, hyperelasticity was stated to be a suitable approximation for confined highly hydrated tissues, always when deformations are sufficiently fast so that the fluid does not have time to flow out (Smallhorn *et al.*, 2001). It was experimentally found that under quasi-static shear, lumbar nucleus pulposus material tended to fully relax as if it was a fluid, whereas at higher loading rates, the tissue behaved more like a solid with its own stiffness (Iatridis *et al.*, 1996). Moreover, intradiscal pressure measurements performed over the whole intervertebral disc depth along its mid-sagittal plane showed that under pure axial compression, eventually combined with sagittal flexion angles of up to 14°, the nucleus pulposus stress response was almost hydrostatic (McNally and Adams, 1992). The hydrostatic condition within the annulus fibrosus was not as evident, indicating that water was mainly confined in the nucleus. For modelling, the nucleus may then be assumed to be a highly hydrated solid enclosed by impermeable tissues. This approximation is physically supported by high concentrations of negatively charged proteoglycans, large osmotic pressures and low hydraulic permeabilities of the intervertebral disc tissues (Urban and McMullin, 1985) that restrict the rate of nuclear fluid loss even under high driving forces. Thus, a biphasic continuum fluid-solid mechanical formulation which respects better than hyperelasticity the structural description of the nucleus should lead to a better description of the intervertebral disc biomechanics. As stated in Chapter 1, the poroelastic theory has been widely used in reduced biomechanical models for different spine studies (Simon *et al.*, 1985; Riches and McNally, 2005; Laible *et al.*, 1993; Martinez *et al.*, 1997; Ferguson *et al.*, 2004). Some other authors went further and developed porohyperelastic models (Duncan and Lotz, 1997; Whyne *et al.*, 2001) or even modelled the charge effects of ionic molecules by using either modified poroelastic (Baer *et al.*, 2003; Sun and Leong, 2004) or multi-phasic mixture theories (Iatridis *et al.*, 2003; Schroeder *et al.*, 2008; Yao and Gu, 2006). Porohyperelasticity was believed to give a better description of the soft tissues behaviours since it represents adequately finite strains behaviours (Simon, 1992; Whyne *et al.*, 2001). Natarajan et al (Natarajan *et al.*, 2006) reported the use of a full lumbar spine segment model where interaction between fluid and proteoglycans were taken into account to predict the initiation and the progression of failure due to cyclic loading. Using a similar poroelastic formulation in a L4-L5 motion segment finite element model, Williams et al (Williams *et al.*, 2007) could reproduce the axial creep response measured *in vivo* over 24h at the same level. However, none of these studies

highlighted the importance of the coupling between nucleus hydrostatic pressure and annulus fibrosus structure, even with static models.

In the present Chapter it is assumed that in a first instance, a linear poroelastic model of the nucleus pulposus would allow a better description of the load transfer from the nucleus to the annulus fibrosus. Then, it was hypothesized that given a specific finite element geometry of a L3-L5 lumbar spine bi-segment model, modelling different physiologic configurations of annulus fibrosus anisotropy reported in the literature may affect the biomechanics of the L3-L5 lumbar spine bi-segment model. Finally, a way to quantify the ability of different annulus fibre configurations to stabilize the modelled segments under various boundary conditions was investigated.

B. Materials and methods

I. Finite element modelling

a. Geometry

The geometrical construction of the L3-L5 lumbar spine bi-segment finite element model used for this study (Fig. 4.2) was presented in details in Chapters 2 and 3, so that only some aspects about annulus fibrosus modelling will be briefly reminded. As described in Chapter 2, the annulus fibrosus composite material was represented by a structural model of the fibres and the matrix ground substance. The 20 radial fibre layers were distributed over four radial layers of rebar brick elements that were superimposed to the solid hexahedral elements of the ground substance (Fig. 2.6).

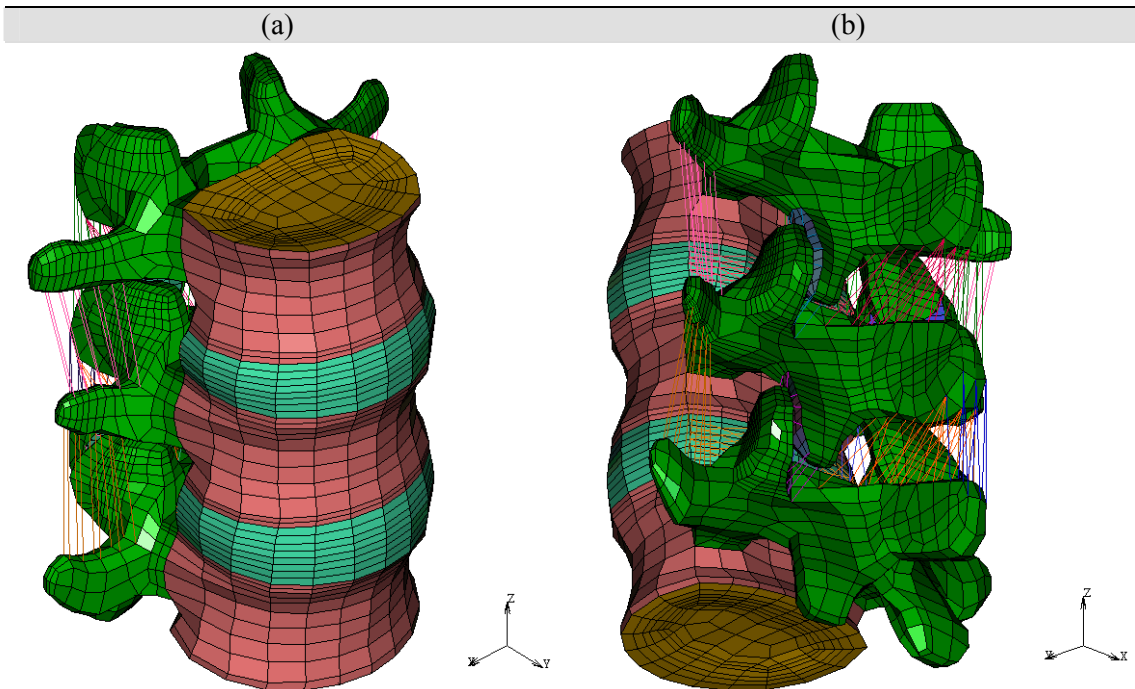


Figure 4.2: representation of the L3-L5 lumbar spine bi-segment model. a) Antero-superior oblique view. b) Postero-inferior oblique view.

The angle between fibres and annulus axial direction alternated from positive to negative into two adjacent layers was used as the varying parameter to build several models of annulus anisotropy according to literature. Its value was varied as a function of the fibre locations within the annulus four radial and tangential areas (Fig. 2.7a) and four distinct models were created:

1. ISO model: the absolute value of the angle between fibres and layer axial direction remained constant through the annulus fibrosus and was equal to 60° (Marchand and Ahmed, 1990; Galante, 1967).
2. RAD model: the absolute value of the angle between fibres and layer axial direction was a function of the radial location of the fibres and decreased from 62° in the outer annulus to 45° in the inner annulus (Cassidy *et al.*, 1989).
3. TAN model: the absolute value of the angle between fibres and layer axial direction was a function of the tangential location of the fibre and decreased from 66.5° in the anterior annulus to 32.7° in the posterior annulus (Eberlein *et al.*, 2001).
4. ANI model: Using the RAD configuration, a ratio was calculated between the radial gradient of fibre orientation and the mean angle value over the annulus thickness. From the TAN configuration data, a mean fibre angle value was computed for each tangential quadrant and in each quadrant, the ratio was used to define a specific radial orientation gradient around the corresponding mean

orientation value. The ANI model was therefore a mix between the TAN and the RAD models, where the fibre angle varied along all the directions of the annulus transversal plane. This definition did not correspond to any of the anatomical descriptions found in the literature but was used to compare the TAN and the RAD models with a further level of fibre-induced anisotropy.

In all models, between the most anterior, posterior, inner and outer points, fibre absolute angles varied linearly from layer to layer and from sector to sector (Cassidy *et al.*, 1989; Eberlein *et al.*, 2004) (Fig. 4.3). As described in Chapter 2, the cross-section and volume fraction of the modelled collagen bundles varied as a function of the annular region (Fig. 2.7b,c). The amount of rebars relative to their element size was correspondingly determined through the annulus model so that the global fibre volume fraction was 16%. Note that the geometrical differences introduced between the L3-L4 and the L4-L5 annuli in Chapter 3 did not affect significantly the relative proportions of collagen in the different radial sections from one level to another (Fig. 4.4).

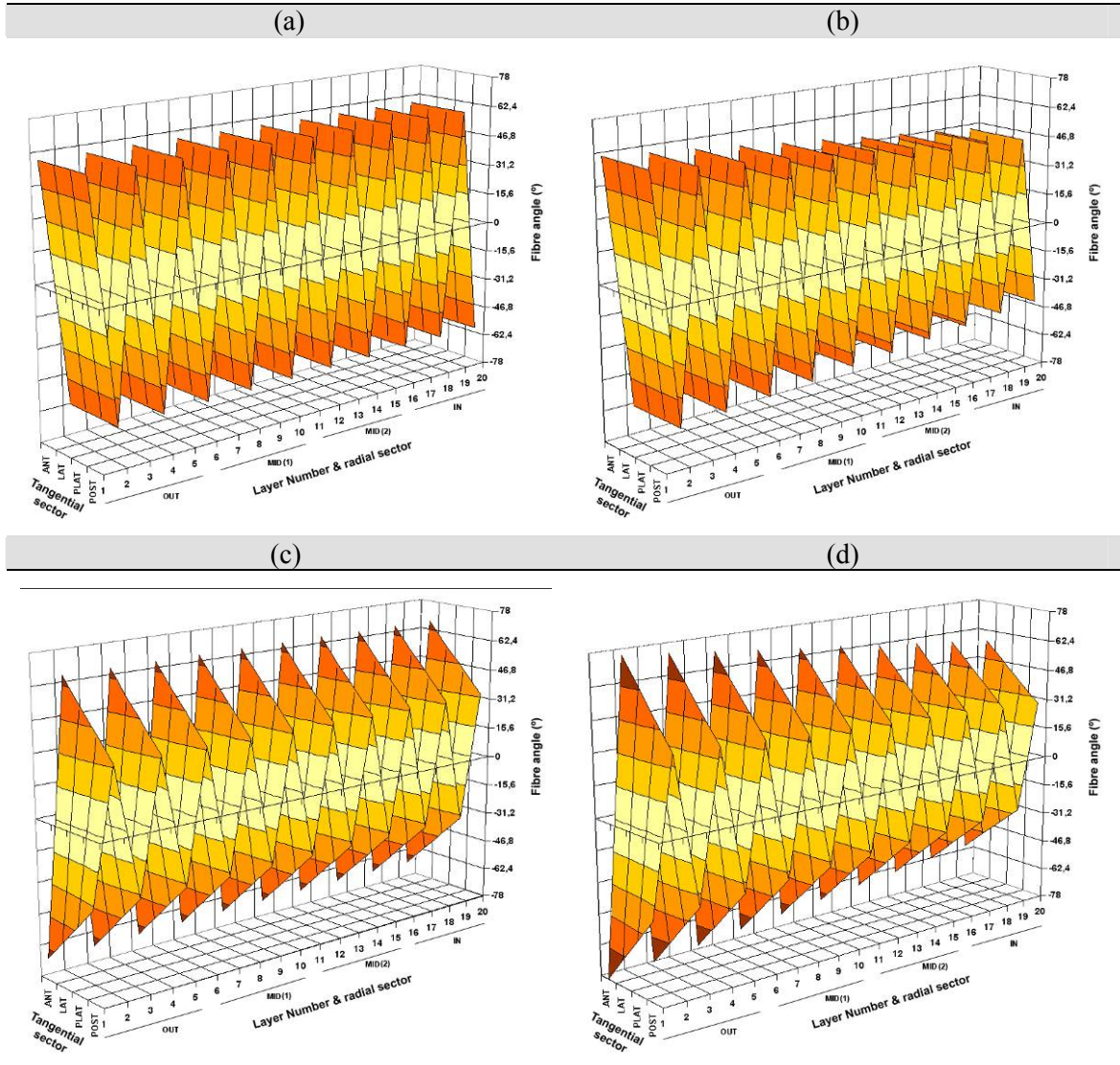


Figure 4.3: Graphic representations of the multidirectional fibre angle changes in the different annulus fibrosus anisotropy models. a) ISO model. b) RAD model. c) TAN model. d) ANI model.

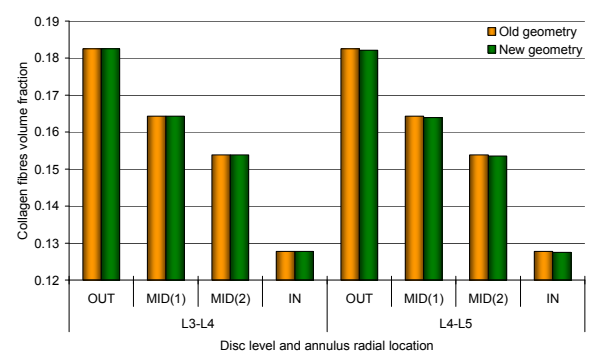


Figure 4.4: Effect of the geometrical differences between the L3-L5 lumbar spine bi-segment models used in Chapter 2 and issued from Chapter 3 on the collagen volume fraction through the thicknesses of the L3-L4 and L4-L5 annuli.

b. Material properties

1) Annulus Fibrosus

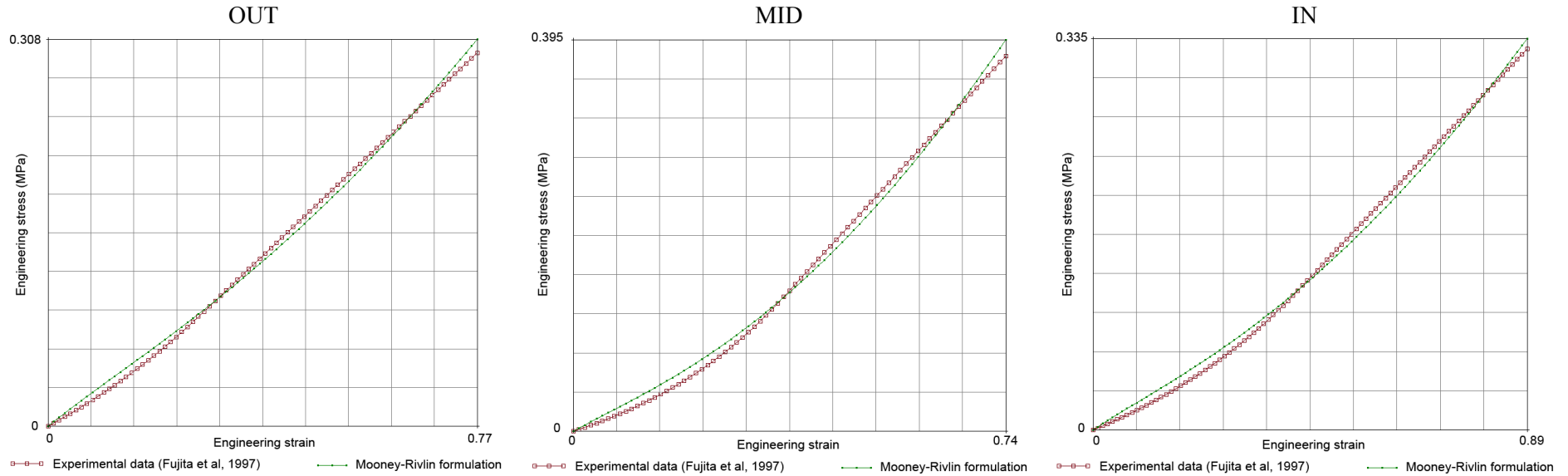
Given that the areas of the annulus collagen bundles were given independently of the type of collagen (Marchand and Ahmed, 1990), no distinctions were made between collagen I and II in the annulus geometrical modelling. Nevertheless, the radial evolution of annulus contents in collagen I and collagen II was quantified through the material properties, so that each of the four radial layers of hexahedral rebar elements had its own fibres material properties (Table 2.4) according to both the relative amount and stiffness of collagen II to collagen I (Brickley-Parson and Glimcher, 1984; Sun *et al.*, 2002) (Fig. 2.15). No significant differences in collagen type relative contents were found in the literature between the L3-L4 and L4-L5 annuli (Brickley-Parson and Glimcher, 1984). Thus, the collagen fibres material properties were taken similar at both levels of the present lumbar spine bi-segment model.

The contribution of fibres in each 3D rebar element layer was only effective in the preferred direction of the layer and the radial interactions fibre-matrix or fibre-fibre could not be taken into account. Nonetheless, some theoretical studies of the annulus fibrosus mechanical behaviour pointed out the relevance of these interactions (Elliot and Setton, 2001; Wagner and Lotz, 2004) and were in good agreement with previously reported mechanical tests (Adams and Green, 1993; Fujita *et al.*, 1997) or histological observations (Bruehlmann *et al.*, 2002). In the present model, the radial contributions of fibres were then taken into account by introducing different matrix material properties that were function of the location along the annulus thickness. According to Fujita *et al.* (Fujita *et al.*, 1997), three zones, namely the outer annulus, (OUT), the middle annulus (MID) and the inner annulus (IN) were chosen. Each zone was characterized by a particular hyperelastic formulation adapted to the tensile properties measured in the radial direction. This mechanical separation into different annular regions was similar as the geometrical compartmenting presented in Figure 2.8a, the MID part including MID(1) and MID(2). Since the model simulated preconditioned tissues under non-pathologic conditions, only experimental data above the yield points were used. Moreover, in MSC MARC2005, as only uniaxial tensile test data were available, the material had to be considered incompressible and complete strain energy formulations could not be used. The reported yield engineering strains in the OUT, MID, and IN regions were respectively 77%, 74%, and 89% (Fujita *et al.*, 1997) and an accurate fit all over the range of experimental data should then be obtained with general polynomial Mooney-Rivlin strain energy functions. Best adjustment to experimental data was obtained with a minimum of three parameters (Fig. 4.5). All the hyperelastic coefficients were optimized by a least square procedure implemented in Marc Mentat 2005r3. In order to ensure that the resulting equation remained physically acceptable out of the experimental data range, an extrapolation of the simulated mechanical behaviour was performed up to 90% strain both under traction and compression. Parameter values computed for each annulus radial layer are given in Table 4.1.

Mooney-Rivlin three parameters fit

(*)

$$W = C_{10}(\bar{I}_1 - 3) + C_{01}(\bar{I}_2 - 3) + C_{11}(\bar{I}_1 - 3)(\bar{I}_2 - 3)$$



(*) W is the strain energy function of the material, and \bar{I}_1 and \bar{I}_2 respectively represent the 1st and the 2nd deviatoric invariants of the right Cauchy-Green tensor, $\underline{\underline{C}}$, so that the Cauchy stress is given by:

$$\underline{\underline{\sigma}} = \frac{2}{J} \left[\left(\frac{\partial W}{\partial \bar{I}_1} + \bar{I}_1 \frac{\partial W}{\partial \bar{I}_2} \right) \underline{\underline{F}} \underline{\underline{F}}^T - \frac{\partial W}{\partial \bar{I}_2} J^{-2/3} \underline{\underline{I}} \right]$$

where. $\underline{\underline{F}}$ is the gradient deformation tensor and J its determinant

Figure 4.5: Tensile behaviour of the different radial layers of annulus matrix as predicted by the fitted three-parameter Mooney-Rivlin formulation, compared to experimental data. Mooney-Rivlin parameter values are given in Table 4.1.

Table 4.1: Optimized values for the three-parameters Mooney-Rivlin coefficients in each AF matrix radial element layer.

	OUT	MID	IN
C10 (MPa)	0.0595	0.053	0.040
C01 (MPa)	0.0002	0.001	0.006
C11 (MPa)	0.0296	0.058	0.032
Global least squares error (MPa) (*)	0.005	0.008	0.006

(*) Global least squares error = $\sqrt{\frac{\sum_{i=1}^n [\sigma_i^{\text{exp}} - \sigma_i^{\text{fit}}]^2}{n-3}}$, σ being the engineering stress (exp: experimental; fit: fitted), and n the number of experimental data point inputs.

2) Nucleus pulposus

According to the introduction of the present Chapter, the nucleus pulposus was modelled as a poroelastic material. Poroelasticity gives a continuum description of the mechanical response issued from the interaction between a fluid and a solid when both are part of the same material. Consistent with the classical continuum approach, any quantity appearing in this description was averaged over a certain length scale that was assumed to be at least 100 times the length scale of the microstructure (Detournay and Cheng, 1993). In the case of the nucleus pulposus, this rule is fully respected, since the largest structures that form the solid phase, namely the collagen fibrils and the aggrecan hyaluronan complexes (Fig. 4.6), are about some hundred nanometres (Bogduk, 1997; Bader and Lee, 2000) while the whole modelled tissue cross-section is several hundred millimetres square.

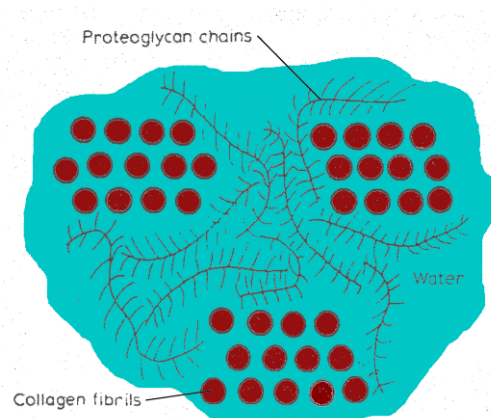


Figure 4.6: Schematic view of the nucleus pulposus composition (adapted from (Urban and McMullin, 1985)).

The material was considered fluid saturated so that the fluid and the solid phases are fully connected to each other (Simon, 1992) and the sum of the phase volume fractions is equal to one. The total density of the mixture can then be expressed as:

$$\rho = n\rho_f + (1-n)\rho_s \quad (4.1)$$

where n is the current volume fraction of the fluid, commonly called “porosity”, and ρ_f and ρ_s are respectively the fluid and solid densities. The concept of a coherent solid skeleton and a freely moving pore fluid implies that the solid displacement vector is determined with respect to a reference configuration and the rate of fluid volume crossing a porous solid unit area was defined as the fluid velocity relative to the solid (Detournay and Cheng, 1993). Hence, if u_i is the displacement of a point in the porous solid phase from X_i to x_i , so that $u_i = u_i(x_i, t) = x_i - X_i$ (Fig. 4.7), the relative fluid velocity at this point has been described as (Simon, 1992):

$$\frac{\partial w_i}{\partial t} = n \left(\frac{\partial u_i^f}{\partial t} - \frac{\partial u_i}{\partial t} \right) = \dot{w}_i = n (\dot{u}_i^f - \dot{u}_i) \quad (4.2)$$

where u_i^f is the average displacement of the pore fluid phase from X_i to x_i , so that the volume of fluid displaced per unit area normal to x_i is nu_i^f .

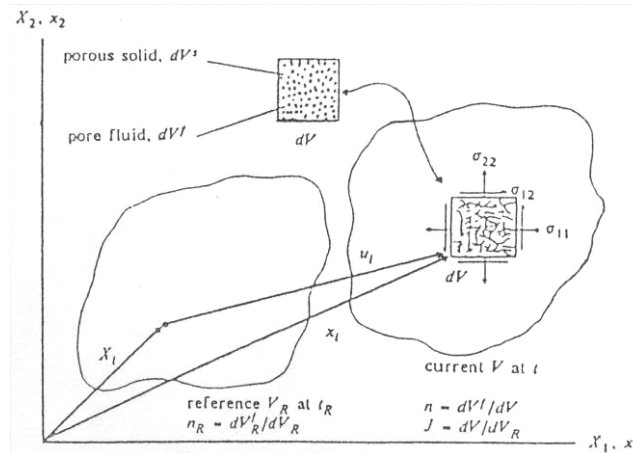


Fig. 4.7: Total Lagrangian view of poroelastic materials (reproduced from (Simon, 1992))

The total stress tensor of the poroelastic material is expressed as:

$$\underline{\underline{\sigma}} = (1-n)\underline{\underline{\sigma}}^s - np\underline{\underline{I}} \quad (4.3)$$

where $\underline{\underline{\sigma}}^s$ is the solid phase stress tensor, p is the pore pressure, and $\underline{\underline{I}}$ the identity tensor. By convention, the components of $\underline{\underline{\sigma}}^s$ are positive in traction and

negative under compression, while the pore pressure is positive under compression. The development of the different terms in (4.3) shows that the poroelastic stress is directly linked to u_i and w_i .

Pore pressure in a material element is defined under a quasi-static approach as the pressure in a hypothetical reservoir where no fluid exchange takes place between the reservoir and the material element (Detournay and Cheng, 1993). In this scope, body forces are neglected and the conservation of momentum for the pore fluid is given by Darcy's law (Simon, 1992):

$$\frac{\partial p}{\partial x_i} = - \frac{1}{k_{ij}} \frac{\partial w_i}{\partial t} \quad (4.4)$$

k_{ij} is the hydraulic permeability which may be a function of the solid phase strain and the porous material fluid content. However, the poroelastic theory used here followed the Biot model, so that stresses and strains were limited to their isotropic component. Moreover, the hydraulic permeability was considered independent of the material strains and its expression was then reduced to a single scalar form:

$$k = \frac{\mu}{\kappa} \quad (4.5)$$

where μ is the dynamic viscosity of the fluid and κ the intrinsic permeability of the porous fluid filled material. The error introduced by the approximation of a constant permeability was included in the calculation of the residual, leading to a true solution of the finite element calculation.

The constitutive equation for the fluid filled solid porous solid was based on the assumption of the linearity between stress and strain both in the solid and the fluid (Detournay and Cheng, 1993). Solid stress may be expressed by Hooke's law:

$$\sigma_{ij}^s = (\lambda \delta_{ij} + 2\mu) \varepsilon_{ij} \quad (4.6)$$

where ε is the strain tensor, and λ and μ are the Lamé constants associated to the Young's modulus and the Poisson's ratio.

In linear poroelasticity, solid and fluid are considered intrinsically almost incompressible, and the bulk deformations occur only through porosity changes (Detournay and Cheng, 1993). In the healthy intervertebral discs, fluid is principally water, and the solid phase of the nucleus pulposus has a high content of proteoglycans whose negatively charged chains repel each other (Urban and McMullin, 1985; Antoniou *et al.*, 1996). Therefore, the assumption of incompressibility for both phases is acceptable, and the continuity equation gives:

$$\frac{\partial^2 u_i}{\partial x_i \partial t} + \frac{\partial^2 w_i}{\partial x_i \partial t} + \frac{n}{K_f} \frac{\partial p}{\partial t} = 0 \quad (4.7)$$

where K_f is the bulk modulus of the fluid. Equation (4.7) allows relating solid and relative fluid velocities with the pore pressure, and the last parameter to determine is the current porosity n . Under the assumptions of incompressibility, this quantity may be related to the initial porosity (n_R) and the determinant of the medium deformation gradient (J) through the equation (Simon, 1992):

$$n = 1 - \frac{1 - n_R}{J} \quad (4.8)$$

This summarised presentation of the linear poroelastic theory shows that the poroelastic modelled nucleus pulposus can be fully characterized through the identification of 6 parameters, namely the Young's modulus and the Poisson's ratio of the porous solid phase, the dynamic viscosity, and the bulk modulus of the fluid phase, and finally, the permeability and the initial porosity of the whole poroelastic medium. All the numerical values of these quantities used in the model are given in Table 4.2. As a specific Poisson's ratio for the nucleus pulposus could not be directly extracted from reported experimental data, its value was estimated from analogy to similar tissue matrices (Li *et al.*, 2000; Lacroix, 2000). For the interstitial fluid, the physicochemical properties of water at 37°C were taken.

Table 4.2: Poroelastic parameters for the nucleus pulposus.

Solid		Fluid		Poroelastic material	
Young's Modulus (MPa)	Poisson's ratio	Dynamic viscosity (kg.mm ⁻¹ .s ⁻¹)	Bulk modulus (MPa)	Permeability (mm ⁴ .N ⁻¹ .s ⁻¹)	Initial porosity
0.31 (Périer <i>et al.</i> , 2005)	0.2	6.92x10 ⁻⁷	2300	0.67x10 ⁻³ (Périer <i>et al.</i> , 2005)	0.8 (Yao and Gu, 2006; Williams <i>et al.</i> , 2007)
(Porous solid)		(Water at 37°C)			

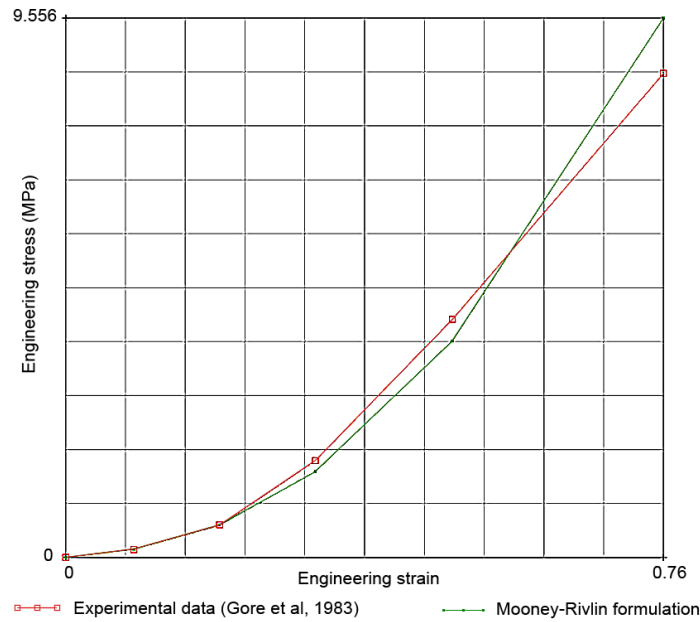
3) Articular facet cartilage

The mechanical law applied to the articular facet cartilages in the above Chapters was derived from unidirectional compressive experimental data. The extrapolation to three dimensions was ensured by a piecewise isotropic linear law controlled by the different values taken by the tangent Young's moduli extracted from the experimental non-linear unidirectional stress-strain curves (Chap. 2). The advantage of this method was that the compressibility defined by the Poisson's ratio could also vary with the normal deformation of the cartilage layer in agreement to (Li *et al.*, 2000; Jurvelin *et al.*, 1997). Nonetheless, depending on the size of the load increments, such method could induce some mechanical discontinuities between the elements of the same material and involved potential convergence problems. In this Chapter, the choice was then made to simulate the non-linearity of the facet cartilage compressive behaviour through a constitutive equation whose parameters were unique and remained valid over the whole range of elastic deformation. Thus, according to the finite element study of Stadler *et al.* (Stadler and Holzapfel, 2006), facet cartilage layers were defined as a hyperelastic

material. Experimental data under unconfined compression of a full thickness cartilage layer (D.M.Gore *et al.*, 1983) were used to fit an almost incompressible phenomenological Mooney-Rivlin model. The best fit results were obtained with a four-parameter strain energy function (Fig. 4.8). The corresponding parameter values are presented in Table 4.3.

Mooney-Rivlin four parameters fit

$$W = C_{10}(\bar{I}_1 - 3) + C_{01}(\bar{I}_2 - 3) + C_{11}(\bar{I}_1 - 3)(\bar{I}_2 - 3) + C_{20}(\bar{I}_1 - 3)^2 \quad (*)$$



(*) W is the strain energy function of the material, and \bar{I}_1 and \bar{I}_2 represent respectively the 1st and the 2nd deviatoric invariants of the right Cauchy-Green tensor, $\underline{\underline{C}}$, so that the Cauchy stress is given by:

$$\underline{\underline{\sigma}} = \frac{2}{J} \left[\left(\frac{\partial W}{\partial \bar{I}_1} + \bar{I}_1 \frac{\partial W}{\partial \bar{I}_2} \right) \underline{\underline{F}} \underline{\underline{F}}^T - \frac{\partial W}{\partial \bar{I}_2} J^{-2/3} \underline{\underline{I}} \right]$$

where $\underline{\underline{F}}$ is the gradient deformation tensor and J its determinant

Figure 4.8: Fitted Mooney-Rivlin hyperelastic formulation used for the facet cartilage layers compared to uniaxial unconfined compression experimental data obtained for full thickness articular cartilage layers. Mooney-Rivlin parameter values are given in Table 4.3.

Table 4.3: Fit results for the five parameters Mooney-Rivlin coefficients of the facet cartilage layer mechanical hyperelastic law.

C_{10}	C_{01}	C_{11}	C_{20}	Global least squares error (MPa) (*)
0.227	0.007	1.824	0.111	0.1

(*) Global least squares error = $\sqrt{\frac{\sum_{i=1}^n [\sigma_i^{\text{exp}} - \sigma_i^{\text{fit}}]^2}{n-3}}$, σ being the engineering stress (exp: experimental; fit: fitted), and n the number of experimental data point inputs.

c. Boundary conditions

Pure rotation moments were used to simulate motions of sagittal flexion, extension, and axial rotation within the L3-L5 lumbar spine bi-segment model. The mechanical fits performed on the different modelled tissues only considered reversible elastic behaviours. Hence, the simulated boundary conditions should correspond to non destructive loads if they were applied to a biologic lumbar spine bi-segment specimen. In accordance to reported *in vitro* experiments (Yamamoto *et al.*, 1989), the corresponding maximum moment magnitudes was 10N.m for all simulated rotations. The compressive load rose up to 1000N (Wilke *et al.*, 2001; Adams and Dolan, 1995). Pure axial compression under follower compressive force was investigated on a reduced model where the L3-L4 segment only was represented. In an additional load case, the constant load exerted by the spinal erector muscle system was approximated by combining axial compression and sagittal extension in a similar proportion as given by the mean values predicted by Bogduk *et al.* (Bogduk *et al.*, 1992) for the L3-L4 and L4-L5 levels (Table 1.1). The maximum load magnitudes were reported to an extensive maximum moment of 7.5N.m to ensure that the modelled tissues remained working in their respective elastic domains. Compressive forces were applied directly on the upper bony endplate of the L3 vertebra, and the rotational moments acted through a modelled network of steel beams. The lower bony endplate of the L5 vertebra, or that of the L4 vertebra for the reduced model, were fixed in all directions (Fig. 4.9).

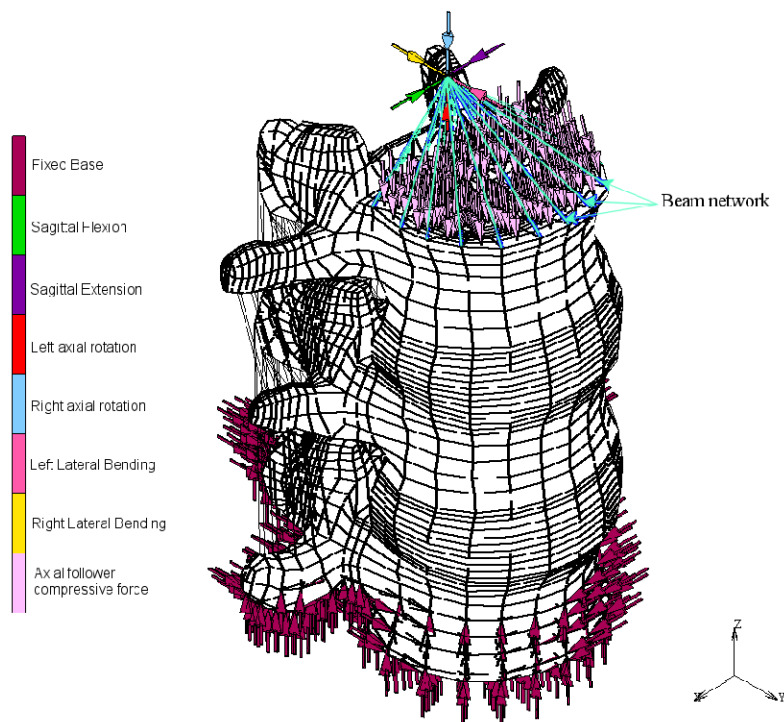


Figure 4.9: Presentation of the boundary conditions modelled for the L3-L5 lumbar spine bi-segment.

The choice of hyperelastic laws and the assumption that nucleus pulposus was enclosed by impermeable materials implied that the loading rate had to be sufficiently high to make the mechanical response of the bi-segment structure independent of the strain-rate. Race et al (Race *et al.*, 2000) showed experimentally that the response of the IVD under axial compression became fairly reproducible above a loading rate of $1\text{MPa}\cdot\text{s}^{-1}$. On one hand, the 1000N external compressive force corresponded to a pressure of about 0.8MPa on the L3 upper endplate. Considering that this load was fully transmitted to the intervertebral discs, the duration of the corresponding load case was chosen to be 0.8s. On the other hand, the pure rotational moments of 10N.m would generate intradiscal pressures of about 0.4MPa under flexion/extension, 0.3MPa under lateral bending and 0.2MPa under axial rotation (Heuer *et al.*, 2007a). From the unique perspective of nucleus pulposus intradiscal pressure increase, these rotations may be respectively associated to the effect of follower axial pressures of 0.4MPa, 0.3MPa and 0.2MPa. A load rate of $1\text{MPa}\cdot\text{s}^{-1}$ gave then durations of 0.4s for the sagittal rotations, 0.3s for lateral bending, and 0.2s for axial rotation. Based on similar criteria, for the combined extension/compression load case simulating the spinal erector system, the selected loading time was 0.28s. Table 4.4 presents a summary of all the simulated load cases.

Table 4.4: Summary of the different load cases applied on the L3-L5 bi-segment modelled for the simulation of its biomechanical behaviour

Load case		Flexion	Extension	Lateral bending	Axial rotation	Spinal erector-like loading
Rotational load	Type	Pure sagittal moment	Pure sagittal moment	Pure frontal moment	Pure transversal moment	Pure sagittal moment
	Maximum magnitude	-10N.m	10N.m	$\pm 10\text{N}\cdot\text{m}$	$\pm 10\text{N}\cdot\text{m}$	7.5N.m
Compressive load	Type	-	-	-	-	Axial follower force
	Maximum magnitude	-	-	-	-	-132.6N
Total loading time		0.4s	0.4s	0.3s	0.2s	0.28s

II. Model verification

The way the nucleus pulposus transfers the loads to the annulus fibrosus was investigated both with the earlier hyperelastic formulation presented in Chapter 2 (Table 2.2) and with the new poroelastic constitutive model defined in the present Chapter. To compare the intradiscal pressures obtained with these two mechanical models, the experimental protocol of McNally and Adams (McNally and Adams, 1992) was simulated (Fig. 4.10). It consisted in maintaining a single lumbar spine segment model

under a constant axial compressive force during 20 seconds while its stress profile was measured with a pressure transducer pulled across the disc in the posterior-anterior direction. Axial and transversal stress profiles were computed along the intersection between the disc mid-transversal and mid-sagittal planes and were compared to the measurements retrieved with an angle of flexion, Φ , equal to zero (Fig. 4.10a).

For the models with the nucleus formulation that best reproduced the experimental intradiscal stress profile, the predicted intradiscal pressures under axial compression were compared to literature data for follower forces ranging from 500N to 2000N. The intersegmental rotations predicted by the L3-L5 bi-segment model at 7.5N.m and 10N.m were also compared to experimental data. Test results, from the Institut für Unfallchirurgische Forschung und Biomechanik (UFB - Ulm Universität, Ulm, Germany) (Chap. 3), and from the protocol reported by Yamamoto et al (Yamamoto *et al.*, 1989), were used. In order to evaluate the influence of the annulus, nucleus, and facet cartilage material property changes from the last developed model to the current models, rotations predicted at 7.5N.m were also compared to the ranges of motion computed with the New Geometry model of Chapter 3.

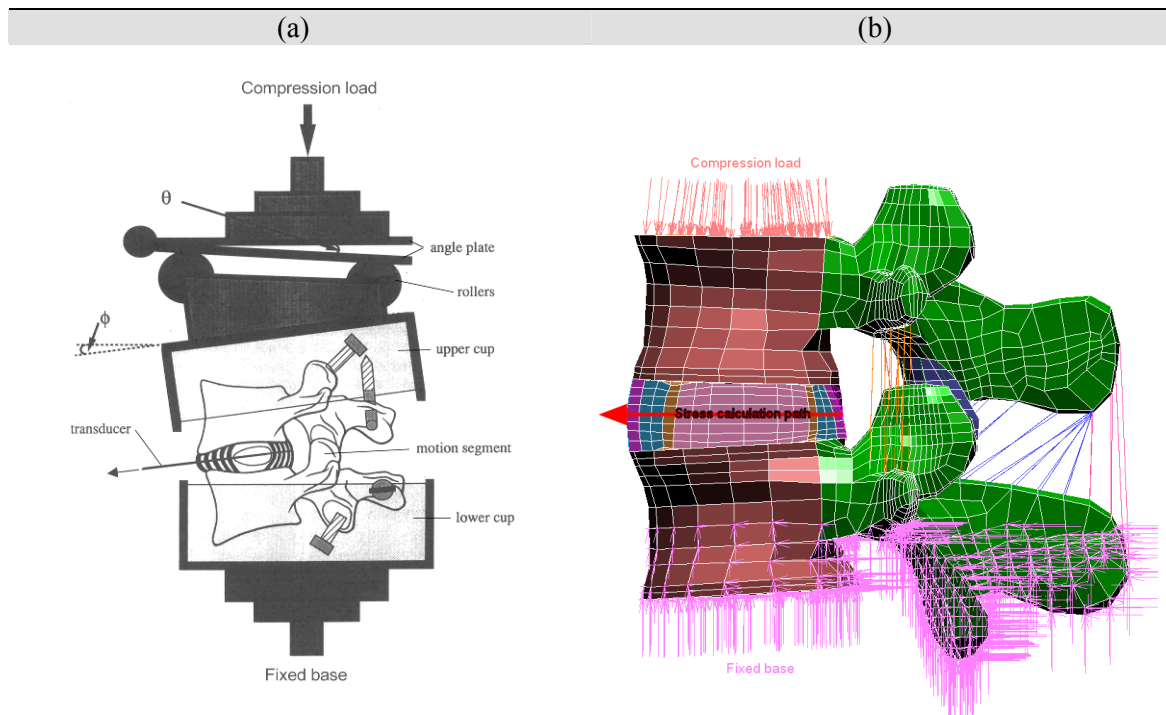


Figure 4.10: Determination of the intervertebral disc axial and transversal stress components.
 a) Experimental protocol of Mc Nally and Adams (McNally and Adams, 1992). b) Finite element modelling.

III. Stabilizing capacity of annulus collagen bundles

In order to quantify the capacity of the annulus collagen bundles to stabilize the intervertebral articulation, the fibre longitudinal tensile stresses were computed at each node of the rebar elements. It was hypothesised that the annulus fibres had to be able to simultaneously limit the intervertebral disc deformations and redistribute across the matrix the consequent stress. Thus, on one hand, an optimal collagen network should be organised so that for a given annulus deformation, its bundles can bear the largest amount of tensile stress as possible. On the other hand, as suggest by comparing the mechanical characteristics of the annulus lamellar structure with thick-walled vessels, these stresses should be as well distributed as possible through the annulus thickness (Skaggs *et al.*, 1994; Holzapfel *et al.*, 2005). Fibre stresses computed from the finite element simulations were then processed to determine three numerical parameters that quantified the relative fulfilment of the above conditions by the different anisotropy models.

a. The Radial Stress Distribution parameter

The Radial Stress Distribution parameter (*RSD*) aimed to quantify the homogeneity of fibre stress distribution through the annulus thickness. The mean fibre longitudinal stress was computed over all the nodes of each radial area of each tangential sector. Values were plotted as a function of their relative position through the annulus thickness. The *RSD* parameter was then taken as the slope of the linear regression over the computed points (Fig. 4.11) so that for each tangential sector, lowest *RSD* values indicated best radial distributions of fibre stresses.

b. The Radial Mean Stress parameter

The Radial Mean Stress parameter (*RMS*) was the mean longitudinal tensile stress of the annulus fibre computed over the all the nodes of each tangential sector. A better fibre contribution within a tangential area was then translated into a higher *RMS* value.

c. The Fibre Contribution Quality parameter

The Fibre Contribution Quality parameter (*FCQ*) evaluated the quality of fibre contribution in each annulus tangential sector and for each configuration of anisotropy. The *FCQ* values allowed choosing the best compromise between *RSD* and *RMS* and were returned by a two-variable function depending on the following conditions:

1. The function $FCQ(RSD, RMS)$ must be defined positive and continue for all $(RSD, RMS) \in \mathfrak{R}^+$.

2. The first partial derivatives of $FCQ(RSD, RMS)$ should have similar absolute values for all $(RSD, RMS) \in \mathfrak{R}^{+2}$, so that no predominance is given to the influence of one particular variable.
3. Since the fibre longitudinal stresses should be distributed as well as possible over the annulus thickness, FCQ should decrease as RSD increases, i.e.

$$\frac{\partial FCQ(RSD, RMS)}{\partial RSD} < 0$$
4. Since the fibres should bear a maximum quantity of tensile stress, FCQ should increase as RMS increases, i.e.

$$\frac{\partial FCQ(RSD, RMS)}{\partial RMS} > 0$$
5. Minimum finite values of $FCQ(RSD, RMS)$ should exist only if $RSD \mapsto +\infty$ and $RMS \mapsto 0$
6. Maximum values of $FCQ(RSD, RMS)$ for any RMS value should be obtained with $RSD = 0$, which corresponds to the most homogeneous radial distribution of fibre longitudinal tensile stresses through the annulus thickness.

Following the above restrictions, the chosen FCQ function was:

$$FCQ(RSD, RMS) = \ln\left(1 + \frac{e^{RMS}}{e^{RSD}}\right) \quad (4.9)$$

The respect of condition 1. by Equation (4.9) is obvious and it can easily be verified that:

$$\frac{\partial FCQ(RSD, RMS)}{\partial RSD} = \frac{-\frac{e^{RMS}}{e^{RSD}}}{1 + \frac{e^{RMS}}{e^{RSD}}} = -\frac{\partial FCQ(RSD, RMS)}{\partial RMS} \quad (\text{conditions 2., 3., 4.})$$

$$\lim_{RSD \mapsto +\infty} FCQ(RSD, RMS) = 0 \quad | \quad (\text{Condition 5.})$$

$$\ln\left(1 + \frac{e^{RMS}}{e^{RSD}}\right) \leq \ln(1 + e^{RMS}) \quad \forall (RSD, RMS) \in \mathfrak{R}^{+2} \quad (\text{Condition 6.})$$

For all annulus collagen network models, the FCQ parameter was evaluated in the anterior, lateral, postero-lateral, and posterior quadrants of the L3-L4 and L4-L5 annuli. Furthermore, results were discussed together with other biomechanical parameters relevant to intervertebral disc stabilization, such as ranges of motion, annulus matrix shear strains, and load shearing with the zygapophysial joints.

Since for all models geometric fibre modelling was asymmetric with respect to the mid-sagittal plane, under lateral bending and axial rotation, simulation results in the lateral and postero-lateral annuli depended on whether right or left rotations were simulated. However, in order to avoid any discussion about patient particularities such as lateralization, and to remain in the framework of a general description of the lower lumbar spine biomechanics, lateral and postero-lateral RMS, RSD, and FCQ parameters, as well as annulus matrix shear strain calculations were averaged over the annulus rotation and anti-rotation side, and for both left and right rotations. The subjacent assumption was then that non-symmetric motions with respect to the mid-sagittal plane occur with equal probabilities either in the left or in the right direction.

C. Results

I. Intradiscal pressure

Figures 4.12a,b compare the mid-sagittal plane stress profiles obtained in the RAD model intervertebral disc, with a poroelastic and a hyperelastic nucleus pulposus respectively. While poroelasticity led to a nearly hydrostatic stress state within the nucleus, the use of hyperelasticity involved significant differences between the axial and the transverse stress profiles. The stress profilometry simulated with the RAD model for a follower force of 500N was fairly close to the measurements obtained by McNally and Adams (McNally and Adams, 1992) (Fig. 4.12c,d).

The mean intradiscal pressure computed in the poroelastic nuclei of the different models was almost independent of the type of collagen fibre arrangement within the annuli fibrosi (Fig. 4.13). With compressive loads of 500N and 1000N, the computed nucleus hydrostatic pressures were in very good agreement with the literature. However with 2000N, relative differences around 20% were found between the predicted and the experimental pressure values. Note that the experimental error from the literature data was unknown.

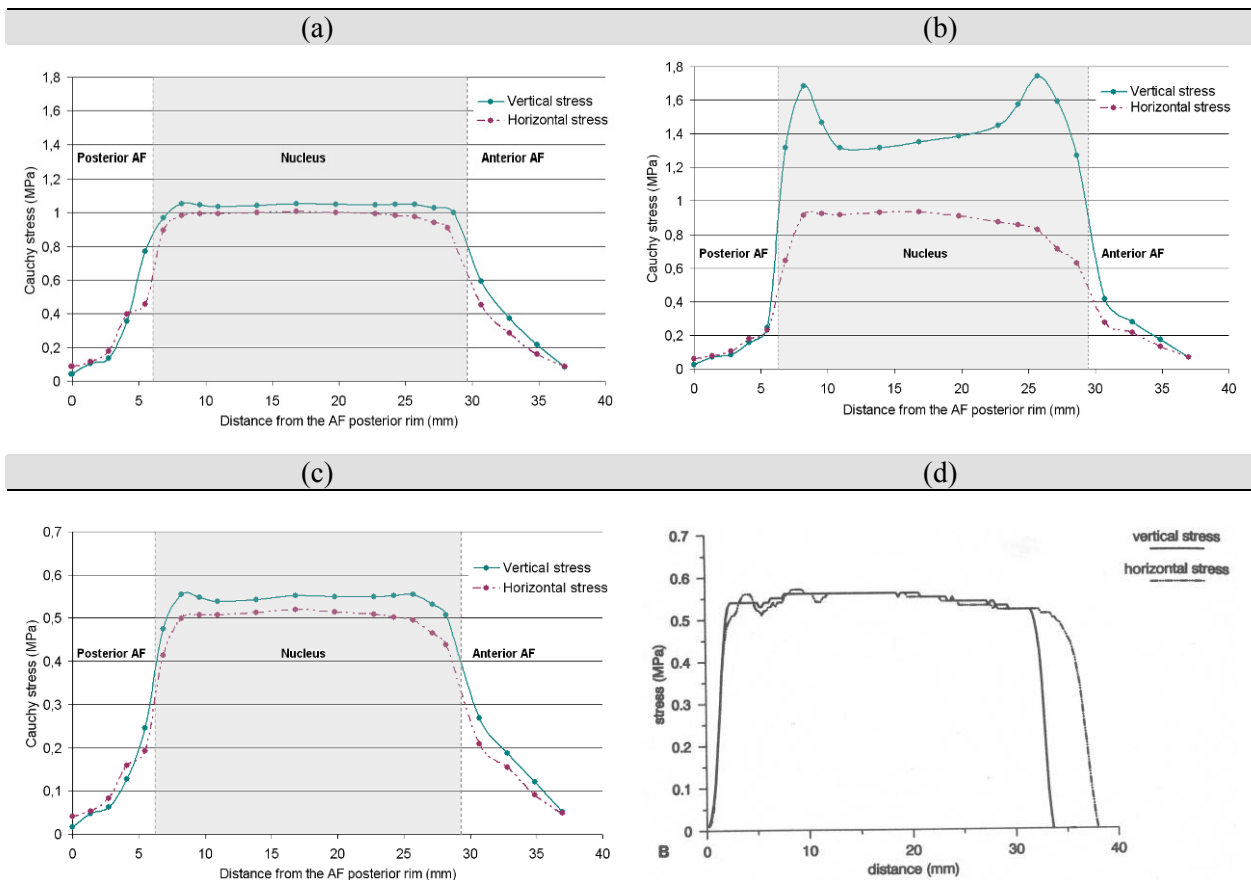


Figure 4.12: Axial (vertical) and transversal (horizontal) stress distributions along the mid-sagittal and mid-transversal plane intersection of a lumbar spine segment intervertebral disc. (a) Predictions performed with the RAD reduced model, under a 1000N axial compressive force, and with a poroelastic nucleus pulposus. (b) Similar as (a) but with a hyperelastic nucleus pulposus. (c) Stress profilometry predicted with the RAD reduced model, an axial compressive load of 500N, and a poroelastic nucleus pulposus. (d) Stress profilometry measured by McNally and Adams (McNally and Adams, 1992) on a grade 0 L2-L3 specimen, under similar boundary conditions as simulated in (c).

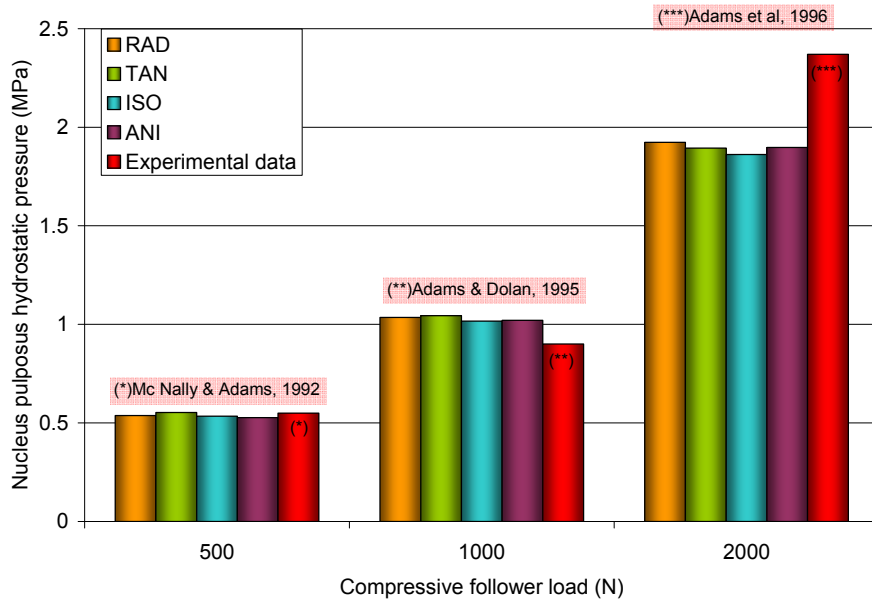


Figure 4.13: Comparison of experimental intradiscal pressures with predictions performed in the poroelastic nuclei pulposi of the reduced models with different annulus anisotropies. Both the experimental data and simulation results were obtained with axial quasi static compressive forces.

II. Intersegmental motions & facet contact forces

a. Intersegmental motions

1) Axial compression (reduced model)

Axial displacements of the upper vertebra computed in the reduced model under axial compression depended on the configuration of the collagen network (Fig. 4.14). While smallest posterior and largest anterior displacements were given by the RAD and the ISO models, largest posterior and smallest anterior displacements were given by the TAN and the ANI models. A slight sagittal flexion clearly appeared coupled to the axial deformation of the segment and was greater for the RAD and ISO models than for the other ones. The ANI model returned the lowest amount of coupled motion.

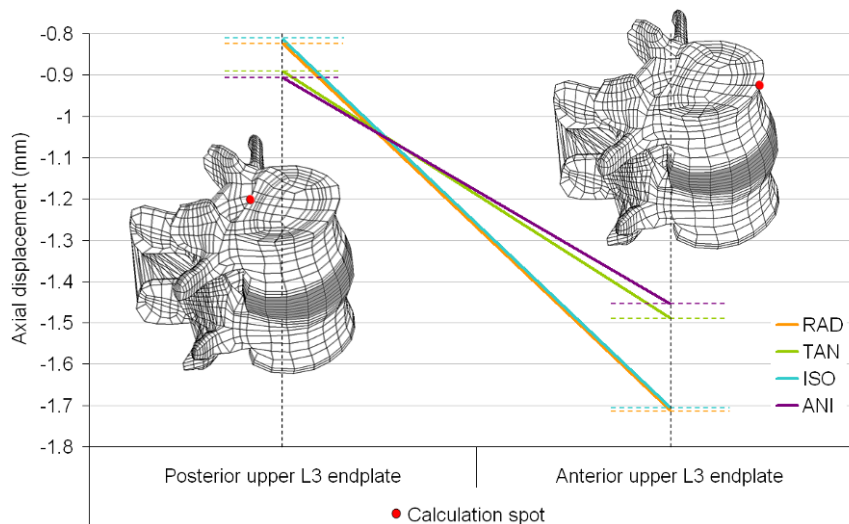


Figure 4.14: Posterior and anterior axial displacements of the L3 vertebrae predicted with a 1000N axial follower force applied on the reduced L3-L4 lumbar spine model. Coloured solid lines schematically represent the amount of coupled flexion by linking the axial displacements computed at the posterior calculation spot to those computed at the anterior calculation spot.

2) Rotational motions

Figure 4.15 compares with experimental data, the intersegmental rotations predicted by the L3-L5 bi-segment models at 7.5N.m and 10N.m. The type of annulus anisotropy influenced somewhat the computed ranges of motion. Both at 7.5N.m and 10N.m, the ISO model showed the highest L4-L5 flexibility under flexion-extension and lateral bending and was the model that most differed from the other ones. The trends and orders of magnitude of the calculated rotations generally compared well with the experimental data. However, under flexion-extension at 7.5N.m, while the L3-L4 simulated rotations were pretty close to the experimental data, the L4-L5 segments could be considered to some extent too flexible. At 10N.m, the tendency was reversed and the rotations predicted at the L4-L5 levels were in better agreement with the experimental data than those computed for the L3-L4 level that could be considered too low.

On Figure 4.15a, the ranges of motion computed for the current models were also compared to those found for the New Geometry model presented in Chapter 3. With a similar geometry and annulus collagen network organisation as the RAD model, the New Geometry model was at both levels significantly stiffer than the RAD model under sagittal rotations. At the L3-L4 level, relative to the New Geometry model, the RAD model was about 18% stiffer under axial rotation and 5% softer under lateral bending. At the L4-L5 level, while differences between the two models were insignificant in axial rotation, under lateral bending, the RAD model was nearly 30% softer than the New Geometry model.

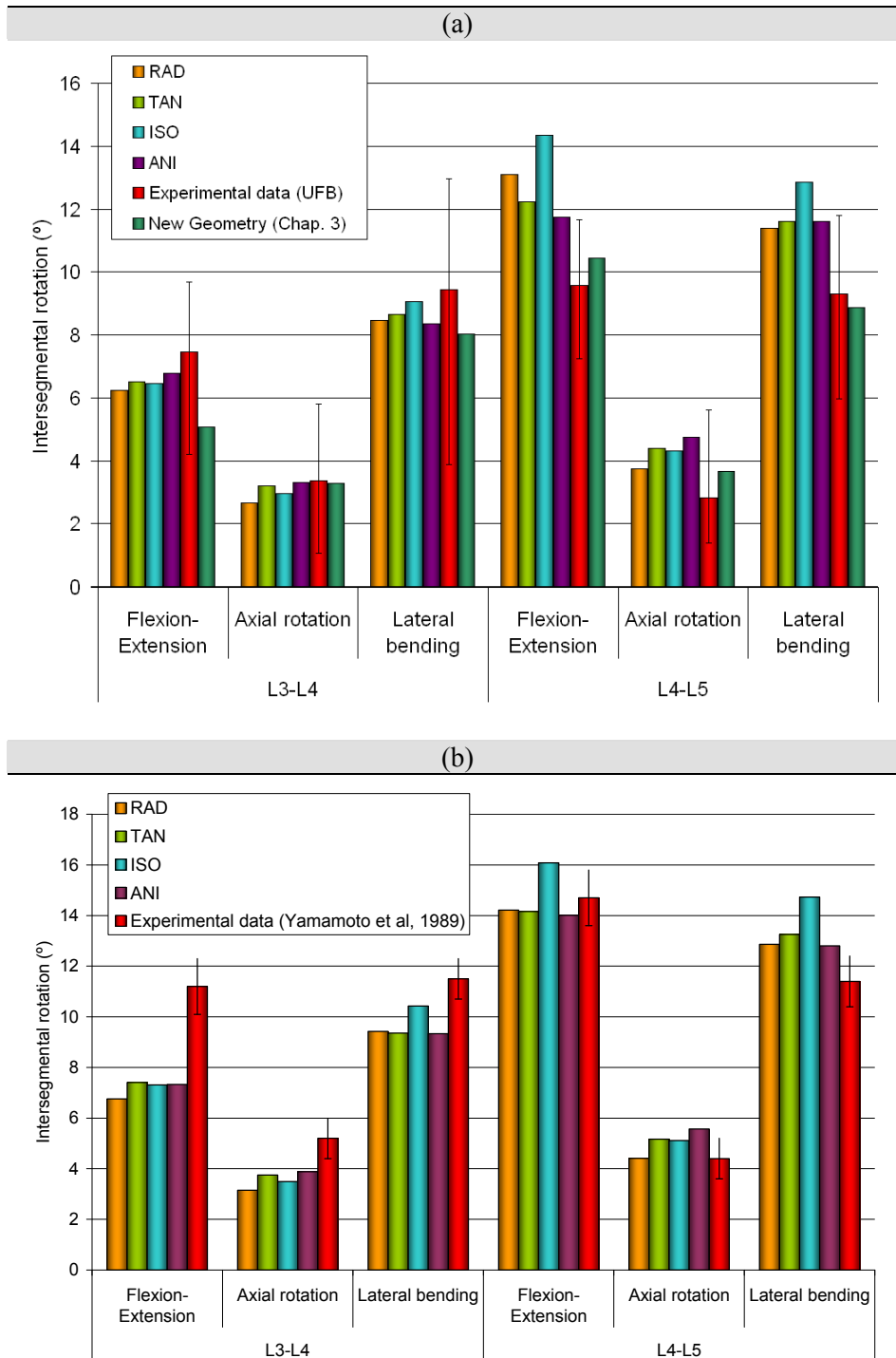


Figure 4.15: Intersegmental rotations predicted by the different annulus anisotropy models compared with experimental data. a) 7.5N.m. The models of the current Chapter are also compared to the New Geometry model presented in Chapter 3. b) 10N.m.

Figure 4.16 shows that with the spinal erector-like loading, superimposing a follower force and a pure extension reduced the intersegmental rotation of at least 10% when compared to the pure extension load-case. The follower force generally

contributed to reduce somewhat the differences between the different models. At the L3-L4 level, in presence of axial compression, the ISO motion segment tended to become the most flexible one, while it tended to be the stiffest one under pure rotation. At the L4-L5 level, the relative differences between the ranges of motion of the different anisotropy models were however qualitatively preserved by the application of the axial follower compressive force.

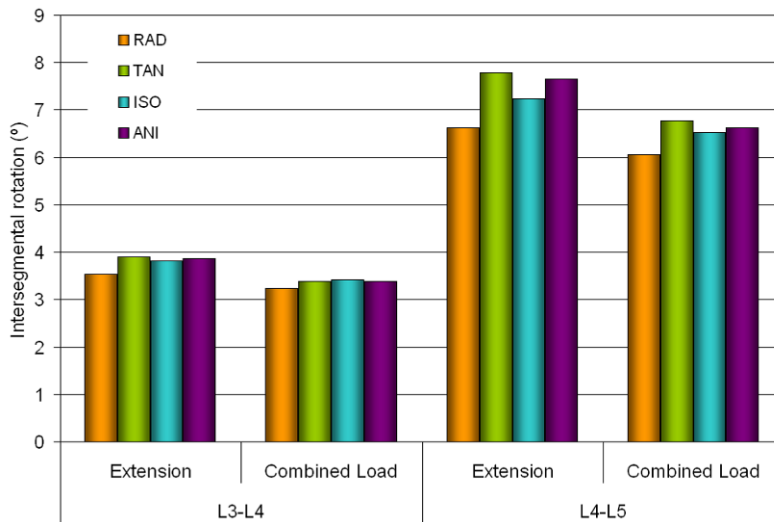


Figure 4.16: Intersegmental rotation in the different anisotropy models under 7.5N.m pure extension and 7.5N.m extension combined with a 132.6N follower force (Spinal erector-like load).

b. Facet contact forces

1) Axial compression (reduced model)

Facet contact forces, presented in Figure 4.17 for the reduced model under axial compression, showed significant differences from one annulus anisotropy model to another. Strongest contact was calculated in the TAN model and values were nearly twice the second highest force values returned by the ANI model. When passing from the RAD to the ISO anisotropy, a considerable contact loss was predicted with a normal force relative difference higher than 50%.

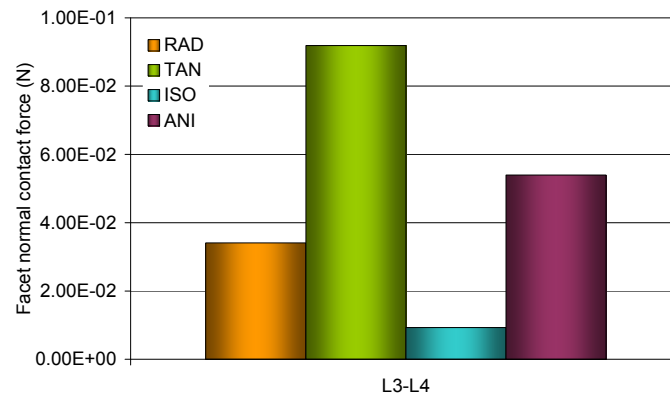


Figure 4.17: Facet normal contact forces computed in the L3-L4 segment of the reduced mono-segment lumbar spine model under 1000N axial compressive follower force.

2) Rotational motions

As shown in Figure 4.18, the type of annulus anisotropy had a significant influence on the facet contact force values. Under flexion, no contact was predicted in the L4-L5 zygapophysial joints. At the L3-L4 level, the lowest and largest contact normal forces were found in the RAD and ISO models respectively (Fig. 4.18a). For all models, contact forces were between 10 and 20 times lower under flexion than under the other load cases.

At the L4-L5 level, extension motion induced the strongest facet contacts, and although the relative differences between the different models appeared lower than with under other motions, around 16% of difference was still computed between the highest forces brought by the TAN model and the lowest ones computed in the RAD model (Fig. 4.18b). At the L3-L4 level, zygapophysial joint contact under extension was almost insensitive to changes in annulus fibre configuration.

Under axial rotation, no contact was predicted to the rotation side. To the anti-rotation side, axial rotation was however the load case with the highest L3-L4 contact forces, and largest force value was returned by the ANI model. The lowest L3-L4 contact force value under axial rotation was about 18% inferior to that predicted in the ANI model and was found in the RAD model (Fig. 4.18c). At the L4-L5 level, the ISO model, followed by the RAD model, led to the greatest contact forces under axial rotation, and the least amount of contact was given by the ISO model.

Under lateral bending, rotation side contact forces were noteworthy greater than the anti-rotation side ones. To the anti-rotation side, contact differences between the different models were almost similar at the L3-L4 and L4-L5 levels, and, as in the L4-L5 facet joints under axial rotation, the ISO and the RAD models returned the highest normal contact forces. To the rotation side, the RAD model was always associated to the lowest contact levels. At the L3-L4 level, as to the anti-rotation side, largest contact was predicted in the ISO model and no significant differences were found between the TAN and the ANI models. At the L4-L5 level, rotation side contact results under lateral

bending were qualitatively similar as those found under sagittal extension, and the TAN and the RAD models were associated to the highest and lowest contact forces respectively (Fig. 4.18d). Excluding sagittal flexion, lateral bending was moreover the only load case where some facet joints, i.e. the rotation side RAD and ISO zygapophysial joints, had larger contact forces at the L3-L4 than at the L4-L5 level.

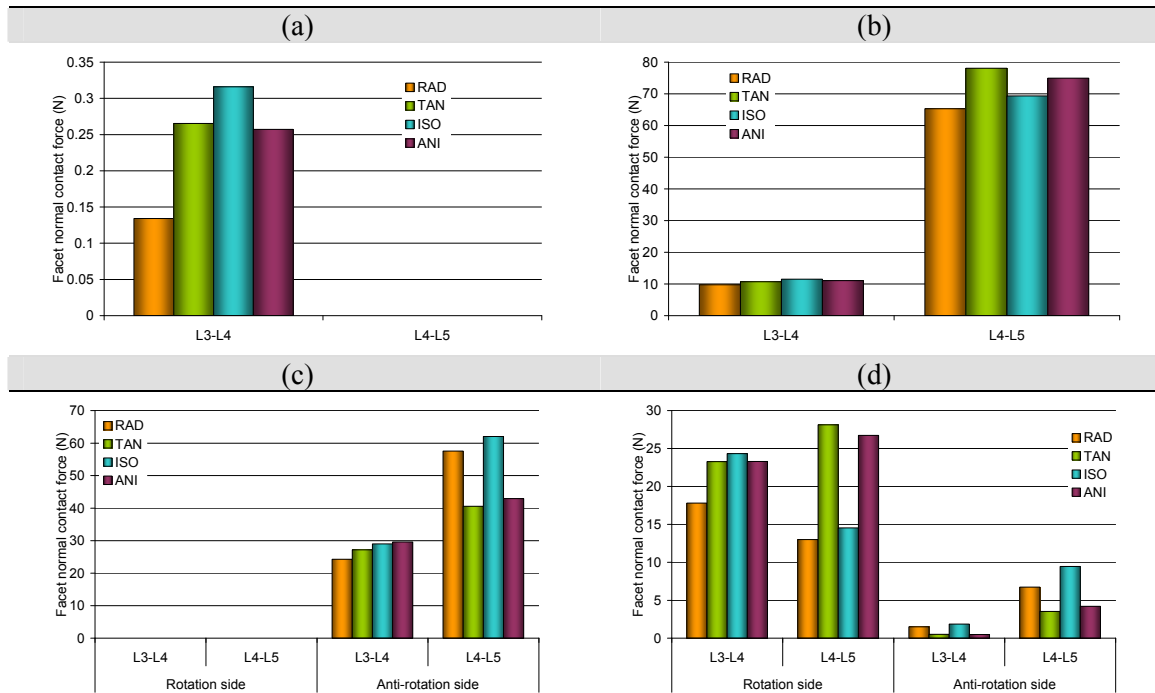


Figure 4.18: Maximum facet contact forces for the different L3-L5 lumbar spine bi-segment models under 10N.m loads. a) Sagittal flexion. b) Sagittal extension. c) Axial rotation. d) Lateral bending.

The compressive follower force, added to the 7.5N.m sagittal extension, increased facet contact normal forces by at least 10% (Fig. 4.19). Either under pure extension or with combined loading, the relative differences between contact forces in the different models at the L3-L4 level did not overcome a maximum of 10% that has been found between the RAD model and the ISO model under pure extension. At the L4-L5 level, more significant contact variations were predicted with the annulus configuration changes. The addition of the compressive force to the pure rotation qualitatively maintained the relations of magnitude between the different models. The RAD model, followed by the ISO model, was always associated to the highest and second highest facet contact forces. Contact increase with the addition of the follower compressive force was however greater in the ISO model.

Comparing Figure 4.19 with Figure 4.18b, the increase of L4-L5 contact forces when passing from 7.5N.m to 10N.m extension was interestingly largely dependent on the type of annulus anisotropy. Generally, model rankings related to contact magnitude was found to change with the moment magnitude, and for example, while the ANI model led to the second greatest contact force at 10N.m, it had the lowest one at

7.5N.m. Conversely, the L4-L5 RAD zygapophysial joints passed to be the most loaded at 7.5N.m, to become the least loaded at 10N.m.

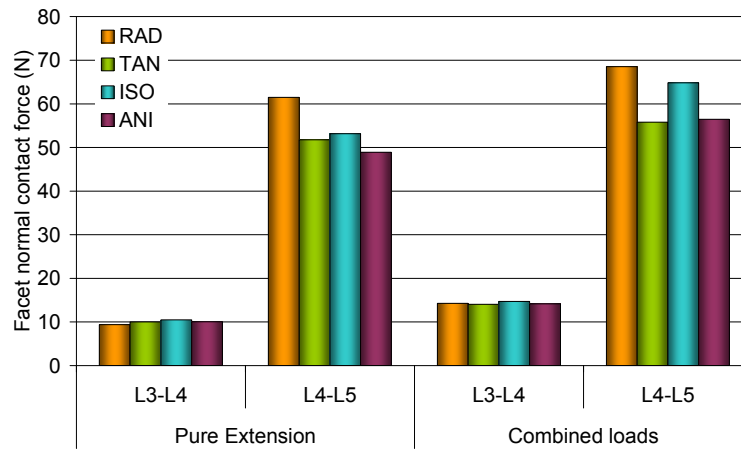


Figure 4.19: Facet normal contact forces predicted in the different anisotropy models under 7.5N.m pure extension and spinal erector-like loading.

III. Annulus stress distribution and fibre contribution quality

a. Flexion

1) Radial Mean Stress (RMS) and Radial Stress Distribution (RSD)

As shown in Table 4.5, in the anterior annulus under sagittal flexion, fibre tensile stresses decreased from the most outer to the most inner layers. Both at the L3-L4 and at the L4-L5 levels, the ANI model predicted the highest radial stress gradient and its external layers were the most loaded ones. Among the three other annulus anisotropy models, the TAN model presented the largest stresses all across the annulus thickness with a RMS parameter similar to that of the ANI model. The ISO model, with the lowest radial stress gradient, returned the smallest RSD parameter.

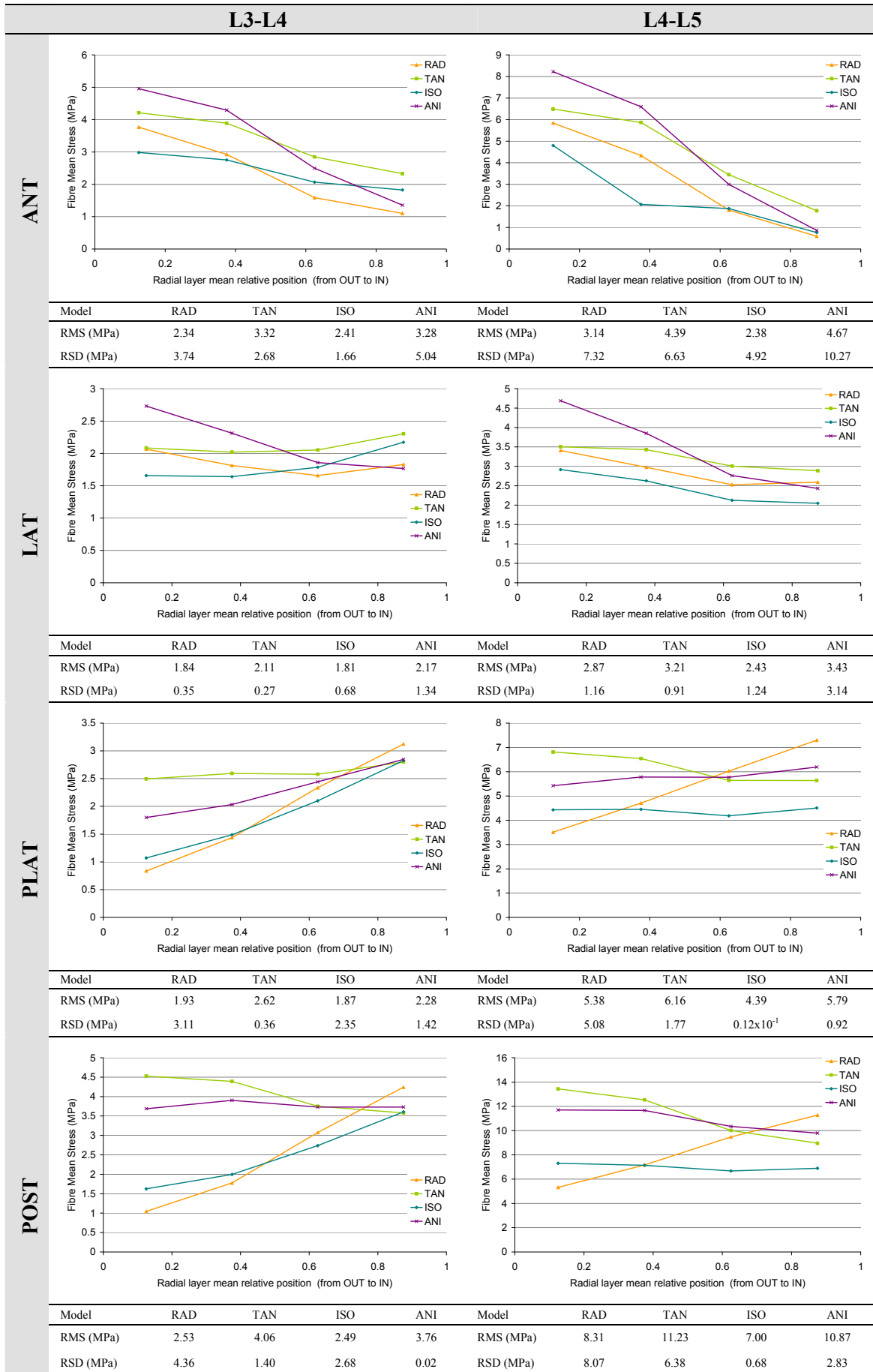
In the lateral area of the annulus, the RMS parameter of the ANI model was again the largest one, but this collagen network configuration also led to a high radial stress gradient. The TAN model predicted both one of the highest fibre stresses and the best stress distribution over annulus thickness, leading simultaneously to a RMS parameter close to that of the ANI model and to the lowest RSD parameter.

At the L3-L4 level and in all models, the postero-lateral annulus fibres were more loaded in the inner than in the outer layers. Predicted radial stress gradients were greater in the ISO and the RAD models. The TAN model led simultaneously to the best stress distribution and major mean postero-lateral fibre stress. At the L4-L5 level, except for the RAD model, fibres were more evenly activated over the annulus thickness than at the L3-L4 level. RMS parameter remained the greatest in the TAN model but the lowest

RSD parameter was predicted in the ISO model. The fibres of the ISO model had however still the least amount of load.

In the posterior area, the situation was quite similar as in postero-lateral annulus except that stresses were generally higher. The fibres of the TAN model were also the most loaded ones but best load distributions were given by the ANI model at L3-L4 level and by the ISO model at the L4-L5 level.

Table 4.5: Radial distribution of the annulus fibre mean stress levels related to the calculation of the RMS and RSD parameters under sagittal flexion.



2) Fibre Contribution Quality (FCQ)

Under flexion, at both levels, the TAN model gave the highest FCQ values in most of the annulus quadrants (Fig. 4.20). At the L3-L4 level, the ISO and RAD models led to similar results as the TAN model, in the anterior and lateral areas respectively. In the posterior annulus, best fibre contribution was provided by the ANI model. At the L4-L5 level, results were comparable, except that in the postero-lateral quadrant, the ISO model led to nearly similar FCQ values as the TAN model, and in the posterior annulus, the ISO collagen network gave the best fibre contribution. Note that fibre contribution differences between anterior and posterior quadrants were much higher at the L4-L5 level than in the L3-L4 segment.

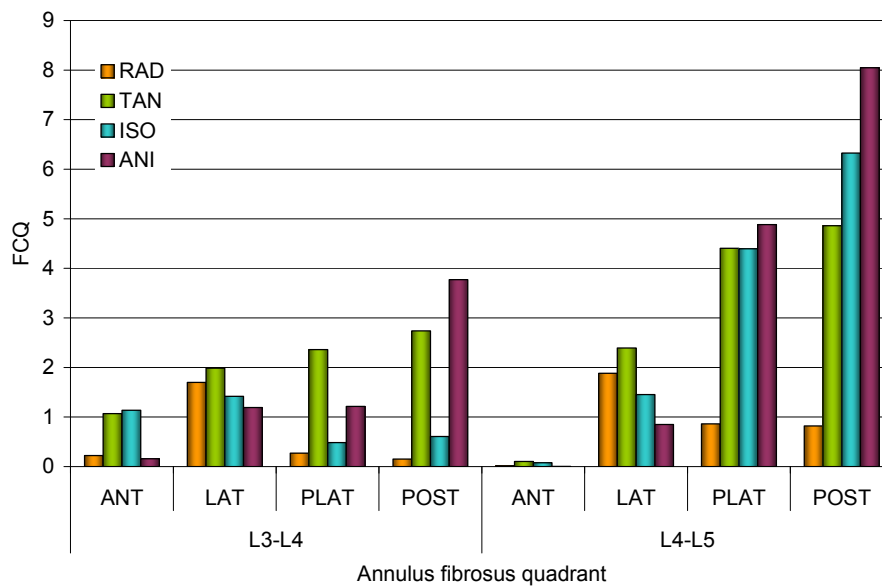


Figure 4.20: FCQ values in the different annulus quadrants of the L3-L5 lumbar spine bi-segment model under 10N.m sagittal flexion.

b. Extension

1) Radial Mean Stress (RMS) and Radial Stress Distribution (RSD)

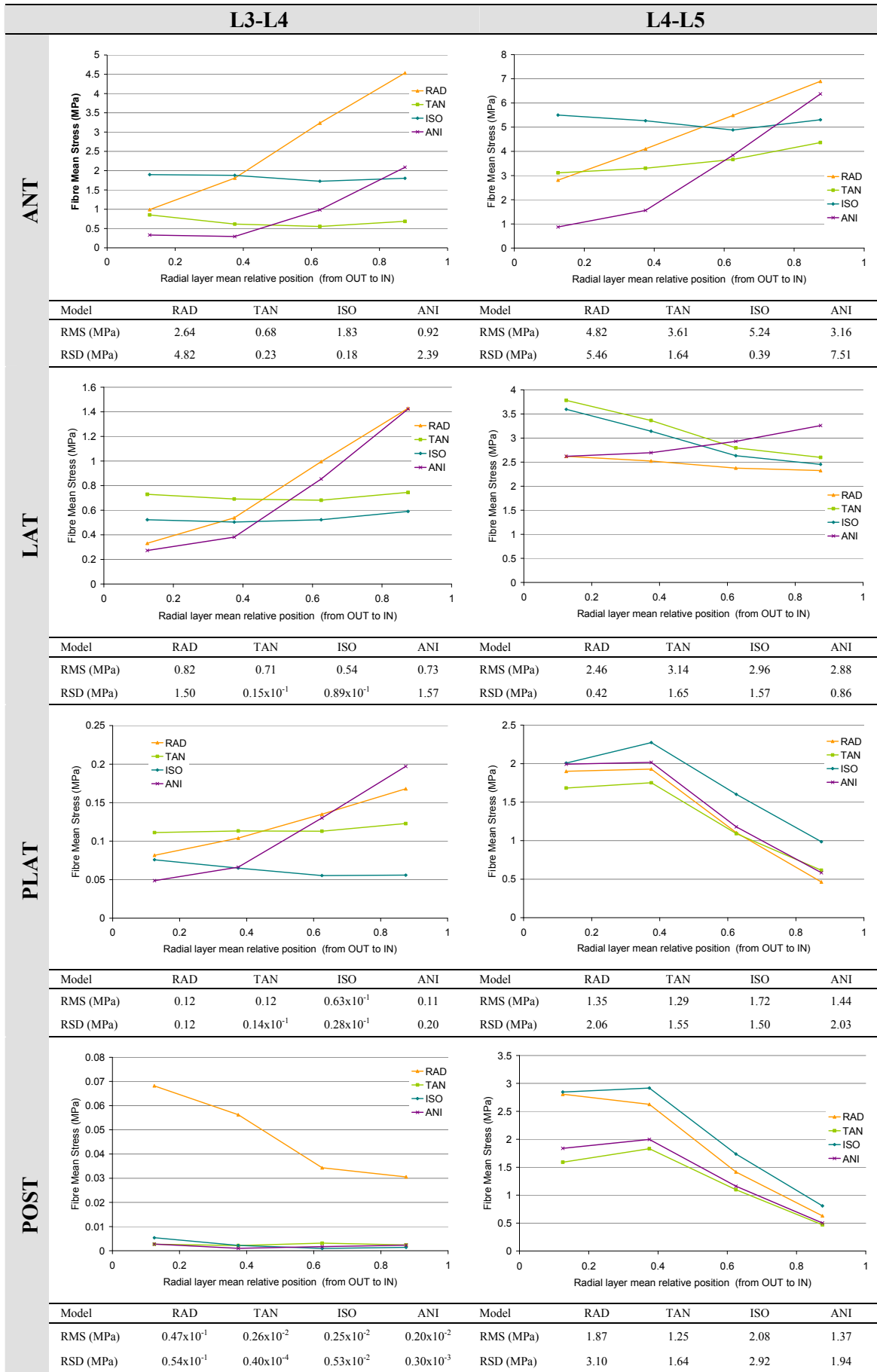
Table 4.6 presents the radial distribution of annulus fibre stress in each tangential sector of the different annulus anisotropy models loaded under sagittal extension. In the anterior annulus and at both levels, the RAD and ANI models gave largest stress gradients between the outer and the inner layers. The ISO model led generally to the best fibre stress distribution all over the annulus thickness, giving the lowest RSD parameter value. The fibres of the RAD model and the ISO model were the most loaded ones at the L3-L4 and L4-L5 levels respectively.

In the L3-L4 lateral annulus, results were similar to the anterior area, except that the most homogeneous stress distribution was given by the TAN model and not by the ISO model. As shown by the RMS parameter values, the RAD and the ANI model had the overall highest fibre stress levels. However, the outer layers of these models were about twice less loaded than those of the TAN model and the RMS parameter predicted in the ANI model resulted close to that of the TAN model. Unlike the predictions performed for the L3-L4 level, at the L4-L5 level, the best radial fibre stress distribution was given by the RAD model followed by the ANI model. In the L4-L5 lateral annulus, the outer fibres and the most external parts of the ISO and TAN mid annuli were highly loaded. They led to a high mean stress level and uneven radial fibre stress distribution.

The fibres of the L3-L4 postero-lateral annulus were fairly low stressed when compared to those of the anterior or the lateral sectors. Both the highest fibre stress level and lowest radial stress gradient were predicted by the TAN model. From the outer to the inner annulus layers, fibre tensile stress radial distributions were the worst in RAD and the ANI models. At the L4-L5 level, a significant stress decrease was predicted in the four models between the mid outer annulus and the inner annulus. In such context, the ISO model had however somewhat higher RMS and lower RSD parameter values than the other models.

In the L3-L4 segment, the TAN, ISO, and ANI posterior annulus fibre stresses were nearly insignificant. In the RAD model, mean load level was nearly 10 times higher than in the other models. Best radial fibre stress distribution was given by the ANI model, but this model was also associated to the lowest RMS value. In the L4-L5 annulus, the fibres of the different models behaved similarly as in the postero-lateral annulus, except that the lowest RSD parameter was computed in the TAN model.

Table 4.6: Radial distribution of the annulus fibre mean stress levels related to the calculation of the RMS and RSD parameters under sagittal extension.



2) Fibre Contribution Quality (FCQ)

Under extension, the ISO model led to the highest FCQ values in the anterior annulus, while the fibres of the RAD and ANI models appeared fairly inefficient (Fig. 4.21). These latter two models had however the largest lateral fibre contribution at the L4-L5 level. In the L3-L4 segment, the best lateral fibre contribution was provided by the TAN model, closely followed by the ISO model. Note that independently from the annulus location, the TAN model brought always one of the largest FCQ values. In the postero-lateral and posterior annulus areas, no great differences were found at the L3-L4 level between the different models. In the postero-lateral and posterior quadrants of the L4-L5 level, the ISO and the TAN model offered respectively the best FCQ results.

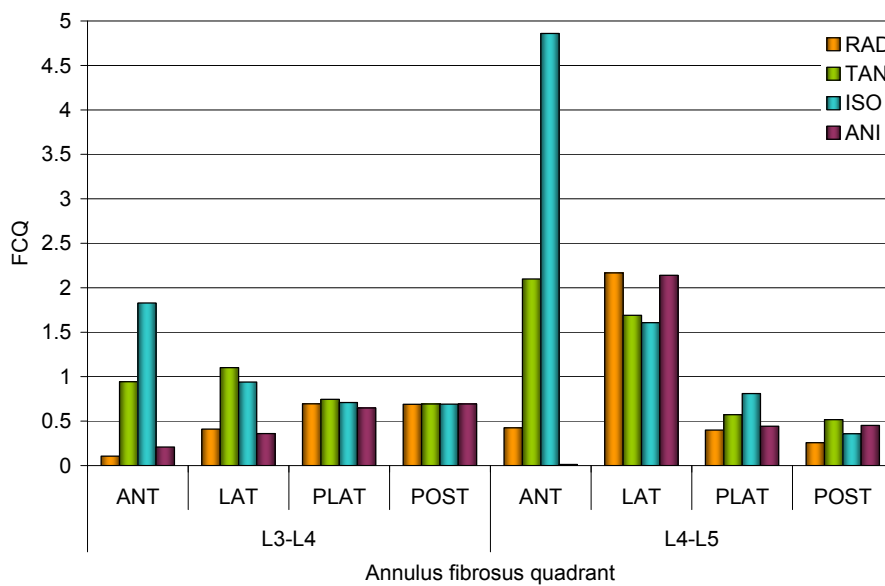


Figure 4.21: FCQ values in the different annulus quadrants of the L3-L5 lumbar spine bi-segment model under 10N.m sagittal extension.

c. Axial compression (reduced model)

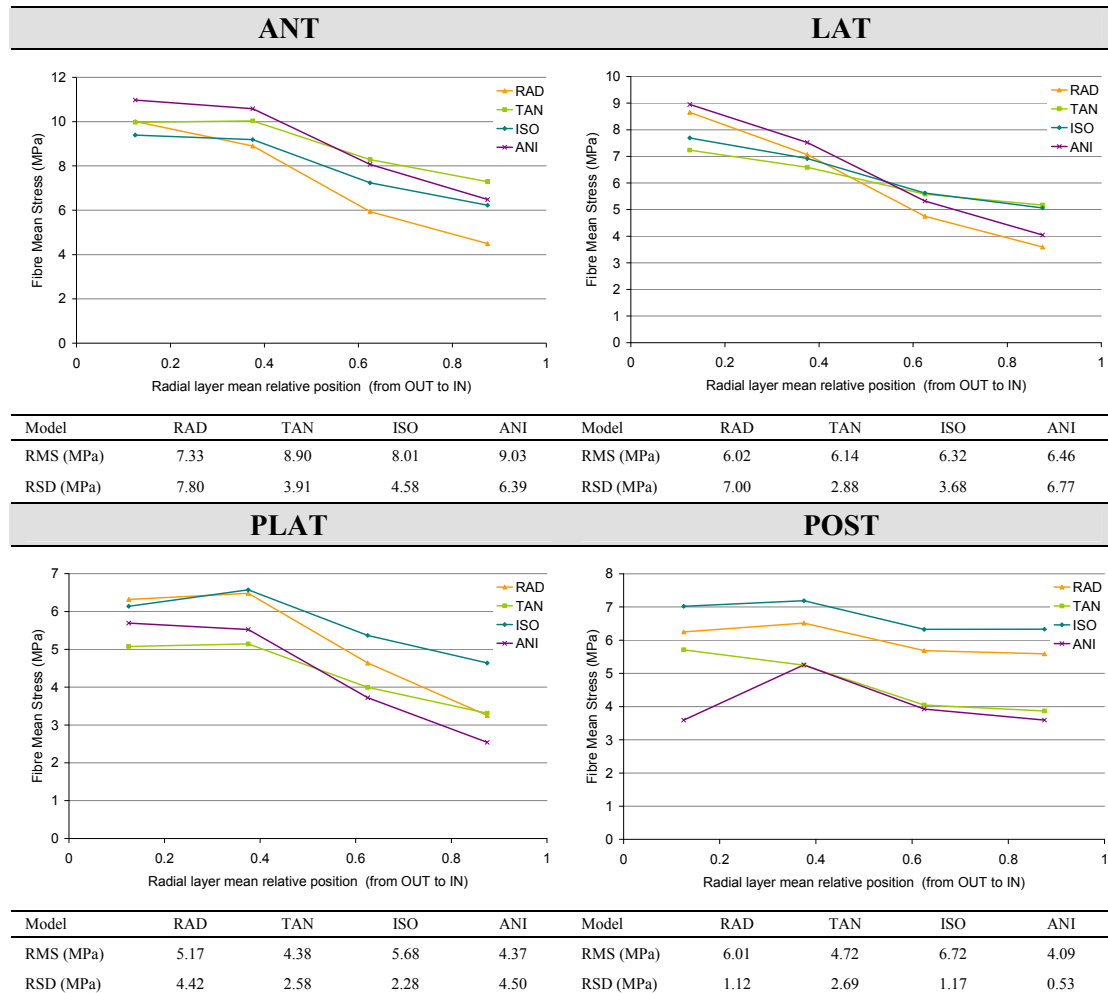
1) Radial Mean Stress (RMS) and Radial Stress Distribution (RSD)

Generally under axial compression, all the four models of annulus anisotropy predicted in each tangential sector similar stress patterns from the outer to the inner annulus (Table 4.7). Fibre stretch was higher in the most external layers than in those close to the nucleus pulposus. The resulting stress gradient tended however to be lower in the posterior annulus. In this sector, the ANI model even led to a lower stress magnitude in the outer layers than in the mid-annulus, the ANI RSD parameter was less than a half of the values predicted by the other models. The mean stress magnitude quantified by the RMS parameter was in change the lowest one in the ANI model. The ISO model provided the highest RMS parameter, but only the third lowest RSD

parameter. The RAD model was associated to the second highest mean stress level and also to the second most homogeneous radial stress distribution.

In the anterior annulus, the smallest radial stress gradient was given by the TAN model that also led to the second higher mean stress level after the ANI model. The ANI model offered however one of the worst radial stress distributions. In the lateral annulus, the highest global mean stress was also given by the ANI model and the best radial distribution was also provided by the TAN model. Nonetheless, the TAN model was associated to the third highest RMS parameter only. The second highest RMS parameter and second lowest RSD parameter were both computed for the ISO model. In the postero-lateral annulus, this later model had both the most favourable RMS and RSD values.

Table 4.7: Radial distribution of the annulus fibre mean stress levels related to the calculation of the RMS and RSD parameters in the reduced model under axial compression.



2) Fibre Contribution Quality (FCQ)

Under axial compression, the FCQ parameter suggested two main optimum annulus fibre organizations that were the TAN configuration in the anterior and lateral annuli and the ISO configuration in the postero-lateral and posterior areas (Fig. 4.22). While the TAN model led to the second highest FCQ value in the postero-lateral annulus, it gave the worst results in the posterior quadrant. The RAD model then occupied the second place.

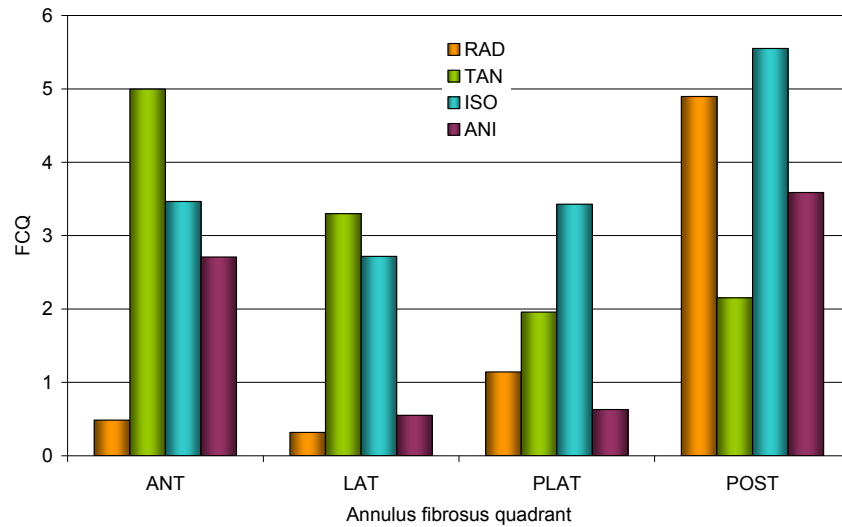


Figure 4.22: FCQ values in the different annulus quadrants of reduced model under 1000N axial compression.

d. Spinal erector-like loading

1) Radial Mean Stress (RMS) and Radial Stress Distribution (RSD)

In the anterior annulus, the application of the combined load led to a fairly homogeneous fibre stress radial distribution in the ISO model (Table 4.8). In the RAD and ANI models, inner annulus loads were approximately between two and four times higher than the outer ones. At both levels, the ISO model gave the second largest radial mean stress magnitude after the RAD model.

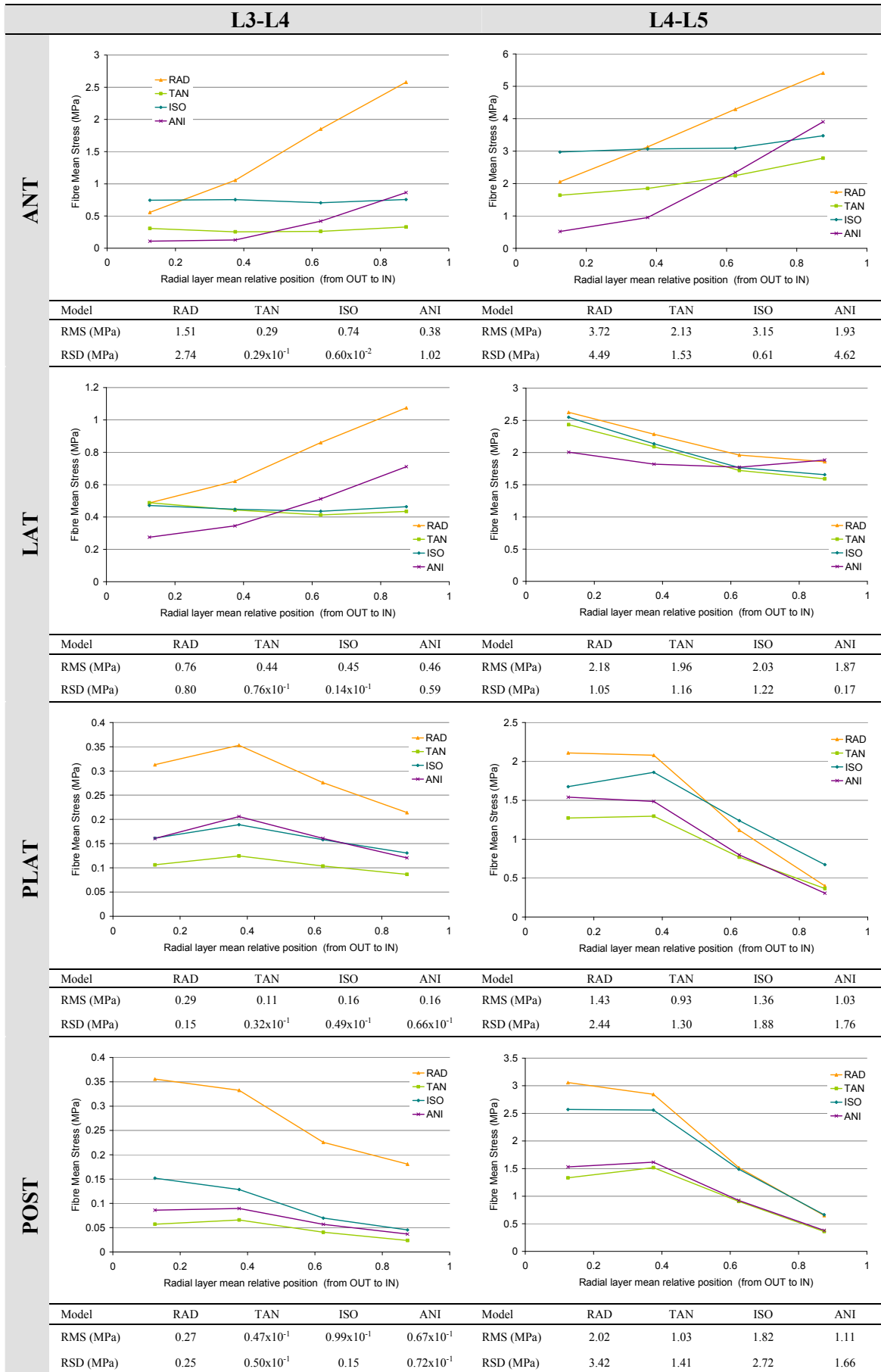
In the lateral sector, the fibre stress profiles in the different models were qualitatively similar as in the anterior annulus, except that the ANI model had the second highest RMS parameter after the RAD model. The mean stress levels in the TAN, ISO and ANI models were only about 2% different from each others. At the L4-L5 level of the RAD, TAN and ISO models, external fibre layers were generally significantly more stretched than the inner ones. As in the L3-L4 level, the RAD model led to the highest global L4-L5 lateral fibre stresses. Best radial load distributions were

given by the ANI model, followed by those of the RAD model. Even though, the RSD parameters respectively computed in the ANI and RAD models diverged significantly.

In the L3-L4 postero-lateral annulus, fibre stresses tended to be larger in the external part of the mid-annulus for all models. In general, the higher is the RMS parameter the worse is the radial distribution of fibre loads. While the RAD provided the highest stress levels, the lowest stresses and RSD parameter were associated to the TAN model. The ANI and the ISO models were in between and had similar RMS values. However, in terms of radial load distribution, the ISO model provided better results. At the L4-L5 level, fibre stresses decreased for all models from the outer to the inner annulus and similarly as in the L3-L4 segment, the mean load magnitude was inversely related to the homogeneity of the radial fibre stretch distribution. The RAD and the TAN models led to the maximum RMS and minimum RSD values respectively. The second best load distribution was associated to the ANI model, while the fibres of the ISO model were the second most loaded ones.

The posterior fibres of the L3-L4 annulus fibrosus were substantially more loaded in the RAD model than in the other models and a significant stress gradient was also found between outer and inner layers. The TAN model offered the lowest radial stress gradient but also the lowest load magnitudes. The ANI and the ISO model had comparable RMS parameters but in the ISO model, the RSD value was one order of magnitude lower than in the ANI model. At the L4-L5 level, results were qualitatively similar to the L3-L4 annulus with the difference that both stresses magnitude and radial gradients were from one to two orders of magnitude higher.

Table 4.8: Radial distribution of the annulus fibre mean stress levels related to the calculation of the RMS and RSD parameters for the spinal erector-like loading.



2) Fibre Contribution Quality (FCQ)

As shown in Figure 4.23, the best fibre contribution in the anterior and lateral parts of the L3-L4 annulus was predicted in the ISO model. The TAN model led to the second largest FCQ value. In the postero-lateral and posterior areas, no significant differences were found by the different models. At the L4-L5 level, the computed fibre efficiency was better with the ISO than with the other collagen arrangements. In the lateral annulus, the ANI model, followed by the RAD model, had the best fibre contributions. No major differences were found between the ISO and the TAN model. In the posterior area, the TAN fibres seemed to be the most able to contribute to the annulus mechanical stability. The ANI model had the second place.

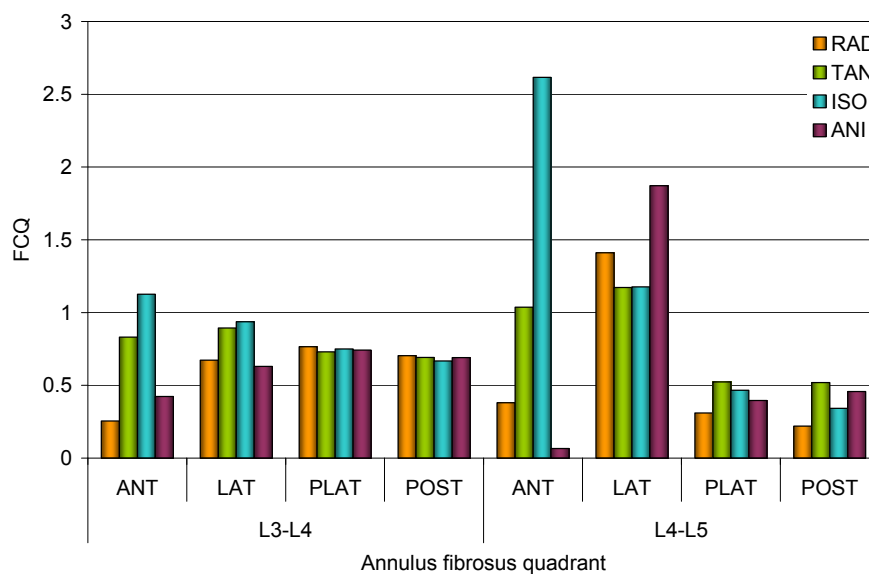


Figure 4.23: FCQ values in the different annulus quadrants of the L3-L5 lumbar spine bi-segment model for the spinal erector-like loading.

e. Axial rotation

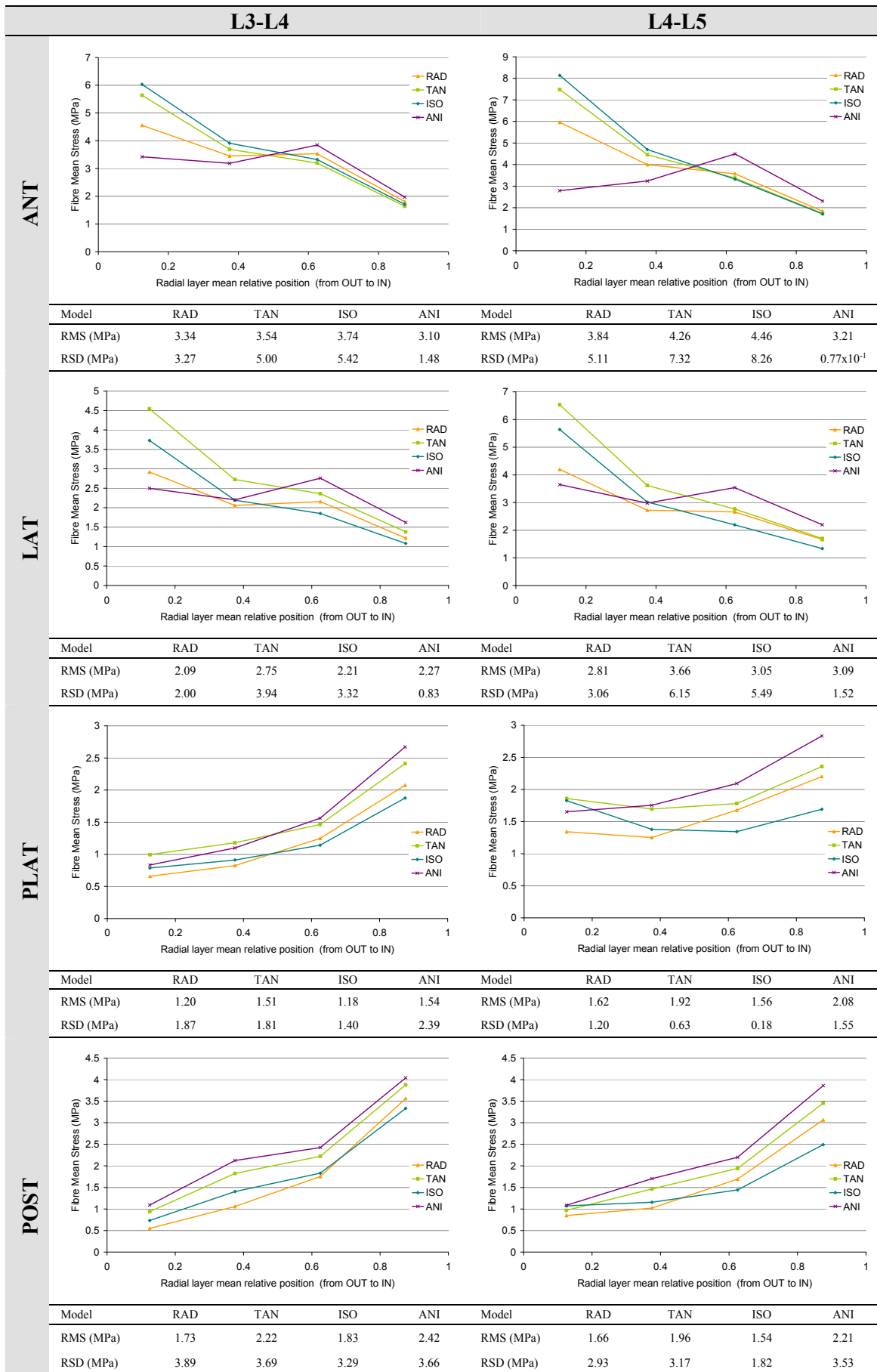
1) Radial Mean Stress (RMS) and Radial Stress Distribution (RSD)

Under axial rotation, fibre stresses in the anterior annulus of the ISO and the TAN models decreased from the outer to the inner layers and although they led to the highest mean load levels, they were poorly distributed (Table 4.9). In the RAD model, stresses were fairly constant over the two parts of the middle annulus and contributed to give a lower RSD parameter. However, although the ANI RMS parameter value was lower than the other RMS parameter values, the ANI model predicted the most homogeneous fibre stresses.

In the lateral annulus, the situation was similar as in the anterior annulus and in postero-lateral area, stresses at the L3-L4 level tended to increase from the outer to the inner layers. While, the TAN model predicted the largest mean stress values across annulus thickness, the ISO model gave the best fibre stress distribution. At both L3-L4 and L4-L5 levels, the ISO model gave the lowest postero-lateral RSD parameter but also the worst mean stress level. At the L4-L5 level, the ANI annulus configuration allowed the fibres bearing the highest general stress. The TAN configuration led to the second greatest and second lowest RMS and RSD parameters, respectively.

As in the postero-lateral quadrants, in the L3-L4 posterior annulus, the ISO model gave the most homogeneous load distributions but the lowest mean stress level. Highest RMS parameter value and second smallest RSD value were both predicted by the ANI model. At the L4-L5 level, the greatest fibre mean loading was found in the ANI model and the best stress distribution in the ISO model. The RAD and the TAN model gave intermediate RMS and RSD results, but as in the ANI and ISO models, the higher the RMS was, the worse the radial distribution of loads was.

Table 4.9: Radial distribution of the annulus fibre mean stress levels related to the calculation of the RMS and RSD parameters under axial rotation.



2) Fibre Contribution Quality (FCQ)

Under axial rotation, the ANI model led to the best FCQ results in the anterior and lateral annuli of both segments (Fig. 4.24). Anterior fibre contributions in the TAN and the ISO models were particularly low. Although the FCQ values given by the RAD model were less than half those found for the ANI model, they were considerably above the values predicted by the TAN and the ISO model. In the postero-lateral quadrants of both L3-L4 and L4-L5 segments, the ISO and the TAN models provided best results. In the posterior annulus, worst results were given both by the ANI model at the L3-L4 level and by the ISO model at the L4-L5 level. The RAD model returned generally the lowest posterior FCQ values.

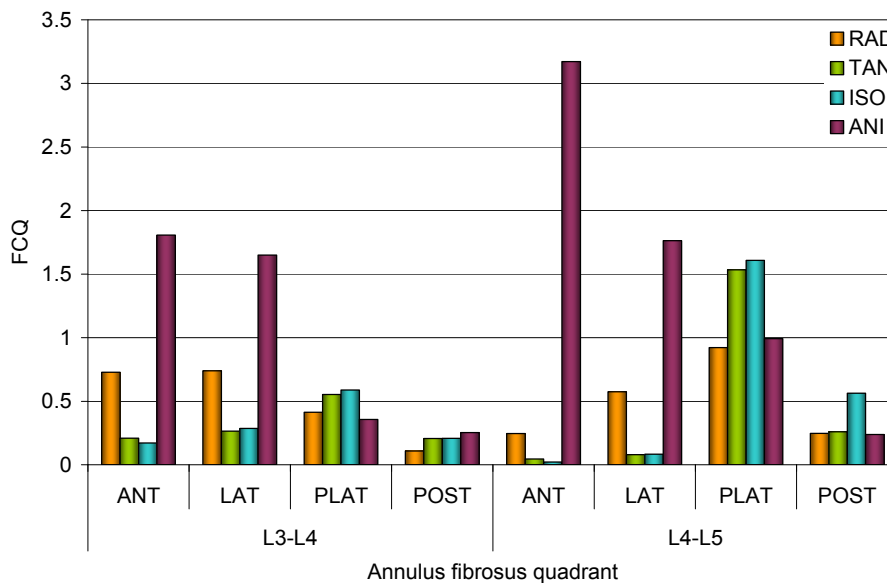


Figure 4.24: FCQ values in the different annulus quadrants of the L3-L5 lumbar spine bi-segment model under 10N.m left axial rotation.

f. Lateral bending

1) Radial Mean Stress (RMS) and Radial Stress Distribution (RSD)

Table 4.10 presents the radial stress distributions predicted by each anisotropy model under lateral bending. The RMS and RSD parameters were also reported for each of the defined tangential sectors. In the anterior annulus, the L3-L4 and L4-L5 most homogeneous fibre stress radial distributions were given by the ISO and the TAN configurations respectively. In both segments of the modelled spine, the fibres of the RAD model were the most loaded ones but fibre stresses were considerably concentrated in the inner layers. In terms of magnitude, the RMS parameter of TAN

model was always in the third position, behind the RMS values returned by the RAD and the ANI models.

In the L3-L4 lateral annulus, the RAD model predicted high inner fibre stresses and the largest mean fibre stress. However, as in the anterior annulus, stress distribution was better with the other modelled fibre arrangements. Best radial stress distribution was returned together with the lowest RMS values by the ISO model. The ANI and the TAN model had the second lowest RSD and the second highest RMS parameter value respectively. In the L4-L5 annulus, the TAN model led simultaneously to the largest global stress level and the worst radial distribution. RAD annulus fibre configuration allowed computing the second highest mean load, as well as the most homogeneous radial distribution.

In the postero-lateral area of the annulus fibrosus, the TAN model led to the largest RMS parameter, but with a high concentration of loads in the outer annulus. At the L3-L4 level, on one hand, the RAD model provided best stress distribution over the annulus thickness. On the other hand, the ANI model returned an equilibrated balance of fibre parameter values with the second lowest RSD and second greatest RMS parameter values respectively. At the L4-L5 level, the ANI model led to the most homogeneous stress levels over the different radial layers and to the second highest RMS value at the same time.

In the L3-L4 posterior annulus, results given by the ANI model in comparison to the prediction performed for the other models, was qualitatively similar as in the L4-L5 postero-lateral annulus. The TAN model had the greatest fibre stresses nearly over the whole annulus thickness, but also the worst fibre stress distribution. In the L4-L5 posterior annulus, both stress distribution and magnitude were comparable in the RAD, TAN and ANI models. The ANI model returned only slightly more favourable RMS and RSD parameters.

Table 4.10: Radial distribution of the annulus fibre mean stress levels related to the calculation of the RMS and RSD parameters under lateral bending.

	L3-L4					L4-L5				
ANT										
	Model	RAD	TAN	ISO	ANI	Model	RAD	TAN	ISO	ANI
	RMS (MPa)	2.96	2.08	1.97	2.28	RMS (MPa)	3.45	2.61	2.56	2.73
	RSD (MPa)	3.30	1.17	0.81	2.54	RSD (MPa)	2.12	0.54x10 ⁻¹	0.94	1.91
LAT										
	Model	RAD	TAN	ISO	ANI	Model	RAD	TAN	ISO	ANI
	RMS (MPa)	3.87	3.66	2.56	3.59	RMS (MPa)	4.86	5.08	3.86	4.66
	RSD (MPa)	1.88	1.67	1.36	1.48	RSD (MPa)	0.79	6.27	6.32	0.91
PLAT										
	Model	RAD	TAN	ISO	ANI	Model	RAD	TAN	ISO	ANI
	RMS (MPa)	2.74	4.33	1.89	3.78	RMS (MPa)	3.41	5.02	2.66	4.76
	RSD (MPa)	0.74	2.04	1.51	1.24	RSD (MPa)	0.21	3.54	3.25	0.14
POST										
	Model	RAD	TAN	ISO	ANI	Model	RAD	TAN	ISO	ANI
	RMS (MPa)	2.00	2.93	1.36	2.77	RMS (MPa)	2.33	2.22	1.73	2.39
	RSD (MPa)	0.72	1.03	0.87	0.28	RSD (MPa)	0.54	0.78	1.84	0.31

2) Fibre Contribution Quality (FCQ)

Under lateral bending, from the lateral to the posterior annulus areas of both levels, the ANI model returned generally the highest fibre contribution parameters (Fig. 4.25). The TAN and the RAD configurations provided to the second best fibre contributions at the L3-L4 and L4-L5 levels respectively. In the anterior annulus, the ISO and the TAN models led to the best results, giving respectively the largest FCQ values in the L3-L4 and L4-L5 segment. However, in the rest of the annulus quadrants, the ISO configuration was globally much less efficient than the other type of fibre arrangements with radial and/or tangential orientation gradients.

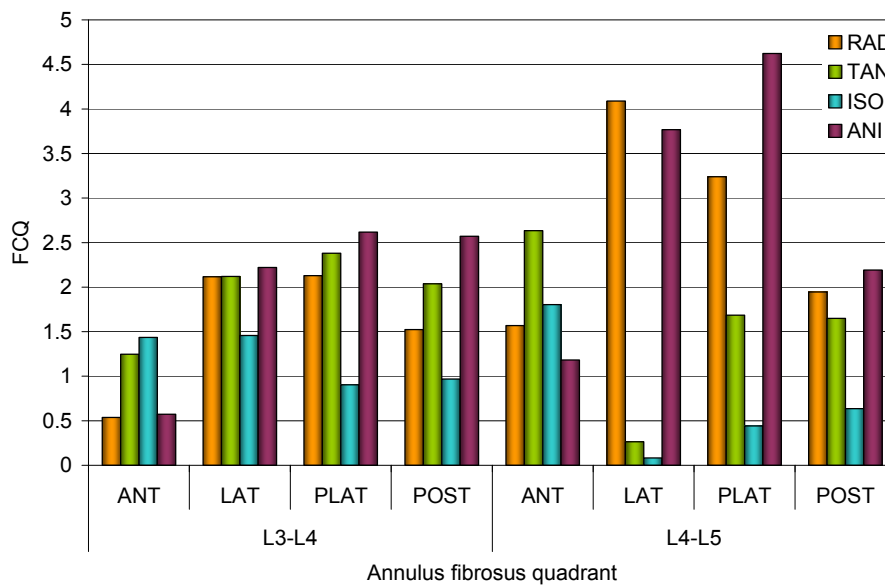


Figure 4.25: FCQ values in the different annulus quadrants of the L3-L5 lumbar spine bi-segment model under 10N.m left lateral bending.

IV. Annulus matrix shear strain

a. Flexion

As shown in Figure 4.26, the type of annulus fibre arrangement had a significant effect on the annulus matrix shear strain under sagittal flexion. For all models, the mean shear strain level was generally greater in the anterior and lateral quadrants. Except in the L3-L4 postero-lateral and posterior annulus where the ISO configuration led to the largest global shear deformations, the RAD model was systematically associated to highest mean shear strain. In all quadrants, the TAN and ANI models led to very similar prediction. The highest differences between these two models were never superior to 6.5% and largest value was predicted in the L4-L5 anterior and posterior annulus.

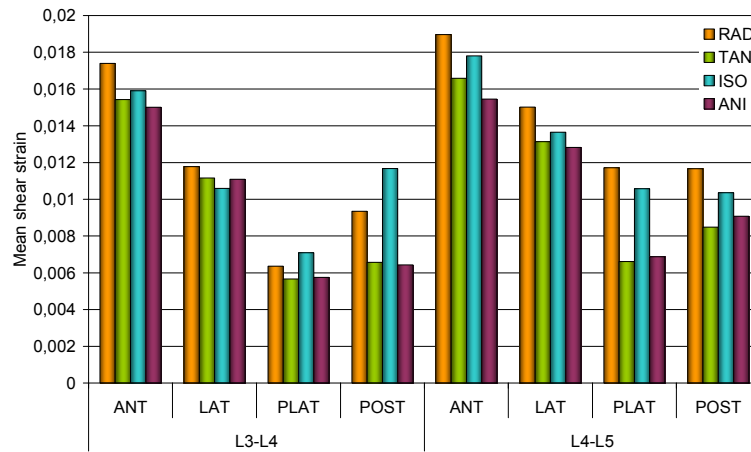


Figure 4.26: Annulus matrix mean total shear strains computed over all the nodes of each tangential sector under sagittal flexion.

In Figure 4.27, shear deformation mechanisms under sagittal flexion were similar in all models. Disregarding the attachment points of the intervertebral disc to the adjacent endplates, changes in shear strain vector orientation were more drastic through the annulus thickness than along the periphery (Fig. 4.27a,b,c,d). Apart from the L3-L4 outer postero-lateral strains that were nearly zero, postero-lateral and posterior strains were in general fairly axial and ran in opposite directions inner and outer shear. In the anterior quadrant, outer and inner shear deformations were not completely opposite and the largest outer shear strain vectors followed annulus bulging. In the lateral annulus, shear strain distributions were more complex than in the other quadrants. From the anterior to the mid part of the lateral annulus, inner shear strain vectors passed progressively from being axially oriented to nearly parallel to the annulus transverse plane. In the outer lateral annulus, the less important disc bulging was, the more transversal shear strain vectors were.

Comparison of the different models revealed that posterior and postero-lateral total shear strains were particularly lower in the inner L3-L4 and outer L4-L5 posterior quadrants of the TAN and ANI models (Fig. 4.27b,d). From the anterior to the mid part of the lateral annulus, shear strain orientation changes were less important in the TAN and in the ANI models than in the other models.

At the attachment points of the annuli to the adjacent endplates, most of the shear deformations occurred in the anterior, postero-lateral and posterior quadrants (Fig. 4.27e,f,g,h). Both a transversally oriented and an axial component were generally present. At the L3-L4 level, the axial component was quasi inexistent in the outer posterior and postero-lateral quadrants of the TAN model (Fig. 4.27f). In the ANI model (Fig. 4.27h), posterior, postero-lateral, and anterior inner strain shear vectors were directed towards the centre of the disc and seemed somewhat higher than in the TAN model. In the RAD and ISO models both axial and transversal shear components were present in the anterior and posterior annulus quadrants (Fig. 4.27e,g). Anterior and

posterior shear strain magnitudes were also generally higher in the RAD and ISO than in the ANI and TAN models.

At the L4-L5 level, the radial shear components at the attachment points between the annuli and the adjacent endplates were insignificant in the upper posterior annulus of the TAN model. For all models, axial shear components were predicted in the posterior and postero-lateral outer annuli. However, in the posterior, postero-lateral, and anterior inner annuli, the ANI model mostly presented transversal shear strain components that pointed toward the nucleus pulposus (Fig. 4.27h).

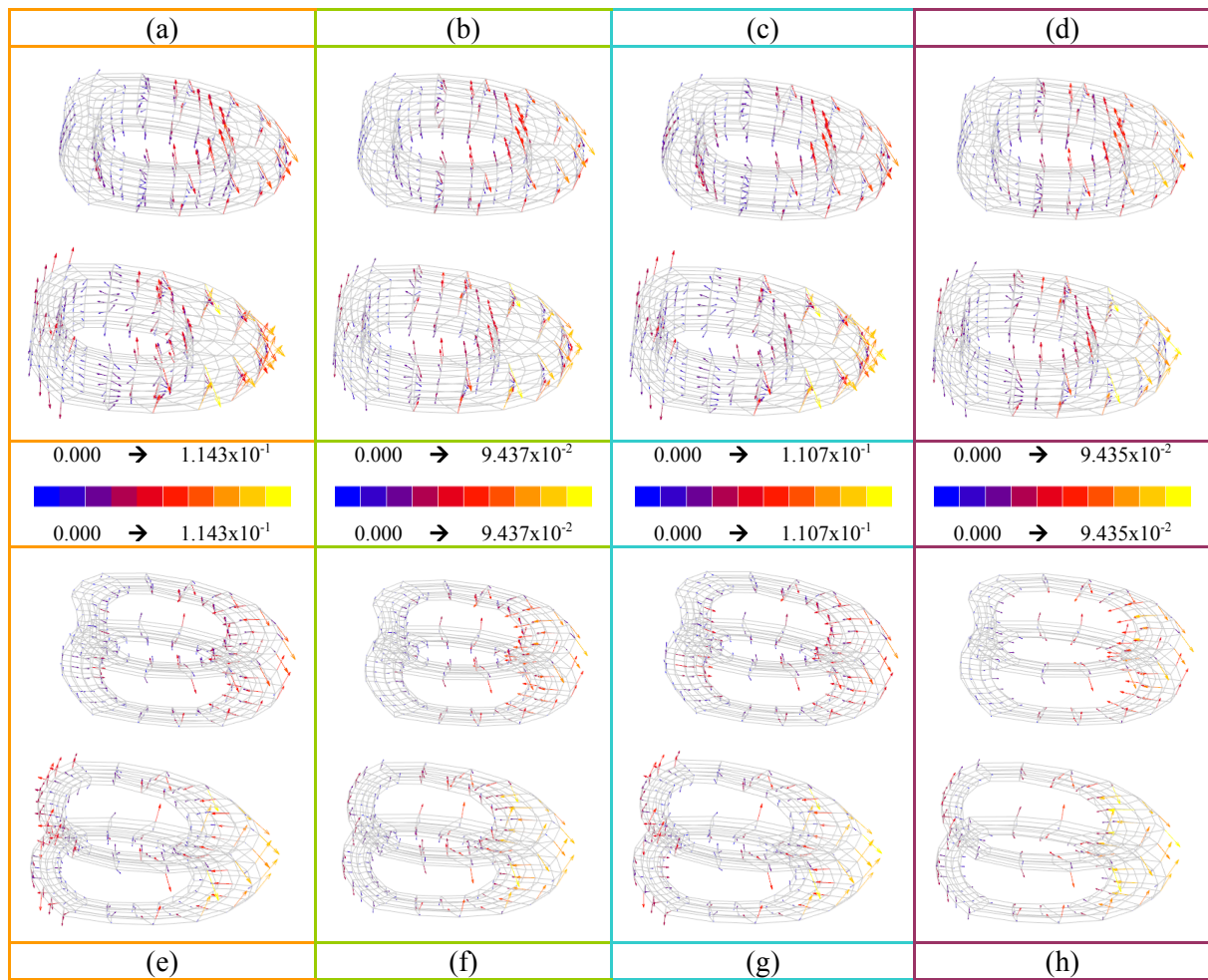


Figure 4.27: Total shear strain directions and extreme values in the L3-L4 and L4-L5 annulus matrices of the RAD (a, e), TAN (b, f), ISO (c, g), and ANI (d, h) models under sagittal flexion. The elements sharing nodes with the surrounding cartilage and bony endplates are represented in pictures e, f, g, h and excluded from pictures a, b, c, d.

b. Extension

Under extension, for all models, mean shear strains in the L3-L4 annulus decreased at the L3-L4 level from the anterior to the posterior quadrant. This tendency was reversed at the L4-L5 level (Fig. 4.28). From one level to another, some differences were found between the different models. While from the L3-L4 to the L4-L5 level, lateral mean shear strain increased in the RAD model, it remained almost constant for the ISO model and decreased for the TAN and ANI models. Strain reduction from the L3-L4 to the L4-L5 annulus was most pronounced in the TAN model. In both segments of the lumbar spine model, the ISO configuration induced minimum strain levels, but together with the ANI model at the L3-L4 level, and with the RAD model at the L4-L5 level. Except in the L3-L4 posterior annulus, the RAD model always led to the lowest mean shear strain levels.

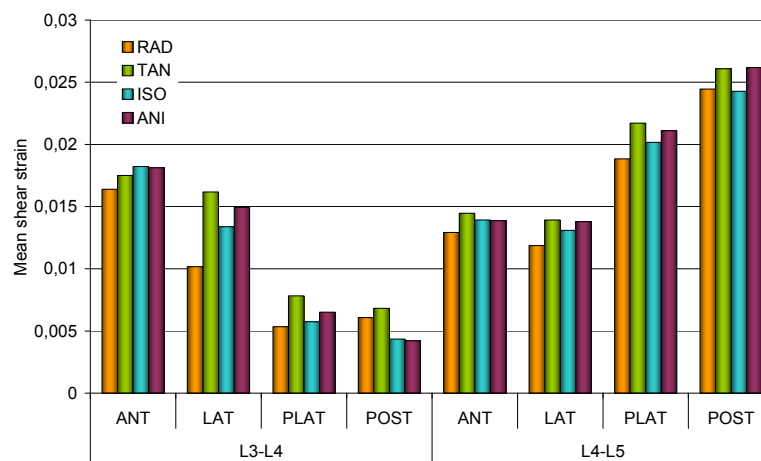


Figure 4.28: Annulus matrix mean total shear strains computed over all the nodes of each tangential sector under sagittal extension.

As shown by Figure 4.29, largest matrix shear strain levels in the different annulus models were always present away from the attachment points between annulus and bony and cartilage endplates. At the L3-L4 level, anterior total shear strain vectors were mostly axial and ran in opposite directions in the outer and inner layers (Fig. 4.29a,b,c,d). In proportion to the deformation state in the other quadrants, anterior shear total strain components were higher in the RAD model than in the other models. Anterior outer total shear strains in the RAD and ISO models tended to orient more transversally than those in the TAN or ANI models. In the anterior parts of the TAN, ISO and ANI lateral annuli, shear strains were almost similar in direction, but higher in magnitude than in the adjacent anterior annuli (Fig. 4.29b,c,d). In the RAD model, shear strains turned principally transversal from the anterior to the lateral quadrant and decreased quickly (Fig. 4.29a). The L3-L4 RAD annulus had however significant postero-lateral and posterior shear deformations. In the outer postero-lateral annulus shear strain vectors returned by the RAD model were mainly transversally aligned.

At the L4-L5 level, anterior outer shear strains were mainly parallel to the transverse plane for all annulus configurations but the ANI one. Inner anterior shear deformations were on the other hand axially oriented. Relative to the outer strains, they were also more significant in the TAN model (Fig. 4.29b) than in the RAD and ISO models (Fig. 4.29a,c). In the anterior part of the lateral annulus, outer and inner shear strains had opposite directions and tended to be more transversally oriented in the RAD model than in the other models. In the RAD model, and to a lesser extent, in the ISO model, matrix strains in the outer mid lateral annulus indicated a beginning of bulging somewhat more important than in the other annulus anisotropy configurations. In the posterior and postero-lateral quadrants, outer strain vectors were mainly function of the disc bulging extent. Inner shear strain vectors oriented axially from the postero-lateral to the posterior annulus. At the transition nodes between anterior and lateral, and between lateral and postero-lateral annulus, inner shear strains were generally approximately aligned along the diagonal of the elements.

For all models, matrix shear deformations at the attachment points between the anterior annulus fibrosus and the endplates had an axial and a transversal component with respect to the deformed annulus shape (Fig. 4.29e,f,g,h). In the posterior annulus, the transversal strain component was also present in the endplates neighbourhood, but the second main component was tangential to disc bulging. At the L3-L4 level, the magnitudes of both transversal and axial shear components present in the RAD and ISO anterior annuli were largely predominant over the shear deformations of the other quadrants (Fig. 4.29e,g). At the L4-L5 level, similar result was found for the posterior annulus transversal shear components predicted by the RAD and ISO models.

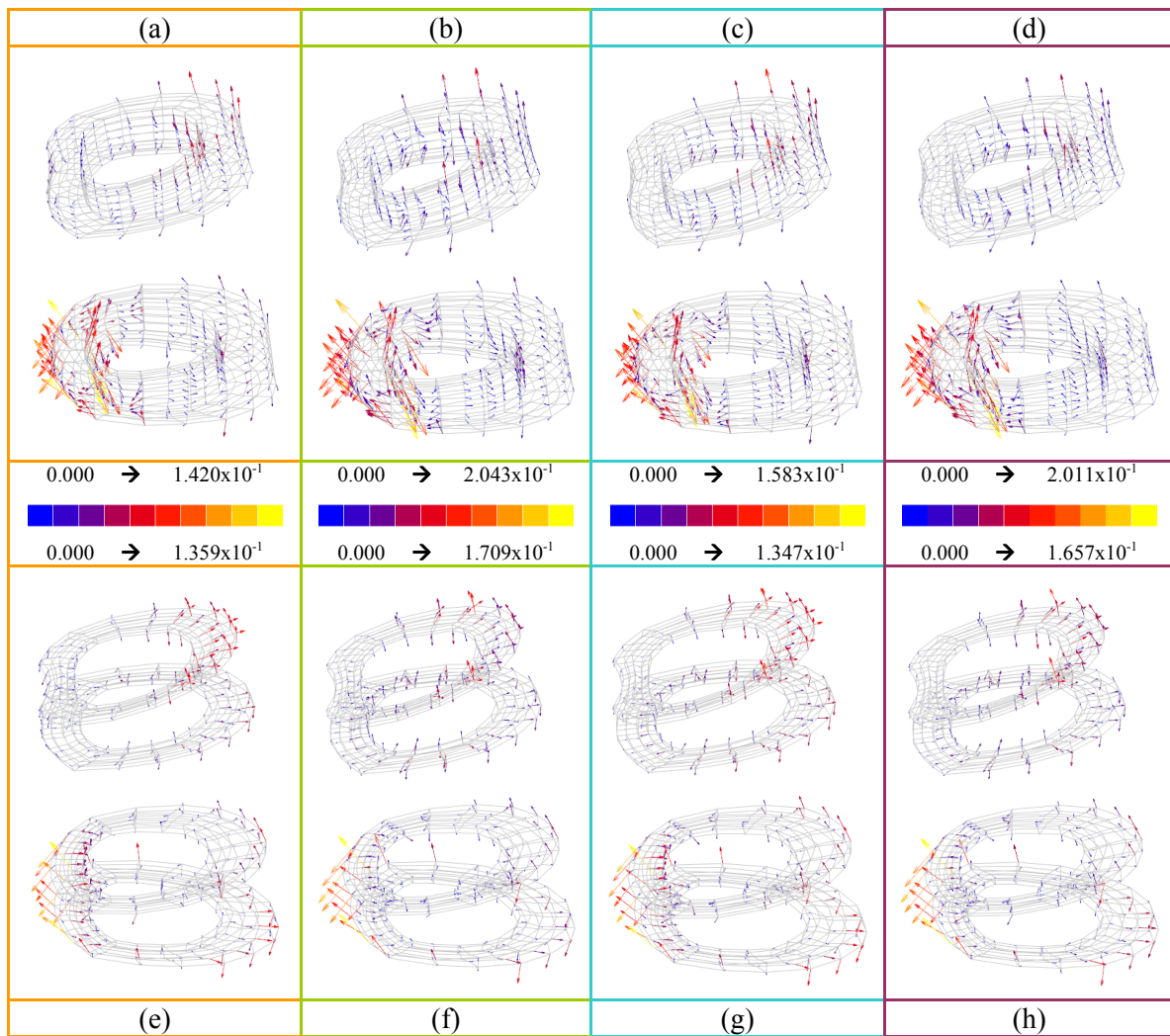


Figure 4.29: Total shear strain directions and extreme values in the L3-L4 and L4-L5 annulus matrices of the RAD (a, e), TAN (b, f), ISO (c, g), and ANI (d, h) models under sagittal extension. The elements sharing nodes with the surrounding cartilage and bony endplates are represented in pictures e, f, g, h and excluded from pictures a, b, c, d.

c. Axial compression (reduced model)

Under axial compression, the largest relative differences between the mean total shear strains of the different annulus models were about 21% and 13% and were respectively found in the anterior annulus, between the RAD and the TAN model, and in the postero-lateral annulus, between the TAN and the ISO model (Fig. 4.30). In the posterior quadrant, the type of anisotropy seemed to have almost no influence on the annulus mean shear deformation. In the anterior and lateral sectors, the RAD model led to the highest mean strain values, while in the postero-lateral quadrant, largest mean strains were predicted in the TAN and ANI annulus matrices. The lowest mean total shear strain values were given by the TAN model in the anterior quadrant, and by the ISO model in the other tangential sectors.

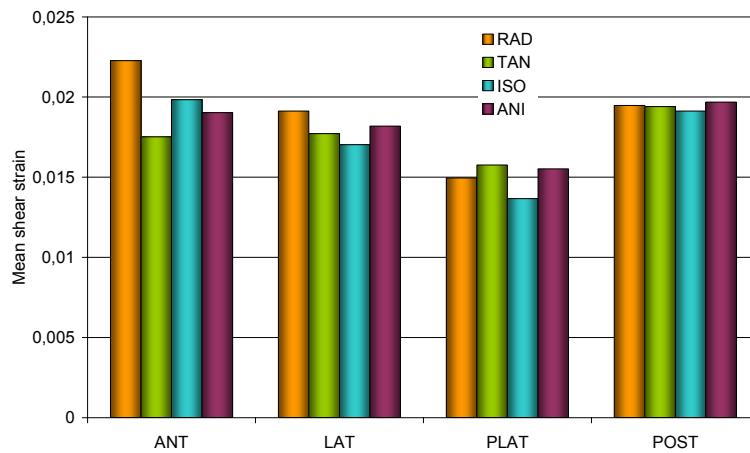


Figure 4.30: Annulus matrix mean total shear strains computed over all the nodes of each tangential sector under axial compression (reduced model).

As shown in Figure 4.31a,b,c,d, external total shear strain vectors basically followed disc bulge all around the annulus periphery. In the inner annulus, anterior and posterior shear strain vectors were nearly collinear and mostly axially oriented. However, at the transition nodes between anterior and lateral, and between lateral and postero-lateral quadrants, inner shear vectors spanned in a fan-like manner. In these areas, node-to-node axial changes of shear orientation were more progressive in the ISO model (Fig. 4.31c) than in the other annulus configurations. Moreover, in the ISO model, shear strains predicted at the nodes between the lateral and the postero-lateral annulus appeared significantly low. At the transition nodes between the lateral and postero-lateral outer annuli, transversal strain components were generally found at annulus mid-height. Compared to the other shear components, these vectors were found somewhat lower in the RAD and in the ISO models (Fig. 4.31a,c) than in the other models. In proportion to the rest of the annulus shear deformations, outer and inner total shear strains of the posterior annulus were larger with the TAN and ANI collagen configurations (Fig. 4.31b,d) than with the other modelled networks.

At the attachment points between the annuli and the adjacent endplates, the TAN and the ANI models showed both in the postero-lateral and posterior annuli, lower transversal shear strain components when compared to the strain components following disc bulging (Fig. 4.31f,h). For all models, total shear strains computed close from the endplates were found higher than away. However, while, away from the endplates, maximum total shear strain values were predicted in the RAD model, close to the endplates, the RAD model returned the lowest total shear strain values (Fig. 4.31a,e).

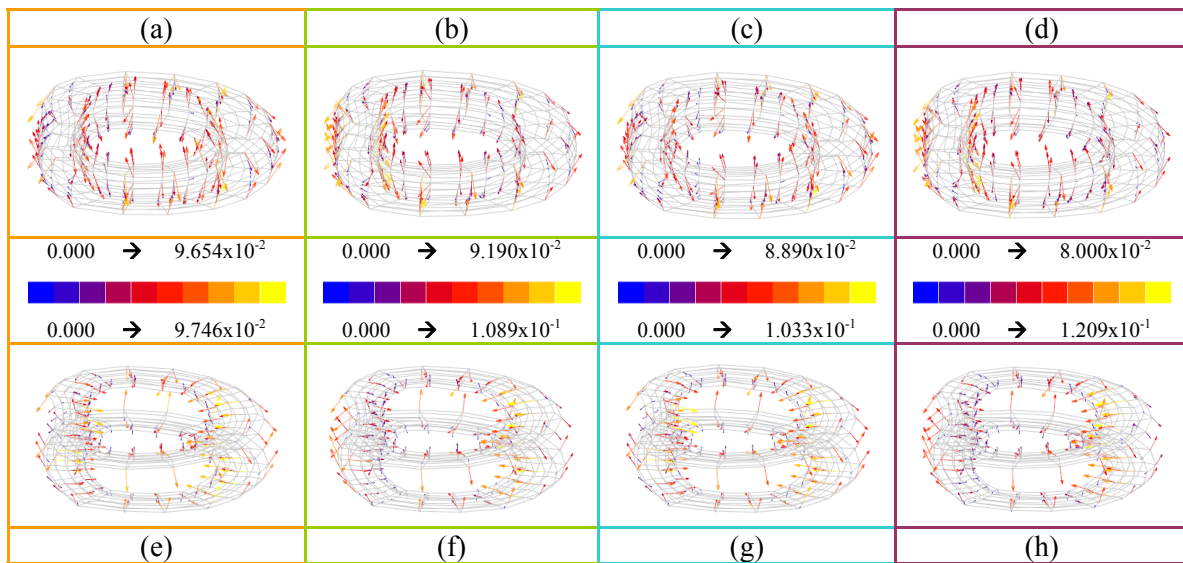


Figure 4.31: Total shear strain directions and extreme values in the annulus matrices of the RAD (a, e), TAN (b, f), ISO (c, g), and ANI (d, h) reduced models under axial compression. The elements sharing nodes with the surrounding cartilage and bony endplates are represented in pictures e, f, g, h and excluded from pictures a, b, c, d.

d. Spinal erector-like loading

When sagittal extension and follower compressive loads were combined, no large differences were found between the mean total shear strain values computed in the L3-L4 lateral and postero-lateral annuli (Fig. 4.32). Anterior and posterior shear strains were higher than lateral posterior and postero-lateral strains, and except for the RAD model, maximum L3-L4 mean shear strain values were generally predicted in the anterior annulus. In the RAD model, highest L3-L4 mean shear deformation took place in the posterior quadrant. This value was also superior to the mean shear values given by the other models at the L3-L4 level. In the postero-lateral annulus, the RAD model led also to higher mean total strains than the other models did. While in the anterior annulus sector, the RAD and the ISO model induced slightly higher mean shear strains than the other annulus fibre configurations, in the lateral quadrant, situation was reversed and highest strains were given in the TAN and ANI annuli.

At the L4-L5 level, the mean total shear strains increased from the anterior to the posterior annulus and particularly from the lateral to the postero-lateral sectors. Fewer differences between models were predicted at the L4-L5 level, than in the L3-L4 segment. A maximum relative difference of only 10% was computed in the anterior quadrant, between the ANI model and the RAD or ISO models. The TAN model in the postero-lateral annulus and the ISO model in the posterior annulus were respectively slightly more and less strained than the other L4-L5 annulus anisotropy models.

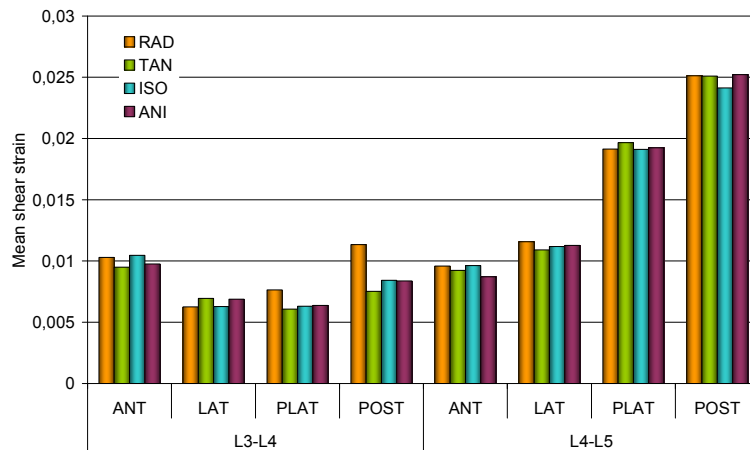


Figure 4.32: Annulus matrix mean total shear strains computed over all the nodes of each tangential sector for the spinal erector-like loading.

Figure 4.33 shows that the L3-L4 anterior shear strains predicted at the outer nodes beside the mid-sagittal plane tended to be more transversal in the RAD and in the ISO models than in the other models. In the inner lateral annulus, upper total shear strain vectors were more axially oriented in the TAN and in the ANI models (Fig. 4.33a,c) than in the RAD and ISO models (Fig. 4.33b,d). In the outer lateral annulus,

some dissymmetry was found between the right and the left side, and the right side was generally less strained than the left one. This was particularly evident for the ISO model where the right outer lateral annulus was nearly totally free of deformation. In the RAD model, the posterior part of the right lateral annulus had in change the most significant outer shear strain vectors. At the transition nodes between the lateral and the posterolateral annuli, proportion of inner shear strains relative to the outer strains was generally lower in the RAD and, to a lesser degree, in the ANI models than in the other models.

In the L4-L5 annulus, the anterior outer total shear strain vectors beside the mid-sagittal plane were clearly less transversally oriented with the ANI configuration (Fig. 4.33d) than with the other models. In the lateral annulus, outer strains were particularly low in the TAN model (Fig. 4.33b) while inner lateral strains were lower in the ISO model (Fig. 4.33c) than in the other models. In the anterior part of the outer lateral annulus, total shear strain vectors of the ANI model pointed generally in a postero-cranial direction, and those of the RAD model began to converge toward the annulus mid-transversal plane, already announcing disc bulging in the mid part of the lateral quadrant (Fig. 4.33a). The RAD model had also more axial shear strain components in the inner lateral annulus than the other models. In the outer posterior annulus, less transversal total shear strain components were present in the TAN model and, to a lesser degree, in the ANI model than in the other models. Peak total shear strains were generally located in the postero-lateral quadrants and were maximal in the ANI model.

For all models, total shear strains calculated in the annulus matrix elements adjacent to the endplates were larger than in the rest of the modelled annulus ground substance (Fig. 4.33e,f,g,h). At the L3-L4 level, apart from differences of magnitude, the four models of anisotropy led to almost equivalent shear strain distributions. In the L4-L5 posterior annuli of the RAD and ISO models, shear strain transversal components were particularly predominant over the other strain components.

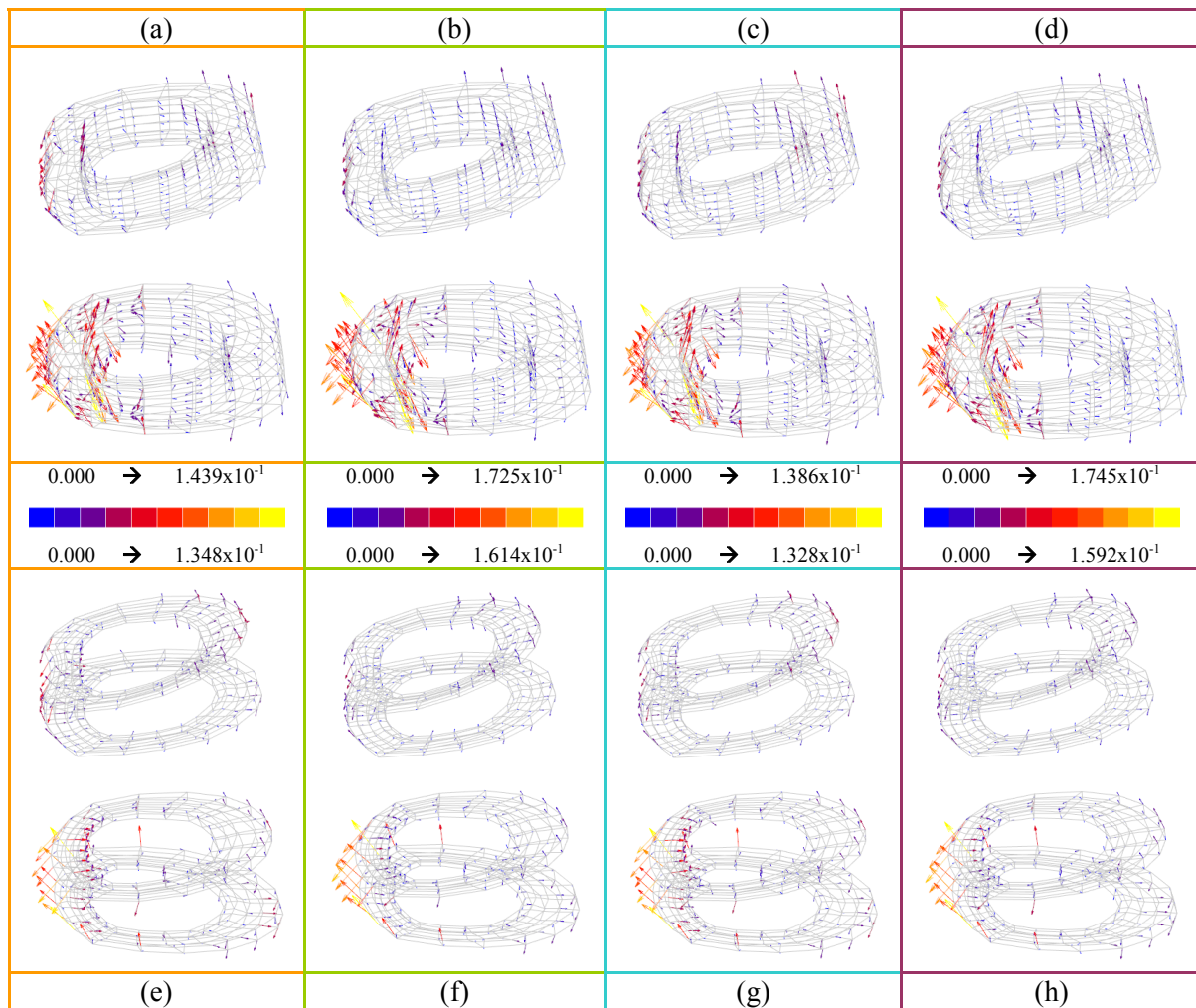


Figure 4.33: Total shear strain directions and extreme values in the L3-L4 and L4-L5 annulus matrices of the RAD (a, e), TAN (b, f), ISO (c, g), and ANI (d, h) models for the spinal erector-like loading. The elements sharing nodes with the surrounding cartilage and bony endplates are represented in pictures e, f, g, h and excluded from pictures a, b, c, d.

e. Lateral bending

Under lateral bending, matrix mean total shear strain computed in the different annulus quadrants showed less sensitivity to changes in annulus anisotropy configuration than under sagittal rotations (Fig. 4.34). Largest mean strain relative differences between the different models were around 7% and 9%. These values were respectively found in the L3-L4 lateral annulus between the RAD and the TAN models, and in the L4-L5 postero-lateral quadrant between the RAD and the ANI models. In the anterior and lateral annuli of both levels, the TAN model led to somewhat less mean shear deformation than the other models did. In the postero-lateral and posterior quadrants, least levels of annulus matrix total mean shear strain were given, at the L3-L4 level by the ISO annulus configuration, and at the L4-L5 level by the RAD configuration. At the L4-L5 level, posterior and poster-lateral mean strain values predicted in the RAD model were however only 3% inferior to those computed in the ISO model. In both the L3-L4 and L4-L5 annuli, mean total shear strains were higher in the lateral and postero-lateral quadrants. Anterior and posterior annuli were generally similarly strained in the L3-L4 segment, but L4-L5 shear deformations were significantly larger in the posterior than in the anterior quadrant.

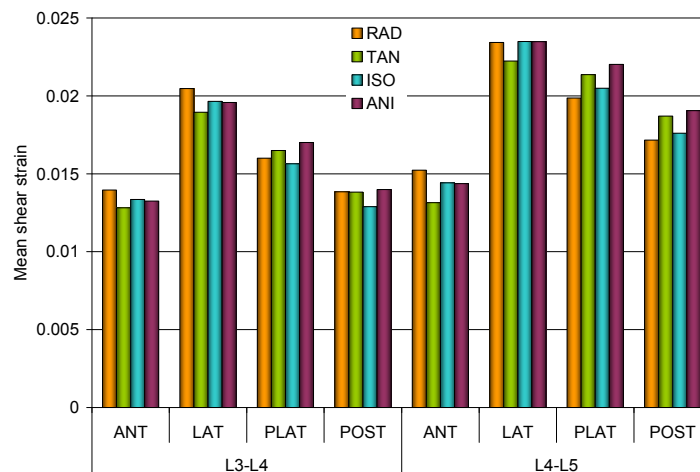


Figure 4.34: Annulus matrix mean total shear strains computed over all the nodes of each tangential sector under lateral bending.

As shown in Fig. 4.35a,c, L3-L4 anti-rotation side outer lateral shear strains appeared, in relation to the other shear components, slightly higher and more axially oriented in the RAD and ISO models than in the other models. For the rest, no great differences in shear strain orientation patterns could be observed between the L3-L4 and L4-L5 levels of the different models. While lateral shear strains were axially oriented to the anti-rotation side and tangent to disc bulge to the rotation side, in the anterior annulus they were mainly transversal. Inner and outer total shear strain vectors had generally almost opposite directions.

In the rotation side part of the anterior quadrant, inner shear strain vectors spanned in a fan-like between the upper and the lower nodes. Such shear strain direction change from node to node was less progressive in the RAD and in the ANI model (Fig. 4.35a,d) than in the other models. From the mid-anterior to the rotation-side lateral annulus, outer shear strain vectors computed in the RAD model markedly pointed toward annulus mid-transversal plane (Fig. 4.35a) as disc bulging appeared. In the inner annulus, each transition zone between the rotation side bulged lateral annulus and the other quadrants was characterized by a fan-like cranio-caudal distribution of the total shear strain vectors. To the anti-rotation side, anterior inner shear strain vectors progressively oriented axially to point in the caudal direction in the lateral annulus. This was more pronounced in the TAN and in the ISO models (Fig. 4.35b,c) than in the other models.

The transition between the rotation-side lateral and postero-lateral annuli was characterized by transversal outer shear strain components that were higher in the TAN and in the ANI models than in the RAD and ISO models. In the anti-rotation side postero-lateral and posterior outer annuli, outer total shear strain vectors predicted along the different axial node paths up to the mid-sagittal plane had successively a fan-like configuration, a transversal orientation, and converged toward the annulus mid-height as disc bulging appeared. Shear strain vector mid-transversal plane convergence associated to disc bulging was less defined in the L3-L4 posterior annulus, than in the L4-L5 posterior annulus. In the mid-sagittal plane posterior annuli of both levels, disc bulging-related outer shear strain distribution was actually clearly defined only in the RAD model. In the other models, mid-transversal plane convergence of the shear strain vectors tended to appear rather above the mid-sagittal plane, to the rotation side.

The only differences observed between the different models in terms of shear strains at the attachment points between the annuli fibrosi and the adjacent endplates, was that total shear vectors generated in the outer L4-L5 posterior annulus were less axial in the RAD and in the ISO models (Fig. 4.35e,g) than in the TAN and ANI models (Fig. 4.35f,h). Both close and away from the adjacent endplates, the maximum values of annulus matrix total shear strain were predicted to the rotation side, in the ANI model. Minimum shear strains were found in the RAD model.

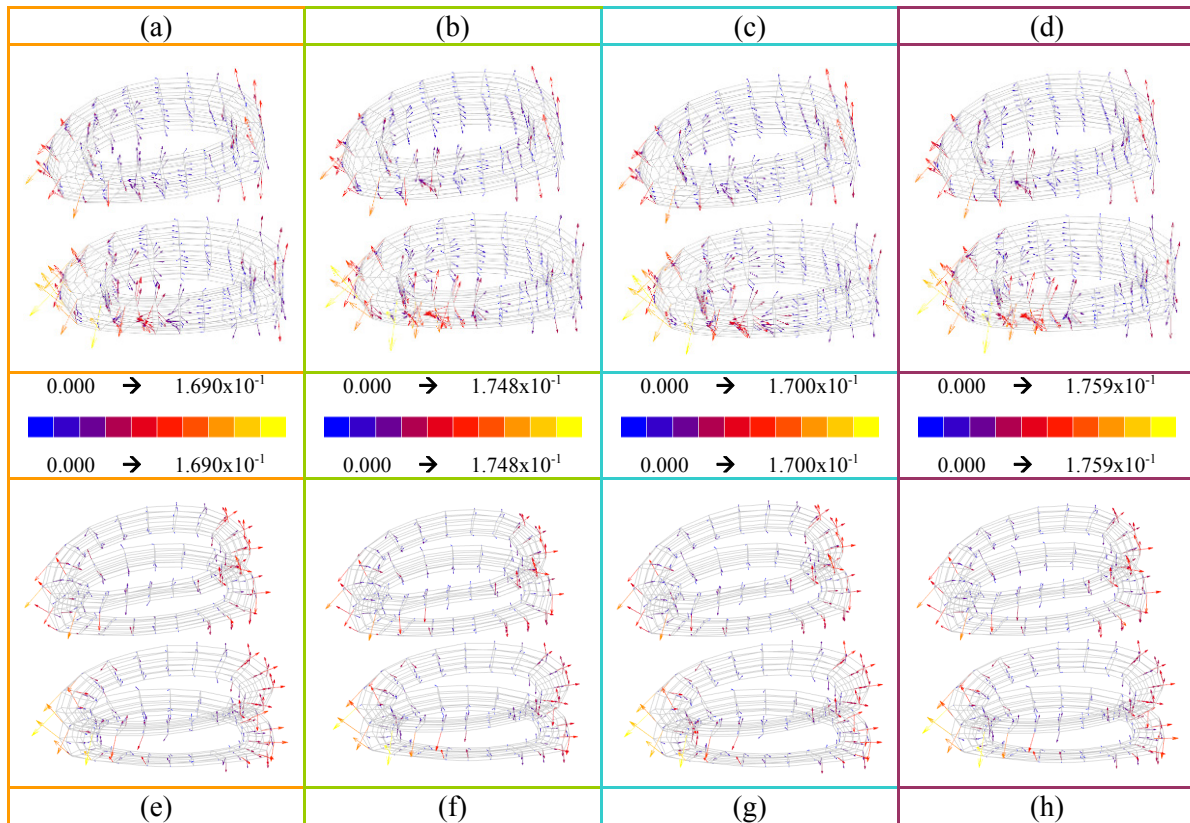


Figure 4.35: Total shear strain directions and extreme values in the L3-L4 and L4-L5 annulus matrices of the RAD (a, e), TAN (b, f), ISO (c, g), and ANI (d, h) models under lateral bending. The elements sharing nodes with the surrounding cartilage and bony endplates are represented in pictures e, f, g, h and excluded from pictures a, b, c, d.

f. Axial rotation

Figure 4.36 shows that under axial rotation, annulus matrix mean total shear strain decreased from the anterior to the posterior annulus. The RAD model generally led to the least mean shear deformations, except in the L3-L4 posterior annulus where the lowest mean shear strain value was computed in the TAN model. At the L3-L4 level, predicted lateral mean shear strain was significantly lower with the ISO collagen network than with, either the TAN, or the ANI modelled networks. Conversely, in the anterior annulus, ISO model led to the largest L3-L4 shear level.

At the L4-L5 level, in the anterior quadrant, the ANI model returned the highest matrix mean shear strain value. In the lateral quadrants, the differences found between models were fairly similar to the L3-L4 level. In the L4-L5 postero-lateral quadrants, the ISO model led to a mean strain level almost as low as that predicted for the RAD model. In the posterior annulus, except for the ANI model, all the predicted mean shear deformations were equivalent. The ANI model was associated with the highest mean matrix shear deformations in almost all the studied annulus tangential sectors.

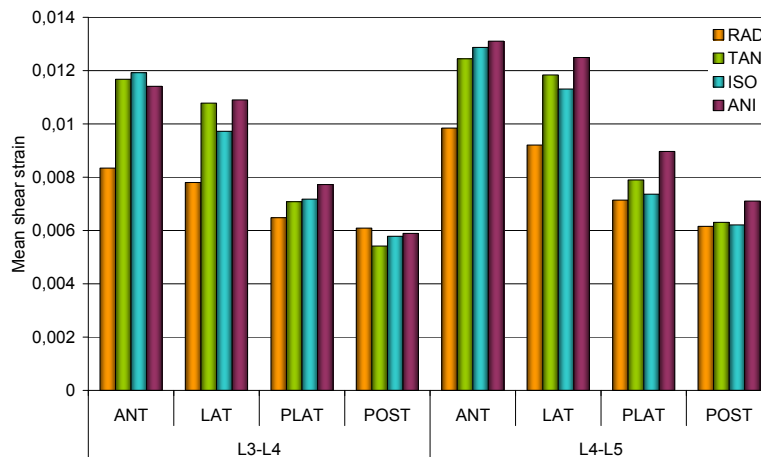


Figure 4.36: Annulus matrix mean total shear strains computed over all the nodes of each tangential sector under axial rotation.

For all models, outer shear strain vectors oriented progressively along the transverse plane from the anterior to the lateral annulus (Fig. 4.37a,b,c,d). Inner strain vectors in the anterior annulus were oblique and pointed toward the annulus mid-transverse plane. In the rotation side lateral quadrant, inner shear strain vectors were almost parallel between each other and oblique with respect to the annulus transverse plane. To the anti-rotation side, inner lateral vectors tended to point toward the mid-transversal plane, similarly as in the anterior annulus. These strains were however nearly insignificant at the L3-L4 level. In both segments of the lumbar spine model, inner total shear strains in the anti-rotation side annulus became progressively fully axial, from the lateral to the postero-lateral and posterior quadrants. While at the L3-L4

level, inner total shear components were generally larger to the anti-rotation side, at the L4-L5 level, they were greater to the rotation side. In the L3-L4 outer postero-lateral annulus there were no great differences in magnitude between rotation and anti-rotation side shear strains. Orientations appeared however opposite. At the L4-L5 level, outer postero-lateral shear strain levels were always lower to the anti-rotation side than to the rotation side.

At the L3-L4 level, in relation to outer strains, inner anterior strains were larger with the ISO fibre arrangement (Fig. 4.37c) than with the other modelled annulus anisotropies. In proportion to other annulus matrix shear strain components, the axial shear total strain vectors of the inner posterior annulus were larger in the RAD model (Fig. 4.37a) than in the other models. In the RAD deformed geometry, a minor general contribution of the external anterior and rotation side lateral shear strains was also found. However, to the anti-rotation side, a large amount of shear deformations was predicted at the nodes between the lateral and the anterior quadrants of the RAD and ISO models.

At the L4-L5 level, similarly as in the L3-L4 annulus, less relative amount of outer total shear strains were computed in the outer anterior, posterior, and anti-rotation side lateral quadrants, of the RAD model than in the corresponding quadrants of the other models. In the anti-rotation side inner lateral quadrant, the most transversal shear strain vectors were found in the ISO and in the RAD annuli. In the RAD model, shear strains in the rotation side inner lateral annulus were generally more concentrated at the transition with the postero-lateral annulus than with the anterior annulus. Inversely, in the other models, rotation side inner shear strain components were greater at the limit between the lateral and anterior annulus and even represented large peak strains.

For all models, annulus matrix peak total shear strains were higher at the attachment with the adjacent endplates than in the rest of the ground substance (Fig. 4.37e,f,g,h). At the L3-L4 level and in the upper annulus, largest concentration of axial shear strains was present in the rotation side lateral annulus and in the adjacent lateral part of the anterior annulus. In the lower annulus, results were similar, but to the anti-rotation side. At the L4-L5 level, anterior axial strain vectors in the upper annulus were fairly low in proportion to those found in the rotation side lateral quadrant. In the lower anterior annulus, axial total shear strains components predicted toward the anti-rotation side tended to be larger than in the lateral quadrant. Transversal shear components generally pointed in the anterior direction and were mainly present to the anti-rotation side parts of the lower anterior annuli.

Compared to the other models, the RAD and the ISO models tended to have a larger relative amount of transversal shear components in the upper L3-L4 and lower L4-L5 posterior quadrants (Fig. 4.37e,g). At the L3-L4 level, the relative amount of anterior total shear strains in the RAD configuration was less important than in the other models. In the L4-L5 annulus, the ANI model presented very large transversal shear strain components between the upper parts of the rotation side, lateral and postero-lateral quadrants (Fig 4.37h).

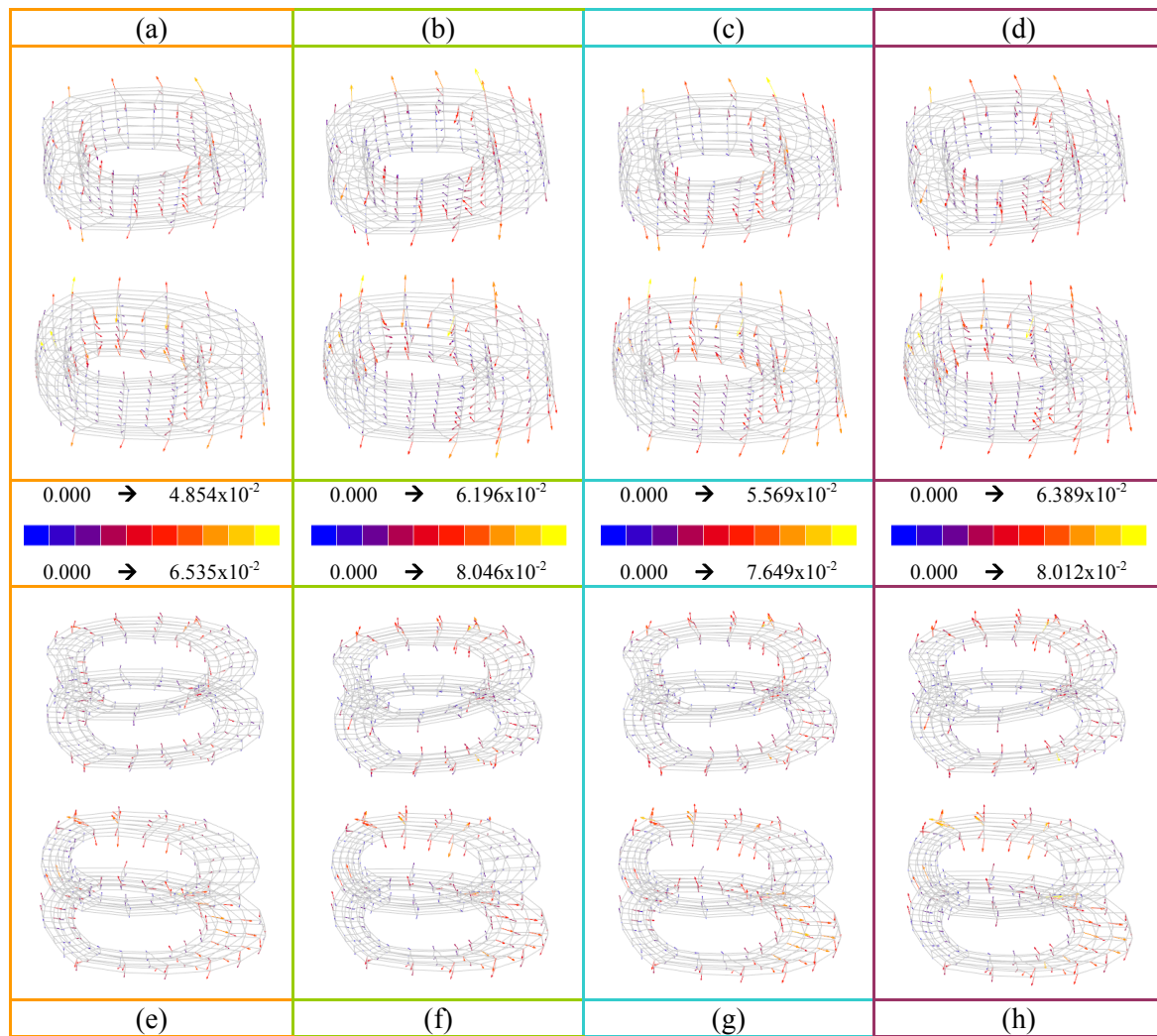


Figure 4.37: Total shear strain directions and extreme values in the L3-L4 and L4-L5 annulus matrices of the RAD (a, e), TAN (b, f), ISO (c, g), and ANI (d, h) models under axial rotation. The elements sharing nodes with the surrounding cartilage and bony endplates are represented in pictures e, f, g, h and excluded from pictures a, b, c, d.

D. Discussion

I. Model verification

a. *Nucleus pulposus constitutive behaviour*

The hyperelastic formulation for the nucleus pulposus could not represent the characteristic hydrostatic behaviour of the tissue under axial compression. In contrast, the poroelastic model led to intradiscal stress profiles similar to the experimental ones but magnitudes of the nuclear pressures diverged from the reported measurements as the compressive force increased from 500N to 2000N. In fact, due to the electrostatic repulsions between the negatively charged proteoglycans, the solid matrix could have been better modelled as non-linear elastic. Although the linearity of the Biot model may then represent a limiting factor for the mechanical description of the nucleus, the formulation still resulted more accurate than hyperelasticity to describe the load transfers from the nucleus to the annulus fibrosus. Differences between retrieved measurements and model predictions could also come from the fact that in the protocol used by McNally and Adams (McNally and Adams, 1992), the posterior bony elements were also embedded and attached to the loading jig, while the simulated compressive follower force was only applied on the superior endplate of L3. Moreover, standard deviations relative to the intradiscal pressure measurements was not reported in the cited experimental papers (McNally and Adams, 1992; Adams *et al.*, 1996; Adams and Dolan, 1995). Thus, given the large experimental errors found in recent works using similar pressure transducers (Heuer *et al.*, 2007a), the difference between the reported measurements and the predictions given by the models could be considered as minimal, especially bellow 1000N, where the compressive forces of interest for this Chapter were.

b. *Intersegmental rotations*

1) *7.5N.m rotational moments*

At 7.5N.m, the predicted intersegmental rotations for the different anisotropy models were generally within the experimental errors, except for the L4-L5 sagittal rotations. When comparing the RAD model to the New Geometry model of Chapter 3, sagittal rotations were systematically higher in the RAD model. Thus, the L3-L4 intersegmental rotation of the RAD model was in better agreement with the experimental data for than the L3-L4 intersegmental rotations returned by the New Geometry model. However, at the L4-L5 level, predictions performed with the RAD model went out of the experimental range. If the flexion and extension component of the overall sagittal range of motion are independently considered, the relative differences between the RAD and the New Geometry models result to be about 30% under flexion and 20% under extension. Sagittal flexion accounted then for most of the softening induced when transforming the New Geometry model into the RAD model. Capsular ligaments and annulus fibrosus were identified as the major resisting

component under flexion (Chap. 2). In both the New Geometry and the RAD model, capsular ligaments and annulus collagen network remained similar and cannot explain the differences. However, the large compression involved on the thick anterior annulus during flexion strongly suggests that the change of annulus matrix material properties was most likely responsible for the higher compliance of the RAD motion segments. Sagittal extension intersegmental motions were found to be mainly influenced by the facet joints and the nucleus pulposus (Chap. 3). However, since the geometry of the facet joints remained similar in the New Geometry and in the RAD model, the different nucleus pulposus formulations were most likely responsible for the different simulated behaviours of the two models under extension.

Under lateral bending, a similar comparison as under flexion-extension was done between the RAD, the New Geometry model, and the experimental at 7.5N.m. In the New Geometry model, the nucleus pulposus was also shown to play a major role in resisting the motion (Chap. 3). The new poroelastic formulation might be then mainly responsible for the higher rotations obtained in the RAD model. The difference of behaviour between the New Geometry and the RAD model was then logically smaller under lateral bending than under flexion-extension where both the nucleus and the annulus material property changes altered the prediction of the intersegmental rotations. Compared to the L3-L4 rotations, the larger relative differences in L4-L5 rotations existing between the predictions of the RAD model and the experimental ranges of motions under lateral bending and extension are coherent with the hypothesis that the poroelastic nucleus pulposus may have a non-linear behaviour that Biot's linear theory cannot reproduce.

Unlike under sagittal rotations or lateral bending, under axial rotation, the L3-L4 segment of the RAD model appeared stiffer than that of the New Geometry model, and no differences were found between both models at the L4-L5 level. A closer look on the results confirmed however the hypothesis about the influence of the poroelastic nucleus pulposus performed in the context of flexion-extension and lateral bending. In fact, as shown in Chapters 2 and 3, the major resistance to the axial rotation motion is provided by the zygapophysial joint contact and by the nucleus pulposus through a coordinated load transfer to the annulus. In Chapter 2, tensile stresses in the annulus under axial rotation were shown to be mainly due to the oriented collagen bundles. Thus, since both annulus collagen network and zygapophysial joint geometry were similar in the RAD and in the New Geometry model, higher stiffness of the RAD model at the L3-L4 level may be explained by differences in nucleus modelling. As shown in Chapter 2, axial rotation involves both an axial compression of the nucleus pulposus and coupled flexion-like segmental motion that tends to discharge the posterior facets (Chap 3). Taking into account that under axial compression, the poroelastic nucleus led to larger axial deformations, but smaller coupled flexions than the hyperelastic nucleus did, it can be deduced that under axial rotation, the poroelastic nucleus pulposus of the RAD model allowed a greater role of the zygapophysial joints than the hyperelastic nucleus of the New Geometry model did. This would explain that axial rotation simulations predicted a higher L3-L4 segment stiffness for the RAD model than for the New Geometry model. At the L4-L5 level, according to Chapter 3, the role of the nucleus pulposus would be less important than at the L3-L4 level. The similar behaviour of the

RAD and the New Geometry models was then most likely due to similar modelling of the annulus collagen network and zygapophysial contact geometry.

2) 10N.m rotational moments

Under 10N.m rotational moments, computed ranges of motions at the L3-L4 level were significantly lower than the experimental ones, but the higher predicted L4-L5 rotations resulted closer to the reported experimental data. Curiously, comparisons between experimental and predicted motions at 10N.m were opposite to the results obtained at 7.5N.m, where best fits were found at the L3-L4 level. At 7.5N.m, the soft linear poroelastic nucleus pulposus was suspected to underestimate the stiffness of the more strained L4-L5 segment. However, if the typical S-shape stress-strain curve found for soft tissues (Chap. 2) is considered, the linearity of the nucleus model could also explain significant stiffness overestimations at intermediate strains. The implication of the nucleus pulposus modelling is strongly suggested by the fact that the overestimation of the L3-L4 stiffness at 10N.m was common to all the simulated motions. Capsular ligaments were also shown to play an important role in every simulated motion (Chap. 3) and the non-linearity of their behaviour could also be matter of investigation. Nevertheless, the experimental data retrieved from Yamamoto et al (Yamamoto *et al.*, 1989) were acquired from L1-S1 spine segments subjected to pure moments applied on the top of L1. Although, such protocol should theoretically produce uniform loading on each motion segment, eccentric axial compressive loads caused by friction and moments of inertia, either within the loading device, or within the specimens it selves, cannot be excluded. Thus, bending moments that would change in an undefined manner as the specimen starts to deform may appear (Kettler *et al.*, 2000), and while at 7.5N.m, numerical and experimental results could be quantitatively interpreted, at 10N.m, only a qualitative analysis can be performed.

II. Annulus fibre-induced anisotropy

a. Intersegmental rotations

Both at 7.5N.m and 10N.m, the most significant differences between the different annulus anisotropy models appeared at the L4-L5 level. Due to the larger dimensions of the L4-L5 intervertebral disc, tissue deformations are greater at the L4-L5 level than at the L3-L4 level. Thus, increased recruitment of the L4-L5 annulus fibres was generally computed, and larger influence of the collagen network organization was found at the L4-L5 level than at the L3-L4 level.

Under axial rotation and lateral bending, differences in stiffness between the L4-L5 segments of the different model were almost preserved from 7.5N.m to 10N.m. However, under flexion-extension, the relative L4-L5 stiffness given by the different models at 7.5N.m differed from those found at 10N.m. As stated in § D.I.b, flexion-extension motion was most likely controlled by the resistance of the anterior annulus to

the local compression associated to the flexion motion. According to this, differences in L4-L5 stiffness given by the different models under 7.5N.m flexion-extension corresponded mainly to the differences in stiffness found in flexion. Stiffest segments under flexion-extension had both the highest anterior RMS and outer fibre stress values under flexion. This confirmed the anterior localization of the main resistance to motion, including the importance of the outer fibres. Loads predicted in the anterior outer fibres were also positively correlated with the transversal orientation of the fibres. Thus, while at 7.5N.m, axial compressive deformations of the annulus fibrosus mainly governed L4-L5 flexion-extension motions through the major activation of the transversal anterior outer fibres, at 10N.m, results suggest a different mechanism. Under such load level, deformations and internal disc pressure was so large that fibre recruitment became more homogeneous across the anterior annulus thickness. Since the TAN and the ANI models had similar mean fibre orientations from the outer to the inner annulus, their similar L4-L5 ranges of motion under 10N.m flexion-extension can be explained. Similar mechanism increased the contribution of the RAD model inner fibres at 10N.m when compared to the 7.5N.m load level. Since these 45° oriented fibres were the best oriented ones to resist postero-anterior shear deformations, their high activation explains the similar L4-L5 stiffness found for the RAD and for the TAN and ANI models, although the anterior outer fibres of the TAN and the ANI models were more transversal than those of the RAD model.

Under 7.5N.m flexion-extension, the key role of the L4-L5 anterior annulus outer transversal fibres is also in agreement with predictions performed in other annulus sectors. If the posterior areas of the annulus are considered, the fibres of the TAN model had slightly higher mean RMS values than the ANI model. The computed flexion-extension rotations showed however that the ANI model was slightly stiffer than the TAN model. In fact, under flexion, fibre mean stress values in the posterior and posterolateral annuli were positively correlated with the axial orientation of the fibres. However, while in the ANI model, the slightly more transversal outer posterior fibres allowed larger deformations of the posterior annulus than the TAN posterior fibres did, the highly transversal antagonist anterior fibres were more efficient than the anterior fibres of the TAN model to lock the flexion motion. In the ISO and RAD models, posterior outer fibres were so transversal that other components such as the capsular or longitudinal ligaments should have contributed to limit the motion (Chap. 2,3). These models offered then a resistance to motion comparable as in the ANI and TAN models. Mean fibre stress values in the RAD and in the ISO models showed that in these models, inner posterior annulus fibres played a substantial role in limiting the motion. Compared to the TAN and ANI models, inner fibres of the RAD and ISO models were probably activated by an increased backward nucleus pulposus mass migration due to a higher compliance of the outer posterior and anterior annulus layers. Since the 45° oriented fibres of the inner RAD annulus could better resist postero-anterior shear deformations than the 60° oriented fibres of the ISO model, the higher stiffness of the RAD model relative to that of the ISO model under flexion-extension is explained.

At the L3-L4 level, although differences between the different models were not as significant as at the L4-L5 level, the mechanisms of resistance to flexion described under 7.5N.m does not seem applicable. In fact, at this level, the zygapophysial joints contributed to resist the motion, but such point will be discussed in a later paragraph.

b. Intervertebral disc biomechanics

1) Axial compression (reduced model)

(i) General mechanisms and anterior annulus response

Under axial compression, according to the discussion of Paragraph D.II.b.1)(i), transversal orientation and stress bearing capacity of the annulus fibres were positively correlated in axially compressed annulus quadrants. Also, in all annulus tangential sectors but the posterior quadrant, FCQ values indicated that radial fibre orientation gradients led to the worst fibre contributions, mainly due to poor radial stress distributions. Actually, the direct axial compressive load and the intradiscal pressure acting on the annulus provoke a biaxial bending of the fibre layers. Nevertheless, for geometrical reasons, annulus layers are freer to expand laterally than axially, and their simulated axial compression- or intradiscal pressure-induced bending both gave place to a preferential activation of the transversal fibres. Such result was in accordance with early simulation results obtained by Shirazi-Adl (Shirazi-Adl, 1989). Then, inhomogeneous radial distribution of annulus fibre stress when collagen orientation radial gradients were modelled with axial inner fibres and transversal outer fibres becomes easily explainable. As inner axial layers are not able to resist the major annulus bending deformation component, transversal tangential strains are transmitted to the outer layers whose transversal fibres become highly activated. This transmission of transversal load might probably even more influent, as intradiscal pressure is high. Accordingly, in the anterior quadrant, the homogeneously and most transversally oriented fibre network of the TAN model led to both the highest FCQ and lowest annulus matrix mean total shear strain values. Conversely, the RAD fibre organization, with its most axially oriented inner fibres, induced a high stress concentration in the outer fibres that was predicted together with a high anterior annulus matrix mean shear strain value. Note that these mechanisms of fibre activation, based on strain differences in the axial and transversal directions of the annulus layers, should be probably influenced by the non-linear stress-strain behaviour of the modelled tissues.

(ii) Lateral annulus

In the lateral annulus, according to the absence of fibre orientation radial gradient, the ISO and the TAN models gave both the two highest FCQ parameter values and two lowest total mean shear strain values. Nevertheless, while the TAN FCQ parameter was higher than the ISO model one, mean total shear strain was found slightly lower in the ISO model. Annulus fibre stresses showed that this apparent contradiction was due to the fact that in the inner annulus, the more axial fibres of the TAN model were similarly activated as the somewhat more transversal fibres of the ISO model. However, in the outer annulus, the more transversal fibres of the ISO model were more able to resist outer annulus bulging than those of the TAN fibres. This conferred to the TAN model, a more homogenous fibre stress radial distribution than predicted in the ISO model, which resulted in a higher lateral FCQ value than in the ISO model. Nonetheless, in the TAN model, the high resistance that the anterior transversal fibre network provided can explain the activation of the adjacent lateral axial fibres. Such anterior fibre resistance in

the TAN model generated a slightly higher intradiscal pressure than in the ISO model, and transferred the transversal strains on the weaker lateral area. This was actually illustrated by the higher matrix shear strains predicted in the inner lateral quadrant of the TAN model when compared to the strains computed in the ISO model. And more generally, lateral mean total shear strain values finally indicated that according to their more transversal orientation, the lateral fibres of the ISO model stabilized better the lateral annulus than those of the TAN model. Also in agreement to the annulus deformation mechanisms discussed in the previous paragraph (§ D.II.b.1)(i)), both the lowest FCQ and highest mean total shear strain value were computed in the RAD model as a result of the axial inner fibres and fibre orientation radial gradient. Note however that the ANI model had similar lateral fibre orientations as the RAD model but returned better results. This was actually due to the extremely transversal outer fibres of the ANI model that stabilized better the anterior annulus than the fibres of the RAD model did. Due to the fibre orientation tangential gradient, this stabilization of the ANI anterior annulus probably contributed to raise the transversal strain level in the adjacent lateral fibre layers, which gave a higher lateral RMS value in the ANI model than in the RAD model. Moreover, as shown by the sagittal anterior and posterior axial displacements of L3, a flexion motion was coupled to the axial compression of the segment. This couple rotation was probably due to both facet joint contacts and posterior location of the nucleus pulposus within the intervertebral disc. Nonetheless, whatever its origin, the secondary motion appeared to be lower in the ANI model than in the RAD model. Anterior ANI fibre resistance most likely played a key role in limiting the coupled flexion, which could have been sufficient to also induce less shear strains in a lateral annulus that represents a transitional area for this coupled motion.

(iii) *Postero-lateral annulus*

In the postero-lateral quadrants, the fibres of the TAN model were sufficiently axial so that the differences between the TAN and the ISO models were clear both in terms of matrix shear strains and FCQ parameter value. According to the general fibre activation mechanism exposed in Paragraph D.II.b.1)(i), the transversal and homogeneously distributed postero-lateral fibres of the ISO model appeared then the best one to locally stabilize the annulus fibrosus quadrant. According to its axial fibres and the orientation radial gradient, the ANI model led to the worst postero-lateral FCQ value. However, the postero-lateral mean total shear strain value returned by the ANI model was slightly lower than that returned by the TAN model. Actually, axial compression in the posterior areas of the annulus fibrosus is limited by postero-lateral zygapophysial joint contacts. Therefore, the nucleus pressure exerting on the inner annulus was relatively more influent. Because the TAN model had more transversal fibres than the ANI model in the anterior and lateral inner annuli, nucleus pulposus was more mechanically confined in the TAN than in the ANI model. Thus, intradiscal pressure predicted in the TAN model was also larger than in the ANI model and could have contributed to produce the postero-lateral mean shear strain value computed in the TAN model. Nevertheless, besides the magnitude of nucleus pore pressure, the extremely transversal outer anterior fibres of the ANI model brought a large resistance to anterior axial annulus deformations and limited the associated coupled flexion more than any other anterior annulus fibre network. Coupled flexion tended to induce a

backward migration of the nucleus mass and since the motion was greater in the TAN than in the ANI model, the resulting pressure on the inner annulus wall was able to generate higher shear strain in the TAN than in the ANI postero-lateral annulus. Note that coupled motions were also associated with postero-anterior displacements of L3 that were around 7% lower in the ANI than in the TAN model. L3 translation should also have contributed to give a lower postero-lateral mean shear strain value in the ANI than in the TAN model.

(iv) *Posterior annulus*

Radial fibre stress distribution was generally more homogeneous in the posterior annulus than in the other quadrants. This was probably due to the small average thickness of the posterior lumbar annulus that naturally limited the deformation gradients between the inner and outer annulus. Nevertheless, the differences in RMS values between the different models were larger in the posterior annulus than in the other quadrants. This was most likely due to the backward migration of the nucleus mass that accentuated posterior annulus deformations and consequently, the response discrepancies between axially and transversally oriented fibres. According to predicted low local FCQ values and large posterior axial intersegmental displacements, the axial posterior fibres of the TAN and the ANI models were generally not optimal to stabilize the posterior annulus. Nevertheless, comparing both models, the ANI model led to a significantly higher posterior FCQ value than the TAN model did. Such outcome was mainly due to a low posterior RSD parameter value computed in the ANI model, as a result of a local drop of fibre stress in the most outer layer. Actually, facet joints locked the axial deformation of the posterior annulus, which locally limited the transversal reorientation of the fibres. The axial inner fibres of the ANI posterior quadrant were then almost uniquely activated by the axial in-sagittal plane fibre layer bending. Transfer of sagittal tensile strain from the inner to the outer layers was drastically reduced, and stress drop in the outer layers came from the fact that fibres were not transversal enough to be loaded by the layer transversal deformation component. Nevertheless, in the posterior annulus, although, the ANI FCQ value was not the lowest one, unlike in the postero-lateral annulus, the extreme axial orientation of the inner ANI fibres led to the largest posterior mean shear strain value, independently of any possible protection from the anterior annulus. Basically, while rest of the posterior FCQ values tended to confirm that transversal fibres were more efficient than axial fibres in stabilizing the posterior annulus, mean shear strain values completed the analysis by discriminating models with fibre orientation radial gradients. Thus, the ISO collagen network model appeared to have the largest stabilizing effect on the posterior quadrant. Nonetheless, the differences between the posterior mean shear strain values computed in the different models were fairly low. Such outcome came probably from the fact that in the ANI and TAN models, the low posterior stabilization provided by axial posterior fibres, together with the high resistance provided by transversal anterior fibres, induced lower coupled flexions than in the RAD and ISO models. As a consequence, in the ANI and TAN models, low relative amount of postero-anterior shear strain were found at the boundary between intervertebral disc and endplates, which probably limited the computed posterior mean total shear strain values.

2) *Sagittal flexion*

(i) *Anterior annulus*

Both at the L3-L4 and at the L4-L5 levels, largest anterior FCQ parameters were found for the TAN and the ISO model. The high FCQ value predicted by the TAN model supports the discussion established in Paragraph D.II.a about the effect of annulus anisotropy on intersegmental rotation. Nevertheless, the fact that the ISO model returned an even higher parameter value was quite unexpected. The high ISO FCQ parameter was however mainly due to a very low RSD parameter, and both the low mean fibre stress magnitude and high anterior and posterior matrix shear strains indicate that anterior fibre stress distribution resulted from a lack of fibre involvement in resisting the motion. As under axial compression, because of their poor radial fibre stress distribution, the ANI and the RAD model led to very low anterior FCQ parameter values. In the case of the RAD model, such result was in accordance with the annulus matrix total shear strains that were the highest ones. In change, the mean total shear strain value calculated in the ANI anterior annulus matrix was the lowest one, which contradicts the FCQ results. As stated in Paragraph D.II.a,b., the transversal orientation of the anterior outer fibre layer of the ANI model was particularly efficient to resist both anterior disc bulging and the overall intervertebral disc axial deformation. Nonetheless, as illustrated by the high anterior RSD value, the radial gradient of the ANI fibre orientations made the outer fibre layers to be highly stressed in comparison to the inner ones. This large outer stress concentration limited the shear deformations of the anterior annulus matrix but did not correspond to the expected role of the annulus fibres, i.e. to redistribute stresses within the fibrocartilage. The absence of fibre orientation radial gradient in the TAN model made the anterior annulus collagen network to be best adapted to both limit anterior intervertebral disc deformations and avoid any stress concentrations in the composite structure.

(ii) *Lateral annulus*

In the TAN model, the presence of anterior fibre transversal orientation and tangential fibre orientation gradient was beneficial to the fibre activation and radial stress distribution within the lateral annulus quadrant. The ANI configuration accounted for a similar fibre orientation tangential gradient as the TAN model. But in the ANI model, fibre orientation radial gradient made the disc bulging, found in the anterior part of the lateral annulus, to favour stress concentrations within the lateral outer fibre layers. Therefore, at both L3-L4 and L4-L5 levels, both the RSD and the FCQ parameters resulted worse for the ANI model than for the TAN model. In the RAD model, in contrast to the predictions performed for the anterior annulus, FCQ results suggested that the fibres of the lateral quadrants seemed fairly efficient to support and distribute annulus loads. However, lateral annulus matrix total shear strains remained the highest ones in the RAD model, which should be due to the low ability of the axial inner fibres to resist the lateral expansion imposed by the axial compression of the anterior incompressible annulus. Although the inner lateral fibres of the ANI model had similar orientation as those of the RAD model, in the ANI model, annulus matrix lateral deformations could be limited, as the transversal outer fibres of the anterior quadrant

were able to restrict disc bulging in the overall anterior annulus. Actually, the large resistance offered by the anterior and lateral external fibres of the ANI model explains why the associated matrix shear strains were reasonable and similar to those computed in the TAN model, even if the lateral FCQ parameters of the TAN model were significantly greater than those of the ANI model.

Despite a worse lateral fibre stress radial distribution and a lower related FCQ value than in the other models, the lateral mean total shear strain value in the L3-L4 annulus of the ISO model was the lowest one. In fact, the major transversal orientation of the lateral total shear strain vectors showed the importance of the annulus lateral expansion. The low mean total shear strain value given in the L3-L4 ISO lateral annulus matrix was then probably due to a more transversal mean orientation of the ISO lateral fibres when compared to the other models. At the L4-L5 level, where anterior and posterior annulus axial strains were the largest, lateral shear solicitations became less transversal and the TAN and ANI configurations gave reduced lateral mean total shear strain values.

(iii) Postero-lateral and posterior annulus

In the postero-lateral annulus, the differences in FCQ values observed between the L3-L4 and the L4-L5 annuli of the TAN, ISO, and ANI models were probably due to the difference in size between the L3-L4 and L4-L5 intervertebral discs. In the L3-L4 postero-lateral outer and mid annulus, the most axial fibres of the TAN model were the most able to resist local annulus matrix deformations. They induced stress levels similar as in the highly stressed inner annulus and allowed the TAN model to have the largest L3-L4 postero-lateral FCQ parameter value. In the inner annulus where both motion induced axial deformations and nucleus induced transversal deformations were present, few fibre stress differences were predicted between the TAN, ISO, and ANI models.

At the L4-L5 level, because of the greater intervertebral disc size than at the L3-L4 level, axial strains were sufficiently large so that differences in fibre orientation had a significant influence on the inner fibre stresses of the postero-lateral annulus. At this location, the most vertical fibres of the ANI model bore a maximum amount of stress. In the outer L4-L5 postero-lateral annulus, axial fibres were also preferentially activated, and largest loading was found in the TAN model. However, thanks to the radial orientation gradient, the more transversal outer fibres of the ANI model could reorient before being stretched, and unlike the TAN fibres, they were at the L4-L5 level, more similarly stressed as the inner fibres. This induced in the ANI model a lower postero-lateral L4-L5 RSD parameter and a higher FCQ parameter than in the TAN model. Although the annulus fibre radial orientation gradient modelled in the ANI model was beneficial for a homogeneous fibre contribution through the L4-L5 postero-lateral and posterior annulus thicknesses, it was associated to a slightly higher postero-lateral mean total shear strain value than in the TAN model. In the ANI model, the presence of transversal shear strain vector components at the attachment points of the annulus with the adjacent endplates suggests that this higher L4-L5 postero-lateral mean total shear strain value is most likely due to a more compliant outer annulus, when compared to the inner annulus. Nonetheless, together with the TAN model, the ANI model still had

significant lower postero-lateral shear strains than the RAD and the ISO models. Note that unlike at the L3-L4 level, the L4-L5 postero-lateral mean total shear strain value computed in the RAD model was significantly higher than that computed in the ISO model. This was basically due to the fact that while the inner axial fibres of the RAD model could locally limit the L4-L5 postero-lateral annulus deformations, outer fibres were too transversal to be activated and let the L4-L5 outer annulus to be affected by a large axial stretch.

As in the L4-L5 postero-lateral annulus, the high posterior FCQ values given by the ANI model are explained by the radial orientation gradient of the model fibres. Reorienting outer fibres led to low RSD values, while they were sufficiently axial to resist as much as possible the axial deformations. Curiously, at the L3-L4 level, despite their considerable horizontal orientation, the postero-lateral and posterior inner fibres of the ISO model were nearly as stressed as those of the ANI and TAN models. In fact, as discussed in Paragraph D.II.a., range of motion was so large in the ISO model that the pressure exercised on the inner annulus wall by the nucleus mass backward migration is large enough to activate the transversal collagen fibres. At the L4-L5 level, because the large anterior annulus bore most of the compressive load, and because of the high level of posterior deformations, nucleus migration was probably not as influential as at the L3-L4 level and axial deformations of the postero-lateral and posterior quadrants were the main fibre activation factor. This explains why the inner fibres of the ISO model just reoriented without being able to bear as much stress as the fibres of the other models. However, the lack of fibre stress across the whole posterior and postero-lateral ISO annuli induced low RSD parameter values and resulted in FCQ parameters as high as, or even higher than those predicted for the TAN model. As expected, mean total shear strain values and total shear strain vectors showed, however, that the ISO configuration was noteworthy less able to stabilize the L4-L5 posterior annulus areas than the TAN configuration was.

In the postero-lateral and posterior annulus quadrants, the RAD model, where the outer fibres were similarly oriented as those of the ISO model, allowed large axial deformability of the posterior annulus areas. In the inner annulus layers, additional pressure, exerted nucleus pulposus on the internal annulus wall, induced then a biaxial strain state that the 45° oriented fibres of the RAD model were particularly able to resist to. This explains why the inner posterior and postero-lateral fibres of the RAD model were always the most loaded ones. At the L3-L4 level, the effect of the nucleus pulposus in the postero-lateral and posterior annuli of RAD and ISO models was also illustrated by the major total shear strain transversal components at the attachment points between the intervertebral discs and the adjacent bony endplates.

3) *Sagittal extension*

(i) *Anterior annulus*

Like under flexion, under extension, the absence of fibre orientation radial gradient in the L3-L4 and in the L4-L5 anterior annuli appeared beneficial for a better

load distribution across the annulus thickness. In fact, as the inner posterior annulus under sagittal flexion, the inner anterior annulus under extension was probably under the influence of a combined loading issued from both the motion-imposed axial stretching and the additional transversal stretch resulting from the nucleus pulposus anterior mass migration. This was strongly suggested by the high stress levels found in the anterior inner fibres of the RAD and ANI models, whose orientations were the closest ones to 45° , the preferred stretch direction generated by a biaxial sollicitation. Note that effect of nucleus mass migration identified under sagittal flexion and extension was in agreement with both magnetic resonance and radiographic observation performed in vitro on deforming osteoligamentous lumbar spine specimens (Fennell *et al.*, 1996; Tsantrizos *et al.*, 2005). Thus, high activation of the inner fibres explains why in the RAD and ANI models, the RSD parameters were so large and led to significantly lower FCQ parameters than those given by the models without radial fibre orientation gradients. A comparison of the similarly oriented outer anterior fibres of the ISO and the RAD models suggests that the high activation of the inner fibres in the RAD model actually shielded the action of the outer fibres. As shown by the anterior mean total shear strain values, the 45° oriented fibres of the RAD model seemed effectively particularly efficient to locally limit annulus matrix deformations. The anterior fibres of the ANI model were more transversal than those of the RAD model and even less activated, which resulted in high anterior mean total shear strains. Likewise, when comparing the RMS parameters returned by the ISO and the TAN models, the more transversal fibres of the TAN model appeared significantly less able to resist the anterior annulus axial stretching. Nevertheless, at the L3-L4 level, computed anterior mean total shear strain value was somewhat lower in the TAN model than in the ISO model. Annulus matrix anterior shear strain vectors in these two models led to think that such outcome was linked to the transversal deformations induced by the nucleus pulposus. Nonetheless, although the inner anterior fibres of the TAN model were more able than the ISO fibres to react to the nucleus influence, the ISO collagen network needed less reorientation than the TAN fibres to withstand anterior axial deformations. L3-L4 ISO fibres offered then a better compromise than the TAN fibres to resist the overall anterior annulus deformation.

In the anterior L4-L5 intervertebral disc, mechanisms of annulus fibre activation were similar to the L3-L4 level. Nonetheless, due to the larger dimensions and deformations of the L4-L5 intervertebral disc, the difference between the ISO model and the other anisotropy configurations in terms of FCQ parameter value was noteworthy greater at the L4-L5 level than at the L3-L4 level. In the TAN model, according to the larger L4-L5 mean total shear strain value than the L3-L4 one, the effect of axial stretch was most likely more important in the L4-L5 than in the L3-L4 intervertebral disc. Correspondingly, in all models, a larger reorientation of the L4-L5 anterior fibres induced higher RMS values and lower relative amounts of axial shear strain components at the L4-L5 level than at the L3-L4 level.

(ii) *Lateral annulus*

As in the anterior annulus, stresses predicted in the inner lateral fibres of the RAD and ANI models were significantly higher than for the other models. In the lateral

annulus, the inner fibres of the ANI model were oriented at 46° and led at both levels to FCQ parameters very similar as those given by the RAD model. However, unlike in the anterior annulus, the pressure exerted by the nucleus pulposus would be a priori low in the lateral annulus. Thus, such activation of fibres around 45° might not be due to the generation of a biaxial strain state. Actually, since the anterior annulus was largely axially deformed and the posterior annulus, axially compressed, the lateral annuli of all models was subjected to a major in-sagittal plane shear strain and a consequent oblique stretch component nearly oriented at 45° . Hence, the large mean total shear strain values found in the ANI model when compared to those returned by the RAD model were probably due to the fact that the more transversal anterior fibres of the ANI model allowed more anterior axial deformations and higher in-sagittal plane shear deformation than the fibres of the RAD model. According to this in-sagittal plane shear deformation mode of the lateral annulus, among the models without radial fibre orientation gradients, the TAN model, with lateral fibres closer to 45° than the lateral fibres of the ISO model, showed a greater ability to bear loads. Also the absence of radial orientation gradient in the ISO and TAN models led to a fairly good load distribution across the annulus thickness and confirms that the solicitation felt by the lateral annulus is mainly antero-posterior. Consequently, the highest L3-L4 FCQ parameter was predicted in the TAN model. Nevertheless, at both levels, highest mean total shear strain values were also found in the TAN model. This was logically due to the large axial deformations generally allowed in the anterior annulus of this model.

For all models, axial deformation of the L4-L5 anterior outer annulus was high enough to increase the relative activation of the L4-L5 lateral outer fibre layers. This allowed re-equilibrating the fibre stress distribution through the annulus thickness and led to higher FCQ values in the RAD and ANI models than in the ISO and TAN models. Although the ANI model had a high lateral L4-L5 FCQ parameter, only about 1% inferior to that of the RAD model, its mean total shear strain level was also nearly the highest one, just below that of the TAN model. In such a case, total shear strain vectors indicated the influence of the large anterior axial strains caused by the very transversal outer fibres of the ANI model.

(iii) Postero-lateral annulus

In the L3-L4 postero-lateral annulus, only slight differences in FCQ values were found between the different models. However, while in both the RAD and ANI models, FCQ values were limited by a non-homogeneous radial stress distribution, in the ISO model the FCQ limiting factor was the fibre stress bearing capacity. As shown by a FCQ parameter value somewhat higher than those given by the other models, the TAN model offered the best compromise between stress distribution and overall magnitude of the L3-L4 postero-lateral fibre. Nevertheless, while the inner annulus fibres of the TAN model had a similar orientation as those of the RAD model, the fibres of the RAD model were significantly more loaded. In fact, the major difference between the RAD and the other models was that the RAD model contained axially oriented inner fibres all around the annulus. Under sagittal extension, these fibres were the only ones to be able to resist the anterior intervertebral disc axial stretch. One consequence is the smaller range of motion found in the RAD model when compared to the other models. Another

consequence is that this reduced deformability of the RAD annulus provided a tight confinement of the enclosed nucleus pulposus, which led to a mean intradiscal pressure at least 156% superior in the RAD than in the other models. This explains the high L3-L4 postero-lateral fibre stresses computed in the inner RAD annulus when compared to the stresses found in the similarly oriented inner layers of the L3-L4 postero-lateral TAN annulus. The anterior annulus deformability also explains why the most axial inner postero-lateral fibres of the ANI model were the most activated ones, as if the main solicitation in the L3-L4 inner postero-lateral annulus layer would be axial stretching. The axial postero-lateral shear strains found in the ANI, TAN, and ISO models showed actually that the transversal mean fibre orientation angles in the anterior annuli of these models, allowed a greater opening angle of the intervertebral space and a more posterior centre of rotation than in the RAD model. According to this analysis, the RAD model was the only model to give L3-L4 postero-lateral total shear strain vectors typical of annulus bulging. Thus, the effect of fibre orientation in the L3-L4 postero-lateral quadrant strongly suggest that the FCQ parameter given by the TAN model cannot reflect the annulus stabilizing capacity of the model collagen network. This is actually in agreement with the high mean total shear strain value computed in the L3-L4 postero-lateral annulus matrix of the TAN model.

At the L4-L5 level, on one hand, annulus deformations were generally greater, and on the other hand, the thicker anterior annulus may have kept the intersegmental centre of rotation more forward than at the L3-L4 level. This most likely explains why in the L4-L5 intervertebral disc, posterior bulging became more significant than in the L3-L4 intervertebral disc, and why the most horizontal L4-L5 postero-lateral fibres were more able to resist the consequent lateral expansion of the postero-lateral annulus. On one hand, the transversal total shear strains in the posterior parts of the lateral annuli in each model gave an illustration of the above interpretation. On the other hand, large intervertebral disc deformations revealed transversal antero-posterior shear deformations at the attachment points between the posterior annulus and the adjacent endplates. These deformations, as shown by the fibre mean stress values, were more supported by the axial posterior fibres of the TAN and of the ANI model. Nonetheless both the RMS and the mean total shear strain values showed that the axial fibres were no able to resist the L4-L5 posterior annulus deformations as well as the more transversal fibres. The higher FCQ parameters given by the ANI and TAN models simply came from more favourable stress distributions due to less ability of the external fibres to resist the external lateral annulus expansion.

(iv) *Posterior annulus*

In the L3-L4 posterior annulus, as discussed for the postero-lateral annulus, since the RAD model was the only model to predict significant bulging, its fibres resulted logically noteworthy more stressed than those of the other models. However, the high difference of activation between the L3-L4 transversal outer and axial inner fibres of the RAD model, made the RAD posterior FCQ value to be not significantly different from the other L3-L4 FCQ parameter values. At this point, it can be hardly decided which fibre organisation model was the best, since the best results obtained in the L3-L4 posterior quadrant are linked to a lack of stabilization of the anterior annulus. However,

taking into account that a stabilized anterior annulus should lead to axial compression of the posterior quadrant, results obtained under axial compression suggest that local transversal fibres as those of the ISO model should be able to better stabilize the posterior annulus (§ D.II.b.1)). In comparison to the RAD configuration, an ISO posterior fibre organisation with stabilized anterior annulus would also avoid stress concentrations in the most inner layers.

At the L4-L5 level, posterior disc bulging was so important that the most transversal layers controlled the highest RMS values. Accordingly, the lower stress in the axial outer fibres of the TAN and ANI models gave both lower RSD and higher FCQ values than given by the RAD and ISO models. Mean total shear strain values showed however that such mathematical outcome was due to a lack of capacity from the TAN and ANI posterior fibres to stabilize the annulus. The transversal external fibres of the ISO configuration were somewhat more loaded than those of the TAN and ANI models, but led to a higher RSD parameter and a lower FCQ value.

4) Spinal erector-like loading

(i) Anterior annulus

Under pure sagittal extension, anterior annulus fibre activation was interpreted as partly controlled by the nucleus pulposus pressure that imposed a compromise between axially and transversally oriented collagen networks (§ D.II.b.3)). Under spinal erector-like loading, a combination of axial compression and sagittal extension did not qualitatively change fibre contributions with respect to pure extension alone, which confirmed this former relation between nucleus pulposus and fibre orientation. However, while under sagittal extension, lowest anterior mean total shear strain value was given by the RAD model, under combined loading the RAD model gave one of the highest anterior mean shear strains. Under spinal erector-like loading, mean shear strain differences found between the different models were actually fairly similar to those obtained under axial compression. Combining axial compression with sagittal extension actually increased the pressure exerted by the nucleus on the anterior annulus. Thus, although the very transversal anterior fibres of the TAN and ANI models were not able to limit the annulus axial deformations, they contributed greatly to limit the resulting transversal total shear strain components.

At the L3-L4 level, low differences of ranges of motion were found between the different models. Therefore, it seems that the influence of the nucleus pulposus on anterior transversal shear strains was predominant over axial stretching, which was probably due to the limitation of anterior axial strains by the follower compressive force. The TAN annulus configuration appeared then as fairly efficient. However, at the L4-L5 level, larger axial deformations than at the L3-L4 level, due to higher L4-L5 intervertebral discs, restored the importance for the anterior collagen network to resist axial stretches. In such a case, the ISO model might represent a better compromise than the TAN model.

(ii) Lateral annulus

In the L3-L4 lateral annulus, as under sagittal extension, the 45° and 46° oriented inner fibres of the RAD and ANI models were preferentially stretched and led to low FCQ parameters because of bad fibre stress radial distributions. However, the presence of the follower compressive load contributed to increase the activation of the peripheral transversal fibre layers of these two models. Therefore, their difference to the other models in terms of FCQ values was not as large as under sagittal extension. Also, the ISO and the TAN model annuli behaved more similarly under spinal erector-like loading than under sagittal extension, and both models showed that the load combination increased the tolerance on preferred orientations for fibre activation. On the contrary, the two models with fibre radial orientation gradients showed dissimilarities although their respective lateral collagen networks were fairly similar over the annulus thickness. Curiously, mean fibre stress resulted significantly lower in the ANI model than in the RAD model. This could be due to a lesser influence of the compressive load component in the lateral quadrant as a consequence of larger anterior axial deformations allowed by the anterior transversal fibres of the ANI collagen network. A higher concentration of the axial total shear strain vectors in the inner lateral annuli adjacent to transversal anterior collagen networks, compared to the inner lateral quadrants adjacent to axial anterior fibres supported such interpretation. Note that, as under sagittal extension, the 45° oriented fibres of the RAD model led to the lowest lateral L3-L4 mean total shear strain value. In the ANI L3-L4 lateral annulus, the poor resistance to anterior axial traction induced high lateral annulus matrix shear strains.

At the L4-L5 level, larger intervertebral disc dimensions and nucleus volume contributed to a larger activation of the external transversal fibre layers of the RAD and ANI models than at the L3-L4 level. The RSD parameters of these two models became then more favourable. The L4-L5 outer lateral fibres of the ANI model remained however less stressed than those of the other models, because of the limited compressive load effect induced by the larger anterior opening angle. This resulted in a significantly better radial fibre stress distribution for the ANI model than for the other lateral annulus configurations, and the ANI FCQ value was then maximal. Like under pure extension or axial compression, L4-L5 lateral mean total shear strain in the ANI model was however not minimal. The TAN model actually gave the minimum L4-L5 lateral mean shear strain value, although the corresponding TAN FCQ parameter value was the lowest one. As shown by the outer total shear strain vectors, the compression induced lateral bulging as well as the nucleus pressure had a lower impact on the L4-L5 lateral annulus of the TAN model than on the L4-L5 lateral quadrants of the other models. Such result probably came from the great rotational compliance of the TAN intervertebral disc allowed by the transversal anterior fibres and explains the low corresponding mean shear strain level. However, this evidently does not demonstrate the stabilizing effect of the TAN L4-L5 lateral fibres.

In the L4-L5 outer lateral annulus of the RAD model, importance of the total shear strain vectors tangent to axial annulus bulging indicate that the posterior axial compression due to the extension motion occurred in a more anterior location than in the other models. In other words, a more anterior centre of rotation may be induced in the RAD model. Such issue was actually already discussed in the case of pure sagittal

extension (§ D.II.b.3)), and was easily explained by the 45° oriented inner fibres of the RAD model that locked the axial opening of the anterior intervertebral disc space. Under spinal erector-like loading, such phenomenon made the lateral annulus deformations to be particularly influenced by the intradiscal pressure of the RAD model. As indicated by the results, intradiscal pressure generated higher shear strains in the L4-L5 lateral annulus quadrants of the RAD model than in the lateral annuli of the other models. In such context, rather than related to intradiscal pressure alone, high shear strains in the RAD L4-L5 lateral annulus were also probably due to axial inner fibres (§ D.II.b.1)(i)). However, as shown by the poor FCQ and shear strain results returned by the transversal fibres of the ISO model that were the farthest away from 45°, 45° oriented fibres, as in the inner RAD annulus, greatly contributed to limit axial strains. Thus, although in the RAD model, no compromise was achieved between resistance to both axial shear and high nucleus pressure, the RAD fibre configuration appeared fairly adequate to resist L4-L5 lateral annulus deformations in comparison to the other modelled collagen networks. Actually, the RAD model gave both the highest RMS and the second lowest RSD parameters. Although the lateral fibres of the RAD and the ANI models have similar orientations, the higher L4-L5 lateral FCQ value given by the ANI model was due to a lower activation of the outer fibres than in the RAD model. This could be directly related to limited nucleus-induced transversal annulus deformations in the ANI model, due to larger anterior annulus deformations and less nucleus confinement than in the RAD model.

(iii) *Postero-lateral and posterior annuli*

In the postero-lateral and posterior annuli, although the outer fibre layers of the RAD and ISO models had nearly the same orientation, the outer collagen network generally resulted significantly more stressed in the RAD model. Comparison of the RAD annulus postero-lateral and posterior total shear strain vectors, with the shear deformations predicted in the annuli of the other models, shows that the above outcome was due to a higher level of bulging in the RAD annulus posterior areas. This was in agreement with the presence of more anterior centre of rotation in the RAD motion segments, as suggested by the stress and strain calculations performed in the lateral annuli. At the L3-L4 level, the fibres of the RAD model were the most stressed ones over the whole annulus thickness. Even in the postero-lateral inner annulus, the 44° oriented fibres of the TAN model were largely less loaded than the 45° oriented fibres of the RAD model. Actually, in the L3-L4 intervertebral disc of the RAD model, locking of the sagittal rotation by the 45° oriented anterior inner fibres gave a mean intradiscal pressure at least 262% higher than in the other models. Such nucleus pressure, added to an extra posterior annulus compression related to the anterior centre of rotation, led, in the RAD model, to a large sollicitation of the postero-lateral and posterior quadrants with large mean total shear strains. In terms of fibre stress, the RAD RMS L3-L4 postero-lateral and posterior parameter values resulted the highest ones. Nonetheless, the relatively poor local activation of the ANI, ISO, and TAN collagen networks induced significantly lower RSD parameter values in these models than in the RAD model. Thus, despite a large activation of the RAD L3-L4 posterior and postero-lateral values, the corresponding FCQ parameter values were only somewhat higher than the ANI, ISO, and TAN model ones. Note, however, that this factor limiting the

magnitude of the L3-L5 postero-lateral and posterior RAD FCQ parameter values is in good agreement with the presence of both axial inner fibres and fibre orientation radial gradient, in annulus areas, where transversal and homogeneous fibre orientations would generally be preferable (§ D.II.b.1)(i),3)(iv)).

Actually, the ISO collagen network had the most transversal mean fibre orientation across the posterior and postero-lateral annulus thicknesses. It should then bring the major resistance to the local compressive deformations of the postero-lateral and posterior quadrants. At the L4-L5 level, this was verified by the low postero-lateral and posterior ISO mean shear strain values. Nevertheless, due to a lack of fibre radial stress distribution, the corresponding ISO FCQ values were not the highest ones. In fact, in the ISO model, anterior annulus axial opening allowed by the transversal anterior fibres, limited the L4-L5 intradiscal pressure and restricted the activation of the postero-lateral and posterior inner fibres, despite their transversal orientation. At the L3-L4 level, similar mechanism took place, but the low activation of both inner and outer postero-lateral and posterior ISO fibres suggested that posterior compressive loads related to the extension motion component were also limited. If postero-lateral and posterior axial fibres are considered, at both the L3-L4 and L4-L5 levels, according to the correlation between axially compressed annulus quadrants and transverse fibre activation, the TAN model returned extremely low RMS parameter values. In the L4-L5 postero-lateral and posterior annuli, TAN mean shear strain values were accordingly of the highest ones. However, at the L3-L4 level, the TAN postero-lateral and posterior mean total shear strain values were the lowest ones, when best results would have been expected to come from the ISO model. Predicted ranges of motion actually showed that the L3-L4 sagittal rotation also tended to be slightly lower in the TAN than in the ISO model. Moreover, at the L3-L4 level, the anterior transversal fibres of the TAN model were found to best stabilize an anterior annulus mainly influenced by the axial compression load case component. Sagittal rotation results suggest then that the activation of the TAN anterior fibres by local transversal annulus strains could have been sufficient to also limit anterior axial strains. Therefore, the low L3-L4 postero-lateral and posterior shear strains in the TAN could be explained by a low extension-related posterior compression component, antagonist to the extension-related anterior traction component. Such mechanism confirms then the efficiency of the anterior TAN fibre configuration, but does not demonstrate that the posterior and postero-lateral TAN collagen networks were locally better than the ISO network for annulus stabilization. Because of its fibre orientation radial gradient, the transversal anterior ANI network was not as efficient as the TAN configuration to stabilize the anterior annulus, but similar reasoning can explain why the ANI model gave almost similar FCQ and mean shear strain results as the ISO model in the L3-L4 postero-lateral and posterior annuli. In the L4-L5 postero-lateral and posterior quadrants, large activation of the outer fibre, relatively to the inner fibres, indicated, according to the results found in the anterior annulus, that the extension-related axial compression of the posterior annulus areas was significantly more influential than at the L3-L4 level. Hence, the shear strains found in the TAN and ANI models were higher than those computed in the ISO model. In the L4-L5 postero-lateral and posterior annulus quadrants, the high FCQ values given by the TAN model were basically due to low RSD parameter values motivated both by the inability of the TAN axial fibres to support axial compressive external loads, and by the homogeneity of the TAN fibre orientations through annulus thickness

5) *Lateral bending*

(i) *Anterior annulus*

Under lateral bending, thanks to their best radial stress distribution, the ISO and the TAN models had the highest FCQ values in the anterior annulus. Presence or absence of fibre orientation radial gradients in the anterior annulus led actually to two different types of local fibre stress radial distributions. In the annulus models with fibre orientation radial gradients, fibres closest to 45° were the most stressed, leading to think that anterior annulus response under lateral bending were most likely due to frontal axial shear deformations. Such deformations constant through the annulus thickness, would then explain that the best radial stress distributions were found without fibre orientation radial gradient. However, by comparing models without fibre orientation radial gradient, the inner annulus 66.5° oriented fibres of the TAN model were somewhat more stressed than the 60° oriented fibres of the ISO model. Actually, as suggested by the transversal inner total shear strain vectors, such result might be due to the effect of the nucleus pulposus transversal pressure on the inner wall of the annulus. These two anterior deformation modes, i.e. axial and transversal shear, were reflected by the more transversal inner shear vector found in the RAD and ANI models when compared to the TAN and ISO models. A comparison of the anterior inner fibre stresses with the anterior mean shear strain values shows that even if anterior fibres seemed to be mostly stressed by the axial frontal shear annulus deformation, the anterior annulus shear state depended more on whether fibres were able to resist nucleus induced transverse strains. In this sense the 55° oriented inner fibres of the ANI model seemed to represent a better compromise than the 45° oriented inner fibres of the RAD model.

At the L3-L4 level, anterior outer fibres were similarly stressed in the ISO and in the TAN collagen networks. However, in the inner layers, nucleus pressure induced higher stresses in the more transversal collagen network of the TAN model than in that of the ISO model. This resulted in a higher RSD parameter and a lower FCQ value in the TAN than in the ISO model, even if the TAN mean total shear strains were lower. At the L4-L5 level, because of larger deformations than at the L3-L4 level, the outer fibres of the ISO model, closer to 45° than those of the TAN model, resulted more stressed. The anterior radial stress distribution in the L4-L5 ISO collagen network was then negatively affected, and comparatively, the TAN anterior annulus organization gave a more favourable FCQ parameter. Nevertheless, independently on the FCQ values, and for all models, mean total shear strains predicted at both levels strongly suggest that nucleus pressure was the most influent load, determining the most suitable fibre orientation, i.e. transversal, to stabilize the anterior annulus.

(ii) *Lateral annulus*

Since under lateral bending, fibre stresses were averaged over the rotation and the anti-rotation sides, the following discussion assumes then that fibres have to be efficient to resist both rotation side axial compression and anti-rotation side axial stretching. Then, at the L3-L4 level, the TAN model led to very similar FCQ values as the RAD and the ANI models, even if in the TAN model, the lateral collagen network was

activated differently from the two other models. Study of the fibre orientations suggests that the less transversally oriented lateral fibres of the TAN model could be activated both by a reorientation in the axial direction to the anti-rotation side, and by a transversal alignment to the rotation side. This dual efficiency of the TAN annulus configuration at the L3-L4 level was supported by the calculation of a lower L3-L4 lateral mean total shear strain value than in the other models. In the lateral RAD and ISO annuli, computed low outer fibre stress, high total shear strain mean values, and axial outer vector components, suggest that external lateral fibres oriented around 60° were not able to reorient sufficiently to stabilise the axially stretched anti-rotation side lateral quadrant. According to their similar lateral fibre orientations, the RAD and the ANI models gave similar L3-L4 lateral FCQ values. Predicted mean total shear strain appeared however somewhat lower in the ANI lateral annulus. The load transfer from the anterior to the rotation side lateral annulus can actually explain this shear strain difference between the RAD and the ANI model. In the L3-L4 anterior annulus of the RAD model, outer total shear strain vectors already indicated a beginning of anterior annulus bulging. However, in the ANI model, the more transversal anterior fibres limited such deformation. Therefore, the amount of strain transmitted to the rotation side lateral annulus due to the anterior expansion of the anterior quadrant was much more significant in the RAD model than in the ANI model.

At the L4-L5 level, larger annulus deformations than at the L3-L4 level increased the activation of the outer fibre layers of the TAN and the ISO models, both to the rotation and to the anti-rotation sides. However, this activation was larger in the outer fibres than in the inner ones, so that the TAN and the ISO models also led to significantly higher RSD parameters than at the L3-L4 level. In the RAD and ANI models, outer fibre stretch was more important as well, but unlike in the ISO and TAN models, this allowed equilibrating outer and inner fibre stresses and led to L4-L5 RSD parameters lower than the L3-L4 ones. The drastic change in FCQ values when passing from the L3-L4 to the L4-L5 level is then explained. Nonetheless, although the TAN model gave an insignificant L4-L5 lateral FCQ value, as at the L3-L4 level, the balanced action of its outer lateral fibres over the rotation and anti-rotation sides led to the least L4-L5 mean total shear strains level. High L4-L5 lateral mean total shear strain values in the ANI and RAD models indicate that despite high FCQ values, fibre orientation radial gradient might not lead to the best configurations to stabilize the L4-L5 lateral annulus under lateral bending. The lowest total shear strain peak values given by the RAD model were probably due to the presence of 45° oriented fibres in the inner anterior and posterior annuli of the model, where frontal axial shear deformations were maximal. Nevertheless, L4-L5 ranges of motion calculated in the RAD and ANI models suggest that the combined action of both axial inner fibres to the anti-rotation side, and transversal outer fibres to the rotation side, significantly contributed to limit L4-L5 motion, which was not the case with only transversal fibres as in the ISO model.

(iii) Postero-lateral annulus

In the postero-lateral annuli, rotation side quadrants were still fairly axially compressed, while the anti-rotation side quadrants were rather axially stretched. In such a case, both the external and internal fibre mean stresses given by the different models

showed that fibre stresses were mostly controlled by the axially oriented anti-rotation side fibres. Thus, at both levels, the TAN and ANI models, that had the most axial postero-lateral fibres, presented the highest RMS values. However, because of fibre orientation radial gradient, while the inner fibres of the ANI model were more stressed than those of the TAN model, the ANI external fibres reoriented before being stretched and were less stressed than the TAN external fibres. This mechanism contributed to a lower RSD parameter value and a higher FCQ value in the ANI model than in the TAN model. Nonetheless, as shown by the total shear strains, matrix shear strain seems to be best limited by the transversal rotation-side fibres. Although it is then difficult to argue what is better, given that under lateral bending, postero-lateral quadrants should be influenced by frontal axial shear deformations, it is obvious that with its 45° oriented axial inner and transversal outer fibres the RAD model might represent a good compromise for local annulus stabilization. Such compromise was actually reflected in a significantly lower RSD parameter in the L3-L4 postero-lateral annulus of the RAD model than in the L3-L4 postero-lateral quadrants of the other models.

At the L4-L5 level, the large annulus deformations activated the 62° and 60° oriented external fibres of the RAD and ISO models respectively. In the RAD model, this led to a very homogeneous fibre radial stress distribution and explained why the RAD L4-L5 FCQ parameter was noteworthy higher than the TAN L4-L5 FCQ value. Although the axial fibres of the TAN and the ANI models seemed quite able to resist annulus postero-lateral deformations, at both levels, they were associated to the highest mean total shear strain values. In fact, as shown by the total shear strain vector distribution, the collagen networks of the TAN and ANI models did not allow limiting the transversal shear strain found in the anterior part of the rotation side postero-lateral quadrant. This may also explain the high peak shear strains associated to rotation side disc bulging in the posterior part of the lateral quadrants and in the postero-lateral quadrants of these two models. Nonetheless, the low L4-L5 RMS value in the ISO model together with large ranges on motion still suggest that the ISO collagen network model represent the worst compromise in locally limiting annulus deformations in the lateral and postero-lateral quadrants.

(iv) *Posterior annulus*

As shown by the total shear strain vectors, posterior annulus deformation was characterized by a beginning of disc bulging to the rotation side. According to the mechanisms pointed out in the postero-lateral annulus, total shear strains associated to disc bulging were larger in the ANI and in the TAN model than in the other models. However, since the anti-rotation side extremity of the posterior quadrant remained under the influence of the motion-induced axial stretch, the axial fibres of the TAN and the ANI models were the first ones to be stretched. This explains the high RMS and FCQ parameters computed for these models at the L3-L4 level. Inversely, the more horizontal fibres of the ISO and the RAD models contributed to limit the annulus transversal expansion associated to bulging. Although this positive action was generally not reflected in the posterior FCQ values, it led to better fibre stress radial distributions and to lower total shear strains. Moreover, the low L3-L4 mean total shear strain value, given by the ISO model, suggests that the most transversal inner fibres of the ISO

model were the only ones to resist transversal loading from the nucleus pulposus, as identified in the anterior annulus. In this sense, none of the RAD, TAN, and ANI posterior collagen networks were able to resist nucleus-induced loading in the inner annulus. Taking such loading into account, in addition to axial stretches, and outer disc bulging, the RAD model might represent the best compromise, and the ANI model the worst compromise.

At the L4-L5 level, the large rotation side disc bulging may explain the high stress observed in the outer fibres of the ISO and of the RAD models when compared to the results obtained at the L3-L4 level. In the RAD model, this placed the L4-L5 posterior RMS parameter above that of the TAN model, contributed to equilibrate the fibre stress radial distribution, and resulted in a higher FCQ value than given by the TAN model. Curiously, for the TAN and ANI models, RMS values were lower in the L4-L5 posterior annulus than in the L3-L4 posterior annulus. In fact, total shear strains at the attachment points between the intervertebral disc and the adjacent endplates indicated that in the RAD and ISO L4-L5 posterior annuli, rotation side strains associated to bulging clearly pointed in a postero-lateral direction. In the TAN and ANI models, the direction of bulging induced strains was posterior. This suggests that in the RAD and ISO models, the posterior part of L4 may have slightly rotated toward the anti-rotation side. Such outcome is in agreement with the coupled rotation identified in Chapter 3 when lateral bending simulations were performed on the New Geometry intact model. This also agreed with the facet contact differences observed between the L3-L4 and L4-L5 levels, on one hand in the TAN and ANI models, and on the other hand, in the RAD and ISO models. A discussion about this point can be found in Paragraph D.II.c.4). The absence of significant combined rotations in the L4-L5 segments of the TAN and ANI models made the larger deformability of the intervertebral disc to allow greater load transfers through the rotation side facet contact. This mechanism would have limited the axial fibre stretch to the anti-rotation side. Radial stress distributions resulted also more homogeneous both in TAN and in the ANI models. Nevertheless, as shown by the high posterior total shear strains predicted by the ANI model, the ANI FCQ parameter did not seem to reflect the stabilization capacity of the corresponding collagen network, according to the above discussed incapability of axial fibres to limit bulging.

6) Axial rotation

(i) Anterior annulus

Under axial rotation, models with fibre orientation radial gradients generally led to the highest anterior FCQ values. This was in agreement with the discussion made in Chapter 2 about the functional role of annulus fibre anisotropy under axial rotation. However, while this interpretation of early simulation results stated that fibres close to 45° should be immediately stretched by the axial rotational motion, in the present results, the nearly 56° oriented inner fibres of the ANI model tended to be more stressed than the 45° oriented inner fibres of the RAD model. In the most inner part of the mid annulus, the fibres of the ANI model were still about 10° more transversal than those of the RAD model, and their load bearing capability, relative to the RAD model fibres,

was even higher than in the inner annulus. Total shear strain vectors in these two models actually showed that the anterior annulus was most likely under the influence of an intradiscal pressure that bulged the inner annulus wall. Such local loading made the deformations of the annulus to diverge from the pure axial rotation-induced shear assumed in Chapter 2. Nevertheless, the present results do not contradict former predictions from Chapter 2, where fibre resistance to the main axial rotation was shown to generate a pressurization of the nucleus pulposus.

At the L3-L4 level, intradiscal pressures in the different models tended to be positively correlated with the ranges of motion that at the same time tended to be positively correlated with the transversal orientation of the anterior fibres. Computed nucleus pore pressures were effectively at least 18% higher for the TAN and ANI models than for the RAD and ISO models. Nevertheless, while the nucleus pore pressure of the TAN model was 10% higher than that of the ANI model, the ANI main rotational motions were slightly higher than those of the TAN model. Similarly, the ISO model gave both a higher L3-L4 axial rotation and a lower intradiscal pressure than the RAD model. In fact, the link between ranges of motion, anterior fibre orientation, fibre stress, and intradiscal pressure, cannot be explained by considering solely pure axial rotation motions. In the anterior outer annuli of all models, prediction of axial total shear strain components, together with the motion-induced transversal and oblique components, suggested the existence of secondary motions. Results of Chapter 3 already pointed out a slight flexion as coupled rotation. However stress distributions within the tissues were not detailed. In the present study, asymmetry of the axial shear strains with respect to the annulus mid-sagittal plane indicates that secondary motions might be considered as combinations of both sagittal and frontal rotations. For all models, coupled motion magnitudes up to 4° were evaluated, according to the range of *in vivo* values determined by Pearcy (Pearcy, 1985) under similar main axial rotations. Predicted rotations also supported previous computational issues suggesting that lumbar spine coupled motions under axial rotation may be mainly due to passive spinal structures as included in the present models (Little *et al.*, 2008). Both sagittal and frontal components of the secondary motions were analyzed by calculating the anterior, posterior and lateral intervertebral disc height changes (Fig. 4.38). In all models, L3-L4 lateral intervertebral disc height changes showed a lateral bending-like rotation directed to the anti-rotation side of the main motion. In the TAN, ANI, and ISO models, L3-L4 postero-anterior disc height changes indicated an extension-like coupled rotation. Coupled motion components were between 4% and 7% higher in the TAN than in the ANI model, explaining why nucleus pore pressure was larger in the L3-L4 TAN intervertebral disc than in the L3-L4 ANI intervertebral disc. L3-L4 coupled rotations were generally smaller in the RAD than in the ISO model. Nevertheless, the RAD antero-posterior L3-L4 disc height changes indicated a slight flexion-like coupled motion component with axial upper translations of the L3 vertebra lower than in the ISO model. This may explain why L3-L4 intradiscal pressure was found larger in the RAD than in the ISO model.

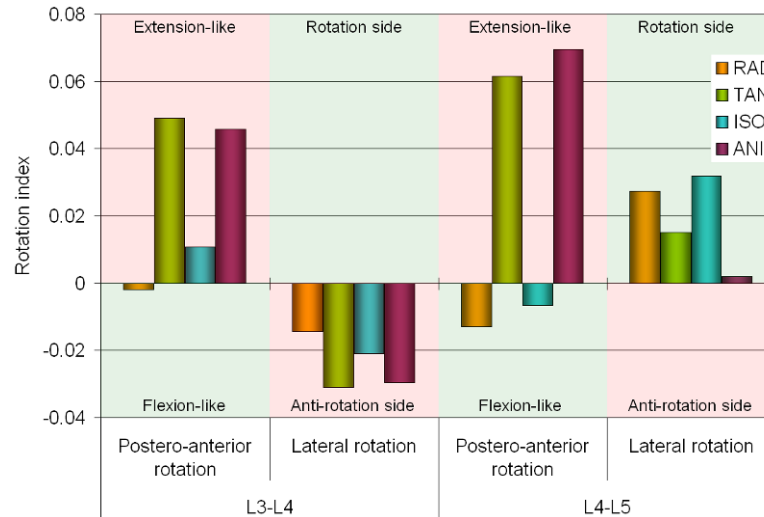


Figure 4.38: Rotation index (RI) relative to the coupled motions computed under axial rotation. Postero-anterior RI values were given by the differences between anterior to posterior disc height ratios in the deformed and undeformed segments. Similarly, lateral RI values were the differences between anti-rotation side to rotation side lateral disc height ratios in the deformed and undeformed segments.

Correlation between anterior fibre orientations and predicted ranges of motion, together with the high fibre stress values computed in the anterior annulus quadrant, suggests that the anterior annulus played a particular role in resisting axial rotation motions. Moreover, in all models, predictions of disc height changes showed that during axial rotation, the anterior annulus could undergo significant coupled axial tensile deformations. It is then not surprising that the RAD model with its 45° oriented most axial inner fibres led to both the lowest ranges of motion and the lowest anterior mean shear strains. As they did not take into account annulus matrix deformation, FCQ calculations gave the highest anterior L3-L4 value for the ANI model. However, computed shear strains successfully illustrated the poor capacity of the anterior ANI collagen network configuration to stabilize the annulus under axial rotation. High L3-L4 anterior ANI FCQ value was principally due to the lack of stress in the highly transversal outer annulus fibres that were unable to resist, neither main, nor antero-posterior coupled motions and allowed a very low RSD parameter value. Anterior outer fibres in the ISO and in the TAN annuli were less transversal than those of the ANI model. Thus, both for the ISO and ANI annulus configurations, high RSD parameters together with low FCQ and high mean shear strain values were predicted. Qualitatively, very similar results were obtained at the L4-L5 level, but larger ranges of motions than at the L3-L4 level contributed to increase the difference in FCQ results between the RAD and the ANI model. At both levels, on one hand, the anterior fibres of the ISO model were activated by the local axial stretch resulting from coupled rotations, but were not axial enough to lock this axial stretch such as the inner fibres of the RAD model did. On the other hand, ISO anterior fibres were not transversal enough to resist the intradiscal pressure. Such collagen configuration was then poorly efficient to limit both anterior annulus axial and transversal deformations, which resulted, at the L3-L4 level, in the highest anterior mean shear strain value. At the L4-L5 level, both main and coupled motions were larger. L4-L5 local axial stretch of the anterior annulus was then

more influent than at the L3-L4 level and, due to its extremely transversal outer fibres, the ANI model gave the highest mean shear strain value.

(ii) *Lateral annulus*

Before interpreting results in the lateral annulus, it is convenient to remind that fibre stresses and matrix mean total shear strains were collected and averaged over the two lateral quadrants under left and right rotation. In both the L3-L4 and L4-L5 lateral outer annuli, according to the lateral bending-like coupled motion component identified from lateral axial intervertebral disc deformations, the 55° oriented fibres of the TAN model were the most axial and most stressed ones. Lateral outer fibres of the ISO model were the second most axially oriented ones, and similar reasoning as for the TAN model can be applied. In the lateral mid-inner and inner annuli of both levels, comparing the ANI, the TAN, and the ISO models, it also appears that the most axial fibres were the most stressed ones. Nevertheless, mean total shear strain values clearly showed that such annulus fibre activation by the lateral bending-like secondary motion component did not reflect any ability of the local collagen network to stabilize the lateral annulus. In fact, given the antero-lateral postero-lateral nature of the overall coupled motions, all lateral annuli were partly under the influence of axial shear deformations that resulted in nearly 45° oriented principal stretches, similarly as the annulus main motion-induced transverse shear deformations. Accordingly, inner total shear strains vectors computed in the anti-rotation side lateral annuli of all models were oblique and mostly parallel to the deformed annuli mid-sagittal planes. Although antero-posterior coupled motions were inverted in the RAD and in the other models, similar orientation of anti-rotation side inner lateral shear strain vectors in all models demonstrates the major influence of the main motion.

At the L3-L4 level, unlike anti-rotation side shear strains, rotation side inner lateral annulus total shear strains were always insignificant. Actually, transversal plane shear stress distributions all around the annuli suggested that the anti-rotation side quadrants were generally protected by the posterior zygapophysial joints. Thus, the pure axial rotation component of the whole annulus deformation would preferentially activate rotation side lateral and anterior fibres. Such dissymmetry of the annulus fibre action with respect to the sagittal plane probably explains the L3-L4 anti-rotation side lateral bending-like coupled rotation that occurred along with axial rotation motions. Therefore, as shown by the L3-L4 lateral RMS parameter values computed in the RAD and ISO models, and in the TAN and ANI models, L3-L4 ranges of motion (allowed by the L3-L4 anterior annulus), activation of L3-L4 lateral fibres, and L3-L4 lateral bending-like coupled rotations, are all positively correlated. In apparent contradiction to this, while L3-L4 axial rotation was greater in the ANI model than the TAN model, the lateral L3-L4 RMS value returned by the ANI model was lower than that returned by the TAN model. Nevertheless, the low L3-L4 ANI RMS parameter value compared to the TAN one was due to the lack of activation of the ANI lateral outer fibres that were too transversal to resist the lateral axial annulus stretch induced by the coupled motion. ANI outer lateral fibres were also probably shielded by the adjacent axial inner fibres. Resistance of the ANI axial inner fibres to the L3-L4 lateral bending-like component of the coupled motions was actually directly reflected by a smaller L3-L4 anti-rotation side

intervertebral disc lateral disc height change than in the other models. However, L3-L4 mean shear strain values clearly showed the parallel between magnitudes of lateral overall shear deformations, and main and coupled motions. It appears then that the stabilization of the L3-L4 lateral annulus under axial rotation is intimately linked to the ability of anterior fibres to lock the motion. A perfect illustration comes through the ANI model. In spite of having a lateral collagen network similarly oriented as that of the RAD model, the ANI model gave both RMS parameter and mean shear strain values greater than those given by the RAD model. Since the 45° oriented fibres of the RAD model contributed to limit greatly the main motion, the established link between range of motion and lateral bending-like coupled rotation explains why the RAD annulus fibres led to both the least L3-L4 lateral bending-like coupled rotation and least lateral mean total shear strain magnitude, without being meaningfully stressed.

Although fibre stress distributions and matrix mean shear strains were qualitatively similar in the L3-L4 and L4-L5 lateral annuli, total shear strain distributions differed substantially from the L3-L4 to the L4-L5 lateral annuli. In fact, at the L3-L4 level, the anti-rotation side lateral bending-like coupled rotation induced a rotation side lateral displacement of the L4 top endplate, resulting in a rotation side lateral bending-like coupled motion at the L4-L5 level. Such analysis was supported by lateral intervertebral disc height changes computed in the L4-L5 segment. Evidently, the segment remained mainly under axial rotation, and anti-rotation side lateral bending-like coupled motions occurred as at the L3-L4 level. Nevertheless, this L4-L5 anti-rotation side lateral bending-like coupled rotation competed with the added rotation side coupled motion induced by L4, leading in the different models to different L3-L4 and L4-L5 lateral bending-like coupled motions (Fig. 4.38). L4-L5 lateral disc height changes showed however a major influence of the rotation side lateral bending-like motion induced by L4 than of the anti-rotation side lateral bending-like coupled motion induced by the L4-L5 axial rotation. As a consequence, apparent L4-L5 lateral bending-like coupled motions were greater in the RAD and ISO model than in the TAN and ANI models. In the TAN and ANI models, important L3-L4 coupled rotations led to large rotation side lateral displacements of the L4 top endplate, which considerably countered the influence of the lateral bending-like coupled motion induced by the L4-L5 axial rotation. In the ANI model, large predicted L4-L5 axial rotation suggests that the main motion related anti-rotation side coupled rotation was so high, that the resulting L4-L5 lateral bending-like coupled rotation was almost insignificant. This contributed to preferentially increased L4-L5 ANI inner fibre stresses, leading to an ANI lateral FCQ value larger at the L4-L5 than at the L3-L4 level. However, as at the L3-L4 level, mean lateral shear strain calculations clearly show that the ANI configuration cannot be considered efficient to resist axial rotation motions and confirm that best lateral annulus stabilization under axial rotation is given by the RAD model. Rotation side lateral bending-like motion component identified in these simulations was probably caused by the immobility imposed to the L5 vertebra. However, qualitative comparison of L3-L4 and L4-L5 FCQ parameter values, fibre stress radial distributions, and matrix total mean shear strain values, showed that such possible modelling artefact did not affect the different model comparisons under axial rotation. Study of segment stability through predicted coupled rotations could however have led to misinterpretations.

(iii) Postero-lateral annulus

Unlike in the anterior and lateral annuli, in the postero-lateral annulus, inner fibres were generally significantly more loaded than the outer ones. Such a difference in fibre stress radial distribution between the anterior/lateral and posterior annulus areas was most likely due to limited posterior annulus deformations as a consequence of the posterior facet joint contact. Zygapophysial joints contributed to lock the axial rotation motion and preferentially protected the closest surrounding annulus layers, i.e. the outer annulus layers. At the L3-L4 level, both in the outer and inner layers of the postero-lateral annulus, most axial fibre layers were locally the most stressed ones. Actually, computation of posterior disc height changes showed that independently of coupled motion particularities in the different models, axial rotation always produced an axial stretch of the posterior annulus areas. A clear correlation was then found between the magnitude of posterior disc stretch and the degree of axial resistance provided by the postero-lateral inner fibre stresses. Sagittal asymmetry of the L3-L4 postero-lateral total shear strain axial components suggests that posterior disc axial stretch was probably a consequence of the lateral bending-like coupled rotation that favoured cranial displacements of the anti-rotation side upper facet once contact is established. Nevertheless, independently of this third coupled deformation component, total shear strain vectors showed that local matrix deformations in the anti-rotation side postero-lateral inner annulus were best limited by the 45° and 44° oriented fibres of the RAD and TAN models respectively. Unlike fibre stress based predictions, matrix shear strain vectors illustrate the major influence of the main motion regardless of coupled rotations, and explain then why the RAD and the TAN models led to lower L3-L4 postero-lateral mean shear strain values than the ISO and ANI models. Hence, although axial inner fibres of the ANI model were highly stressed due to posterior annulus stretch, the ANI L3-L4 mean shear strain value was the highest one. Note that in the L3-L4 outer annulus, most axial fibre orientations were also the closest ones to 45°, i.e. the preferred fibre stretch direction under pure axial rotation. Thanks to the load bore by its outer fibres, the TAN model gave then the second highest L3-L4 FCQ value, which agreed with the matrix total shear results to underline that the TAN annulus fibre local organization was fairly efficient to stabilize the L3-L4 postero-lateral annulus. Highest L3-L4 FCQ parameter was given by the ISO model, but was due to a lack of fibre stress. This was particularly evident in the inner annulus, because the ISO 60° oriented fibres were not able to resist neither main, nor coupled motion induced deformations. Therefore, the L3-L4 ISO FCQ value cannot be considered representative of the model ability to stabilize the L3-L4 postero-lateral annulus, as underlined by the corresponding high mean shear strain value. Nonetheless, no great differences were predicted between the L3-L4 annulus matrix mean shear values of ISO and the TAN models. Moreover, taking the RAD model as a positive reference for annulus stabilization, the L3-L4 postero-lateral mean shear strain value given by the TAN model was significantly higher than that given by the RAD model, despite similar local inner fibre orientations in the two models. These outcomes can actually be easily explained by taking into account that as a result of large L3-L4 main and coupled rotations, nucleus pore pressure predicted in the TAN model was 30% higher than that returned by the RAD model and 70% higher than that returned by the ISO model. Note that high shear strains in the L3-L4 postero-lateral quadrant of the ANI model can also be explained by a high intradiscal pressure that inner axial fibres were unable to resist to. The role of nucleus

pressure in the L3-L4 postero-lateral annuli underlines the fact that in a given quadrant, local results may be conditioned by the deformation mechanisms involved in other quadrants.

At the L4-L5 level, due to greater ranges of motion, all postero-lateral fibre layers were generally more stressed than at the L3-L4 level. Nevertheless, relative fibre stress increases from the L3-L4 to the L4-L5 level were strongly model dependent, indicating a likely high influence of the change of coupled motion from one segment to another. Actually, L4-L5 postero-anterior disc height changes showed significantly larger L4-L5 than L3-L4 extension-like coupled rotation components for both the TAN and ANI model. Flexion-like coupled motion predicted for the RAD model was also larger at the L4-L5 than at the L3-L4 level, and while the antero-posterior coupled motion component computed in the ISO model was extension-like at the L3-L4 level, it was flexion-like at the L4-L5 level. Together, with the L4-L5 apparent coupled rotations resulting from the contributions of both the L4-L5 segment axial rotation and the lateral displacement of the L4 vertebra top endplate, L4-L5 antero-posterior coupled motions led to L4-L5 posterior disc height changes noteworthy different from those computed at the L3-L4 level. Nevertheless, before discussing the effect of these L4-L5 posterior disc height changes on the L4-L5 postero-lateral annulus fibres, secondary antero-posterior motion component showed in Figure 4.38 should be analyzed.

Antero-posterior coupled rotations could be explained by the fact that through zygapophysial joints action, main and coupled rotations both generated unbalanced annulus deformations in the posterior and anterior annulus areas. Thus, depending on motion magnitudes and differences between posterior and anterior fibre orientations, flexion- or extension-like secondary motions can be generated. Basically, three different disc deformations, i.e. main axial torsion, lateral bending-like coupled deformation, and posterior axial disc stretch, were shown to influence annulus fibre activations. While main axial rotation should induce a fibre reorientation around 45° , lateral bending-like motion, and posterior axial disc stretch were shown to activate preferentially the most axial fibres. In the TAN and ANI models, anterior fibres needed an average reorientation of 21.5° to align to 45° , while posterior fibres only needed a mean reorientation of 12.3° . Moreover, in these two models, axial posterior fibres were better oriented than the anterior ones to locally resist the axial tractions induced by secondary disc deformations. Therefore, it is not surprising that both in the TAN and in the ANI models, antero-posterior coupled motion components appear under the form of extension-like rotations. In the RAD and ISO models, posterior and anterior fibres had exactly the same orientations. In the RAD model, with 45° oriented fibres in all quadrants, predicted flexion-like antero-posterior coupled motions were then clearly attributable to larger anterior than posterior annulus deformations. However, in the ISO model, an extension-like coupled rotation was predicted at the L3-L4 level. When compared to the results given by RAD model, the large L3-L4 anti-rotation side lateral bending-like rotation induced in the ISO model could have been sufficient to promote more fibre reorientation from 60° toward 45° in the posterior annulus areas than in the anterior annulus. This would evidently have resulted in the slight extension-like secondary motion component predicted in the L3-L4 segment. At the L4-L5 level, the thick anterior annulus should have allowed main motions large enough to favour anterior fibre reorientation, leading to the apparition of a flexion-like coupled rotation.

Such phenomenon explains why the outer L4-L5 postero-lateral fibre layers of the ISO model were nearly as stressed as the inner ones, leading locally to the lowest RSD and highest FCQ parameter values. In the RAD model, the L4-L5 increased flexion-like coupled motion component contributed to preferentially activate the most axial inner fibres of the postero-lateral quadrant, which was detrimental to the fibre stress radial distribution and led to the lowest L4-L5 postero-lateral FCQ parameter value. At the contrary, in the TAN model, an increased L4-L5 extension-like coupled rotation led to a more even radial distribution of postero-lateral fibre stresses in the L4-L5 annulus than in the L3-L4 annulus, and resulted in both the second lowest and second highest L4-L5 postero-lateral RSD and FCQ parameters, respectively. In the ANI model, although comparable L4-L5 antero-posterior coupled rotation as in the TAN model were predicted, the fibre radial orientation gradient contributed to maintain a high RSD parameter value, and the resulting L4-L5 postero-lateral FCQ parameter value of the ANI model remain significantly lower than that of the TAN model. Also, the high L4-L5 postero-lateral mean shear strain value predicted in the ANI model can be linked to the non beneficial association of the fibre orientation radial quadrant with an extension-like coupled motion (§ D.II.b.3)). Coupled motions allowed then explaining L4-L5 postero-lateral FCQ values according to several local annulus deformation mechanisms. However, total mean shear strain values were still positively correlated with the overall ranges of motions and seemed more representative of the stabilizing effect of each modelled annulus collagen network than the FCQ parameter values.

(iv) *Posterior annulus*

In the L3-L4 outer posterior annulus, most stressed fibres were the closest ones to 45°. This indicated a more direct relation to the main rotation than in the other quadrants, probably due to the posterior annulus stabilization brought by the zygapophysial joint contact (Chap. 3). Such stabilization was actually shown at both levels by the mean total shear strain values that were always smaller in the posterior than in the other quadrants. In the inner annulus, most axial fibres were however the most stressed ones. Posterior total shear strain axial vectors strongly suggest that L3-L4 inner fibre stresses were probably caused by the antero-posterior coupled motion components. In comparison to the predictions made in the postero-lateral annulus, the large RSD parameter and inner fibre stress values computed in the posterior annulus, actually pointed out that the postero-lateral location of the zygapophysial joints may have made the antero-posterior coupled rotations to be more influent across the posterior than across the postero-lateral quadrants. At the L3-L4 level, the only predicted coupled flexion-like motion took place in the RAD model. In this model, postero-anterior coupled rotation increased then the effect of the posterior annulus tractions brought by the interaction between facet joint contact and lateral bending-like coupled motion component. Therefore, the L3-L4 posterior annulus quadrant was the only one where the RAD model led to a higher mean shear strain than the other three models. The smallest L3-L4 posterior mean total shear strain value was then given by the axial and homogeneously oriented posterior fibres of the TAN model. Moreover, among the models without fibre orientation radial gradient, the TAN model had the closest posterior fibre orientation to 45°.

At the L4-L5 level, the differences of range of motion between the RAD and the other models were globally larger than at the L3-L4 level. Hence, relatively to the other models, the limited L4-L5 ranges of motion in the RAD model reduced the effect of the local posterior annulus stretch induced by the flexion-like coupled motion, and allowed a slightly smaller L4-L5 mean shear total strain value. The ISO model also gave a low L4-L5 posterior mean shear strain value, similar to that predicted in the RAD model. Actually, the coupled flexion-like rotation predicted in the ISO model contributed to generate the highest intradiscal L4-L5 pressure. With its posterior transversal inner fibres, the ISO model was then the only model to have a L4-L5 posterior local configuration adapted to the effect of coupled rotations. For the other models, taking into account local fibre orientations, mechanisms explaining the rest of posterior annulus fibre related results were very similar as in the postero-lateral annulus.

c. Zygapophysial joint contacts

1) Sagittal Flexion

Under sagittal flexion, according to the discussion performed in Chapter 3 about the role of bony posterior elements in the New Geometry model, only L3-L4 low facet contact forces were found for all the models. Some differences between models were predicted, but contrary to any expectations, L3-L4 contact normal forces and ranges of motion were not correlated. On one hand, the maximum relative difference between the different L3-L4 flexion motions was computed between the “softest” RAD L3-L4 segment and the “stiffest” ANI L3-L4 segment and did not overcome 4%. On the other hand, lowest L3-L4 facet contact forces were obtained with the RAD model and were about 135% lower than the highest ones, given by the ISO model. The L3-L4 ISO segment was only 2% stiffer than the RAD segment and the “stiffest” ANI L3-L4 segment returned in-between contact forces. Actually, according to the capability of the different fibre networks to stabilize the annulus fibrosus under sagittal flexion (§ D.II.b.2)), the largest postero-anterior and axial translations of both L3 and L4 were found in the ISO and in the TAN model. Nevertheless, because of its fibre orientation radial gradient, the RAD model was found inefficient to stabilize both the anterior and posterior annuli, while the ISO fibre organization was inadequate in the posterior annulus areas only. Consequently, the centres of rotation were more anterior in the ISO model than in the RAD model, which led to higher ISO than RAD posterior contact forces. In the TAN and in the ANI models, assuming that ideally, anterior fibres would maximum re-orientate up to 90°, and posterior fibres, up to 0°, anterior fibres should reach their maximum reorientation at lower local annulus strains than posterior fibres. Thus, thanks to their axial posterior fibres, these two models gave less anterior centres of rotation than that of the ISO model, but still more anterior than that of the RAD model. This explains why the TAN and the ANI models gave zygapophysial joint contact forces in-between those computed in the ISO and RAD models.

2) *Sagittal extension*

(i) *10 N.m*

Under 10 N.m sagittal extension, the RAD model led to the lowest facet contact forces at both the L3-L4 and L4-L5 levels. According to this result, the RAD model also gave the lowest ranges of motion, and its collagen network was identified as the most able to stabilize most of the annulus quadrants (§ D.II.b.3). At the L3-L4 level, the ISO model led to both best posterior annulus stabilization and second lowest range of motion, but its facet contact normal forces were the highest ones. Actually, the TAN and ANI models both gave slightly lower L3-L4 zygapophysial joint contact forces than the ISO model did, which could be explained by the instability of the TAN and ANI annuli under sagittal extension. In the TAN and ANI models, a poor resistance to anterior and posterior annulus deformations, caused by both extremely transversal anterior fibres and extremely axial posterior fibres, allowed large antero-posterior translations of L3 and L4. These translations tended to separate the superior and inferior facets of the L3-L4 contact and were sufficient to limit contact forces.

At the L4-L5 level, because of the fixed position of L5, and because of large segmental rotations, the antero-posterior translations of the ANI and TAN L4 vertebrae were not sufficient to limit facet contact forces. Therefore, the pure rotational motion component had a predominant effect, and according to the fact that the TAN annulus organization appeared to be the less efficient in stabilizing most of the L4-L5 annulus quadrants, the corresponding zygapophysial joint contact forces were the highest ones. The ISO collagen network, that satisfactorily stabilized both the postero-lateral and posterior annulus quadrants, gave the second lowest facet contact forces. Actually, under sagittal extension, anterior annulus stabilization, as provided by the RAD model, seemed preferable to limit L4-L5 posterior facet contacts. Nevertheless, as shown by the results at the L3-L4 level, facet contact forces may not be always a good descriptor for intervertebral disc stabilization.

(ii) *7.5 N.m*

Under 7.5 N.m sagittal extension moment, contrarily to the results found under 10N.m load magnitude, L4-L5 fact contact forces were maximum in the RAD model, and minimum in the ANI model. Nevertheless, the RAD model gave very similar normal force values at both 7.5 N.m and 10 N.m. Increasing the sagittal extension load from 7.5 N.m to 10 N.m amplified both translational and pure rotational motions of the vertebrae. Nonetheless, as stated when facet contact results at 10 N.m were discussed, while transverse displacements might limit zygapophysial joint contacts, vertebra rotations favour contact. Therefore, in the RAD model, invariance of contact from 7.5 N.m to 10 N.m extension is explained by a compensation of the rotation- induced contact increase, by a translation-induced contact release. Remembering the discussion of Paragraph D.II.b.3), such compensation was most likely possible because, in the RAD model, the most axial inner anterior fibres promoted more anterior centres of rotation than in the other models. Conversely, in the ISO, TAN and ANI models, the more posterior centre of rotation than in the RAD model, made that, at a low load level,

the rotation of L4 had a lower relative influence on zygapophysial joint contact than the vertebra postero-anterior translation had. At higher load level, such as 10N.m, the ANI, TAN, and ISO L4-L5 rotations were sufficiently large to take over the effect of L4 postero-anterior translation and significantly affect posterior facet contact forces.

3) *Axial compression and spinal erector-like loading*

Under axial compression, as shown by the anterior and posterior axial disc deformations, facet contact forces were generally correlated with the stabilization of the posterior annulus quadrants. As such, highest zygapophysial joint contact forces were found in the TAN and in the ANI model, whose axial annulus posterior fibres allowed large local intervertebral disc deformations. Nevertheless, while posterior axial displacements were not so different in both models, zygapophysial joint contact forces were substantially higher in the TAN model than in the ANI model. Actually, as discussed in Paragraph D.II.b.1), the extremely transversal outer fibre layers of the anterior ANI annulus provided a larger resistance to the local annulus deformations than the TAN anterior fibres could provide. This had been identified to allow a lower L3 postero-anterior displacement in the ANI than in the TAN model, which most likely explains facet contact force results in both models. According to the capability of its homogenous transversal fibre orientation to stabilize posterior annulus areas, the ISO model gave the lowest zygapophysial joint normal contact forces. Note that, respecting the natural limited role of the zygapophysial joints under axial compression (Chap. 1), the simulated axial follower compressive force led to extremely low facet contact force values, in comparison to the rotational load cases.

In relation to the low facet contact force magnitudes obtained under axial compression alone, combining the compressive follower force with a 7.5 N.m sagittal extension loading had a large effect. L3-L4 and L4-L5 normal contact force values predicted under spinal erector-like loading could respectively increase up to 150% and 120% of their magnitude under pure extension. However, except for the L3-L4 RAD segment, the axial compressive follower load did not significantly affect the qualitative relation obtained between the facet contact forces of the different models under sagittal extension alone. Quantitatively, contact forces were higher under spinal erector-like loading than under 7.5 N.m pure extension, and L4-L5 contact force increases were significantly higher in the RAD and in the ISO models than in the TAN and ANI models. Nevertheless, such outcome is in accordance with the different locations of centre of rotation identified in the different models, as a result of anterior annulus stabilization (§ D.II.b.3,4). The better the anterior annulus stabilization was, the shorter the postero-anterior transversal distance between the upper and lower facets should be. Thus, it can be easily understood that the axial compressive load preferentially increased facet contact forces in segments with the most anterior centres of rotation and the smallest postero-anterior translations of the upper vertebra, i.e, the RAD and the ISO models. In the RAD model, centre of rotation was so anterior that such effect brought the L3-L4 zygapophysial contact forces from the lowest magnitude under pure extension, to the highest magnitude under spinal-erector like loading.

4) *Lateral bending*

Under lateral bending, major contact forces were always computed to the rotation side, where predicted contact area was also the largest one. According to the annulus stabilization discussed in Paragraph D.II.b.5), zygapophysial joint results indicate that L3-L4 facet contact forces were first of all best limited by the annulus models most able to stabilize the postero-lateral and posterior annulus quadrants, i.e., the RAD model. The ISO collagen network, identified as the worst annulus configuration for lateral and postero-lateral quadrant stabilization, gave the highest L3-L4 normal contact force values. The TAN fibre-induced annulus anisotropy, found to be locally particularly efficient in the anterior and lateral quadrants, led to L3-L4 facet contact forces only somewhat inferior to those given by the ISO model. Also, according their low capacity to stabilize the posterior annuli, the TAN annulus fibres gave maximum contact forces very similar to those predicted in the ANI model. All together, these results strongly suggest that the high activation of the rotation side L3-L4 zygapophysial joints was mostly controlled by the local stabilization of the postero-lateral annulus.

At the L4-L5 level, as at the L3-L4 level, the ISO postero-lateral annulus was found to be the worst stabilized one. However, unlike the predicted L3-L4 contact forces, L4-L5 rotation side facet contact forces computed in the ISO model were the second lowest ones. Actually, as at the L3-L4 level, L4-L5 postero-lateral annulus stabilization may have influenced L4-L5 facet joint contact forces. But most likely, the coupled axial rotation identified both in Chapter 3 and in Paragraph D.II.b.5)(iv) had a predominant effect on zygapophysial joint activation. As discussed in Paragraph D.II.b.5)(iv), total shear strain vector indicated an axial rotation of the posterior part of the ISO and RAD L4 vertebrae toward the anti-rotation side of the main motion. Such coupled motion tended to open the rotation side zygapophysial joint contact and explains then the low L4-L5 facet contact forces found in the ISO and RAD, independently on postero-lateral annulus stabilizations. Observing rotation side L4-L5 contact areas, it appears that for all models, the lower L4 facet cartilage layer pressed the anterior part of the L5 superior facet cartilage. Therefore, due to the antero-posterior C shape of the L5 superior facet (Chap. 1,3), inferior L4 articular process tended to slide toward the transversal centre of the L5 superior facet cartilage, provoking a slight rotation-side axial rotation of L4. In the TAN and ANI models, the general better stabilization of the large anterior and lateral quadrants than in the ISO and RAD models (§ D.II.b.5)(i),(ii)) could have impeded such slight contact-induced coupled rotation. Note that at both levels, anti-rotation side contact forces seemed fairly independent on the presence of coupled motion. They were always significantly lower in the TAN and ANI models than in the RAD and ISO models, and appeared rather correlated with the ability of the collagen networks to lock the anti-rotation side annulus axial stretch.

5) *Axial rotation*

Under axial rotation, on one hand, the RAD annulus configuration led to the best L3-L4 annulus stabilization from the anterior to the postero-lateral annulus (§ D.II.b.6). On the other hand, the ANI model, that worst stabilized the L3-L4 postero-lateral

annulus, gave the highest L3-L4 ranges of motion. Accordingly, the RAD and ANI L3-L4 facet contact forces were respectively the lowest and the highest ones. Second lowest contact force value was given by the TAN model, that was suspected to provide one of the best L3-L4 posterior annulus stabilization. Nevertheless, the L3-L4 facet contact force results provided by the TAN model might also be due to the extremely transversal anterior fibres of the model that allowed large anterior axial stretches. This anterior axial annulus stretch, coupled with the axial rotation could have compensated the effect of large main motions and partially relieved the facet contact loads. The ISO model that had significantly less transversal fibres than the TAN model, but that also still gave larger L3-L4 ranges than the RAD model, led to the second highest L3-L4 facet contact force. Therefore, it seems that, under axial rotation, L3-L4 facet contact forces tend to be correlated with the ranges of motion, but this correlation is not direct, and depends on the transversal orientation of the anterior annulus fibre network. Thus, since anterior annulus fibres may also differently affect facet contact forces in case of extreme coupled motions, the relation between zygapophysial joint contact and main ranges of motion has to be carefully considered.

At the L4-L5 level, highest facet contact forces were found in the RAD and ISO model, without any apparent relation, neither with the stabilization of any quadrant, nor with the predicted segmental ranges of motion. Higher L4-L5 coupled lateral bending-like coupled motions computed in the ISO and RAD models in comparison to those given by the ANI and TAN model could actually be held as responsible for such result. Nevertheless, L4-L5 lateral bending-like coupled flexion occurred to the rotation side of the main motion (Fig. 4.38). Thus, given that simulated axial rotation and lateral bending motions produced highest facet contact forces to their respective anti-rotation and rotation sides, a lateral bending-like coupled motion occurring to the rotation side of a main axial rotation would be expected to have a low effect on the anti-rotation side facet contact forces. If it is sufficiently large, the coupled rotation could at most induce anti-rotation side contacts. Furthermore, at the L3-L4 level, where anti-rotation side lateral bending-like secondary motions had been predicted, no correlation could be found between coupled motion and facet contact forces, suggesting then that such secondary motion was not likely to affect zygapophysial joint activation. Actually, the most fundamental difference between the L3-L4 and the L4-L5 segments was that L5 was rigidly fixed in all directions. Hence, L4-L5 intersegmental motions were due to the L4 vertebral only. According to the discussion of Paragraph D.II.b.6)(i), the transversal anterior fibres of the TAN and ANI models allowed the anterior quadrant to be significantly axially stretched. Conversely, the axial posterior fibres of the two models limited the posterior coupled axial stretch. Such antero-posterior combination of the TAN and ANI fibres produced then large coupled extension-like motions whose centres of rotation were rather posterior. Given the immobility of L5, the associated antero-posterior translations of L4 were probably sufficiently large to induce a L4-L5 facet joint opening and limit the TAN and ANI normal contact forces that resulted lower than the RAD and ISO ones.

Such outcome raises then the question whether rigidly fixing a vertebra, as done in most of the lumbar spine finite element studies, is not affecting the predictions and the interpretations of the models. Note that artefacts from this type of extreme boundary condition had been already pointed out in Chapter 3. Fixing an upper or a lower

vertebra in finite element simulations is most often done to reproduce mechanical boundaries impose in the *in vitro* tests used to verify some of the model predictions. Nevertheless, once the predictive power of the models has been verified by comparison with *in vitro* experimental results, further biomechanical analyses of the modelled spine segment should include more “physiologic” boundary conditions to avoid misinterpretations of the functional spine mechanics.

III. Summary and perspectives

Mechanical study of annulus fibres and matrix clearly demonstrated that intervertebral disc mechanics depended greatly on the annulus fibre orientation. Important interactions were also shown between fibre orientation, intradiscal pressure, and stress transfer between nucleus pulposus and annulus fibrosus. These interactions also highly depended on the simulated load case, local annulus loading, and spine level (i.e. intervertebral disc geometry). As a general outcome, transversal fibres were more able to withstand annulus axial compressive loading, and nucleus pulposus pressure. Axial fibres were shown to be efficient to resist annulus axial tractions, and oblique fibres could best stabilize annulus quadrants under axial and transversal shear deformations. Accordingly, the ISO and the RAD annulus fibre configurations were found particularly adequate to stabilize the overall annulus under axial compression and axial rotation, respectively. Under axial rotation, the positive results given by the RAD model were probably mainly due to the 45° oriented inner fibres, but the role of the RAD outer fibres remained somewhat unclear. Contrary to the common idea that fibre orientation radial gradient would be positive for intervertebral disc stabilization, the RAD and the ANI models often led to both large inner or outer fibre stress concentrations, and higher annulus mean shear strains than the other models did. This was particularly true when quadrants were under the influence of local axial compressive loads, and/or nucleus pressure. Under sagittal flexion, the transversal anterior and axial posterior fibres of the TAN model were also shown to have a positive effect on the stabilization of most L3-L4 and L4-L5 annulus quadrants. However, the distinction between the different models under sagittal flexion was not as direct and as clear as under axial compression or rotation, where most of the quadrants were locally under the influence of similar types of load. In general, under frontal and sagittal rotations, heterogeneity of annulus deformations in the different quadrants, impeded to point out any best global stabilization from one particular collagen network organization. Moreover, as underlined in almost all load cases, the specific mechanical response of one quadrant can positively or negatively affect other quadrants. Obviously, this led to possibly different conclusions about the stabilizing effect of two similar local collagen networks inserted in different annulus anisotropy models. Thus, although the presence of local annulus deformations demonstrated the need to study the annulus fibrosus mechanics quadrant by quadrant, each quadrant should be analyzed by taking into account the interaction it may have with the rest of the annulus. Such interaction can be a direct load transfer, either between two adjacent quadrants, as identified under sagittal flexion and lateral bending, or between geometrically opposite quadrants, as predicted under axial compression. Inter-quadrant mechanical interactions could also be indirect, either conditioned by the nucleus pulposus pressure, as under sagittal extension

or spinal erector-like loading, or conditioned by the zygapophysial joints, as identified under axial rotation.

The study of the annulus composite structure could then be easily biased by insufficient accuracy in the modelling of the facet cartilage or nucleus pulposus. In particular, it was shown in this Chapter that hyperelastic modelling of the nucleus pulposus failed in reproducing the hydrostatic tissue stress, experimentally identified in a normal intervertebral disc. It can be then hypothesized that the use of a hyperelastic nucleus model would have led to different interpretations of the different annulus anisotropy model mechanics. In absence of any a priori knowledge about the detailed mechanical behaviour of biological tissues, it appears then highly important to choose modelling assumptions that respect as much as possible the physico-chemical characteristics of the tissue. The strong interaction between the nucleus pulposus and inner fibre activation was repeatedly cited along the discussion of the results. Such interaction made the computed inner fibre stress to be often comparable to the outer fibre stress, or even higher. Because of the modelling of collagen II increasing content in the inner annulus layers, the tangential stiffness of the inner fibre layers was about 10% lower than that of the outer fibres. This means that tensile strains predicted in the inner fibre layers could be even larger than the tensile stresses computed in the outer layers. Such outcome was actually reported in different numerical studies of the lumbar spine (Natarajan and Andersson, 1999; Kim, 2000; Schmidt *et al.*, 2007c; Wang *et al.*, 2000) and agrees with the identified tendency of inner annulus layers to experience larger failure strains than outer layers (Skaggs *et al.*, 1994; Holzapfel *et al.*, 2005). Nonetheless, it apparently contradicts the common hypothesis that synthesis of collagen II in the inner annulus is due to local compressive loading (Brickley-Parson and Glimcher, 1984; Humzah and Soames, 1988). In spite of this, prediction of significant inner annulus tensile strains is also in agreement with the identification of thicker inner than outer collagen bundles after dissection of human lumbar annuli (Marchand and Ahmed, 1990). Tensile strains in the inner annulus is also supported by a confocal microscopy study performed by Bruehlmann *et al.* (Bruehlmann *et al.*, 2002), who reported inner annulus cells with long processes and multiple branching. Moreover, according to the hypothesis that nucleus pulposus pressure may activate the annulus fibres, the authors found the above-cited cells to be more abundant at the border of the nucleus pulposus. They also pointed out that connexin 43, a cellular gap junction protein believed to be exclusively expressed in tensile environments, was expressed both in the outer and inner annulus. Actually, *in vitro* experiments showed that both outer and inner annulus cells may have similar response in similar environments (Chou *et al.*, 2008), implying that tensile strains such as predicted in this study could result in thick inner collagen bundles with significant production of collagen I, as in the outer annulus. However, unlike the outer annulus, the inner annulus is under the influence of the high osmolarity induced by the nucleus pulposus. Extra-cellular matrix osmolarity has been shown to stimulate the expression of collagen II and inhibit collagen I expression (Wuertz *et al.*, 2007). Thus, without contradicting the prediction of inner fibre high tensile strains, local osmotic pressures could explain that inner annulus contains both lower and higher respective amounts of collagen I and II than the outer annulus. This analysis, therefore, demonstrates that the prediction of tensile mechanical environments in the inner annulus is acceptable. Nevertheless, given the relative amounts of collagen I to collagen II throughout the annulus thickness, present fibre

stress results suggest that radial distributions of fibre strains might give a better idea of the different collagen network stabilizing effects than fibre stress radial distributions did.

All the discussion about annulus fibre stabilizing effect in the different collagen-induced anisotropy models was based on fibre stress bearing capacity, fibre stress radial distribution, and annulus matrix shear strain. The developed mathematical FCQ parameter successfully took into account the ability of fibres to bear and distribute local stresses in the annulus quadrants. The parameter assumed that if fibres were adequately oriented to resist the load, they should bear a maximum of stress. However, it did not consider that large fibre stresses could also be a consequence of inadequate organization of the network, leading to substantial matrix deformations and fibre reorientation. In such cases, large ranges of motions were generally found, and the FCQ values were most often in contradiction with the predicted annulus matrix mean shear strain values. FCQ parameter values were then not representative of the annulus collagen network stabilizing capacity. Conversely, in some cases, both annulus matrix total shear strain and FCQ parameter values were found minimal. Low FCQ values were then generally due to high RSD parameters values, indicating that shear deformations were limited through preferential activation of only few fibre layers. In these cases, neither the inadequate orientation of the low activated fibre layer, nor the stress concentration in the other layers, were represented by the shear strain mean values. Divergences between matrix strain and fibre stress related parameters were summarized in Table 4.11, together with the collagen network efficiencies evaluated from the discussions of Section D.II.b. These discussions that fully integrated FCQ, matrix shear strain, and range of motion results, clearly show that the mathematical balance between the RMS and RSD parameters giving the FCQ values (Eq. (4.9)), should be weighted by the annulus matrix mean shear strain values. Among the other studied biomechanical parameters not included in Equation (4.9), facet contact force results were affected by the annulus collagen network organization. Nonetheless, variances in zygapophysial joint activation were most often explained by the different response of only few annulus quadrants to loading. Thus, facet contact forces can hardly be taken as a parameter contributing to a general mathematical criterion for local annulus stabilization. Ranges of motion were also often mainly controlled by specific annulus quadrants. Nevertheless, quality of the fibre-induced stabilization in these specific quadrants frequently influenced the tensional or deformational state of the other quadrants. Therefore, ranges of motions were indirectly linked to the overall mechanical response of the intervertebral disc and could be integrated to the computation of the FCQ parameter to take into account the interactions between different annulus quadrants. However, the role of the intervertebral disc is obviously, neither to limit the ranges of motion as much as possible, nor to allow infinite deformations of the motion segments. Ranges of motion need to be within some limits that ensure overall segment flexibility, stability and integrity of the tissues. Therefore, optimal ranges of motions need to be defined relatively to a reference.

Table 4.11: Summary of the different fibre network evaluations. Best and worst local fibre efficiencies were reported based on FCQ parameter values, annulus matrix mean total shear strain values, and on the discussions of Paragraph D.II. that included FCQ, mean total shear strain values, and ranges of motion. a) Sagittal flexion.

Load case	Level	Quadrant	Collagen fibre network stabilizing effect					
			FCQ based criteria		Annulus matrix shear strain based criteria		Interpretation based criteria	
			Best	Worst	Best	Worst	Best	Worst
Flexion	L3-L4	ANT	ISO	ANI	ANI	RAD	TAN Most transversal fibres – No orientation radial gradient	RAD Axial inner fibres – Orientation radial gradient
		LAT	TAN	ANI	ISO	RAD	TAN Fibre orientation tangential gradient – No orientation radial gradient	RAD Axial inner fibres – Orientation radial gradient
		PLAT	TAN	RAD	TAN	ISO	TAN Most axial fibres throughout annulus thickness	ISO Most transversal fibres throughout annulus thickness
		POST	ANI	RAD	ANI	ISO	ANI Most axial inner fibres – Outer fibres reorient and become activated	ISO Most transversal fibres throughout annulus thickness
		ANT	TAN	ANI	ANI	RAD	TAN Most transversal fibres – No orientation radial gradient	RAD Axial inner fibres – Orientation radial gradient
	L4-L5	LAT	TAN	ANI	ANI	RAD	TAN Fibre orientation tangential gradient – No orientation radial gradient	RAD Axial inner fibres – Orientation radial gradient
		PLAT	ANI	RAD	TAN	RAD	ANI Most axial inner fibres – Outer fibres reorient and become activated	RAD 45° oriented inner fibres efficient but transversal outer fibres do not reorient
		POST	ANI	RAD	TAN	RAD	ANI Most axial inner fibres – Outer fibres reorient and become activated	RAD 45° oriented inner fibres efficient but transversal outer fibres do not reorient

Table 4.11: Summary of the different fibre network evaluations. Best and worst local fibre efficiencies were reported based on FCQ parameter values, annulus matrix mean total shear strain values, and on the discussions of Paragraph D.II. that included FCQ, mean total shear strain values, and ranges of motion. b) Sagittal extension.

Load case	Level	Quadrant	Collagen fibre network stabilizing effect					
			FCQ based criteria		Annulus matrix shear strain based criteria		Interpretation based criteria	
			Best	Worst	Best	Worst	Best	Worst
Extension	L3-L4	ANT	ISO	RAD	RAD	ISO	RAD 45° oriented inner fibres resist both nucleus pressure and axial stretch	ANI Inner fibre stress concentration – Extremely transversal outer fibres
		LAT	TAN	ANI	RAD	TAN	RAD 45° oriented inner fibres resist in-sagittal plane axial shear	ANI Inner fibre stress concentration due to lack of anterior stabilization – transversal outer fibres
		PLAT	TAN	ANI	RAD	TAN	RAD Anterior and lateral stabilization due to 45° oriented inner fibres	TAN Lack of anterior stabilization
		POST	RAD ? TAN ? ISO ? ANI ?	RAD ? TAN ? ISO ? ANI ?	ANI	TAN	ISO Most transversal fibres – No orientation radial gradient	TAN Most axial fibres throughout annulus thickness
	L4-L5	ANT	ISO	ANI	RAD	TAN	RAD 45° oriented inner fibres resist both nucleus pressure and axial stretch	TAN Most transversal fibres throughout annulus thickness
		LAT	RAD	ISO	RAD	TAN	RAD 45° oriented inner fibres resist in-sagittal plane axial shear	TAN Great lack of anterior stabilization
		PLAT	ISO	RAD	RAD	TAN	ISO Most transversal fibres throughout annulus thickness	TAN Most axial fibres throughout annulus thickness
		POST	TAN	RAD	ISO	ANI	ISO Most transversal fibres – No orientation radial gradient	ANI Most axial inner fibres – Orientation radial gradient

Table 4.11: Summary of the different fibre network evaluations. Best and worst local fibre efficiencies were reported based on FCQ parameter values, annulus matrix mean total shear strain values, and on the discussions of Paragraph D.II. that included FCQ, mean total shear strain values, and ranges of motion. c) Axial compression.

Load case	Level	Quadrant	Collagen fibre network stabilizing effect					
			FCQ based criteria		Annulus matrix shear strain based criteria		Interpretation based criteria	
			Best	Worst	Best	Worst	Best	Worst
Axial compression	L3-L4	ANT	TAN	RAD	TAN	RAD	TAN Most transversal fibres – No orientation radial gradient	RAD Axial inner fibres – Orientation radial gradient
		LAT	TAN	RAD	ISO	RAD	ISO Most transversal fibres – No orientation radial gradient	RAD Axial inner fibres – Orientation radial gradient – Bad anterior stabilization
		PLAT	ISO	ANI	ISO	TAN	ISO Most transversal fibres – No orientation radial gradient	TAN Axial fibres – Not sufficiently compensated by anterior fibres
		POST	ISO	TAN	ISO	ANI	ISO Most transversal fibres – No orientation radial gradient	ANI Extremely axial inner fibres

Table 4.11: Summary of the different fibre network evaluations. Best and worst local fibre efficiencies were reported based on FCQ parameter values, annulus matrix mean total shear strain values, and on the discussions of Paragraph D.II. that included FCQ, mean total shear strain values, and ranges of motion. d) Spinal erector-like loading.

Load case	Level	Quadrant	Collagen fibre network stabilizing effect					
			FCQ based criteria		Annulus matrix shear strain based criteria		Interpretation based criteria	
			Best	Worst	Best	Worst	Best	Worst
Spinal erector-like loading	L3-L4	ANT	ISO	RAD	TAN	ISO	TAN Transversal fibres most able to resist major nucleus influence	RAD Extremely axial inner fibres – Inner stress concentration – no resistance to nucleus pressure
		LAT	ISO	ANI	RAD	TAN	RAD 45° oriented inner fibres resist in-sagittal plane axial shear	ANI Inner fibre stress concentration – High matrix shear due to lack of anterior stabilization
		PLAT	RAD	TAN	TAN	RAD	ISO Most transversal fibres throughout annulus thickness	ANI Most axial inner fibres – Orientation radial gradient
		POST	RAD	ISO	TAN	RAD	ISO Most transversal fibres throughout annulus thickness	ANI Most axial inner fibres – Orientation radial gradient
	L4-L5	ANT	ISO	RAD	ANI	ISO	ISO Best compromise to resist axial stretch and nucleus pressure	RAD Extremely axial inner fibres – Inner stress concentration – no resistance to nucleus pressure
		LAT	ANI	TAN	TAN	RAD	RAD 45° oriented inner fibres resist in-sagittal plane axial shear	ISO Farthest fibres from 45°
		PLAT	TAN	RAD	RAD ?	TAN	ISO Most transversal fibres throughout annulus thickness	ANI Most axial inner fibres – Orientation radial gradient
		POST	TAN	RAD	ISO ?	ANI	ISO Most transversal fibres throughout annulus thickness	ANI Most axial inner fibres – Orientation radial gradient

Table 4.11: Summary of the different fibre network evaluations. Best and worst local fibre efficiencies were reported based on FCQ parameter values, annulus matrix mean total shear strain values, and on the discussions of Paragraph D.II. that included FCQ, mean total shear strain values, and ranges of motion. e) Lateral bending.

Load case	Level	Quadrant	Collagen fibre network stabilizing effect					
			FCQ based criteria		Annulus matrix shear strain based criteria		Interpretation based criteria	
			Best	Worst	Best	Worst	Best	Worst
Lateral bending	L3-L4	ANT	ISO	RAD	TAN	RAD	TAN Most transversal inner fibres, able to resist major nucleus influence	RAD Most axial inner fibres – Orientation radial gradient
		LAT	ANI	ISO	TAN	ISO ? ANI ?	TAN Best compromise to resist rotation side disc bulge and anti-rotation side axial stretch	ISO Most transversal fibres throughout annulus thickness – Do not resist anti-rotation side axial stretch
		PLAT	ANI	ISO	ISO	ANI	RAD 45° inner fibres and transversal outer fibres resist axial shear, axial stretch and bulging	ISO Most transversal fibres throughout annulus thickness do not resist neither axial stretch nor axial shear
		POST	ANI	ISO	ISO	ANI	RAD 45° inner fibres and transversal outer fibres resist axial shear, axial stretch and bulging	ANI Extremely axial inner fibres do not resist nucleus loading – Outer fibres not sufficiently transversal
		ANT	TAN	ANI	TAN	RAD	TAN Most transversal inner fibres, able to resist major nucleus influence	RAD Most axial inner fibres – Orientation radial gradient
	L4-L5	LAT	RAD	ISO	TAN	ISO ? ANI ?	TAN Most transversal inner fibres, able to resist major nucleus influence	ISO Most transversal fibres throughout annulus thickness – Do not resist anti-rotation side axial stretch
		PLAT	ANI	ISO	RAD	ANI	RAD 45° inner fibres and transversal outer fibres resist axial shear, axial stretch and bulging	ISO Most transversal fibres throughout annulus thickness do not resist neither axial stretch nor axial shear
		POST	ANI	ISO	RAD	ANI	RAD 45° inner fibres and transversal outer fibres resist axial shear, axial stretch and bulging	ANI Extremely axial inner fibres do not resist nucleus loading – Outer fibres not sufficiently transversal

Table 4.11: Summary of the different fibre network evaluations. Best and worst local fibre efficiencies were reported based on FCQ parameter values, annulus matrix mean total shear strain values, and on the discussions of Paragraph D.II. that included FCQ, mean total shear strain values, and ranges of motion. f) Axial rotation.

Load case	Level	Quadrant	Collagen fibre network stabilizing effect					
			FCQ based criteria		Annulus matrix shear strain based criteria		Interpretation based criteria	
			Best	Worst	Best	Worst	Best	Worst
Axial rotation	L3-L4	ANT	ANI	ISO	RAD	ISO	RAD 45° inner fibres resist transversal shear and coupled axial stretch	ISO Fibres optimized neither for coupled axial nor for nucleus-induced transversal deformations
		LAT	ANI	TAN	RAD	ANI	RAD 45° inner fibres resist main transversal and coupled axial shear	TAN Highly stressed outer fibres – high shear strains – large coupled rotation due to lack of anterior stabilization
		PLAT	ISO	ANI	RAD	ANI	RAD 45° inner fibres resist main transversal shear	ANI Highly axial inner fibres unable to support high intradiscal pressure due to large motions
		POST	ANI	RAD	TAN	RAD	TAN Homogeneous fibre network most closely oriented to 45°	RAD Highly stressed inner fibres – Highest shear strains due to flexion-like coupled motion
		ANT	ANI	ISO	RAD	ANI	RAD 45° inner fibres resist transversal shear, and coupled axial stretch	ANI Extremely transversal outer fibres not able to resist main and coupled motion
	L4-L5	LAT	ANI	ISO	RAD	ANI	RAD 45° inner fibres resist main transversal and coupled axial shear	ANI High coupled motions and shear strains due to lack of anterior stabilization
		PLAT	ISO	RAD	RAD	ANI	RAD 45° inner fibres resist main transversal shear	ANI High shear strain and postero-anterior coupled rotation due to orientation radial gradient and axial inner fibres
		POST	ISO	ANI	RAD	ANI	ISO Homogeneous transversal network adapted to coupled rotation-induced local nucleus loading	ANI High shear strain and postero-anterior coupled rotation due to orientation radial gradient and axial inner fibres

Taking into account the different elements of discussion about fibre strain radial distributions, fibre activation, matrix shear strains, and ranges of motion, an improved form of Equation (4.9) was defined as follow:

$$FCQ_{quadrant}^{segment} = \ln \left(1 + \frac{e^{RMS_{quadrant}^{fibre}}}{e^{(RED_{quadrant}^{fibre} + MSE_{quadrant}^{matrix})}} e^{-|ROM^{segment} - ROM_0^{segment}|} \right) \quad (4.10)$$

where $FCQ_{quadrant}^{segment}$ is the Fibre Contribution Quality parameter characterizing a given annulus quadrant of a given spine segment. $RMS_{quadrant}^{fibre}$, $RED_{quadrant}^{fibre}$, and $MSE_{quadrant}^{matrix}$, are respectively the associated fibre radial mean stress, fibre strain radial distribution, and matrix mean total shear strain parameters. $ROM^{segment}$ defines the range of motion of the studied segment, and $ROM_0^{segment}$ is a reference optimal motion. In Equation (4.10), the fibre stress related RSD parameter used in (4.9) was replaced by the fibre strain related $RED_{quadrant}^{fibre}$ parameter. Both parameters quantified the homogeneity of fibre activation through annulus thickness. However, in Equation (4.9), the RSD parameter was the absolute slope value of the linear regression given by fibre stress changes, from the outer to the inner element radial layer of an annulus quadrant. One limitation of this linear parameter was that it was not able to capture uneven fibre stress radial distributions due to stress divergences in mid-annulus element layers only. Therefore, unlike the RSD parameter values, the $RED_{quadrant}^{fibre}$ parameter values were computed from a second order polynomial regression on mean fibre tensile strain changes from the outer to the inner annulus radial element layers. Given a and b , the respective second and first order coefficients of such polynomial regression in a given annulus quadrant, $RED_{quadrant}^{fibre}$ was then calculated as:

$$RED_{quadrant}^{fibre} = \sqrt{4a^2 + b^2} \quad (4.11)$$

It can be easily verified that, as Equation (4.9), Equation (4.10) satisfies the following essential conditions:

$$1. \quad \frac{\partial FCQ_{quadrant}^{segment}}{\partial RED_{quadrant}^{fibre}} = \frac{\partial FCQ_{quadrant}^{segment}}{\partial MSE_{quadrant}^{matrix}} = - \frac{\partial FCQ_{quadrant}^{segment}}{\partial RMS_{quadrant}^{fibre}} < 0$$

2a. For a given load case, as the segment range of motion diverges from the optimal reference, $ROM_0^{segment}$:

$$\left(\frac{\partial FCQ_{quadrant}^{segment}}{\partial ROM^{segment}} \right) \frac{\partial |ROM^{segment} - ROM_0^{segment}|}{\partial ROM^{segment}} > 0 = \frac{\partial FCQ_{quadrant}^{segment}}{\partial RED_{quadrant}^{fibre}} = \frac{\partial FCQ_{quadrant}^{segment}}{\partial MSE_{quadrant}^{matrix}} < 0$$

2b. As the range of motion evolves toward the reference, $ROM_0^{segment}$:

$$\left(\frac{\partial FCQ_{quadrant}^{segment}}{\partial ROM^{segment}} \right) \frac{\partial |ROM^{segment} - ROM_0^{segment}|}{\partial ROM^{segment}} < 0 = \frac{\partial FCQ_{quadrant}^{segment}}{\partial RMS_{quadrant}^{fibre}} > 0$$

3. $FCQ_{quadrant}^{segment}$ becomes minimum when, either the fibre strain distribution parameter, or the matrix mean shear strain parameter, or the divergence of the range of motion to the optimal reference, become infinite:

$$\lim_{\substack{RED_{quadrant}^{fibre} \rightarrow +\infty \\ \text{or } MSE_{quadrant}^{matrix} \rightarrow +\infty \\ \text{or } |ROM^{segment} - ROM_0^{segment}| \rightarrow +\infty}} [FCQ_{quadrant}^{segment} (RMS_{quadrant}^{fibre}, RED_{quadrant}^{fibre}, MSE_{quadrant}^{matrix}, ROM^{segment})] = 0$$

4. Minimum $RED_{quadrant}^{fibre}$, $MSE_{quadrant}^{matrix}$, and $|ROM^{segment} - ROM_0^{segment}|$ physically acceptable values always give maximum $FCQ_{quadrant}^{segment}$ values:

$$\ln \left(1 + \frac{e^{RMS_{quadrant}^{fibre}}}{e^{(RED_{quadrant}^{fibre} + MSE_{quadrant}^{matrix})}} e^{-|ROM^{segment} - ROM_0^{segment}|} \right) \leq \ln \left(1 + e^{RMS_{quadrant}^{fibre}} \right)$$

$$\forall (RMS_{quadrant}^{fibre}, RED_{quadrant}^{fibre}, MSE_{quadrant}^{matrix}, ROM^{segment}) \in \mathfrak{R}^{+4}$$

For any load case, at each spine level, and in each annulus quadrant, Equation (4.10) is then *a priori* able to quantify the balance between different biomechanical parameters identified to be relevant to annulus stabilization. Similarly to Equation (4.9), each parameter of Equation (4.10) has a similar influence on the absolute variation of the FCQ parameter. Nevertheless, the already calculated RMS, RSD parameters, and matrix mean total shear strain values, shows that the different terms of Equation (4.10) may vary over different orders of magnitude. Therefore, in order to definitively ensure equal influence of each parameter in the computation of the $FCQ_{quadrant}^{segment}$ values, the $RMS_{quadrant}^{fibre}$, $RED_{quadrant}^{fibre}$, $MSE_{quadrant}^{matrix}$, and $|ROM^{segment} - ROM_0^{segment}|$ values were only allowed to vary between 0 and 1. This was achieved by normalizing each of these parameters by the maximum value found over the whole set of models to compare. Terms of Equation (4.10), i.e., $RMS_{quadrant}^{fibre}$, $RED_{quadrant}^{fibre}$, $MSE_{quadrant}^{matrix}$, and $|ROM^{segment} - ROM_0^{segment}|$ were then respectively replaced by $\overline{RMS}_{quadrant}^{fibre}$, $\overline{RED}_{quadrant}^{fibre}$, $\overline{MSE}_{quadrant}^{matrix}$, and $\overline{dROM}^{segment}$ that were defined for each model, by:

$$\overline{RMS}_{quadrant}^{fibre} = \frac{RMS_{quadrant}^{fibre}}{\max \left\{ (RMS_{quadrant}^{fibre})_{RAD}, (RMS_{quadrant}^{fibre})_{TAN}, (RMS_{quadrant}^{fibre})_{ISO}, (RMS_{quadrant}^{fibre})_{ANI} \right\}} \quad (4.12a)$$

$$\overline{RED}_{quadrant}^{fibre} = \frac{RED_{quadrant}^{fibre}}{\max\left\{\left(RED_{quadrant}^{fibre}\right)_{RAD}, \left(RED_{quadrant}^{fibre}\right)_{TAN}, \left(RED_{quadrant}^{fibre}\right)_{ISO}, \left(RED_{quadrant}^{fibre}\right)_{ANI}\right\}} \quad (4.12b)$$

$$\overline{MSE}_{quadrant}^{matrix} = \frac{MSE_{quadrant}^{matrix}}{\max\left\{\left(MSE_{quadrant}^{matrix}\right)_{RAD}, \left(MSE_{quadrant}^{matrix}\right)_{TAN}, \left(MSE_{quadrant}^{matrix}\right)_{ISO}, \left(MSE_{quadrant}^{matrix}\right)_{ANI}\right\}} \quad (4.12c)$$

$$\overline{dROM}^{segment} = \frac{dROM^{segment}}{\max\left\{\left(dROM^{segment}\right)_{RAD}, \left(dROM^{segment}\right)_{TAN}, \left(dROM^{segment}\right)_{ISO}, \left(dROM^{segment}\right)_{ANI}\right\}} \quad (4.12d)$$

With

$$dROM^{segment} = \left| ROM^{segment} - ROM_0^{segment} \right| \quad (4.12e)$$

As previously discussed, parameter $dROM^{segment}$, described in (4.12e), take into account coupling between annulus quadrants, illustrated by the fact that quadrants with a decisive role in limiting ranges of motion can positively or negatively affect other quadrants. However, in the study of annulus collagen network local stabilizing effect, $dROM^{segment}$ values should not be allowed to fully compensate other parameter values that are exclusively associated to local annulus mechanics. Therefore, influence of $dROM^{segment}$ was controlled by associating the parameter to a real positive coefficient, α , so that $\alpha \in [0,1]$.

Taking into account the parameter value normalization, and the control of the influence of ranges of motion in local calculations, Equation (4.10) was re-expressed as:

$$FCQ_{quadrant}^{segment} = \ln \left(1 + \frac{e^{\overline{RMS}_{quadrant}^{fibre}}}{e^{\left(\overline{RED}_{quadrant}^{fibre} + \overline{MSE}_{quadrant}^{matrix}\right)}} e^{-\alpha \overline{dROM}^{segment}} \right) \quad (4.13)$$

Equation (4.13) was tested with the simulation results obtained under axial rotation, where Equation (4.9) mostly failed in returning FCQ parameter values representative of local annulus stabilizations. In these new calculations, α was set to 0.5, and according to the discussion developed in Paragraph D.II.b.6), $dROM^{L3-L4}$ and $dROM^{L4-L5}$ parameter values were computed by taking as optimal motion references, i.e. ROM_0^{L3-L4} and ROM_0^{L4-L5} , the smallest main motion values returned by the RAD model. Results are shown in Figure 4.39.

On one hand, Table 4.11f shows that the L3-L4 and L4-L5 FCQ parameter values computed from Equation (4.9) respectively predicted 0% and 25% of the annulus networks identified, after discussion, to best stabilize the annulus quadrants under axial rotation. On the other hand, comparing Table 4.11f with Figure 4.39, reveals that at both levels, FCQ values returned by Equation (4.13) were able to predict 75% of the discussed best stabilizing networks. L3-L4 annulus collagen networks, identified as the worst stabilizing ones, after discussion, were all predicted by Equation (4.9), but only 50% of them were predicted by Equation (4.13). At the L4-L5 level, Equation (4.13) had a similar rate of success as at the L3-L4 level, but Equation (4.9) could only predict 25% of the discussed worst stabilizing annulus configurations. Note, however, that the discussion developed in Paragraph D.II.b.6), as all the other discussions of Section D.II.b., was only qualitative, and mainly served to highlight the contradictions between the FCQ values given by Equation (4.9), the annulus matrix mean shear strains, and the ranges of motion. Equation (4.13), in change, represents an equilibrated mathematical balance between all the biomechanical parameters found to be linked to annulus stabilization. Study of the individual $\overline{RMS}_{quadrant}^{fibre}$, $\overline{RED}_{quadrant}^{fibre}$, $\overline{MSE}_{quadrant}^{matrix}$, and $\overline{dROM}^{segment}$ parameter values obtained under axial rotation, suggests that the major discrepancies between the discussion results reported in Table 4.11f and Equation (4.13) results, were due to the quadratic variation of fibre strain radial distributions. In the discussion based on Equation (4.9), such behaviour could not be taken into account, since radial homogeneity of fibre activation was quantified by fibre stress linear radial variations. Moreover, differences in quadratic variations of fibre activation in the different models could hardly be qualitatively evaluated. Nevertheless, identifying sharp fibre strain variations within the annulus fibrosus was relevant, as it allowed better detections of local fibre peak strains and showed local over- or under activations due to non-adequate distributions of the fibre orientations. To a lower extend, but also contributing to explain differences between Equation (4.13) predictions, and discussion based results, was the parameter $\overline{dROM}^{segment}$. $\overline{dROM}^{segment}$ depended on the choice of reference ranges of motion. Smallest main axial rotation motions were taken to respect the subjective judgment made about ranges of motion in discussion D.II.b.6) and to be able to compare the corresponding conclusions with the results of the objective mathematical function (4.13). $\overline{dROM}^{segment}$ would then probably need to be differently adjusted. Nevertheless, in case of having a model and experimental data matching together, this parameter could allow Equation (4.13) to estimate the influence of the annulus collagen network on the biomechanical compromise required to fit simulated motions to experimental data. Obviously, Equation (4.13) should be tested with the other studied load cases and its predictions confronted to the discussion based on both Equation (4.9) and matrix shear strain results. However, preliminary results under axial rotation suggest that this updated mathematical formulation is promising in quantifying the stabilizing effect of specific collagen network organizations.

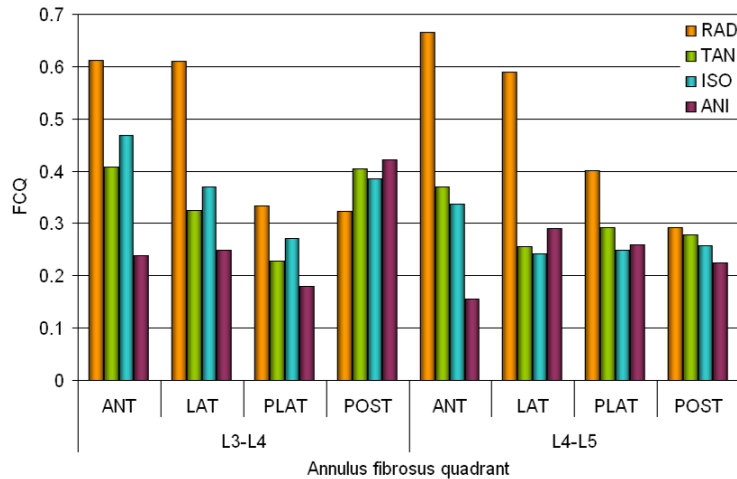


Figure 4.39: Fibre Contribution Quality parameter calculated from Equation (4.13), in each annulus quadrant of each level of the L3-L5 lumbar spine bi-segment finite element model.

E. Outcomes

I. Modelling remodelling?

The study developed in this Chapter demonstrates the large influence of modelling different natural non-pathologic annulus fibrosus collagen orientations, on both, intervertebral disc mechanics, and other related lumbar spine biomechanical characteristics, i.e. ranges of motion, and zygapophysial joint contact forces. The general biochemistry (Brickley-Parson and Glimcher, 1984) and the collagen criss-cross pattern (Hickey and Hukins, 1980) of non-degenerated human lumbar spine annuli fibrosi were both found almost independent of ageing. Thus, it was suggested that these features result more from genetic programming than from acquired functional adaptations. Moreover, to our knowledge, besides degenerative or post-traumatic changes, mechanically driven structural remodelling of the annulus has often been suggested (Brickley-Parson and Glimcher, 1984; Humzah and Soames, 1988; Hayes *et al.*, 2001; Bruehlmann *et al.*, 2002; Melrose *et al.*, 2008), but never demonstrated. *In vivo* studies reported specific changes in annulus and nucleus cell gene expressions when rat tail intervertebral discs were immobilized (MacLean *et al.*, 2003) and/or dynamically loaded under compression by means of an external fixator (MacLean *et al.*, 2008; MacLean *et al.*, 2005). However, maximum duration of the reported mechanical stimulations was 4h, which is insignificant in comparison to the time scales of repetitive disc loading patterns, possibly occurring in an active patient. Furthermore, the slow turnover of large avascular structures, such as the intervertebral disc, would probably impose follow-up periods of months or years, before tissue structural changes could be observed. Nevertheless, non-unique collagen geometrical organizations in non-degenerated human lumbar annuli, together with the ability of annulus fibres to reorient in the load directions (Guerin and Elliot, 2006), lead to believe that long-term production of annulus extra-cellular matrix should be affected when cells are under the

influence of repetitive loading patterns. Actually, regional composition differences were observed between normal and scoliotic annuli fibrosi, and were related to the shift of local compressive and tensile mechanical environments impose by the deformity (Brickley-Parson and Glimcher, 1984). A reduction in the apparent criss-cross angle of anterior annulus collagen fibrils with age was also reported (Hickey and Hukins, 1982). Since axial compression is the dominant load in the lumbar spine (Chap. 1), and transversal annulus fibres best resist to external axial compressive loads, such observation could be interpreted as a mechanical adaptation of the annulus organization. Furthermore, results obtained in the present Chapter indicate that optimal collagen organizations of the lumbar annuli fibrosi should be locally considered, given that most of the motions involved different loading regimes in different annulus areas. A functional annulus adaptation to long-term and repetitive loads would then explain the apparition of topographic differences in the collagen of mature adult annuli, as a function of both quadrants and distance to the nucleus pulposus (Brickley-Parson and Glimcher, 1984).

The existence of a long-term mechanical adaptation of the annulus fibrosus collagen network organization would have a significant impact on the development of lumbar spine models. On one and, in Chapter 1, it has been shown that annulus collagen fibres exert strong tractions on the adjacent vertebral cortex. On the other hand, a strain energy density-based bone remodelling theory has been successfully applied to a lumbar spine model to explain the natural overall shape of the vertebral bodies and their cortex (Goel *et al.*, 1995b; Grosland and Goel, 2007). Remodelling resulted mainly from the mechanical interaction of the vertebrae with the soft tissues, and under axial compression, largest geometrical changes were predicted nearby the annuli fibrosi (Goel *et al.*, 1995b). Thus, geometry (and material properties) of lumbar vertebral bodies can be considered in equilibrium with mechanical forces, mainly imposed by both, external loads, and the reaction of the intervertebral disc. This idea was supported by the results presented in Chapter 3 and in Section C.III, indicating a strong interaction between lumbar spine segment geometries and annulus fibre stresses. Therefore, particular bone geometries acquired by any imaging technology for further modelling, should have been shaped by the *in vivo* interactions the bones had with particular intervertebral disc configurations. It becomes then obvious that mechanical coherence of models created from particular geometries implies at least the modelling of annulus characteristics somehow adapted to the shape of the vertebral bodies. Unfortunately, a thorough characterization of the annulus fibrous organization is a highly demanding and time consuming task (Holzapfel *et al.*, 2005) that involves dissection techniques and cannot be systematically performed. One possibility to ensure coherence between one known bone geometry and one unknown annulus fibrosus configuration would be to play with the apparent material properties of annulus fibres, until some criteria suggesting mechanical stability (as used in this study) are fulfilled. Nevertheless, according to the low turnover expected from the avascular intervertebral disc, it has been shown that mechanical properties of the annulus fibre layers were not likely to change with time, except in the outer annulus (Skrzypiec *et al.*, 2007). Global increase of collagen I content was identified with age, but relative distributions of collagen I to collagen II were reported to remain constant (Brickley-Parson and Glimcher, 1984). Moreover, Marchand and Ahmed (Marchand and Ahmed, 1990) reported that ageing may induce topographical changes in the annulus laminate structure, but the overall size of the

collagen bundles was not significantly affected with age. Hence, reasonable and straightforward modifications of annulus fibre mechanical properties would be restricted either to a parameterization of the overall network stiffness related to collagen I content, or to a variation of collagen stiffness according to the range of mechanical properties available in the literature. Nevertheless, according to annulus contents in collagen type I and II (Brickley-Parson and Glimcher, 1984), stiffness of the fibre layers has been found to only significantly differ from the outer to the inner annulus (Holzapfel *et al.*, 2005). Therefore, playing with annulus fibre material properties limits the chance to locally adapt the tissue response, which appeared to be a necessity for lumbar spine model calibration (Schmidt *et al.*, 2006).

As shown by the present study, and according to experimental evidences (Guerin and Elliot, 2006), annulus fibres are able to follow and limit local annulus deformations by reorienting. This process greatly affects the local biomechanical response of the intervertebral disc, depending on both simulated load cases and undeformed fibre orientations. Therefore, taking profit of the existence of non-unique collagen network orientation patterns in non-pathologic intervertebral discs, the orientation of the undeformed annulus fibres could be locally adapted to specific bone geometries for the creation of biomechanically coherent models. As a first approach to lumbar spine modelling, such method would be more efficient and more respectful of the actual knowledge about vertebrae and intervertebral disc remodelling than modifying the material properties of the modelled collagen. Mechanically adapted fibre orientations could then be determined through maximization or minimization of an objective function, similar to Equation (4.13), in a non-linear optimization procedure. Note that such a study would be highly relevant for the creation of patient specific models or for the assessment of composite artificial disc designs as presented in (Noailly *et al.*, 2005) and Chapter 5. Nevertheless, more physiological mechanical boundary conditions should be investigated, in terms of both static loading and loading history.

II. Improving models

In this study, some of the predictions, i.e. ranges of motion and intradiscal pressure, affected by the annulus collagen network organization are experimentally accessible and were often used as criteria for model validation (Chap. 3). In case of mismatch between *in vitro* and simulated data, the most common way used to adjust predictions has been to adapt the material properties of several components, such as ligaments or intervertebral disc tissues, until desired predictions are obtained (Chap. 3, (Schmidt *et al.*, 2006; Schmidt *et al.*, 2007a; Bowden *et al.*, 2008)). Due to the simplifying assumptions used in biologic tissue modelling, and to the large result variations in tissue experimental characterizations, some flexibility exists regarding the material properties of the intervertebral disc components. Playing with this flexibility to calibrate lumbar spine models makes then sense. However, the present work suggests that, doing so, intervertebral disc or other tissue material properties allowing a good match between *in vitro* and simulated range of motion and/or intradiscal pressure will depend on the initial choice of the collagen network. Thus, it would be interesting to verify whether different validated combinations of vertebral geometry, annulus collagen

orientations, and adjusted mechanical properties would lead to similar load transfers within the modelled spine segments. This is, however, hardly feasible using the literature and should be matter of a specific research. Interestingly, one of the most thorough model calibration procedures reported so far, included a modification of the facet joint orientation, together with ligament, annulus, and nucleus material properties, to be able to take into account a large set of experimental data (Schmidt *et al.*, 2007a). Such a procedure led to a model able to accurately reproduce a number of experimental ranges of motion. However, orientation of the articular processes was part of the geometrical information acquired from CT scans and should have remained fixed, naturally fitted to the rest of the segment geometry. Instead, as annulus fibre orientation is related to the load transfer through the zygapophysial joints (§ D.II.c.), the authors could have tried to parameterize the arbitrary chosen annulus fibre collagen network orientation. Therefore, considering annulus collagen fibre orientation as a possible calibration factor could allow approximating in vitro data while keeping some control on the load transfers and taking into account the particular geometry of the model. This could be done by maximizing Equation (4.13) over a set of experimental ranges of motion, introduced through parameter $dROM$ (Eq. (4.12e)).

The present study also highlighted the importance of load transfers between nucleus and annulus, for annulus fibre activations and, consequently, for the overall disc biomechanics. Such outcome is highly relevant to model calibration studies involving variations of the intervertebral disc material properties. Structure- and/or physical chemistry- related specific behaviours of disc components such as collagen fibres, or proteoglycan matrices, are generally recognised as part of the disc functional mechanics, but are not always modelled. Due to their complexity, mechanistic equations representing such behaviours are rarely used in large models, where they are replaced by phenomenological formulations. The present simulations showed that phenomenological hyperelastic formulations for the nucleus pulposus do not allow predicting the characteristic hydrostatic stress state of the disc core and may limit the accuracy of load transfer predictions from the nucleus to the surrounding tissues. Focussing on multiphase disc materials, adjusting phenomenological hyperelastic or linear Hookean parameters for a given structure, could then simply lead to a positive compensation of modelling errors, giving acceptable global behaviours. However, such kind of model calibration would not allow complementing clinical or experimental data, by predicting the hardly accessible three-dimensional mechanical environments of the spine components. Some studies have already focussed on more realistic mechanical descriptions of intervertebral disc tissues and seem promising for better description of the spine biomechanics, at both organ and tissue levels (Williams *et al.*, 2007; Schroeder *et al.*, 2008). Nonetheless, if structure- or composition-related mechanistic models cannot be implemented to simulate tissue behaviours, directly using experimental phenomenological material parameters reported in the literature seems preferable. In such case, intervertebral disc calibration is still possible by adjusting undetermined parameters, such as fibre orientation, rather than tissue equations with already known limitations.

At such point, instead of attempting reproducing experimental data with great inter-individual and inter-protocol variations, researchers should first investigate the most controllable and truthful modelling hypotheses to understand the coherence of the

lumbar spine biomechanics in terms of functional tissue strain/stress distributions. Indeed, the present investigation of different natural collagen network organizations in the annulus followed this kind of approach. Some new relevant hypotheses were drawn about the stabilizing mechanisms induced by the organized fibrous network of the intervertebral disc. One of these hypotheses was that an optimal annulus fibre arrangement should distribute strains as good as possible through the thickness of the tissue. This hypothesis was motivated by the inhomogeneous stiffness distribution in the composite structure and by the idea that tensile strain concentrations in the softest inner annulus layers should be limited. Nevertheless, mapping of annulus collagen stiffness is due to the presence of high contents of collagen II in the inner layers, which has been related to the nucleus-induced osmolarity. Beside collagen II, extra-cellular matrix osmolarity has been shown to stimulate the expression of proteoglycans by intervertebral disc cells (Wuertz *et al.*, 2007), which is in agreement with increasing content of proteoglycans from the outer to the inner annulus (Iatridis *et al.*, 2007). It appears then obvious that modelling both collagen types through the annulus fibrosus is conceptually consistent only if the annulus matrix is modelled as a progressively hydrated material from the outer to the inner annulus. At such point, the hypothesis of even strain distributions through the fibrous structure should be re-examined by taking into account the water load bearing capacity in the most inner annulus layers. This is a good example to show how literature-based annulus tissue phenomenological model and parameters can raise relevant questions that motivate further model enhancements as part of a logical and progressive process. Such coordinated process could be called “model remodelling”.

Chapter 5

*"Stars not where they seemed or where calculated to be, but
nobody need worry."*

(*"Einstein theory triumphs", The New York Times, November 10, 1919*)

Chapter 5

- CASE STUDY -
APPLICATION OF THE MODEL FOR THE EVALUATION OF A
NOVEL INTERVERTEBRAL DISC SUBSTITUTE

A. Introduction	317
B. Materials and methods	320
I. Models Geometry	320
a. Intact model	320
b. Disc substitute	323
1) Device body	323
2) Endplates	325
c. Treated model	326
II. Material properties & model corroborations	327
a. Intact model	327
b. Device substitute	328
III. Boundary conditions & Studied parameters	331
C. Results	333
I. Model corroborations	333
a. Intact model	333
b. Device model	335
II. Comparison of intact and treated models	337
a. Ranges of motion	337
b. Zygapophysial joint contact forces	338
c. Vertebral body loading	340
1) Load distribution under pure rotations	340
2) Body weight-like load effect	344
(i) Trabecular bone	344
(ii) Cortical bone	345
(iii) Bony endplates	347
d. L3-L4 intervertebral disc loading	348
1) Annulus fibrosus	348
(i) Load distribution under pure rotations	348
(ii) Body weight-like load effect	352
2) Nucleus pulposus	354
III. Prosthesis “biomechanics”	355
a. p-HEMA/PMMA matrix	355
b. PET fibres	357
c. General load distribution	359
D. Discussion	360
I. Device modelling	360
II. Ranges of motion	361
III. Zygapophysial joints	362
a. Axial rotation	362

b. Sagittal rotations	363
1) Flexion	363
2) Extension	364
IV. Prosthesis “biomechanics”	364
a. Internal loads & device resistance	364
b. Functional load distributions	365
V. Vertebral bodies	366
a. Unloaded areas	367
1) Away from the disc substitute	367
2) Adjacent to the disc substitute	367
b. Overloaded areas	368
1) Away from the disc substitute	368
2) Adjacent to the disc substitute	369
VI. Intact L3-L4 intervertebral disc	370
a. Pure rotations	370
1) Load- & displacement-controlled flexion.....	370
2) Extension & axial rotation	371
b. Body weight-like load effect	372
VII. Comparison with other studies.....	373
E. Conclusion	374

A. Introduction

Low back pain is a common pathology that has always affected human beings. For example, as early as 600 B.C., electric eels were applied to the painful areas of the back. At present, the western population's marked sedentary lifestyle has converted this pathology into one of the major healthcare burdens. In U.S.A., 0.7% of the population of the late eighties had suffered lumbar intervertebral disc surgical treatment at least once (Lee *et al.*, 1991a) and the European Agency for Safety and Health at Work reported in 2000 that 90% of the active European population was likely to undergo back pain problems (OpDeBeek and Hermans, 2000). Medulla, zygapophysial joints and bony endplates are the main potential sources of chronic pain. However, whatever the source, in a simplified scheme, pain is often a consequence of intradiscal pressure loss, intervertebral disc height reduction, and annulus fibrosus lesion. Indeed, these events are linked through a progressive biomechanical degradation process of the spine tissue behaviour and mechanical environment that follows an initial pathological situation. In 1934, Mixter and Barr (Mixter and Barr, 1934) showed that sciatic pain could be eliminated by means of an intervertebral disc excision. Then, spinal fusion was proposed by Barr (Barr, 1947) in order to stabilize the spinal structure and has since improved dramatically. The outcomes of fusion are matter of many discussions. In most cases, good pain relief is obtained at short term (Takeshima *et al.*, 2000; Lee *et al.*, 1992). But at long term, because of the self-stabilisation of the surgically untreated spine, differences between fusion and non-fusion patients were found to be not statistically different, in both terms of back pain and mobility (Kumar *et al.*, 2001). However, for fusion patients, greater degeneration symptoms at levels adjacent to the treatment are generally observed (Lee *et al.*, 1992; Kumar *et al.*, 2001; Lee, 1988; Ghiselli *et al.*, 2004). A major issue in vertebral fusion is the sudden complete loss of mobility of the treated segment. Decompression is another alternative for low back pain treatment, but loss of segmental stability makes this treatment to fail in most cases (Lee *et al.*, 1991a).

Consequently, total or partial replacements of pathologic intervertebral disc have been seen as solutions to low back pain. In this scope, prostheses can be classified into two groups: implants replacing the nucleus pulposus only, and total intervertebral disc substitutes. Nucleus pulposus replacement may be a good alternative to intervertebral disc restoring since the treatment is more conservative than a total replacement. It has been clinically used since 1996 and provided between 75% and 90% of positive outcomes in pain relief (Blumenthal *et al.*, 2002). However, reported follow-up periods had a maximum length of 5 years and more time is needed to draw conclusions about the clinical efficiency of the technique. First trial of total disc replacement was performed in 1955 by David Cleveland, who injected methylmethacrylate into the disc space of 14 patients after discectomy (Cleveland, 1955). In 1959, Hamby and Glaser reported that compared to discectomy alone after one year, replacement with methylmethacrylate did not lead to significant improvements in terms of disc height maintenance, back pain, hospital stay, or return to work (Hamby and Glaser, 1959). Apart from surgical technique and patient pre-operative conditions (Tropiano *et al.*, 2006; Siepe *et al.*, 2006) that possibly affect post-operative results, high stiffness, mechanical plasticity, failure, or migration of the disc substitutes may be largely

responsible for the unsuccessful clinical outcomes. Among the designs able to restore the mobility of the treated segment, injection of silicone rubber and implantation of stainless steel spheres were tried during the 1960s and the 1970s (Blumenthal *et al.*, 2002). However, it is now known that silicone migration in the body may involve a high risk of morbidity and stainless sphere devices were abandoned due to their penetration in the adjacent vertebral bodies.

During the last 20 years, the most used and successful devices were the SB CHARITÉ[®] and the PRODISC[®]. Both prosthesis designs consist in a frictionless polyethylene core articulated between two metallic endplates anchored into the adjacent vertebral bone (Fig. 5.1). These implants are able to restore both the 6 main rotations (anterior and posterior sagittal, left and right frontal and axial rotations), and intervertebral disc height. However, SB CHARITÉ[®] and PRODISC[®] structures remain far away from a physiologic intervertebral disc and both the high stiffness and the low damping coefficients of their solid materials impede them any absorption of cyclic and constant compressible loads. Such situation may induce non physiologic compressive strains in the natural adjacent soft tissues. For example, metallic endplates can lead to long-term complications such as migration into the adjacent vertebral body (David, 2002). Despite these structural limitations to mimic a healthy intervertebral disc, both the SB CHARITÉ[®] and the PRODISC[®] led to positive clinical results in 70% to 90% of the cases for follow-up periods ranging from 5 to 11 years (Blumenthal *et al.*, 2002; Tropiano *et al.*, 2005; David, 1999). Nevertheless, for young patients, the maximum reported follow-up period only represents a fifth part of the required prosthesis life time and as supported by the findings of Huang *et al.* (Huang *et al.*, 2005), this is probability still not sufficient to conclude about the long term result of an implant. As an example for comparison, the long-term results of lumbar spine fusion performed by Lehman *et al.* (Lehmann *et al.*, 1987) involve follow-up periods of 21-33 years. For hip prosthesis, a time period over 10 years is necessary to notice the well-known stress shielding effect.



Figure 5.1: The main clinically used total disc substitute; a) SB CHARITÉ[®]. b) PRODISC[®].

The development of new composite materials able to mimic the structure of a natural intervertebral disc would be one way to further improve the design of the disc

substitute, beyond the limitations of the current commercial devices. In such approach, each component of the implanted composite structure is chosen to mechanically correspond to a component of the substituted intervertebral disc and assume a well-defined biomechanical role within the spinal structure. Thus, a study determining the stress distribution mechanisms between the composite device components is necessary to understand the mechanical interactions of the prosthesis with the implanted spine and the related outcomes. Theoretical mechanics is then often required to complete the information given by the accessible experimental data. Several finite element analyses have been reported about the evaluation of disc prosthesis designs. Many of these studies are summarized in Table 1.2, and only some examples are given in this introduction. Goel *et al* (Goel *et al.*, 2005) coupled a L3-S1 tri-segment finite element model with a CHARITÉ[®] artificial disc in order to investigate the outcomes of a L5-S1 disc substitution under flexion and extension. They found that, despite an increased mobility of the implanted segment, under realistic boundary conditions, no overloading of the zygapophysial joints is likely to occur. The authors also investigated the stress state of the bony endplates adjacent to the prosthesis, but pegs of the prosthesis that normally penetrates into the bone were not modelled and their effect could not be included into the analysis. Moreover, no information was given about possible mechanical changes in the remaining intact discs, which would have been valuable for the implant rating. Adjacent level effects due to the substitution of a L3-L4 intervertebral disc by a PRODISC[®] II prosthesis were predicted by Chen *et al* (Chen *et al.*, 2008) in a L1-L5 lumbar spine model under simplified boundary conditions. They found that the implant respected well the mechanical integrity of the mechanical environment in the adjacent segments, but highly overloaded the remaining tissues of the implanted segment, due to large motions. From a conception point of view, Langrana *et al* (Langrana *et al.*, 1991) created a synthetic intervertebral disc finite element model, where artificial endplates, nucleus pulposus, and annulus fibrosus matrix and fibres, were represented. The authors studied optimum fibre configurations and material properties, within a range of commercially available materials, so that the prosthesis could behave similarly as an intact intervertebral disc. Dooris *et al* (Dooris *et al.*, 2001) modelled a prototype of articulated disc substitute whose design was fairly close to that of the PRODISC[®]. They used a L4-L5 lumbar spine functional unit model to investigate the level of instability involved by different placements of the device. They compared the effect of possible surgical techniques on the segment stability and could recommend those that might minimize facets and lamina overload.

The present study was part of the European Project DISC, funded in the scope of the European Framework Program V (contract G5RD-CT-2000-00267). The main goal of the project was the development of a novel intervertebral disc substitute that could have similar characteristics as a healthy intervertebral disc. A composite design was then proposed, based on the natural functional structure of lumbar intervertebral discs. Difficulty was to deal with biologically neutral synthetic materials that could offer the most important mechanical characteristics of biologic tissues such as swelling capacity, elastic deformability and high mechanical resistance. Thus the device prototype was modelled and virtually implanted as a L4-L5 disc substitute in a L3-L5 lumbar spine bi-segment. An analysis of the system under different sets of boundary conditions was achieved in order to study the mechanical interactions between the different prosthesis components and the spinal segments. Possible limitations induced by the design were

then identified. Unfortunately, because of the schedule of the project, this work did not involve the latest version of the lumbar spine bi-segment model but an intermediate version of the models presented in Chapters 2 and 4.

B. Materials and methods

I. Models Geometry

a. Intact model

The L3-L5 lumbar spine bi-segment finite element model used in this project included almost all the overall geometrical updates as presented in Chapter 3 (Fig. 5.2). The main differences with this later updated model came from mesh refinement and ligaments (Fig. 5.2b,c,e,f,h,i, Fig. 5.3b,c). Compared to the first version of the bi-segment model presented in Chapter 2, the current model presented corrected orientations of the interspinous ligament, distributed action of the intertransverse ligament along the transverse process, and capsular ligaments forming a ring around the zygapophysial joint instead of covering only its posterior aspect (Fig. 5.2a,b,d,e,g,h, Fig. 5.3a,b). However, the anterior longitudinal ligament still only formed a narrow band on the anterior intervertebral disc, and the postero-lateral extensions of the posterior longitudinal ligament were not modelled (Fig. 5.3b). Although in the present intermediate version of the L3-L5 lumbar spine model, posterior ligaments generally spread over larger bony part areas than in the first version (Fig. 5.3a,b), compared to the latest model, ligament interconnections were still incomplete (Fig. 5.3b,c). In the zygapophysial joints, thickness of the L4-L5 facet cartilage layers remained similar as in the first model version.

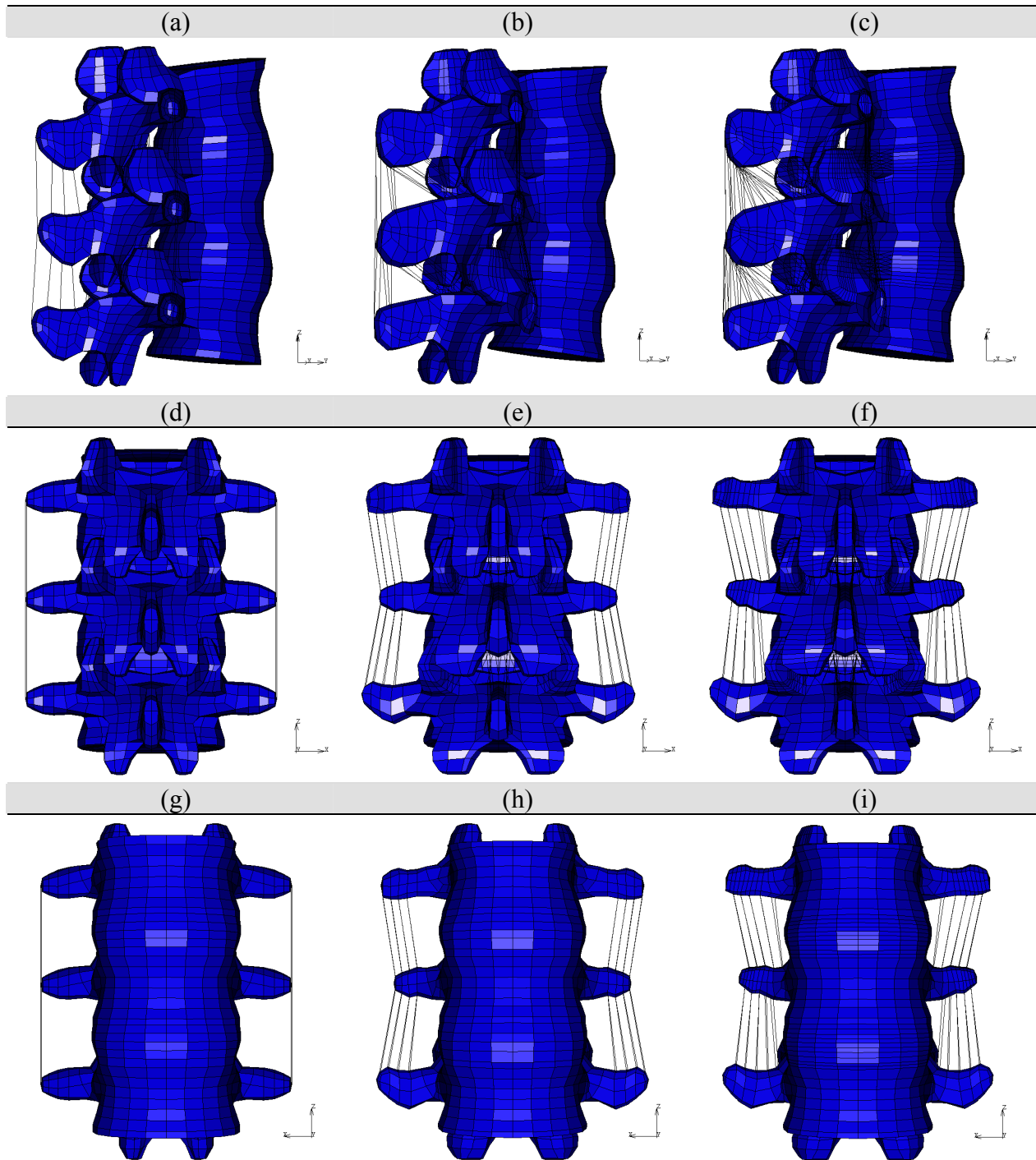


Figure 5.2: Postero-lateral, dorsal and frontal views of the lumbar spine bi-segment model at three different steps of geometrical development. a,d,g) First version (Chap. 2). b,e,h) Model used in the present Chapter. c,f,i) Final version (Chap. 3).

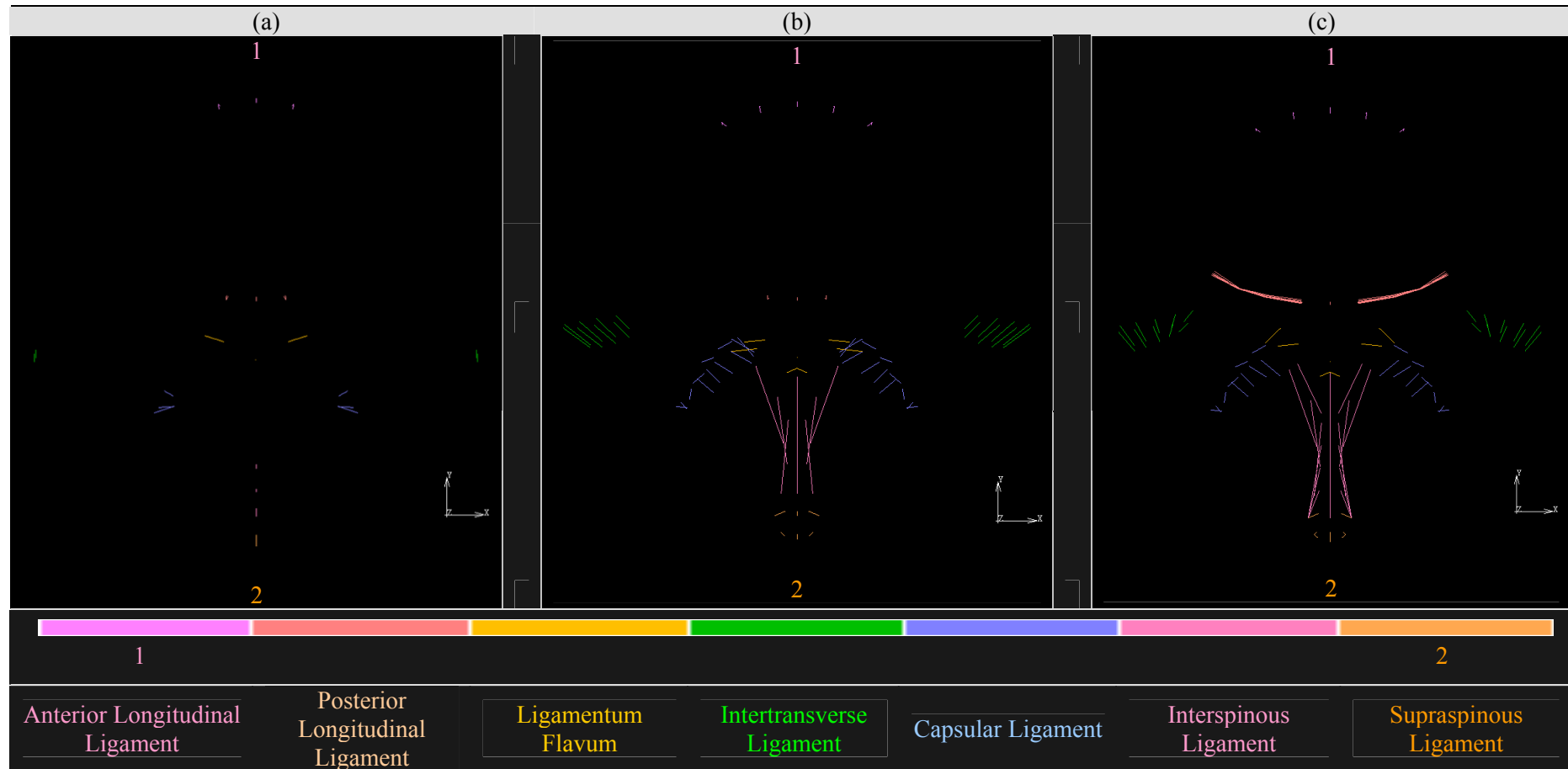


Figure 5.3: Coronal view of the ligamentous network at three different steps of the lumbar spine model geometrical development. a) First version as presented in Chapter 2. b) Version used in this Chapter. c) Latest geometrical version presented in Chapter 3.

b. Disc substitute

1) Device body

The device body was designed and manufactured by the Institute for Composite and Biomedical Materials (IMCB - Naples, Italy). The piece consisted in a matrix of 2-hydroxyethyl-methacrylate (HEMA) hydrogel stirred at room temperature with low molecular weight polymethyl-methacrylate (PMMA) pellets (80/20 weight ratio). At the periphery, the obtained poly-HEMA/PMMA (p-HEMA/PMMA) semi-interpenetrated polymeric network was reinforced with wounded polyethylene terephthalate (PET) fibres (Ambrosio *et al.*, 1998). In a first step, the core containing only p-HEMA/PMMA was moulded to form the nucleus-like part (Fig. 5.4a). A negative of the nucleus mould was used as a mandrel to wound the fibres embedded in the matrix and form the prosthesis annulus-like part (Fig. 5.4b,d). The two matching parts were then assembled to give the prosthesis body (Fig. 5.4c). PET fibres had a diameter of 1.2 mm and were rolled around the mandrel so that they formed mono-oriented concentric layers organized in a criss-cross pattern, along the annulus-like radial direction. Fibre angle with respect to the prosthesis transversal plane ranged from 45° for the most inner layer to 35° for the most outer layer.

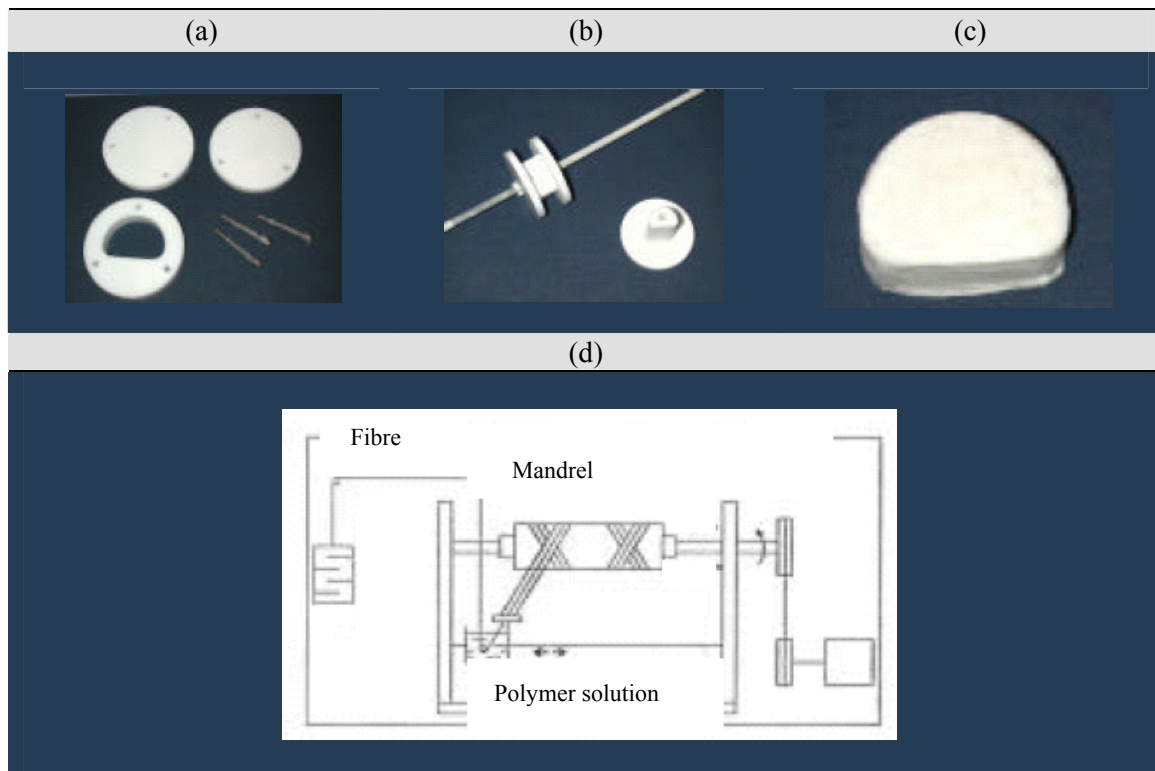


Figure 5.4: Manufacture and design of the intervertebral disc substitute body, developed by the Institute for Composite and Biomedical Materials (IMCB - Naples, Italy). a) Mould used for the nucleus-like part. b) Negative of the nucleus mould used as mandrel for annulus-like wounding. c) Postero-coronal view of the final device prototype. d) Schematic description of the wounding

process leading to the peripheral criss-crossed mono-oriented fibre layers, embedded in the *p*-HEMA/PMMA matrix.

A great advantage of the device manufacturing process is that the shape of the nucleus mould controls the overall transversal shape of the disc substitute (Fig. 5.4a,c). The geometry of the nucleus-like part can then be adapted to the morphology of the segment to treat and convert the prosthesis into a patient-specific device. Such potential was used in the simulation and the prosthesis was directly modelled so that it matched the contour of the surrounding vertebrae, when inserted as a L4-L5 disc substitute in the lumbar spine bi-segment model. According to the wounding technique, the thickness of the modelled annulus-like part was constant all over the periphery of the device. It was calculated to equal the ratio between the total sagittal disc diameter and the anterior annulus thickness of the modelled prosthesis, to that defined in the original drawings provided by IMBC and used to manufacture the first prototype (Fig. 5.5). Like in the bi-segment model intact annulus, device fibres were represented by rebar elements (Chap. 2). A total of 7 fibre layers were defined, so that an integer number of PET fibre could fill the annulus-like thickness. Nonetheless, since a minimum of two layers need to be defined in a rebar element to ensure the numerical stability of the formulation [MARC], a 1.2mm diameter PET fibre was simulated by two adjacent rebar layers with similar orientation (Fig. 5.6). 14 rebar layers were then generated. Fibre volume fraction was set to 0.4, as used for the manufactured prototype. For some result analyses, the prosthesis annulus-like model was virtually divided into four radial areas, namely the outer (OUT), mid-outer (MID(1)), mid-inner (MID(2)), and inner layers (IN). Division was done according to the radial regions defined for the intact intervertebral disc models (Fig. 2.8a).

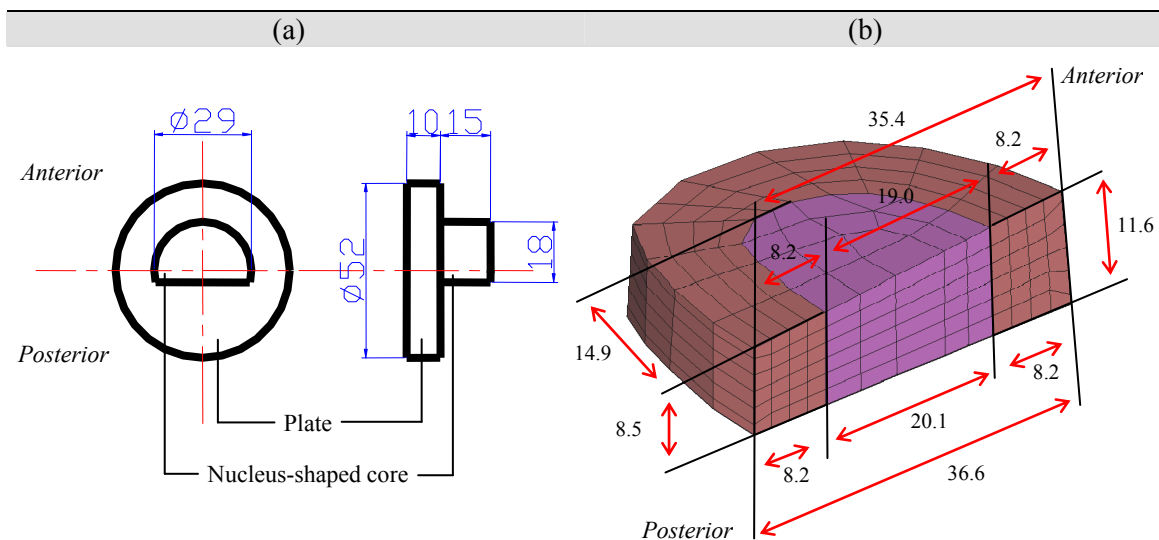


Figure 5.5: a) Geometrical description of the mandrel used by IMBC for the annulus-like wounding as shown in Figure 5.4b. Fibres were wounded around the nucleus-like shaped core until the anterior boarder of the mandrel plate is reached. b) Linear dimensions of the “patient specific” device finite element model. All dimensions are given in mm.

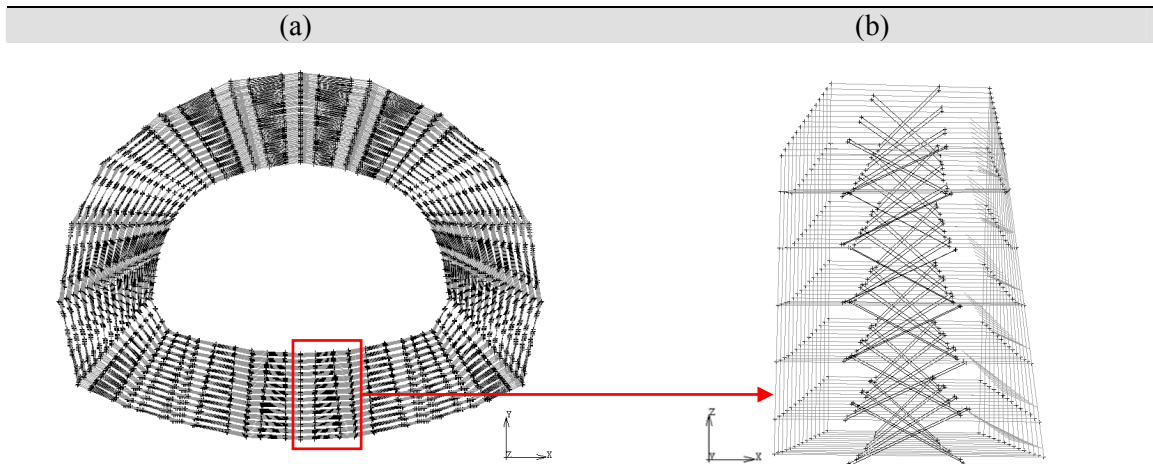


Figure 5.6: Detail of the fibre modelling and organization in the device annulus-like material.
 a) Coronal view. b) Posterior view of the artificial annulus posterior section.

2) Endplates

Device endplates were designed by the Interdisciplinary Research Centre (IRC) in Biomedical Materials, of the Queen Mary and Westfield College, (QMC-IRC, London, England). They were made of a hydroxyapatite and polyethylene composite material, known as HAPEX® (Wang *et al.*, 1998). Central part of the piece was 1mm thick and borders were 2mm thick, so that the sagittal cross-section appeared U-shaped (Fig. 5.7). A field of 1mm high pegs, equidistant from about 2mm, uniformly covered outer surfaces. In the modelled prosthesis, pegs geometry, as defined in the original drawings provided by the QMC-IRC, was preserved, but transversal contours of the endplates were adapted so that the inner borders fitted to the modelled body (Fig. 5.8). In order to limit the number of elements, the mesh of the body was kept coarser than that of the endplates and both parts were linked together through a contact model, where separations were not allowed (glue contact). One of every four nodes of the artificial endplates was usually superimposed to a node of the prosthesis body. This partial mesh congruency allowed ensuring accurate contact detection and avoided mesh penetration problems.

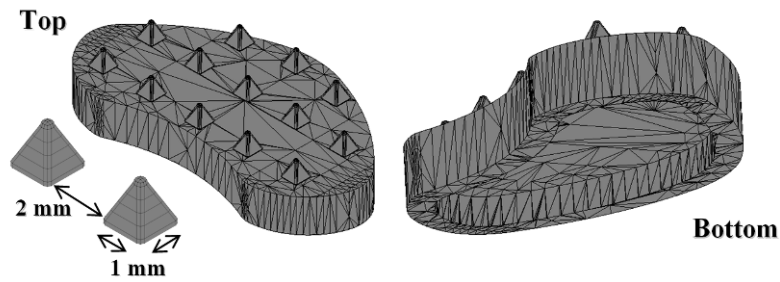


Figure 5.7: Prototype of the device artificial endplate designed by the Interdisciplinary Research Centre in Biomedical Materials (QMC-IRC, London, England) for sheep lumbar vertebrae.

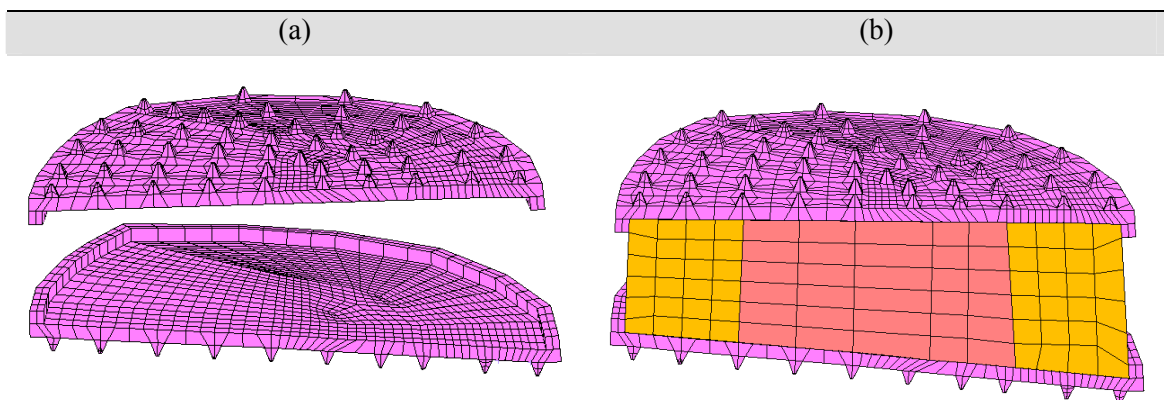


Figure 5.8: a) Sagittal cut of the modelled device endplate. b) Sagittal cut of the device body inserted in the endplates.

c. Treated model

The L4-L5 intervertebral disc of the L3-L5 lumbar spine bi-segment model was removed and replaced by the device model (Fig. 5.9a). Adjacent longitudinal ligaments were also suppressed. In agreement with the literature (Oxland *et al.*, 2003; McAfee, 2002), bony endplates adjacent to the prosthesis were slightly thinned at the periphery, simulating surgical thawing that offers planar peripheral areas and good placement of the artificial disc. The most peripheral pegs penetrated into the vertebrae through the endplate and the trabecular bone. The central pegs stand in the cavity between the vertebra and the prosthesis. Two types of contacts were then created between the endplates and the vertebral body: a peripheral glue contact impeded separations between the bone and the anchored pegs, and a touch contact procedure at the centre allowed the pegs of the cavity to come into contact and press against the bony endplates. In order to avoid unwanted penetrations between bone and HAPEX[®] and improve predictions of load transfer between both materials, the mesh of the vertebrae was refined around the device and was made congruent with the mesh of the pegs (Fig. 5.9b). This refined vertebral body volume was linked to the rest of the bony structure by means of a glue contact analysis with partial mesh congruency.

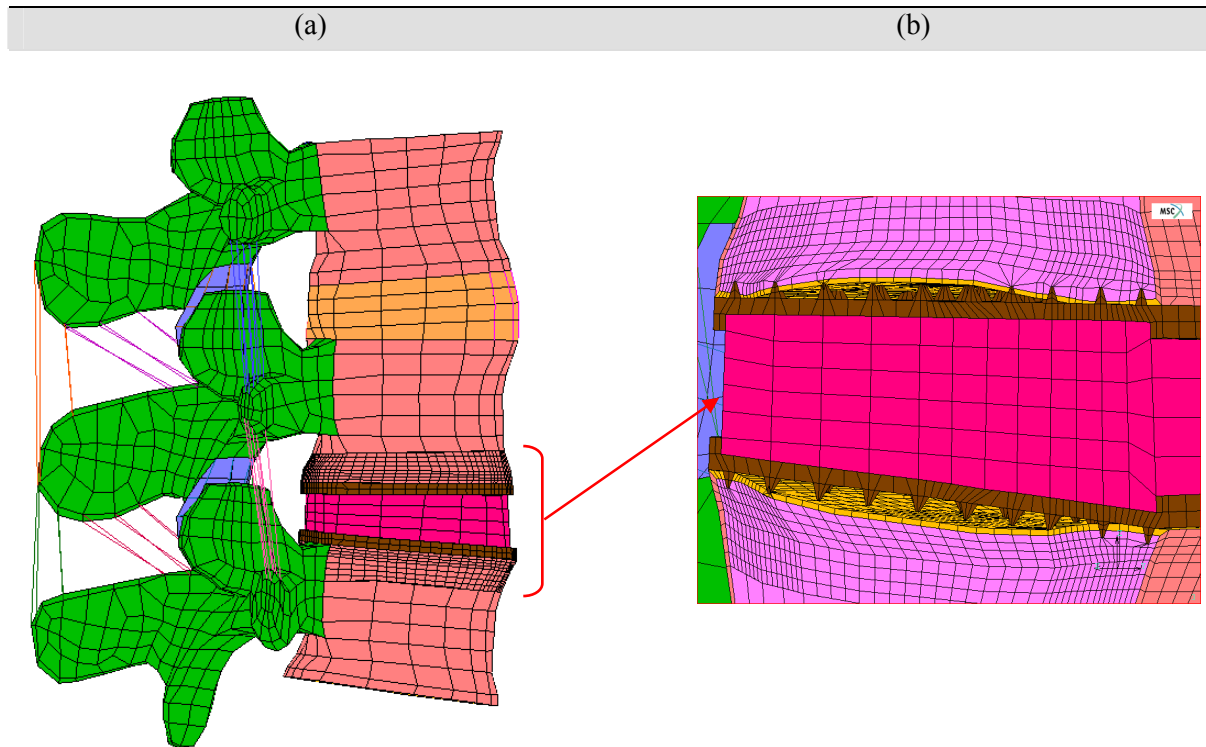


Figure 5.9: The treated model. a) Sagittal view of the lumbar spine bi-segment model with the device inserted as L4-L5 intervertebral disc substitute. b) Antero-lateral view of a mid-sagittal cut of the inserted prosthesis with detail of the device – vertebra interface.

II. Material properties & model corroborations

a. Intact model

Except for the facet cartilage layers, material properties of the lumbar spine tissues were similar as those presented in Chapter 2, (Tables 2.2-2.4, Fig. 2.10,2.12-2.14) and used in Chapter 3. According to Chapter 4 the facet cartilage layers were modelled with a five parameters Mooney-Rivlin constitutive equation (Fig. 4.8, Table 4.3), instead of using the hypoelastic three-dimensional model proposed in Chapter 2.

Experimental results of ranges of motion for the L3-L4 and L4-L5 segments were obtained from *in vitro* experiments performed at the Institute of Orthopaedic Research and Biomechanics (UFB) in Ulm, Germany (Fig. 3.10). Tests were driven at 7.5N.m under sagittal flexion-extension, axial rotation and lateral bending (pure moments) (Wilke *et al.*, 1994), and a total of 12 human specimens without muscles were used. Quality of the axial load transmission from segment to segment through the disc was also verified by applying compressive follower loads of 400N, 500N, 1000N and 2000N on L3. Maximum compressive axial forces predicted in the nucleus pulposus were then compared to values reported in the literature (Berkson *et al.*, 1979; McNally and Adams, 1992; Adams and Dolan, 1995; Adams *et al.*, 1996).

b. Device substitute

The PET fibres had a stiffness of 13000 MPa in tension and no compressive stiffness. HAPEX[®] endplates had an elastic modulus of 5000 MPa and a Poisson's ratio of 0.4. The ASTM D695 standard mechanical tests provided by IMBC showed that the p-HEMA/PMMA matrix of the device body was elasto-plastic with an initial stiffness, $E_{HEMA-PMMA}$, of 42MPa and a yield stress, σ_y , of 1 MPa (Fig. 5.10a). In the model, the rebar formulation sums the stiffness contributions in the fibre directions, but the rule of mixtures, for fibre reinforced composite materials, is not truly computed. Thus, assuming that PET fibres should have influenced the initial Young's modulus of the annulus-like p-HEMA/PMMA matrix, an apparent initial stiffness, $E_{Annulus-like}^{apparent}$, was estimated. Along the axial direction, the prosthesis was considered as a parallel assembly of the nucleus-like and annulus-like materials. Respective contributions of these materials to the overall stiffness were then modelled according the rule of mixtures for parallel composites:

$$E_{Annulus-like}^{apparent} = \frac{E_{Device} - f_{Nucleus-like}^{Device} E_{HEMA-PMMA}}{f_{Annulus-like}^{Device}} \quad (5.1)$$

where, E_{Device} is the initial axial stiffness of the prosthesis construct, extracted from the measured compressive behaviour of the manufactured prototype (Fig. 5.10b). $f_{Annulus-like}^{Device}$ and $f_{Nucleus-like}^{Device}$ were the volume fractions of the annulus-like and nucleus-like materials, respectively. These volume fractions were computed from the volumes of the modelled device elements. All parameters values presented in Equation (5.1) are summarized in Table 5.1.

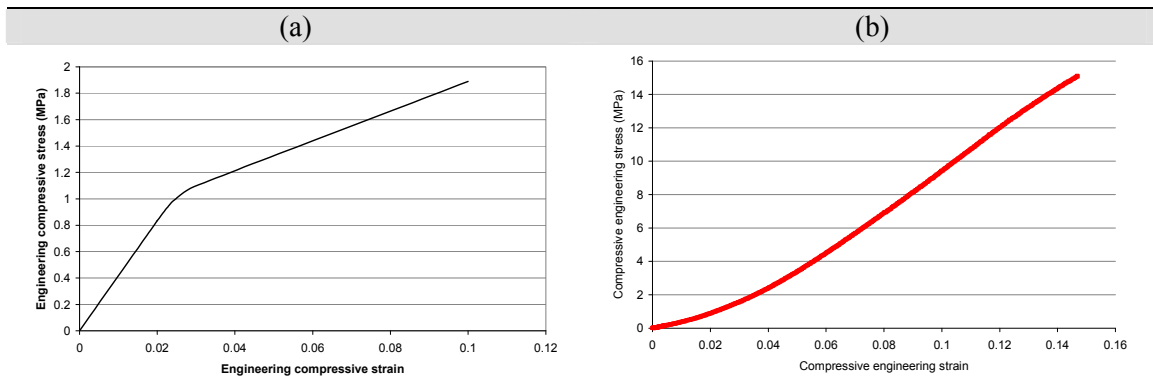


Figure 5.10: Compressive behaviour of the device materials. a) p-HEMA/PMMA matrix (ASTM D695 standard). b) Whole composite device under displacement control with test speed of $1\text{mm}\cdot\text{min}^{-1}$.

Table 5.1: HEMMA-PMMA matrix effective stiffness in the different parts of the modelled prosthesis and experimental initial stiffness of the device and the p-HEMA/PMMA material

$E_{HEMA-PMMA}$ (MPa)	E_{Device} (MPa)	$f_{Nucleus-like}^{Device}$	$f_{Annulus-like}^{Device}$	$E_{Annulus-like}^{apparent}$ (MPa)
42 ^(e)	37.8 ^(e)	0.34 ^(m)	0,66 ^(m)	See Results ^(c)

^(c) computed data (Eq. (5.1)); ^(e) experimental data; ^(m) modelling data

For the p-HEMA/PMMA matrix, two types of constitutive equations were assessed. First of all, a linear piecewise elasto-plastic mechanical law based on Figure 5.10a was used. Criteria for 3D plasticity, was established according to a von Mises Yield surface. Moreover, in the domain of plastic deformations, an isotropic work hardening rule was chosen, with a work hardening coefficient corresponding to a uniaxial elasto-plastic stiffness equal to 66% of the uniaxial elastic stiffness (Figure 5.10a). Considering only loading situations, elastic and plastic matrix deformations were then governed by the following equations:

$$\bar{\sigma} = \frac{1}{2} \sqrt{(\sigma_{11} - \sigma_{22})^2 + (\sigma_{22} - \sigma_{33})^2 + (\sigma_{11} - \sigma_{33})^2 + 6(\sigma_{23}^2 + \sigma_{31}^2 + \sigma_{12}^2)} \quad (5.2)$$

$$\forall \sigma_{ij} | \bar{\sigma} < \sigma_y \quad (\text{elastic domain})$$

$$d\underline{\sigma} = \underline{k} : d\underline{\varepsilon} \quad (5.3a)$$

$$d \begin{pmatrix} \sigma_{11} \\ \sigma_{22} \\ \sigma_{33} \\ \sigma_{12} \\ \sigma_{23} \\ \sigma_{31} \end{pmatrix} = \frac{E}{(1+\nu)(1-2\nu)} \begin{pmatrix} 1-\nu & \nu & \nu & 0 & 0 & 0 \\ \nu & 1-\nu & \nu & 0 & 0 & 0 \\ \nu & \nu & 1-\nu & 0 & 0 & 0 \\ 0 & 0 & 0 & \frac{1-2\nu}{2} & 0 & 0 \\ 0 & 0 & 0 & 0 & \frac{1-2\nu}{2} & 0 \\ 0 & 0 & 0 & 0 & 0 & \frac{1-2\nu}{2} \end{pmatrix} d \begin{pmatrix} \varepsilon_{11} \\ \varepsilon_{22} \\ \varepsilon_{33} \\ \varepsilon_{12} \\ \varepsilon_{23} \\ \varepsilon_{31} \end{pmatrix} \quad (5.3b)$$

$$\forall \sigma_{ij} | \bar{\sigma} \geq \sigma_y \quad (\text{plastic domain})$$

$$d\underline{\sigma} = \underline{l}^{ep} : d\underline{\varepsilon} \quad (5.4a)$$

$$\underline{l}^{ep} = \underline{k} - \frac{\left(\underline{k} : \frac{\partial \bar{\sigma}}{\partial \sigma_{ij}} \right) \otimes \left(\underline{k} : \frac{\partial \bar{\sigma}}{\partial \sigma_{ij}} \right)}{0.66E + \frac{\partial \bar{\sigma}}{\partial \sigma_{ij}} : \underline{k} : \frac{\partial \bar{\sigma}}{\partial \sigma_{ij}}} \quad (5.4b)$$

From (5.2) to (5.4), σ_{ij} are the engineering stress components, $\bar{\sigma}$ is the von Mises equivalent stress, $d\bar{\sigma}$ and $d\bar{\epsilon}$ are the engineering stress and strain increment vectors, and \underline{k} and \underline{l}^{ep} are the elastic and elasto-plastic small strain stiffness tensors, respectively. ν and E are the matrix Poisson's ratio and Young's moduli. E was taken equal to $E_{HEMA-PMMA}$ in the nucleus-like part, and equal to $E_{Annulus-like}^{apparent}$ in the annulus-like part (Eq. (5.1)). σ_y was extracted from Figure 5.10a for the nucleus-like part. For the annulus-like part, experimental σ_y value was pondered by the ratio $E_{Annulus-like}^{apparent} / E_{HEMA-PMMA}$.

Beside its elasto-plastic characteristics, in a fluid environment, the p-HEMA/PMMA hydrogel was shown to uptake significant amount of water (swelling ratio at equilibrium = 0.36). The device was actually designed for implantation in a swelled state, and axial compression results presented in Figure 5.10b were obtained after previous 30 days of construct free swelling, in saline solution at 37°C. Thus, considering that further fluid outflow is hindered both, by the HAPEX[®] endplates at the prosthesis top and bottom ends, and by PET fibres through lateral walls, the apparent constitutive behaviour of the device matrix was expected to be affected by the absorbed water. In the device assembly, the p-HEMA/PMMA matrix was then alternatively considered as an almost incompressible fluid filled body. A compressible Neo-Hookean model, where compressibility could be parameterized, was implemented to assess such hypothesis. The corresponding strain energy function was given by:

$$W = \frac{9}{2}K\left(J^{1/3} - 1\right)^2 + \frac{G}{2}\left(\bar{I}_1 - 3\right) \quad (5.5)$$

where J is the Jacobian determinant, \bar{I}_1 is the first invariant of the deviatoric left Cauchy-Green tensor, and K and G are the initial bulk and shear moduli, defined by the following infinitesimal strain relations (Holzapfel, 2000):

$$K = \frac{E}{3(1-2\nu)} \quad (5.6a)$$

$$G = \frac{E}{2(1+\nu)} \quad (5.6b)$$

In (5.6), E was set equal to $E_{HEMA-PMMA}$ for the nucleus core, and equal to $E_{Annulus-like}^{apparent}$ for the composite annulus-like part (Table 5.1). 2nd Piola Kirchhoff stress was given from the strain energy by (Holzapfel, 2000):

$$\underline{\underline{S}} = J \frac{\partial W}{\partial J} \underline{\underline{C}}^{-1} + 2 \left(\frac{\partial W}{\partial \bar{I}_1} + \bar{I}_1 \frac{\partial W}{\partial \bar{I}_2} \right) \underline{\underline{I}} - 2 \frac{\partial W}{\partial \bar{I}_2} J^{2/3} \underline{\underline{C}} \quad (5.7)$$

where $\underline{\underline{C}}$ represents the left Cauchy-Green tensor.

Replacing expression (5.5) into (5.7) and taking into account the relation $\underline{\underline{\sigma}} = J^{-1} \underline{\underline{F}} \underline{\underline{S}} \underline{\underline{F}}^T$, Cauchy stress can be expressed as:

$$\underline{\underline{\sigma}} = \frac{3}{2} K \frac{\frac{1}{2} - 2 \left(J^{-1/3} - \frac{1}{2} \right)^2}{J} \underline{\underline{I}} + \frac{G}{J} \underline{\underline{B}} \quad (5.8)$$

where $\underline{\underline{B}}$ is the right Cauchy-Green tensor.

According to the available experimental data (Figure 5.10b), the prosthesis model was simulated under axial compression, with a loading of 16% engineering strain. The best mechanical constitutive law for the p-HEMA/PMMA matrix was selected based on the potential of each formulation, i.e. elasto-plastic, and nearly incompressible Neo-Hookean, to fit the prototype experimental compressive behaviour. In (5.8), compressibility was controlled by the bulk modulus, itself controlled by the unknown Poisson's ratio, ν (Eq. 5.6a). In the isotropic linear stiffness matrix, $\underline{\underline{k}}$, defined by (5.3b) and used in (5.4b), ν values also represented the compressibility of the elasto-plastic material. Thus, for both the elasto-plastic and hyperelastic models, apparent compressibility of the prosthesis matrix was assessed, by varying ν between 0.4 and 0.499. Poisson's ratio was considered similar for both the annulus- and nucleus-like materials. Compressibility and constitutive model that best fitted the prototype experimental behaviour were chosen for further calculations in the treated model.

III. Boundary conditions & Studied parameters

Biomechanical behaviours of both the intact and treated models were studied under sagittal flexion-extension, and axial rotation. Ranges of motion, facet contact forces, and stress distributions, given by each model, were compared. In order to limit the level of extrapolation brought by the simulations, maximum rotational moment values were 7.5 N.m, as used for the intact bi-segment model verification.

The effect of different types of boundary condition, i.e. load-controlled and displacement-controlled motions, was investigated under sagittal rotation, in both the intact and treated models. For the displacement-controlled sagittal flexion, imposed rotation was similar to that achieved in the intact model under load control. Moreover, effect of body weight on the stress transfers between the prosthesis and the adjacent vertebral bone was assessed. A body weight-like follower load of 370N (Chap. 4) was then added to all rotational load cases, in both the intact and treated models. Compressive forces were applied as superficial loads, exerting on the superior endplate of L3. Rotational loads were applied on a converging beam element network, rigidly fixed to the L3 upper endplate (Fig. 4.9). Ranges of motion, facet contact forces, and strain energy density (Eq. (2.21)) distributions, were computed.

For any type of boundary condition, the effect of the prosthesis was alternatively compared in terms of relative differences, according to the following expression:

$$\begin{aligned} \forall (X_{treated}, X_{intact}) | X_{treated} \geq X_{intact}, \quad RD = 100 \left(1 - \frac{X_{intact}}{X_{treated}} \right) \\ \forall (X_{treated}, X_{intact}) | X_{treated} < X_{intact}, \quad RD = -100 \left(1 - \frac{X_{treated}}{X_{intact}} \right) \end{aligned} \quad (5.9)$$

where RD is the relative difference, in %. X_{intact} and $X_{treated}$ refer to any biomechanical parameter X , predicted by the intact and treated model, respectively. Negative RD values always show decreased X values in the treated model, when compared to the intact one. Conversely, positive RD values showed higher X values in the treated than in the intact model. Effect of the L4-L5 disc substitute on the relative pressure distribution within the L3-L4 pulposus was also evaluated by calculating a hydrostatic stress-based dimensionless parameter:

$$I_{\Delta hp} = 2 \left| \frac{\sigma_S^{\max} - \sigma_S^{\min}}{\sigma_S^{\max} + \sigma_S^{\min}} \right| \quad (5.10)$$

$I_{\Delta h}$, defined by (5.10), is the hydrostatic stress gradient index where σ_S^{\max} and σ_S^{\min} are the maximum and minimum values of the spherical stress components, locally computed in the nucleus as one third the trace of the stress tensor (Eq. (2.10)). $I_{\Delta h}$ is ideally zero for pure hydrostatic stress states, and increases as effective stress gradients appear.

Mechanical data computed in the bony parts of the vertebral bodies were reported for specific sections, sufficiently away from nodes with prescribed constraints, such as external loads, fixed displacements, or induced by mesh discontinuities. These sections were distributed along the lumbar spine bi-segment model as illustrated in Figure 5.11.

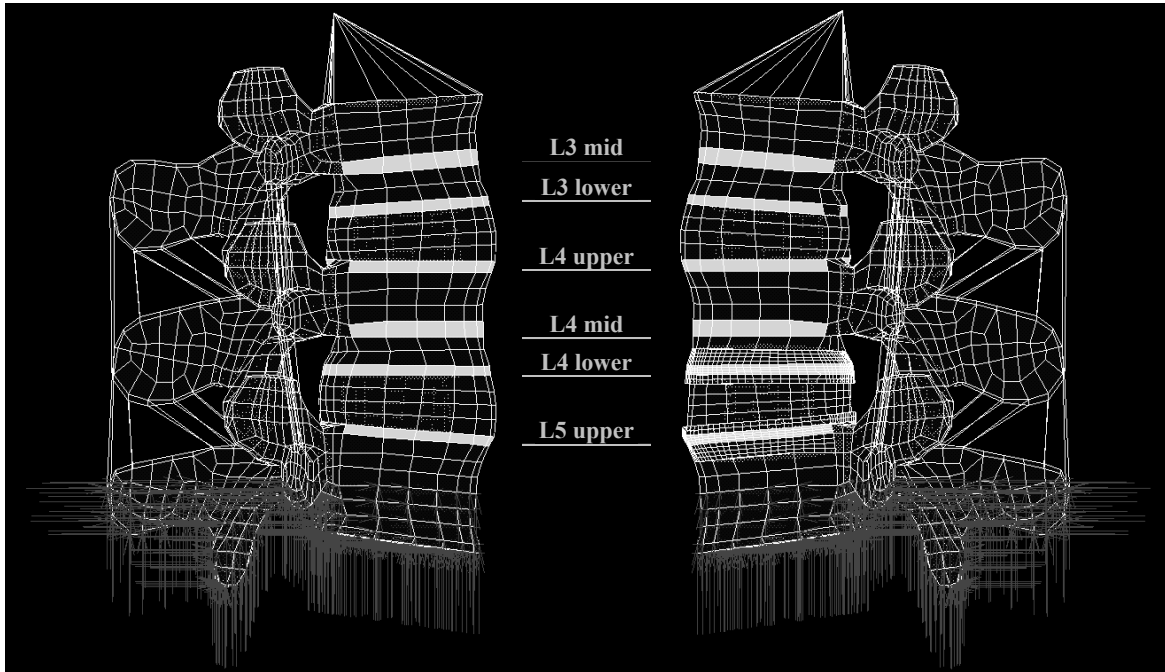


Figure 5.11: Vertebral body sections used for the analysis of bone-related mechanical predictions (left: intact mode, right: treated model).

C. Results

I. Model corroborations

a. Intact model

Figure 5.12 shows the experimental ranges of motions provided by UFB and the segmental rotations predicted by the intact model. Although the L3-L4 segment appeared systematically somewhat stiff compared to the mean experimental responses, simulated motions were always within the range obtained over the set of tested specimens.

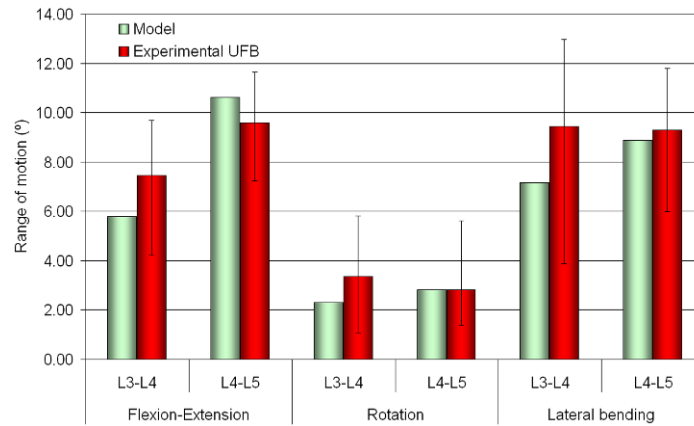


Figure 5.12: Comparison of the ranges of motion predicted by the L3-L5 lumbar spine bi-segment model under 7.5N.m pure moments, with experimental results obtained from in vitro experiment performed under similar load conditions to those used in the simulations.

On Figure 5.13, maximum axial compressive stresses calculated in the nuclei pulposi of the intact model under increasing follower compressive forces, are presented and compared to measurements extracted from the literature. Only simulation values computed in the L3-L4 intervertebral disc were reported, as no significant differences between the L3-L4 and the L4-L5 discs were found. In general, computed stresses corresponded well to the experimental results. Largest discrepancy was found at 1000N, where the measured intradiscal pressure was around 0.9 MPa, while simulation returned a value of 1.1 MPa. Unfortunately, experimental errors were not available and could not be reported.

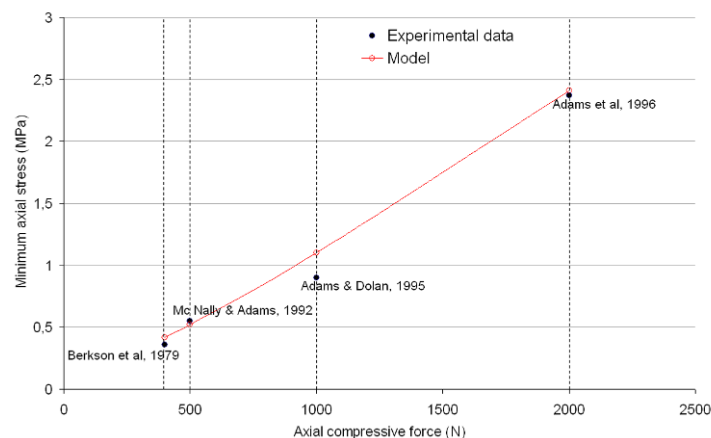


Figure 5.13: Comparison of the maximum compressive stresses predicted in the nucleus pulposus under 470N, 500N, 1000N, and 2000N, with literature-based experimental values.

b. Device model

Equation (5.1) returned an apparent Young's modulus of 35.6 MPa, for the annulus-like p-HEMA/PMMA matrix, which was somewhat smaller than the initial stiffness measured for the p-HEMA/PMMA matrix alone. The apparent yield stress of the annulus-like p-HEMA/PMMA matrix, given by σ_y , multiplied by $E_{Annulus-like}^{apparent} / E_{HEMA-PMMA}$, was then equal to 0.8 MPa.

As shown in Figure 5.14a, independently of the tested ν values, the elasto-plastic piecewise linear model for the p-HEMA/PMMA matrix was unable to predict the strain stiffening of the composite prosthesis. Largest divergences between computed and experimental stresses occurred in the plastic domain. On the other hand, varying the compressibility of the Neo-Hookean model allowed approximating fairly well the prototype experimental compressive curve (Fig. 5.14b), and best fit was obtained with a Poisson's ratio value of 0.483 (Fig. 5.14c).

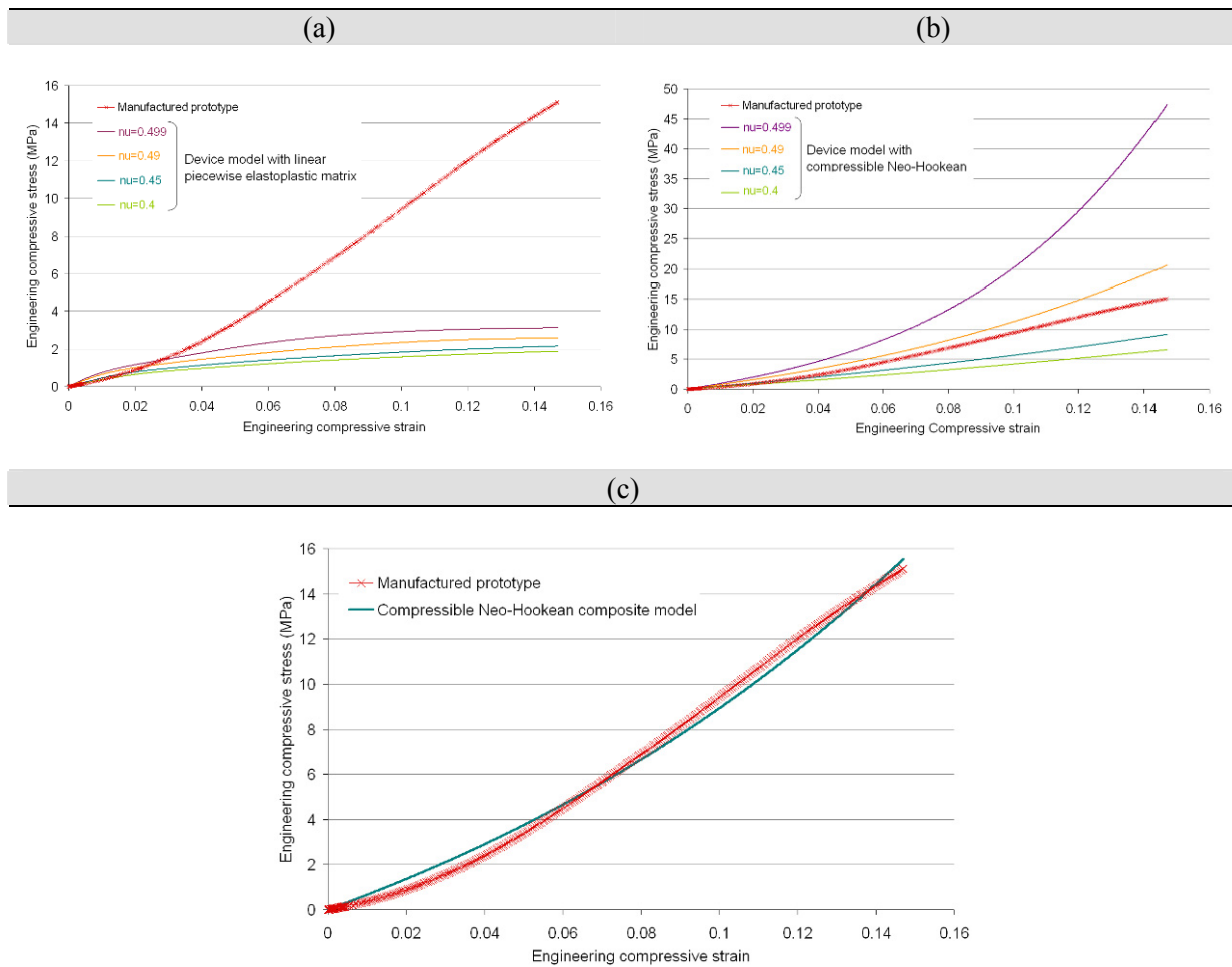


Figure 5.14: Experimental compressive behaviour of the prototype compared to the predictions returned by the prosthesis composite model, with different p-HEMA/PMMA ν values. a) Elasto-plastic p-HEMA/PMMA matrix. b) Compressible Neo-Hookean p-HEMA/PMMA matrix. c) Best fit, as returned by the Neo-Hookean composite model, with $\nu=0.483$.

II. Comparison of intact and treated models

a. Ranges of motion

Figure 5.15 reports the predictions of range of motion changes, due to replacement of the intact model L4-L5 intervertebral disc by the device model. Generally, the prosthesis induced large loss of mobility at the treated level. Remaining L4-L5 motions were not zero, but nearly insignificant compared to the rotations allowed by the intact segment. Under load-controlled rotations, the device did not significantly affect the non-treated L3-L4 level. Only slight increases of less than 10% in L3-L4 rotation angles were predicted under sagittal extension and axial rotation (Fig. 5.15b). However, under displacement-controlled flexion, the L4-L5 disc substitute did increase the L3-L4 range of motion by nearly 30%. For this load case, although a 7° fixed rotation of L3, as obtained under load-controlled flexion, was imposed, the sum of the L3-L4 and L4-L5 intersegmental rotations was always inferior to the prescribed rotation value (Fig. 5.15a). This loss of effective angle of rotation over the whole L3-L5 bi-segment model was larger in the treated than in the intact model, and for both models, it was somewhat smaller with the additional body weight-like load than without.

Simulation of the body weight lowered somewhat the ranges of motion obtained under load-controlled rotations and slightly increased those given by the displacement-controlled load case (Fig. 5.15a). Relative differences between intact and treated model ranges of motion were also somewhat affected by simulation of the additional body weight-like load (Fig. 5.15b). However, maximum effect only consisted in a reduction of 10% of the prosthesis-induced L4-L5 stiffening, under axial rotation.

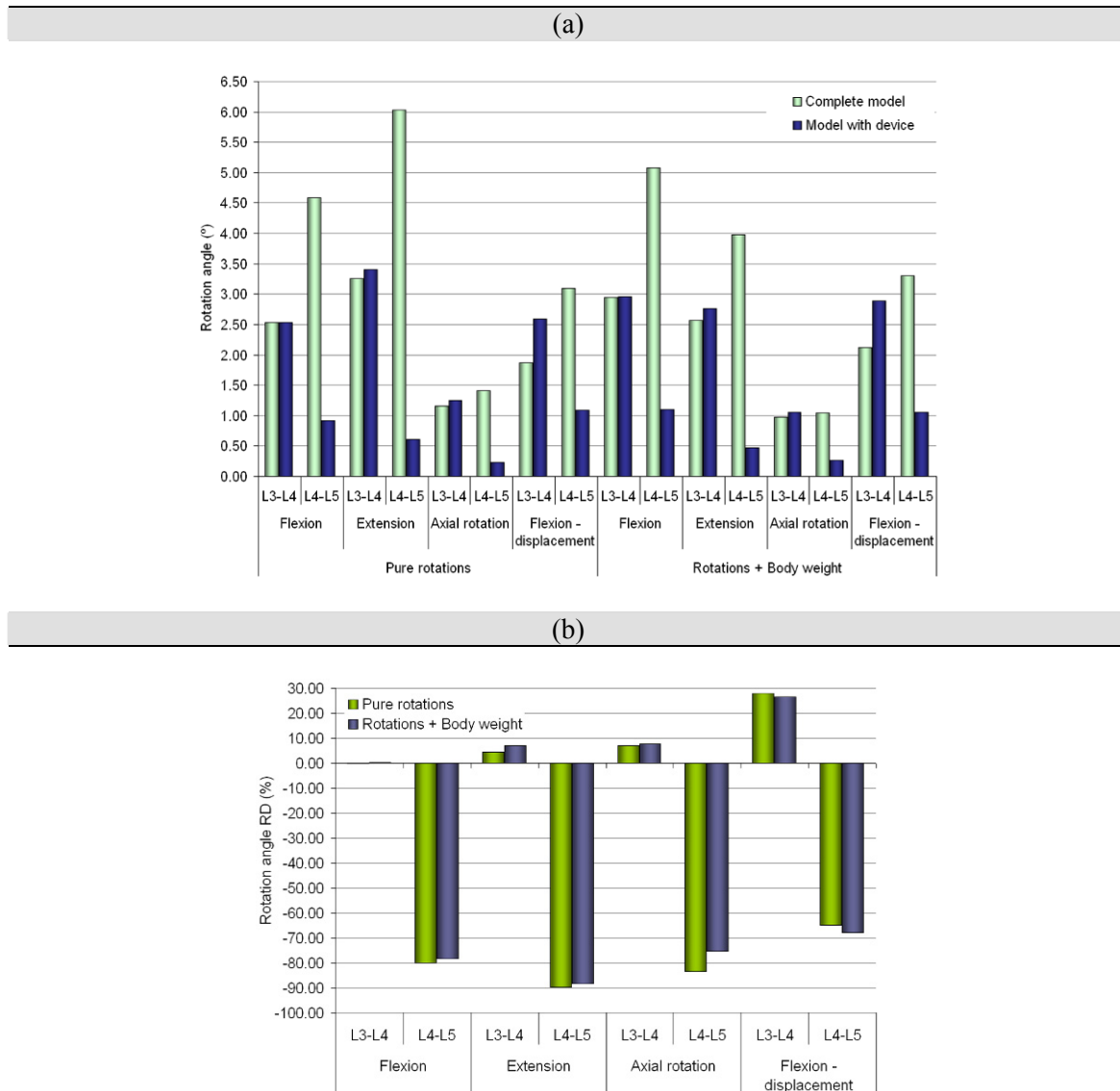


Figure 5.15: Intersegmental Ranges of motion. a) Rotation angles predicted by the intact and the treated model under pure rotational moments with or without body weight follower compressive force. b) Relative differences predicted under rotational moments, with and without body weight compressive force, after intact model L4-L5 intervertebral disc was substituted by the device model.

b. Zygapophysial joint contact forces

The presence of the prosthesis, at the L4-L5 level, had generally less effect on facet contact forces (Fig. 5.16) than on ranges of motion (Fig. 5.15b). As shown in Figure 5.16, except under sagittal flexion, the device generally induced a loss of the L4-L5 zygapophysial joint facet contact. Both under load- and displacement-controlled flexion, large L4-L5 contact force increases of nearly 90% appeared after virtual implantation of the device. For the rest, without body weight compressive follower

force, contact reduction was about 50% under axial rotation, and less than 40% under sagittal extension.

At the non-treated L3-L4 level, facet contact normal forces under load-controlled flexion and extension were decreased by the presence of the L4-L5 implant. Under extension, relative reduction in L3-L4 contact forces was larger than under load-controlled flexion, and similar to the relative contact reduction computed at the L4-L5 level. Under both axial rotation and displacement-controlled flexion, L3-L4 facet contact forces were about 10% higher in the treated than in the intact model.

Body weight-like load occasionally affected the predictions of prosthesis effect on the zygapophysial joint biomechanics. Under extension, additional body weight increased somewhat both the L3-L4 and L4-L5 contact force relative differences, calculated between the intact and treated model zygapophysial joints. Similar trend was predicted, at the L3-L4 level, under axial rotation, and at the L4-L5 level, under load-controlled flexion. Under displacement-controlled flexion, body weight had an inverse effect on the L4-L5 joint when compared to load-controlled flexion. Note that under displacement-controlled flexion, increase of L3-L4 facet contact forces in the treated model was about 20% more important in presence of the body weight-like compressive follower force than under pure rotation only. Conversely, body weight decreased by about 10% the effect of the prosthesis insertion on the L3-L4 facet joints, in both load-controlled flexion and axial rotation.

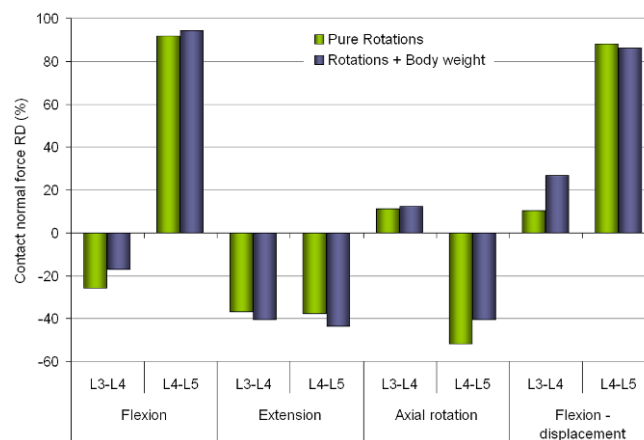


Figure 5.16: Relative differences in maximal contact normal forces, predicted in the zygapophysial joint facets, after intact L4-L5 intervertebral disc was substituted by the device model. Results are given under rotational motions, with and without body weight compressive force.

c. Vertebral body loading

1) Load distribution under pure rotations

Figures 5.17 clearly show that, for all pure rotational load cases, the presence of the L4-L5 disc substitute significantly affected the mechanical energy stored in the different bony parts of the L3-L5 bi-segment model vertebral bodies. Under load-controlled sagittal flexion, neither the lower half of the L3 vertebral body, nor the upper parts of L4 were significantly affected by the implant (Fig. 5.17a,b). However, maximum strain energy density computed in the mid-height trabecular and cortical sections of L4 was significantly lower in the treated model than in the intact model. In the intact model, the largest mechanical energy was actually found to be stored in the mid-transversal cortical bone of the L4 vertebral body, whereas in the treated model, it was found to be stored in the lower parts of the cortex. The L4 and L5 bony endplates, and the L4 trabecular and cortical bone sections, adjacent to the L4-L5 intervertebral disc, were all generally more loaded when the natural disc model was replaced by the prosthesis model. Largest prosthesis-induced strain energy density increase, under load-controlled flexion, was predicted in the L5 upper bony endplate. Curiously, the upper cortical section of the L5 vertebral body was about one third less loaded in the treated, than in the intact model, and no differences were calculated in the corresponding trabecular section. More generally, the L4-L5 prosthesis made the L5 upper endplates to bear most of the load, while in the intact model, the L4 cortical shell stored most of the bone strain energy.

Under displacement-controlled flexion, (Fig. 5.17c,d), bony parts of the L3 vertebral body were fairly sensitive to the presence of the L4-L5 disc substitute. As such, maximum strain energy density values computed in the mid and lower trabecular bone sections were significantly higher in the treated than in the intact model. As a consequence, unlike in the intact model, in the treated model, the L3 trabecular bone provided higher mechanical work than the cortical shell did. Some load increase was also predicted in the L3 mid-transversal cortical section, but the lower L3 cortical section resulted somewhat less loaded in the treated than in the intact model. On the contrary, both the lower L3 and upper L4 endplates stored more elastic energy in presence of the L4-L5 disc substitute. In the L4 vertebral body, all the studied bony parts, except the cortical mid-transversal section, experienced strain energy density increases with the prosthesis. Both trabecular bone and cortex were most affected in the L4 lower vertebral body section. Largest difference between the intact and the treated models was predicted in the L5 upper endplate, where maximum strain energy value became maximal in presence of the implant model. Loads also increased in both the trabecular and cortical upper sections of the L5 vertebral body. Note that in the intact model, bone strain energy density values were generally lower under displacement-controlled flexion than under load-controlled flexion. However, in the treated model, both load cases led to more similar results than in the intact model. As under load-controlled flexion, displacement-controlled flexion results indicated that without any device, the mid-transversal section of the L4 cortical bone provided the highest mechanical work. Conversely, in the treated the L5 upper endplate, adjacent to the prosthesis, stored the largest amount of strain energy.

Under sagittal extension, vertebral body parts nearby the area of implantation, i.e. the lower and upper bone sections of the L4 and L5 vertebral bodies, respectively, were mostly affected by the presence of the disc substitute (Fig. 5.17e,f). However, in opposition to the predictions performed under sagittal flexion, cortical bone and endplate strain energy density values, computed in the lower L4 vertebral body, were both smaller in the treated than in the intact model. On the other hand, trabecular strain energy density of the same L4 lower section was increased by the presence of the prosthesis. In the upper L5 vertebral body, all different bony parts resulted considerably more loaded in treated than in the intact model.

Under axial rotation, similarly as under sagittal extension, the L3 vertebral body and the superior half of the L4 vertebral body were both only slightly influenced by the presence of the L4-L5 disc prosthesis model (Fig. 5.17g,h). Maximum strain energy density was significantly increased in both the L4 and L5 trabecular sections surrounding the implant. However, cortex mechanical loading, in these lower L4 and upper L5 vertebral body sections, was generally lower in the treated than in the intact model.

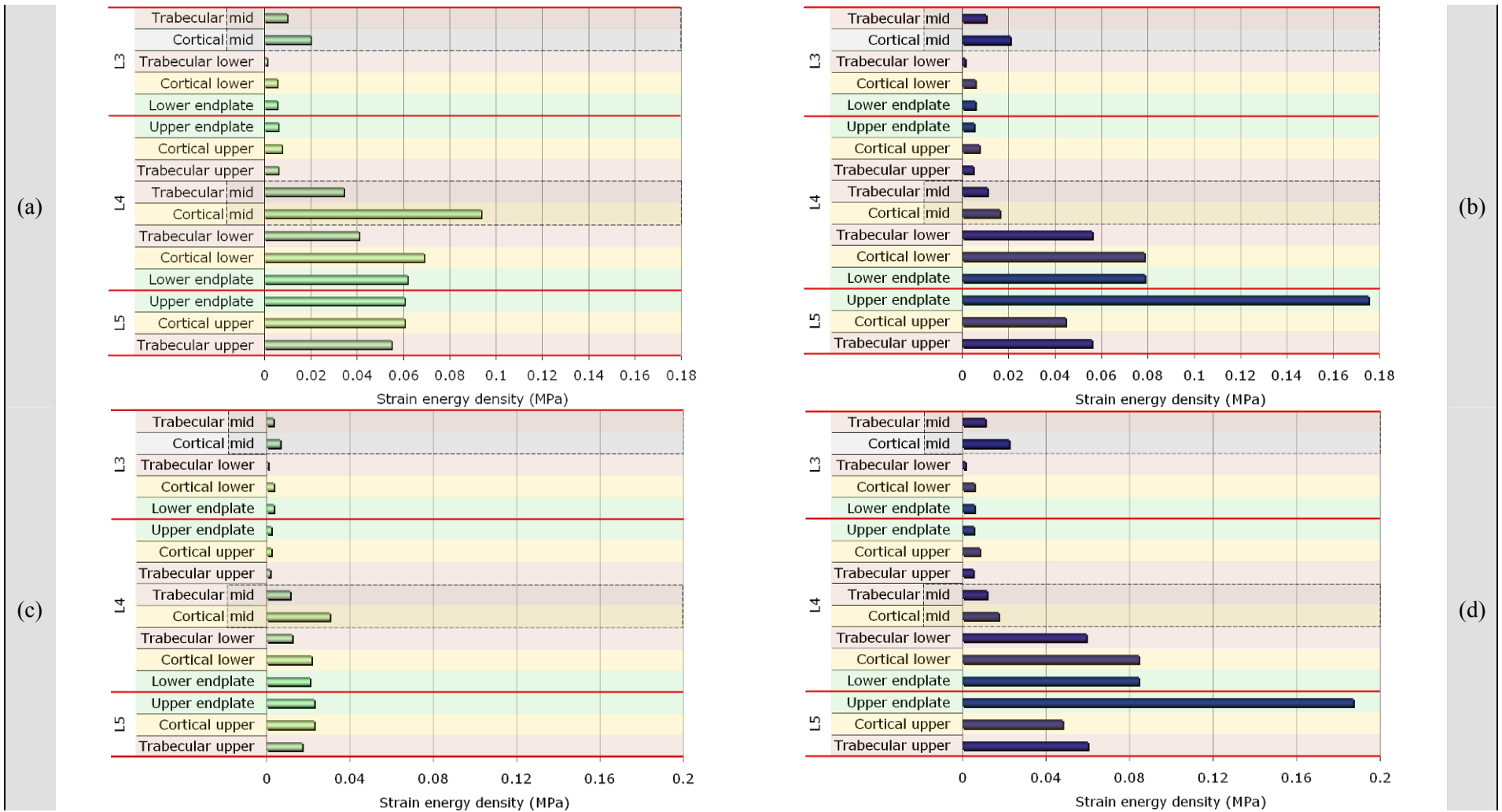


Figure 5.17: Strain energy density distribution in different part of the L3-L5 lumbar spine bi-segment model vertebral bodies. a) Intact model, load-controlled flexion. b) Treated model, load-controlled flexion. c) Intact model, displacement-controlled flexion. d) Treated model, displacement-controlled flexion.

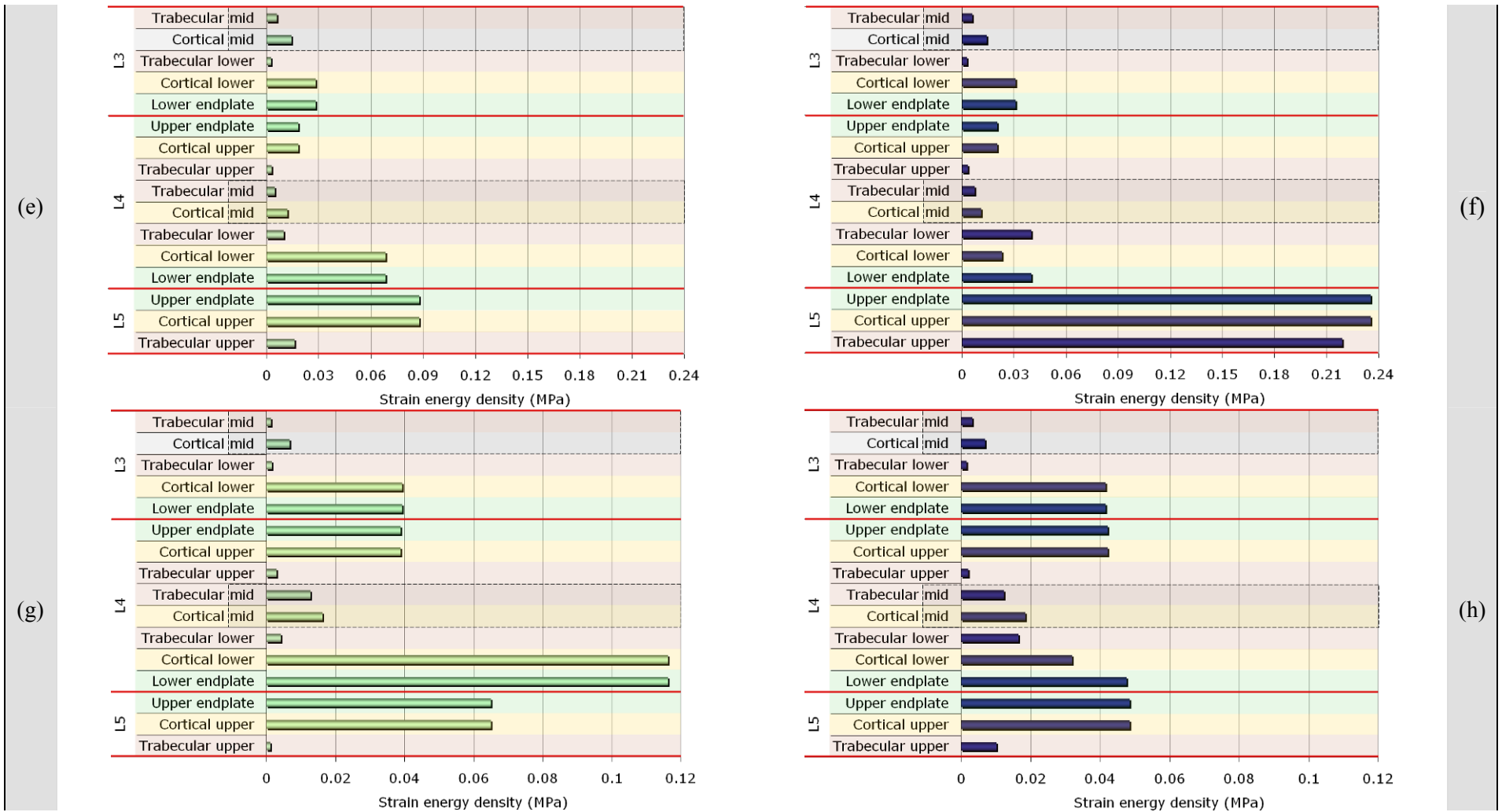


Figure 5.17: Strain energy density distribution in different part of the L3-L5 lumbar spine bi-segment model vertebral bodies. e) Intact model, extension. f) Treated model, extension. g) Intact model, axial rotation. h) Treated model, axial rotation.

2) *Body weight-like load effect*

(i) *Trabecular bone*

As shown in Figure 5.18, effect of the L4-L5 disc substitute on the trabecular bone loading was strongly modulated by the additional follower force, in all simulated rotational motions. Under load-controlled pure sagittal flexion, the upper section of the L5 trabecular bone was found to be only slightly affected by the presence of the adjacent device (Fig. 5.18a). However, simulating the motion with the additional follower compressive load, raised by nearly 80% the maximum strain energy density value resulting from the substitution of the intact disc model by the implant.

Under displacement-controlled flexion, the compressive follower load lowered, up to more than 20%, the overloading effect of the L4-L5 device on the lower and upper trabecular bone sections, of the L3 and L4 vertebral bodies, respectively (Fig. 5.18b). However, in both the rest of the L4, and all the L5 trabecular sections, simulated body weight contributed to reinforce the strain energy density increases due to the device. As such, while under pure flexion, the L4 trabecular mid-section was almost not affected by the implant, combining rotation and compressive follower force made the local mechanical energy to rise by about 60%. In the lower and upper trabecular sections of, respectively, the L4 and L5 vertebral bodies, body weight-like load had a smoother but significant effect, with an enlargement of the prosthesis influence ranging between 10% and 25%.

Under sagittal extension, the compressive follower compressive force also contributed to increase considerably the extra loading generated in the L4 vertebral body trabecular bone sections, by the presence of the L4-L5 disc substitute (Fig. 5.18c). Such increase was about 45% in the L4 upper trabecular section, and 20%, in the mid and lower sections. Note that in the L5 upper trabecular section, body weight-like additional load, had a limited effect, and emphasized the prosthesis-induced relative overload by less than 10%.

Simulating axial rotation motion with the additional follower compressive force, led to a quasi-zero device effect on the L3 vertebra body trabecular bone sections (Fig. 5.18d). For the rest of the bi-segment model trabecular sections, presence of the body weight-like load made almost no differences for the evaluation of the device effect.

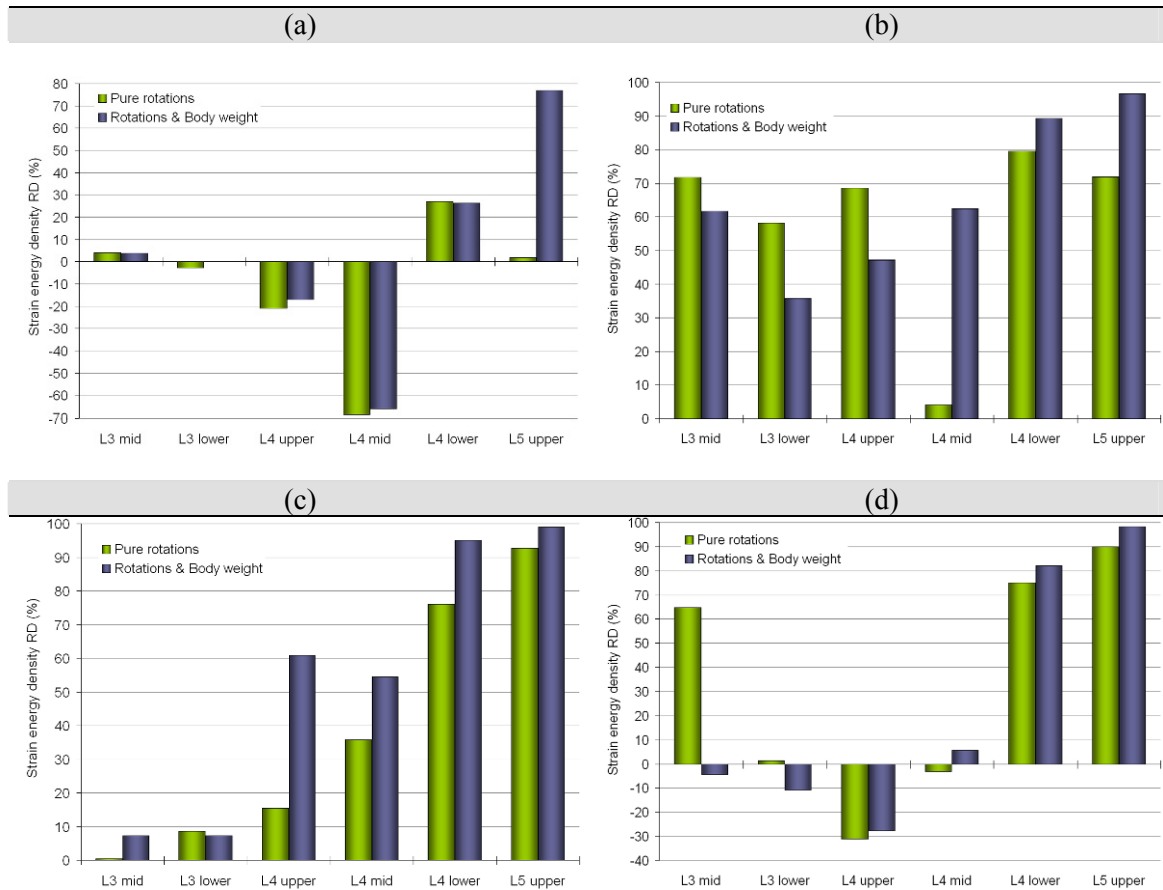


Figure 5.18: Effect of the body weight-like load on the relative differences in trabecular bone maximum strain energy density, predicted in vertebral bodies after the intact model L4-L5 intervertebral disc was substituted by the device model. a) Load-controlled flexion. b) Displacement-controlled flexion. c) Extension. d) Axial rotation.

(ii) Cortical bone

In most of the studied cortical bone sections, simulating the load-controlled sagittal flexion, with or without body weight-like follower compressive force, had few influence on the predicted prosthesis effect (Fig. 5.19a). In presence of the follower compressive load, the prosthesis-induced reduction of maximum strain energy density, computed in the mid-transversal cortical section of the L4 vertebral body, was lowered by about 10%. In the lower L4 cortical section, while under pure moments, L4-L5 disc substitute was found to increase the maximum strain energy density by more than 10%, with the additional body weight-like load, the implant reduced the stored elastic energy by about 35%.

Under displacement-controlled flexion, additional follower compressive force led to about 10% less prosthesis-induced overloading than the pure rotation, in the L3 mid-transversal and lower cortical sections (Fig. 5.19b). In the upper cortical section of the L4 vertebral body, similar results were found, but reduction of the prosthesis-induced overloading with the simulated body weight was around 30%. In the L4 cortical mid

section, the L4-L5 disc substitute was found to locally decrease the maximum strain energy density by more than 40%, under pure rotations. However, when both the treated and intact models were under the effect of the additional body weight-like follower load, this local energy increased by more than 55%. The compressive force also enlarged the implant effect on the upper L5 cortical bone, by about 20%.

Simulating sagittal extension motion with the body weight-like load did not modify the prosthesis effect on the L3 vertebral body sections (Fig. 5.19c). In the L4 vertebral body, the L4-L5 disc substitute was found to produce no significant overload in the different cortical bone sections. A large strain energy decrease was even calculated in the lower cortical area. However, unlike in L3, the compressive follower force made the prosthesis to generate more than 20% and nearly 50% of strain energy increases, respectively in the mid and lower L4 cortical sections. In the L5 upper cortical area, the implant, under pure extension, led to a higher locally stored mechanical energy that was further amplified by nearly 20%, with the body weight-like load.

Under axial rotation, prosthesis effect on cortical bone sections away from the implantation areas remained mostly the same, with or without additional follower compressive force (Fig. 5.19d). Nevertheless, adjacent to the device, the maximum strain energy density of the L4 lower cortical section decreased by more than 70% when the implant effect was assessed with the additional body-weight load. Conversely, in the upper L5 cortical section, a prosthesis-induced strain energy density increase, of more than 55%, was predicted when body weight was simulated with the intact and treated models.

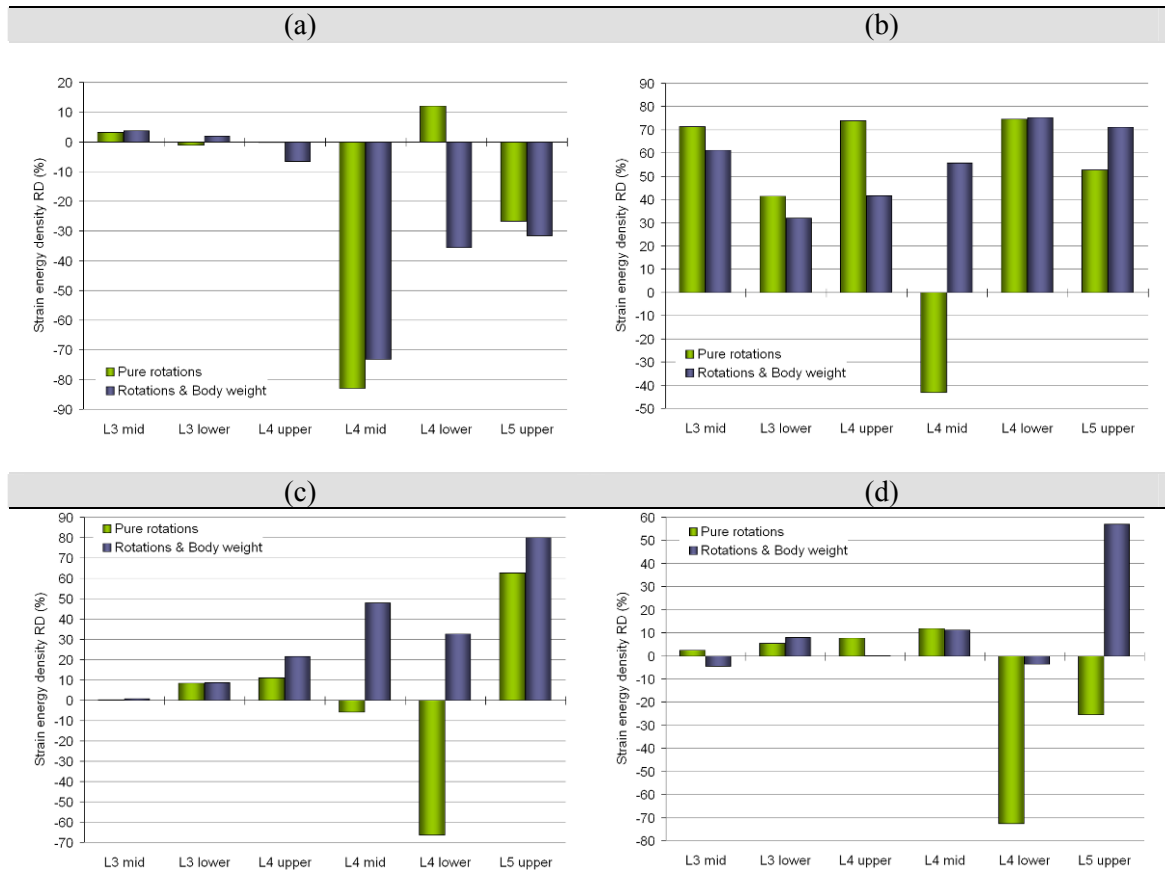


Figure 5.19: Effect of the body weight-like load on the relative differences in cortical bone maximum strain energy density, predicted in the vertebral bodies after the intact L4-L5 intervertebral disc was substituted by the device model. a) Load-controlled flexion. b) Displacement-controlled flexion. c) Extension. d) Axial rotation.

(iii) Bony endplates

As shown by Figure 5.20, simulating motions with or without the body weight-like compressive follower force, generally significantly modified the way the prosthesis affected the remaining adjacent bony endplates. Under load-controlled flexion, in presence of the L4-L5 disc substitute, pure moment alone led to more than 20% of maximum strain energy increase, in the L4 lower bony endplate. Simulation of the motion with the additional follower compressive load made the prosthesis to reduce by more than 25% the elastic energy stored in the L4 lower bony endplate. Also, with the body weight-like load, the L5 superior bony endplate adjacent to the implant was further overloaded by about 10%, when compared to the results obtained under the pure moment alone. Under displacement-controlled flexion, except a limited maximum strain energy density reduction of somewhat more than 10% in the non-treated segment, the additional follower compressive load did not significantly affect the prosthesis effect on the L3-L5 bi-segment model bony endplates.

Under pure sagittal extension, the prosthesis reduced the elastic energy of the L4 lower endplate and increased the loading of the L5 superior endplate, by more than 40% and 60%, respectively. However, when motion was simulated with the body weight-like additional load, the L4-L5 disc substitute overloaded the adjacent L4 and L5 endplates, respectively by nearly 70% and 90%. Under, pure axial rotation, the device was predicted to significantly reduce the adjacent endplate maximum strain energy densities. When combined with the follower compressive force, rotational motion made the implant to overload by less than 10% and by about 85% the lower L4 and upper L5 bony endplates, respectively.

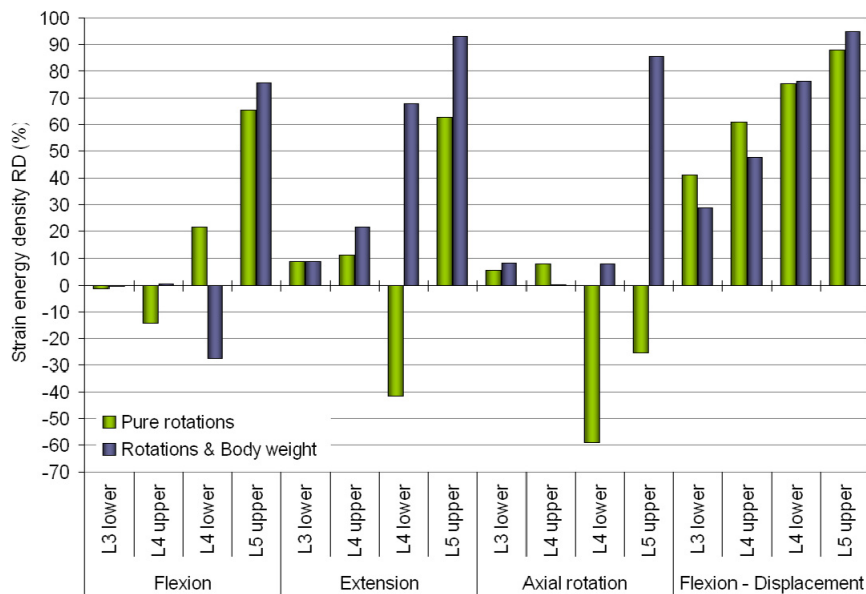


Figure 5.20: Effect of the body weight-like load on the relative differences in bony endplate maximum strain energy density, predicted after the intact L4-L5 intervertebral disc was substituted by the device model.

d. L3-L4 intervertebral disc loading

1) Annulus fibrosus

(i) Load distribution under pure rotations

Figures 5.21 show the maximum strain energy density computed in different L3-L4 annulus fibrosus areas (Figure 2.8a) of the intact and treated models. Note that for the lateral (LAT) and postero-lateral (PLAT) quadrants, no distinctions were made between the intervertebral disc left and right sides. For each of these quadrants, only one representative maximum energy value was reported, making the symmetry presented by the different diagrams 5.21 to be purely figurative.

Under load-controlled sagittal flexion, significant mechanical work differences were predicted between the L3-L4 annuli of the intact and treated models (Fig. 5.21 a,b). However, under displacement-controlled flexion, maximum strain energy density values increased dramatically in all the L3-L4 annulus areas after the L4-L5 intervertebral disc model was replaced by the prosthesis device (Fig. 5.21c,d). Some differences in strain energy distributions were also computed between the intact and the treated model. As such, the mid-outer (MID(1)) radial layer was more similarly loaded as the outer layer (OUT), in the treated than in the intact model. Conversely, dissimilarity of stored elastic energy between the mid-outer and the mid-inner (MID(2)) layers was relatively smaller in the intact than in the treated model. L3-L4 annulus fibrosus strain energy distributions respectively obtained under load- and displacement-controlled flexions, were comparable in the treated model (Fig. 5.21b,d), but diverged greatly in the intact model (Fig. 5.21a,c).

Under sagittal extension, maximum strain energy density values predicted in the L3-L4 annulus fibrosus were somewhat greater in the treated than in the intact model (Fig. 5.21e,f). Such energy increase, in presence of the L4-L5 disc substitute, was particularly noteworthy in both the anterior and lateral inner quadrants, and in the anterior mid-inner part of the annulus. In general, the posterior quadrant did not seem largely affected by the insertion of the device. Under axial rotation, only the outer and mid-outer sections of the anterior, lateral, and postero-lateral annulus quadrants resulted somewhat larger in the treated than in the intact model (Fig. 5.21g,h). On the contrary, in the posterior annulus, the different annulus radial layers were generally less loaded in presence of the L4-L5 disc substitute than without.

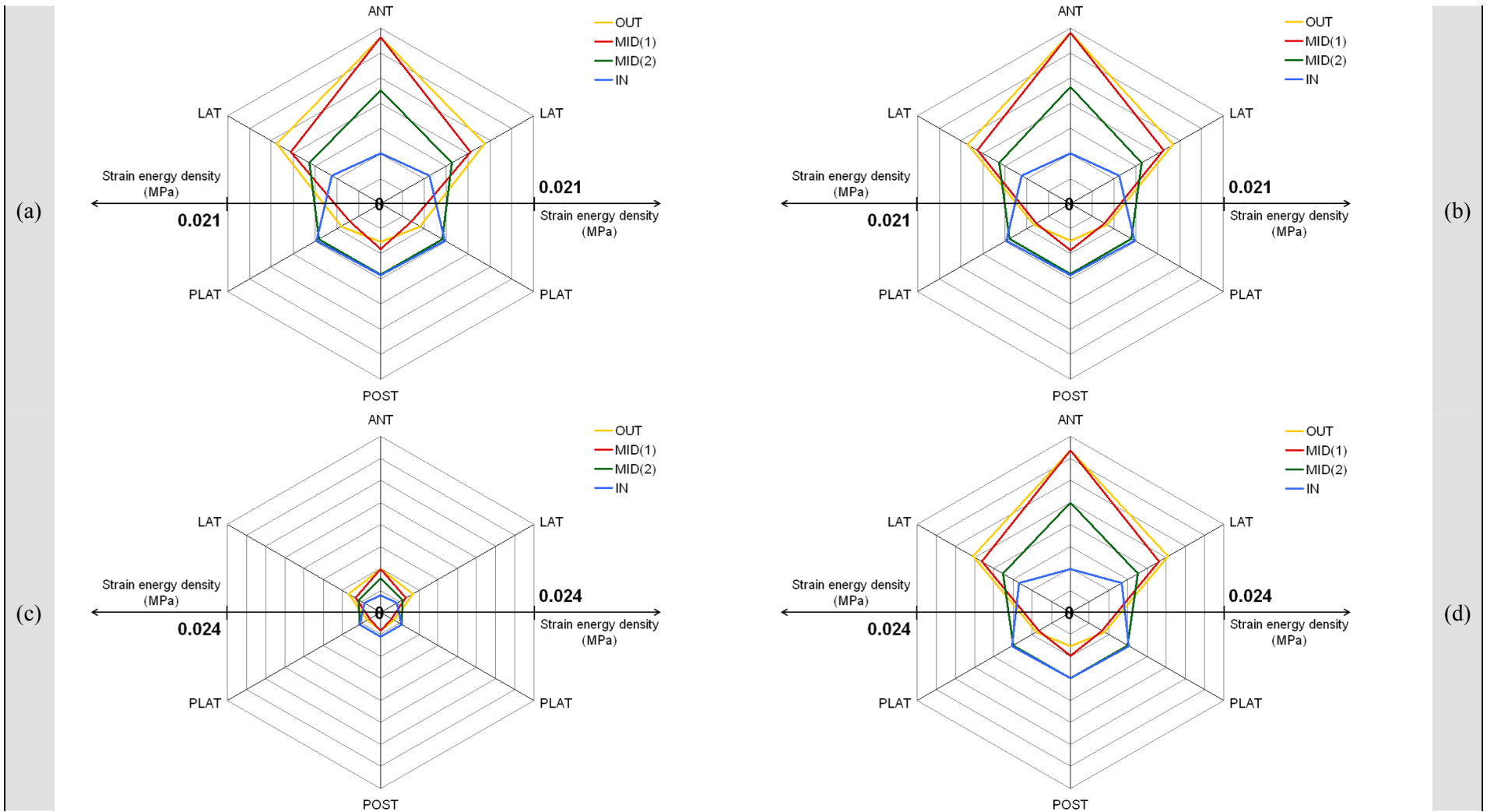


Figure 5.21: Strain energy density distribution in the different quadrants of the L3-L4 intervertebral disc. a) Intact model, load-controlled flexion. b) Treated model, load-controlled flexion. c) Intact model, displacement-controlled flexion. d) Treated model, displacement-controlled flexion.

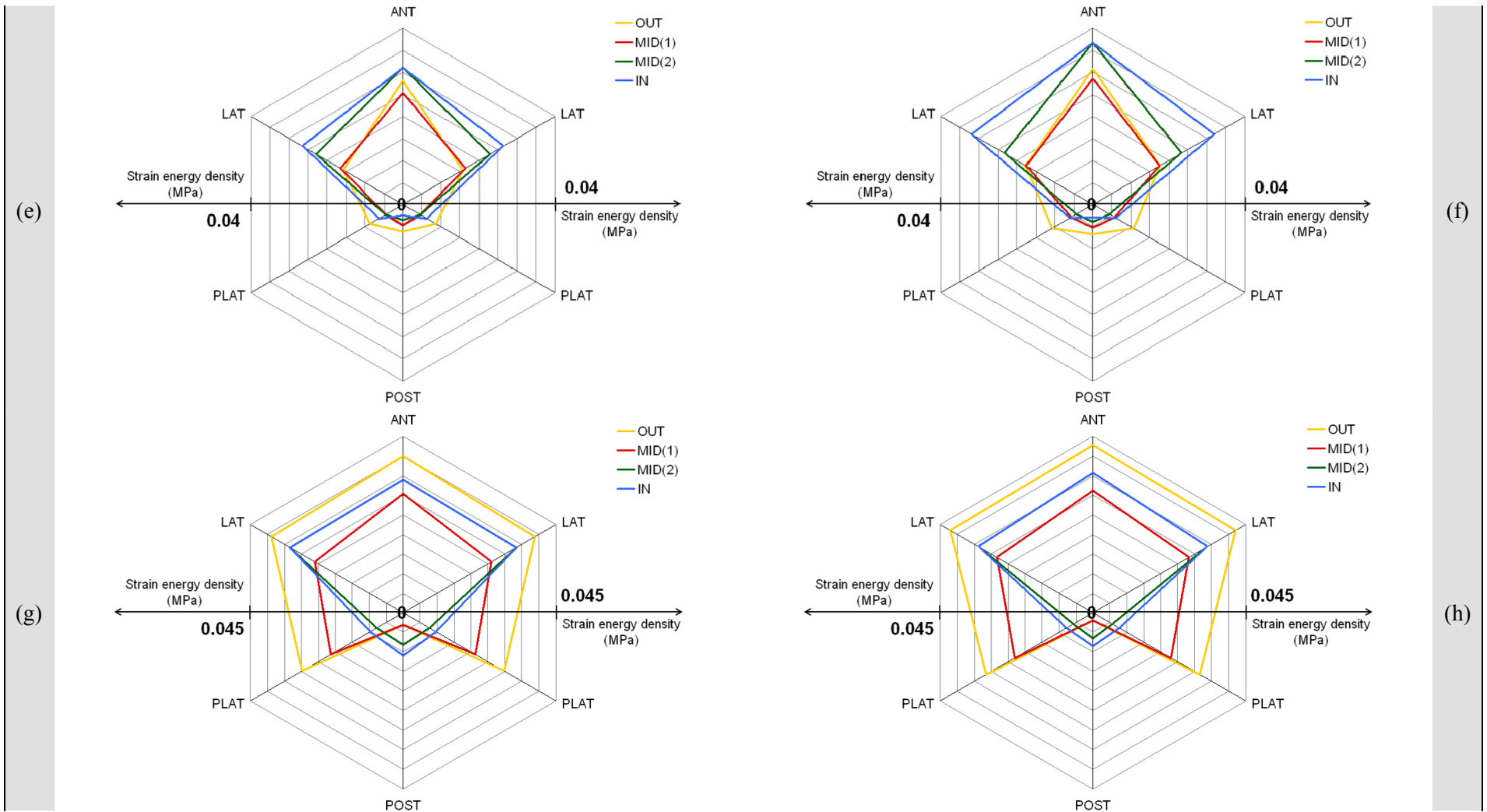


Figure 5.21: Strain energy density distribution in the different quadrants of the L3-L4 intervertebral disc. e) Intact model, extension. f) Treated model, extension. g) Intact model, axial rotation. h) Treated model, axial rotation.

(ii) *Body weight-like load effect*

Under load-controlled flexion, additional body weight-like load qualitatively modified the way the L4-L5 disc substitute affected the L3-L4 annulus fibrosus strain energy density (Fig. 5.22a). However, independently of the compressive follower force, the prosthesis only slightly quantitatively influenced the L3-L4 annulus fibrosus biomechanics.

When body weight was added to the displacement-controlled flexion motion, the overloading of the L3-L4 annulus fibrosus induced by the L4-L5 disc substitute was generally reduced (Fig. 5.22b). Depending on the location within the annulus, such reduction ranged from 15%, in the inner postero-lateral area, to up to about 50% for the inner anterior and lateral annulus areas. Both with and without follower compressive force, the most pronounced differential effects of the prosthesis across the L3-L4 annulus thickness were computed, in the anterior quadrant, between the inner and other regions, and in the posterior quadrant, between the outer and other regions.

Simulating sagittal extension together with the body weight-like load, completely suppressed the slight strain energy density increases computed in the respective outer and inner regions of the L3-L4 anterior and posterior annulus (Fig. 5.22c). However, the additional follower compressive force also locally emphasized the prosthesis overloading effect in several areas of the annulus, such as the anterior area, the lateral, and posterior mid-outer and outer areas, and the postero-lateral mid-inner area. In simulations involving pure rotations only, with a strain energy density increase of about 21%, the mid-outer postero-lateral L3-L4 annulus section was most negatively affected by the L4-L5 implant. Conversely, including the follower axial compression to the load case, the anterior mid-outer region became the most affected part of the L3-L4 annulus, with a mechanical work increase of nearly 18%. Globally, prosthesis-induced energy increase over the whole L3-L4 annulus was about 50% under pure rotations against 38% with the additional body weight-like load.

Under axial rotation, simulating pure moment only, the prosthesis reduced the postero-lateral and posterior strain energy density values of the L3-L4 annulus, by between 20% and more than 35% (Fig. 5.22d). Nonetheless, simulating the motion together with the follower compressive force greatly reduced such implant effect. In the inner and mid-inner postero-lateral regions, annulus even became locally overloaded, but such overload did not overcome 8%. For the rest of the L3-L4 annulus areas, independently on the modelled boundary conditions, the L4-L5 disc substitute had only little effect.

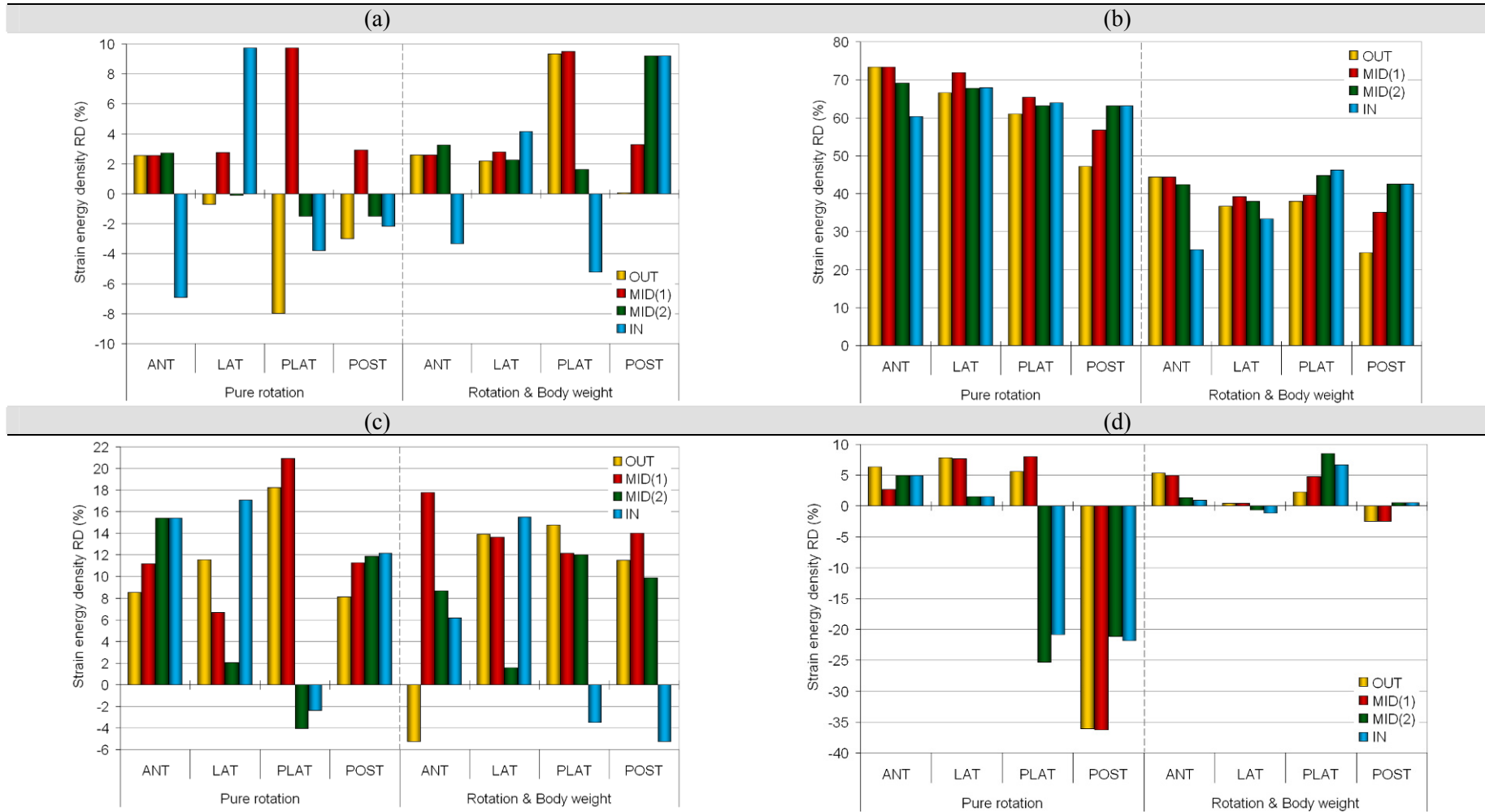


Figure 5.22: Effect of the body weight-like load on the relative differences in maximum strain energy density, predicted in the L3-L4 annulus fibrosus after the intact model L4-L5 intervertebral disc was substituted by the device model. a) Load-controlled flexion. b) Displacement-controlled flexion. c) Extension. d) Axial rotation.

2) Nucleus pulposus

Under pure rotations, maximum strain energy density values computed in the L3-L4 nucleus pulposus generally corresponded to the maximum values predicted in the adjacent inner annulus layer. They were summarized in Figure. 5.23. According to the results presented in Figure 5.21, the prosthesis did not significantly affect the nucleus maximum strain energy density, under load-controlled flexion. But it did under displacement-controlled flexion, and also, to a lesser degree, under extension. Under axial rotation, maximum energy computed in the L3-L4 nucleus pulposus was somewhat smaller in the treated than in the intact model.

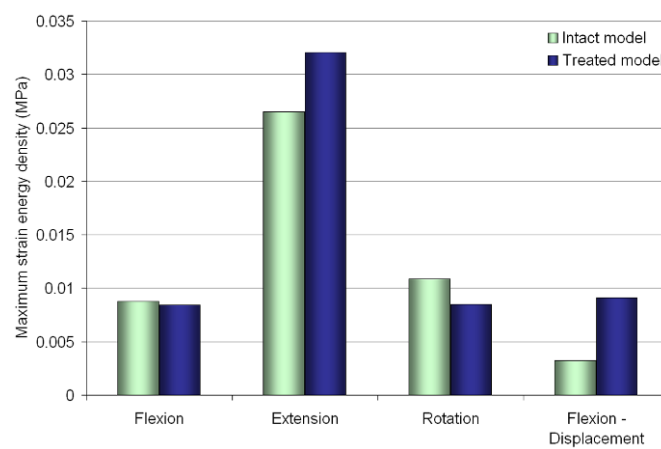


Figure 5.23: Maximum strain energy density values computed in the L3-L4 nucleus pulposus of the intact and the treated model.

As shown in Figure 5.24, the presence of the L4-L5 disc substitute the L3-L4 nucleus hydrostatic stress gradient index tended to slightly increase, under both pure extension and pure axial rotation. Conversely, under displacement-controlled flexion, $I_{\Delta h}$ was somewhat lower in the treated than in the intact model. In the treated model, results given by the displacement- and load-controlled flexion motions were also more similar than in the intact model. Simulating the different motions with the additional body weight-like compressive force lowered considerably the hydrostatic stress gradient indexes. Such decrease was particularly important under sagittal extension. The follower compressive force also considerably reduced the differences in nucleus pressure relative distribution, between the different load-cases. Moreover, when the additional body weight was simulated, prosthesis was found to have no effect anymore on the predicted $I_{\Delta h}$ values.

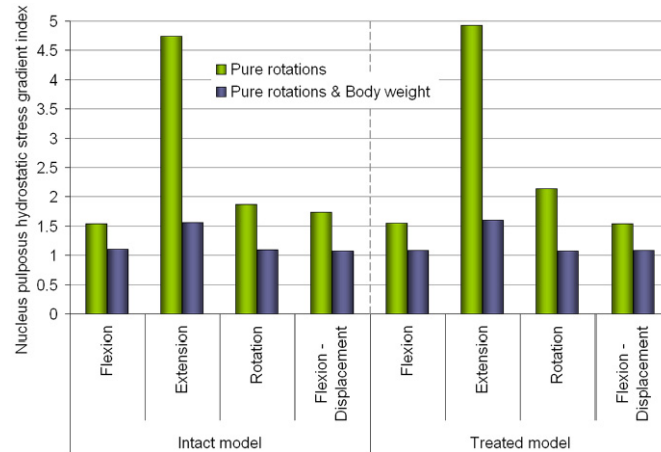


Figure 5.24: Nucleus hydrostatic stress gradient index (Eq. (5.10)) computed in the L3-L4 intervertebral disc of the intact and treated models, both simulated under pure rotations and pure rotations plus body weight-like load.

III. Prosthesis “biomechanics”

a. *p*-HEMA/PMMA matrix

As shown in Figure 5.25, the major principal strains computed in the *p*-HEMA/PMMA matrix of the L4-L5 disc substitute were always below 2.5%, where plastic deformations were experimentally found to occur (Fig. 5.10). Nevertheless, when the body weight-like load was additionally simulated, maximum principal strains increased up to nearly 2.4%, under extension, and minimum principal strains decreased as low as about -2.3%, under load-controlled flexion. For a given motion, tensile and compressive deformations in the device were always higher in presence of the follower compressive force. Maximum strains were generally computed in the outer annulus-like part of the prosthesis.

While pure sagittal flexion led to the highest tensile strains in the posterior annulus-like outer wall (Fig. 5.25a,d), additional body weight-like compressive load induced largest matrix deformations in the anterior outer wall (Fig. 5.25e,h). No large differences were predicted between load- and displacement-controlled pure flexions. With the body weight-like load, displacement-controlled sagittal flexion returned absolute strain values somewhat lower than under pure flexion. Under axial rotation, the follower compressive force led to large anterior tensile strains, compared to the results given by the pure moment only (Fig. 5.25c,g). Axial rotation was generally the load case leading to the lowest principal strain values. Note that for all load cases, slight tensile strains were usually computed in large parts of the nucleus-like part area, even with the body weight-like compressive follower force.

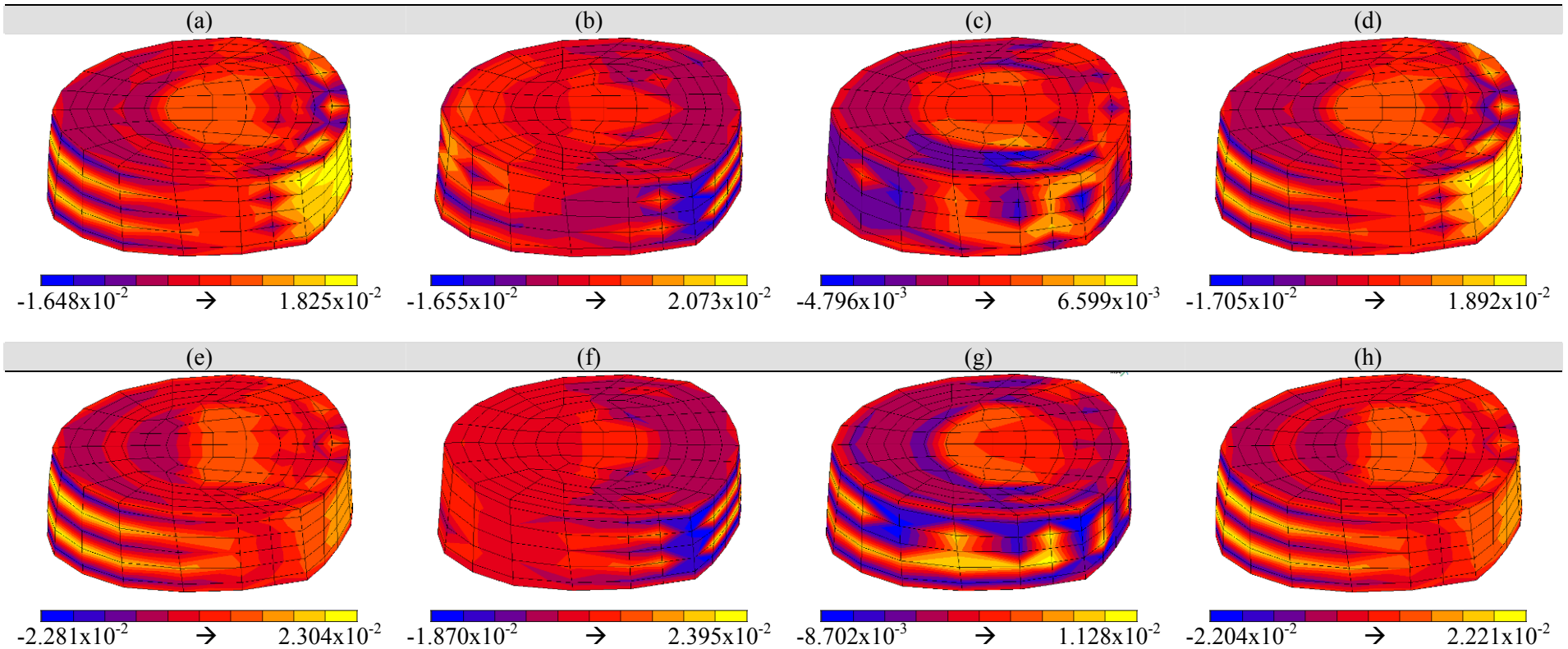


Figure 5.25: Major principal strain values (obtained by analogy with Eqs. (2.13)-(2.19)) computed in the *p*-HEMA/PMMA matrix of the device placed in the L3-L5 lumbar spine bi-segment model as a L4-L5 disc substitute. a) Pure load-controlled flexion. b) Pure extension. c) Pure axial rotation. d) Pure displacement-controlled flexion. e) Pure load-controlled flexion with body weight-like load. f) Pure extension with body weight-like load. g) Pure axial rotation with body weight-like load. h) Pure displacement-controlled flexion with body weight-like load.

b. PET fibres

Figure 5.26 compares the tensile stresses computed in the annulus-like PET fibres of the device, with the tensile stresses computed in the L4-L5 annulus fibres of the intact model. In general, much less fibres were activated in the device model than in the corresponding natural disc model. For all load cases, inner fibre layers of the device annulus-like part were rarely stressed.

Flexion was the load-case where the least amount of activated device PET fibres was found (Fig. 5.26a,d), and where the PET fibre stress distribution differed more from the fibre stress distribution predicted in the intact L4-L5 annulus (Fig. 5.26e,h). Largest prosthesis fibre stresses were computed in the annulus-like posterior outer wall, while annulus-like anterior fibres were hardly activated. Conversely, in the intact L4-L5 annulus, anterior fibres were mostly stressed. Moreover, under load-controlled flexion, better antero-posterior fibre activation balance was found in the intact intervertebral disc than in the composite device. Note that in the intact model, L4-L5 annulus fibres were significantly less loaded under displacement-controlled than under load-controlled flexion. Within the implant annulus-like part, such outcome was also predicted, but much less pronounced than in the substituted intervertebral disc.

Under sagittal extension, difference in fibre peak stress, between the treated model composite device and the intact model substituted disc (Fig. 5.26b,f), was relatively two times lower than under load-controlled flexion. In both the device and the substituted intervertebral disc, maximum fibre tensile stress occurred in postero-lateral outer layer. However, while in the intact model, L4-L5 posterior outer fibres were also highly stressed by the extension motion, in the treated model artificial disc, posterior outer fibres were almost not activated. Among all the simulated load cases, axial rotation returned the most similar fibre stress distributions and magnitudes in both the treated model prosthesis and the intact model substituted disc (Fig. 5.26c,g). Nevertheless, as for flexion and extension, most of the device inner and mid-inner PET fibres remained unstressed.

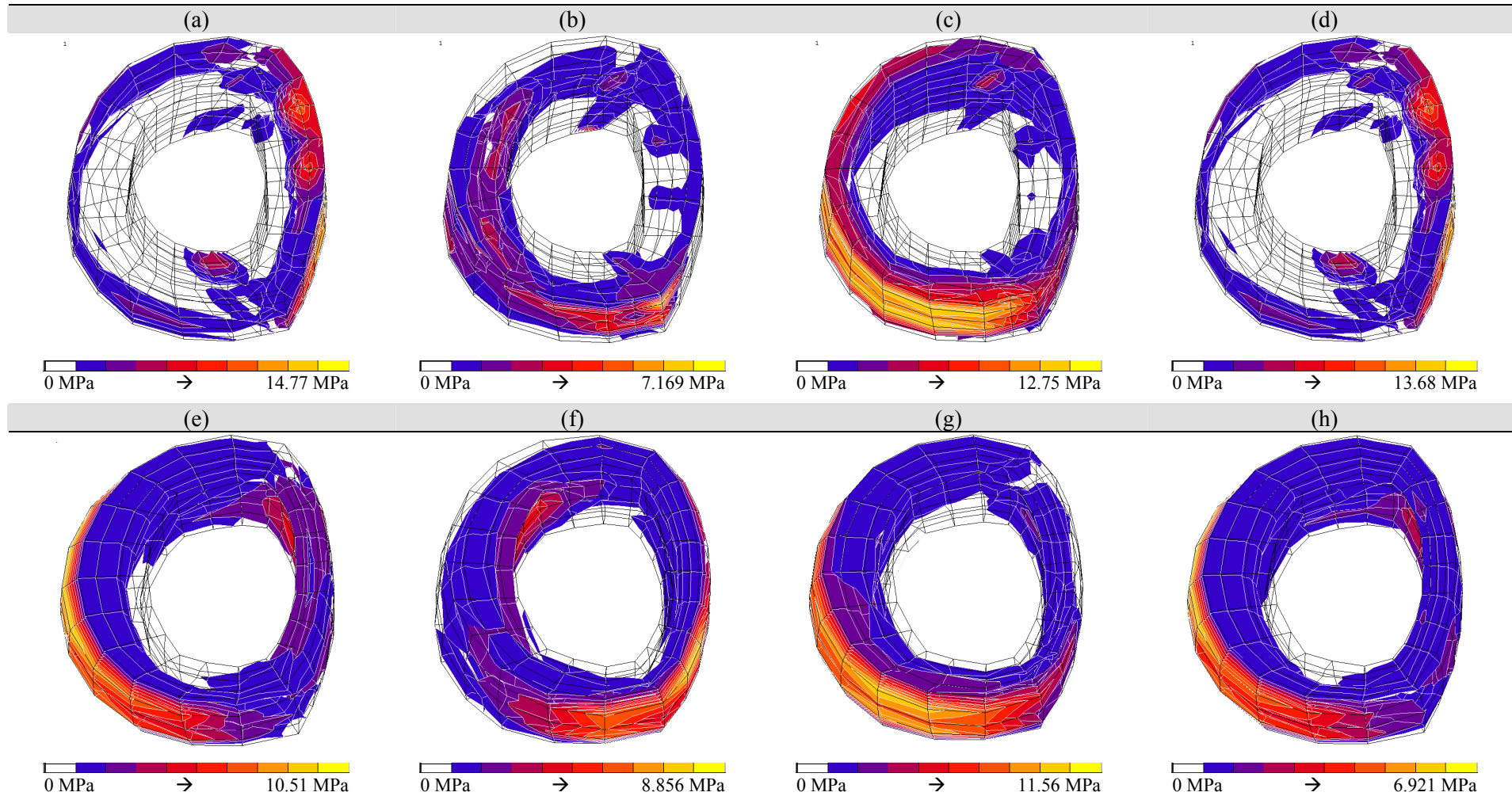


Figure 5.26: Maximum principal stresses (Eqs. (2.13)-(2.19)) computed under pure rotations with body weight-like load, in the rebar elements of both the device annulus-like part (a,b,c,d) and the intact model L4-L5 annulus fibrosus (e,f,g,h). a,e) Load-controlled flexion. b,f) Extension. c,g) Axial rotation. d,h) Displacement-controlled flexion.

c. General load distribution

General load distributions in the L4-L5 disc substitute are presented in Figure 5.27, in terms of maximum strain energy density distribution. They were compared to the load distribution predicted in the L4-L5 intervertebral disc of the intact model. Under pure rotations, both with and without body weight-like load, the elastic energy stored in the implant was generally the highest in the outer annulus-like part and decreased toward the nucleus-like part. However, in the substituted intervertebral disc of the intact model, pure flexion and extension motions both led to the highest maximum strain energy density values in the mid-inner and inner annulus layers (Fig. 5.27a). Under load-controlled flexion and extension, contrary to the results obtained in the implant, the outer annulus of the intact L4-L5 intervertebral disc returned the lowest elastic energy peak values. From the outer to the mid-inner radial sections of both L4-L5 intact and artificial annuli, pure axial rotation qualitatively gave the best match of peak strain energy density between the intact and the treated model. In terms of global loading, the displacement-controlled flexion simulated in the intact model led to the lowest L4-L5 annulus fibrosus strain energy density values. However, in the treated model, displacement-controlled flexion gave the highest annulus-like peak energy values, closely followed by the load-controlled flexion results. Implant nucleus-like part also mostly worked under flexion, while in the substituted intervertebral disc, largest nucleus pulposus strain energy density value was predicted under sagittal extension. Pure extension was also the load case where the intact model returned the highest strain energy density peak values, in the different L4-L5 annulus radial sections.

When rotation motions were simulated together with the body weight-like compressive force, both in the intact and treated models, peak strain energy density variations from load case to load case were significantly reduced (Fig. 5.27b). Also, with follower compressive load, peak energy distributions in the different areas of the disc substitute were more similar to those predicted in the substituted L4-L5 intervertebral disc, than under pure rotations. However, some important differences between the intact L4-L5 intervertebral disc and the prosthesis remained. For example, under flexion, the additional follower compressive load increased elastic energy peak values in the intact model, while it decreased it in the treated model. Moreover, whereas the energy increase, computed in the L4-L5 intact intervertebral disc, mostly occurred in the outer and mid-outer annulus layers, energy decrease in the disc substitute was roughly homogeneous over the different radial sections. When sagittal extension was simulated in the intact model, L4-L5 annulus strain energy density was lower with body weight-like load than without. In the outer annulus layer, such strain energy decrease with the follower compressive force was nearly insignificant when compared to the rest of the intervertebral disc areas. Conversely, in the treated model, body weight-like load made prosthesis strain energy density peak values to globally increase. Under axial rotation, additional compressive force raised the strain energy peak values computed in the nucleus and in both the outer and mid-outer annulus layers of the L4-L5 intact intervertebral disc. However, maximum energy stored in the annulus mid-inner and inner areas decreased. In the treated model, body weight-like load, added to the axial rotation motion, induced larger mechanical work in all the prosthesis areas, but the annulus-like mid-outer layer.

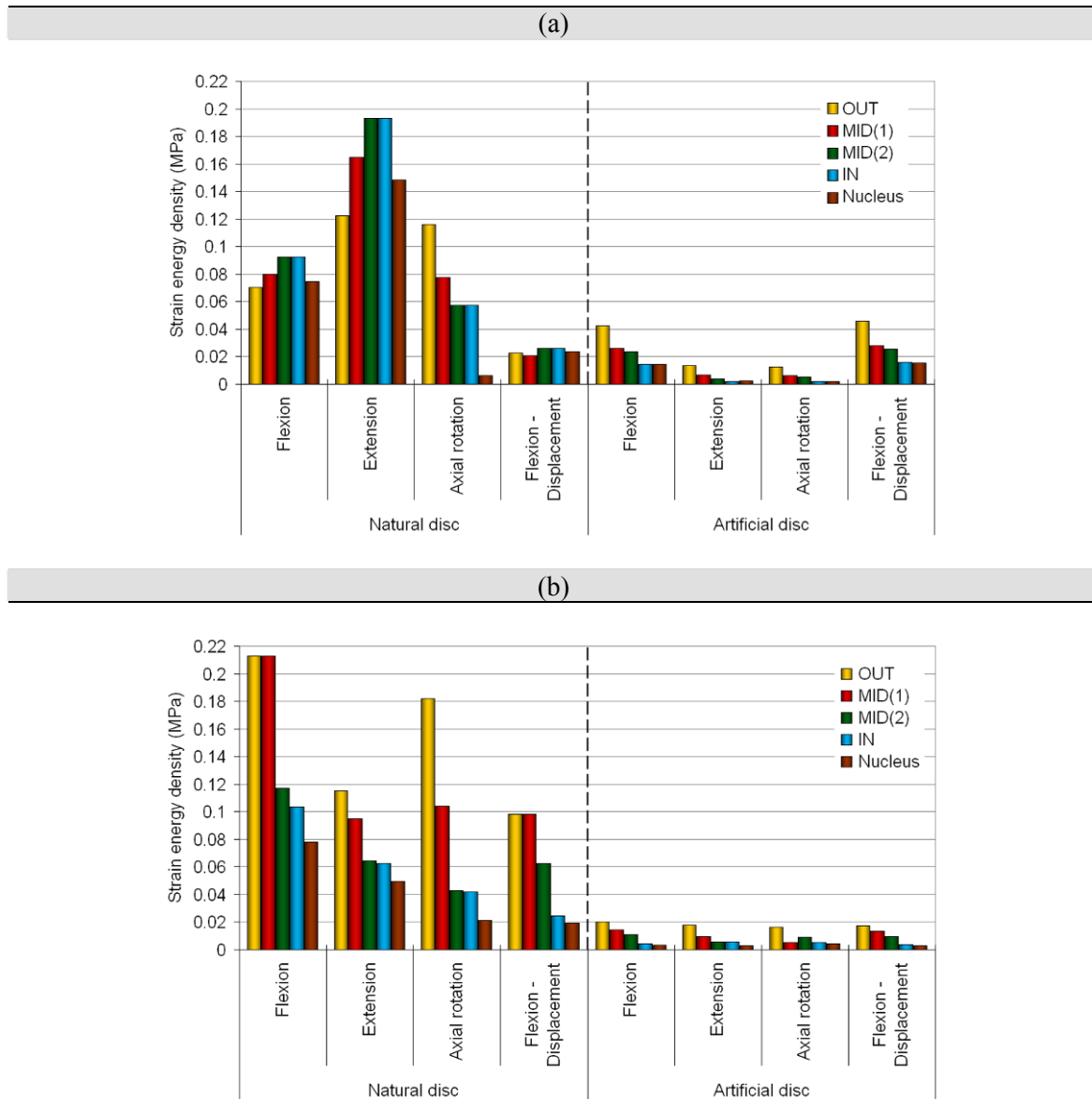


Figure 5.27: Peak strain energy density distribution in different areas of the intact model L4-L5 intervertebral disc and treated model L4-L5 disc substitute.

D. Discussion

I. Device modelling

Device mechanical modelling was performed, based on uniaxial reaction forces (transformed into engineering stress) measured for elasto-plastic p-HEMA/PMMA samples, and for the non-linear assembly of a composite prototype. Under static conditions, failure of the elasto-plastic composite model to reproduce the prototype compressive behaviour showed, however, that the composite device could not be simply modelled by superimposing the p-HEMA/PMMA experimental behaviour and the PET fibres. First of all, compared to the elastic Young's modulus measured for the p-

HEMA/PMMA bulk material, the lower initial stiffness measured for the prototype suggested that the PET fibres had some softening effect on the apparent axial compressive stiffness of the composite. Therefore, the annulus-like and nucleus-like HEMMA-PMMA matrices had to be considered as different materials, to compensate the limitation of Rebar modelling in taking into account material volume fractions different from one. According to the hypothesis that along fibre directions, contribution of the PET material to the device compressive stiffness should be insignificant, the rule of mixtures theory for composite materials allowed estimating a reasonable apparent elastic stiffness for the annulus-like part p-HEMA/PMMA matrix. Nevertheless, since PET fibres were not parallel, but oblique to the device axial direction the above approach still represents a rough approximation of the composite material mechanics. Moreover, as the nucleus-like part is mechanically constrained by the annulus-like part, the hypothesized parallel model leading to Equation 5.1 may be questioned. Some mechanisms such as fibre-matrix slippage could have actually influenced the experimental results, but could not be considered for theoretical modelling. Therefore, a mechanical characterization of mono-oriented fibre reinforced p-HEMA/PMMA samples with measurements parallel and perpendicular to the fibre directions could have been useful to establish the real orthotropic properties of the layered material and lower the amount of modelling approximations.

Besides the problem of composite modelling, while the elasto-plastic p-HEMA/PMMA model failed in reproducing the prototype compressive behaviour, the nearly incompressible hyperelastic matrix model allowed reproducing the experimental data. Hyperelastic model was built from the assumption that once p-HEMA/PMMA free swelling equilibrium was achieved, both the device endplates and circumferential PET fibres should act as natural barriers to hinder water outflow from the matrix. Pressurized interstitial fluid was then showed to be a possible important load-bearing component. Even if successful, the hyperelastic composite representation of the device was mostly phenomenological and might be unable to capture behaviours beyond the duration of the experiments used to adjust matrix compressibility. Indeed, matrix compressibility should not be homogeneous, but at least change with the apparent material permeability, from the outer to the inner prosthesis wall. Modelling the p-HEMA/PMMA matrix as a poroelastic material could have assessed this, but the nature of the p-HEMA/PMMA experimental data, available for the novel intervertebral disc modelling, did not allow integrating such possible phenomena. Moreover, in the present study, such limitation was not dramatic, since the effect of the prosthesis was assessed under quasi-static conditions only, by comparing between different simulations with a strict control of the varying parameters.

II. Ranges of motion

Compared to the models presented in Chapters 3 and 4, the intact L4-L5 bi-segment model used in this study was not the best developed, neither in terms of geometry, nor in terms of tissue mechanical modelling. Nevertheless, all predicted ranges of motion were in fairly good agreement with the reported *in vitro* data. Yet, as underlined in the two previous Chapters of this thesis, such comparisons need to be cautiously considered, as their quality may not prove the quality of detailed descriptions

of the model biomechanics. Therefore, it is highly important to always consider the following discussions as a strict comparison of models and not as an absolute evaluation of the implant effect.

For all studied load cases, the disc substitute was too stiff to preserve the L4-L5 inter-segmental mobility as simulated with the intact L4-L5 intervertebral disc. Under any load-controlled rotations, almost homogeneous distributions of the local moments along the bi-segment model made the intact L3-L4 segment, adjacent to the treated level, to be not significantly affected by the loss of L4-L5 motion. Under displacement-controlled flexion, however, the lack of flexibility of the implanted L4-L5 segment reported most of the imposed rotation on the adjacent level. The divergence observed between the rotations imposed on the beam network (Fig. 4.9) and the total effective segmental rotations was mainly due to the creation of shear deformations in the L3-L4 bi-segment model. At the L3-L4 level, these shear deformations were even more influent with the additional stiffness generated by the L4-L5 disc substitute. Actually, a debate about experimental evaluation of the spine biomechanics, already pointed out that displacements imposed on the most superior vertebral body generate complex loads of varying magnitudes along the rest of the spine segments (Goel *et al.*, 1995c). Moreover, these uncontrolled loads were reported to be likely to change with alterations, such as the presence of an implant could be. At this point, it is interesting to highlight that the body weight-like force had a slight stabilizing effect that could eventually be even stronger, if the additional compressive follower forces due to muscles were modelled (Patwardhan *et al.*, 2003).

III. Zygapophysial joints

This section makes often reference to the upper and lower facets of the zygapophysial joints. In this context, “upper facets” refers to the lower facets of the intervertebral joint upper vertebra, and “lower facets” refers to the upper facets of the lower vertebral.

a. Axial rotation

When axial rotation was simulated with the treated model, the large mobility of L3 with respect to L4 increased the pressure of the anti-rotation side L3 inferior facet against the anti-rotation side L4 superior facet. At the L4-L5 level, the low intersegmental motion allowed by the prosthesis simply reduced the L4-L5 zygapophysial joint anti-rotation side contact. The large device-induced additional loss of L4-L5 facet contact forces, when axial rotation was simulated together with the body weight-like force, can be attributed to an additional stiffening of the device, due to its non-linear compressive behaviour.

b. Sagittal rotations

Under load-controlled flexion, the relative immobility of L4 induced simultaneously a L3-L4 facet contact force decrease and a L4-L5 facet contact increase. However, under extension, the implant led to contact force reductions at both levels. Indeed, L4-L5 facet contact results under sagittal rotations can be explained by different modulations of vertebral anterior, posterior, and axial translations that normally occur during sagittal motions.

1) Flexion

Flexion motion induced global anterior translations of all the moving vertebrae, whose effect was to close the zygapophysial joint articular contact. However, the posterior bony elements simultaneously moved in the cranial direction, which tended to open the zygapophysial joints. Obviously, the reduced translation capacity of the implant-bounded L4 vertebra enlarged the motion-induced translation effects of L3 on the facet joint contacts. Thus, under load-controlled flexion, facet contact loss predicted at the L3-L4 level, between intact and treated models, was mainly due to a lower effect of L3 anterior translation, than of L3 axial translation, relatively to L4. Note, however, that under displacement-controlled flexion, prosthesis made the L3-L4 intersegmental rotations to be so large, that the L3-L4 contact force relieve, predicted under load-controlled conditions, was inexistent and even replaced by a slight contact force increase.

At the L4-L5 level, situation was reversed and the L4-L5 contact force increase in presence of the disc substitute was induced by a larger antero-posterior than axial effect of L4 mobility, relatively to L5. Actually, because of the small gap between the zygapophysial joint upper and lower facets, in order to limit facet contact forces, upper facets axial displacements along the lower facets need to be significantly larger than the antero-posterior deformations of the joint. Thus, the L4-L5 facet contact increase under load-controlled flexion can be naturally attributed to a general low deformability of the treated L4-L5 intervertebral joint. Note also that the p-HEMA/PMMA matrix constitutive model could also have a significant influence. Being modelled as a nearly incompressible material, the loaded matrix will more easily experience deviatoric deformations, than normal deformations. Thus, in the posterior annulus-like part of the prosthesis, postero-anterior deformations could be locally preferred to axial tensile deformations.

Under flexion, additional body weight-like compressive force limited the axial tensile deformations. It consequently tended to enlarge prosthesis-induced zygapophysial joint contact force increases, or reduced possible facet force decreases, as predicted in the L3-L4 zygapophysial joint, under load-controlled flexion. At the treated level, simulated compressive force seemed insufficiently high to affect the stiff disc substitute. Nevertheless, in apparent contradiction with the discussed effects of axial and anterior vertebral translations on the facet contact forces, prosthesis-induced L4-L5 facet contact increase was somewhat lowered by the additional body weight-like load. Actually, in the treated model, the large rotation of L3 with respect to L4 largely

oriented the follower load in an antero-posterior direction, reinforcing the effect of the postero-anterior deviatoric deformations in the L4-L5 posterior disc substitute. Nevertheless, the follower compressive loads applied on the top of L3 cannot take into account L4 muscle attachments (Chap.1,(Bogduk *et al.*, 1992)), and simulating real muscle forces could qualitatively lead to different outcomes. Moreover, in the deformed configuration, effect of top compressive force rotations might be sensitive to the length of the modelled spine segment.

2) Extension

The extension motion involved both posterior and axial translations of the vertebrae. Unlike flexion, axial translations were directed toward the caudal end of the bi-segment model and contributed to close the joint. However, posterior translations tended to move the superior facets of the zygapophysial joints away from the adjacent inferior facets. Hence, at the L4-L5 level, reduction of the facet contact forces with the prosthesis suggests that, as under load-controlled sagittal flexion, the disc substitute preferentially favoured the relative effect of the local antero-posterior deformations. At the L3-L4 level, the low mobility of L4, compared to L3, also made L3 posterior translation to significantly decrease the facet contact forces, showing the importance of the transversal translations, even in the intact L3-L4 intervertebral disc. Additional body weight-like compressive force should logically increase the relative influence of the posterior axial deformations and reduce the prosthesis effect on the facet joint contacts. However, in the present simulations, when acting on the deformed segments, the follower compressive force tended to separate the facet contact areas and somewhat reinforced the L4-L5 disc substitute effects predicted under pure rotation.

IV.Prosthesis “biomechanics”

a. Internal loads & device resistance

Major principal strains within the device showed that the fibre reinforced p-HEMA/PMMA matrix was not likely to deform plastically. However, strain values computed under flexion and extension, with the body weight-like load, were less than 10% lower than the first plastic strain limit, experimentally found for the p-HEMA/PMMA samples. Moreover, the most demanding loads, simulated in this study, were only 7.5N.m moments combined with a follower load of 370N. On one hand, such loads could be about one order of magnitude lower than the local forces possibly exerted by the muscles (Chap. 1, Table 1.1). Simulated load-cases would then highly underestimate *in vivo* loads and overestimate the device mechanical integrity. On the other hand, as an element of spine stabilization, estimated muscle forces help maintaining the functional spine curvatures against daily loading variations. And since the non-linear passive structures of the normal spine are naturally adapted to these curvatures, it is not clear whether the effective internal loads they support are proportional to the muscle-induced external forces. It is therefore difficult to conclude about the possible existence of permanent deformations in the prosthesis, based on

simplified load-cases. Nevertheless, *in vivo*, the spine is not subject to single, but to combined moments, that, even in absence of muscle modelling, are likely to locally increase intervertebral joint loadings (Schmidt *et al.*, 2007c). Thus, although the present results suggest that highest strains only occur at the periphery of the device, predicted deformations less than 10% lower than the first plastic strain value of the prosthesis matrix seem to give an insufficient security margin.

It is also worth to precise that a principal strain criterion, as discussed above, does not provide sufficient level of confidence to safely assess the risk of plastic deformations within a loaded material. However, according to the available experimental data, the prosthesis compressive behaviour was best simulated when the water-saturated p-HEMA/PMMA hydrogel was modelled as a hyperelastic material. With such model, a virtual water pore pressure was implicitly included in all stress calculations, but not in a controlled way. Thus, possible plastic deformations within the solid phase of the hydrogel could be hardly assessed with stress-dependent criterions such as Mohr-Coulomb or Drucker-Prager, generally adapted to fluid-filled porous structures. Moreover, as highlighted in Paragrah D.I., the present analysis does not take into account that long times of *in vivo* loading might significantly reduce the water content of the implant. Depending on the effective permeability of the composite structure, this could affect the long-term shape and/or the functional load-bearing capability of the prosthesis matrix. Accordingly, a similar device has been tested during 60 days of compression cycles interrupted by 8h of resting periods, without any signs of failure, but with remaining deformations up to more than 7% high (Gloria *et al.*, 2007). An experimentally based assessment of the p-HEMA/PMMA biphasic properties seems then mandatory to truly evaluate the nature of the internal loads that the implant may experience and confirm the long-term mechanical functionality of its materials.

b. Functional load distributions

Maximum values of strain energy density in the L4-L5 substituted disc and disc substitute show that the different materials of the composite device respond very differently to spine loading, when compared to a natural disc model. Under pure moments, internal loads in the composite prosthesis were always decreasing from the peripheral to the central parts of the composite structure, showing a direct relation to the imposed deformations, as if the structure were homogeneous. Conversely, in the L4-L5 intervertebral disc of the intact model, large loads were predicted in the inner annulus layers and in the nucleus, especially under sagittal rotations. Except under axial rotation, this led to strain energy density distributions, more homogeneous in the natural than in the artificial L4-L5 disc. Such results show contribution of the intact disc nucleus and inner annulus layers to redistribute across the structure the mechanical energy transferred by the external rotational moments. On the contrary, the annulus-like and nucleus-like parts of the composite device were not able to assume such role.

With the additional body weight-like load, outer bulging in the intact L4-L5 intervertebral disc model activated the outer annulus fibres (Chaps. 2,4). Compared to the results obtained under pure rotations, this fibre activation returned strain energy density distribution patterns more similar as those calculated in the prosthesis. For both the device and the L4-L5 intervertebral disc, mechanical energy was more even

distributed from load case to load case, with the additional follower force than without. Compressive follower force could then have had a stabilizing effect on both the intact and treated L4-L5 segments, by reducing the influence of the rotation-induced shear loads. As such, predictions suggest that the evaluation of the device biomechanics is highly load-dependent and could be more positive under load regimes including the natural *in vivo* compressive forces that constantly act on the lumbar spine (Chap. 1). Nevertheless, results also show that while load transfers into the intact disc can adapt to particular external forces, the variability of the device response is more limited.

Indeed, calculation of fibre stresses in the composite disc substitute demonstrated that, even with the body weight-like load, fibre activation in the device annulus-like part was significantly lower than fibre activation in the L4-L5 intact annulus. Divergence between prosthesis and intervertebral disc fibre activation was particularly pronounced around the nucleus and nucleus-like areas, and in the annulus and annulus-like areas directly subjected to compression. This was related to the high stiffness of the HEMMA-PMMA matrix and to the absence of bulging, the only mechanism making possible the transfer of axial compressive loads to the peripheral PET fibres. Deformation and mass migration of the nucleus-like material was also largely insufficient to transfer any load to the inner layers of the annulus-like part. Absence of mass migration could even induce tractions in the nucleus-like part. However, tensile strains predicted in the nucleus-like part could also be the result of HAPEX[®] endplate bending. In the composite device annulus, despite the higher order of magnitude of the PET fibre stiffness compared to collagen, matrix stiffness made the axial tractions to generally induce fibre stresses only somewhat superior than in the intact L4-L5 annulus. The low deformability of the p-HEMA/PMMA matrix and the insignificant relative load transfer to the PET fibres explained then the different strain energy density results between the device and the intact disc model, both in terms of distribution, and magnitude. A softer matrix could probably lead to a biomechanical behaviour of the composite disc substitute, closer to that of the substituted disc. Nevertheless, matrix deformation need to stay in the elastic domain, and from a point of view of biomaterial design, this is truly a challenge.

V. Vertebral bodies

Strain energy density calculations showed that for all load-cases, the presence of the L4-L5 disc substitute altered the load distribution, at least in the directly adjacent vertebral bodies. Absolute strain energy density values largely depended on the external loading approximations. It is therefore hard to extrapolate the present predictions to decide whether prosthesis-induced load alterations will generate pathological situations in the vertebral bodies. Nevertheless, according to the circumstantial relationships found between local strain energy density concentrations, and osteoblast and osteoclast activities (Huiskes, 2000; Jang *et al.*, 2009), active bone remodelling could be induced by the disc substitute. Strain energy density-based mechano-sensitive factors, used to predict reasonable trabecular structures (Ruimerman *et al.*, 2005), actually suggest that daily cell activity could be already modified if the altered energy density values computed in this study persist over time periods as short as several hundred seconds.

a. Unloaded areas

1) Away from the disc substitute

Under load-controlled sagittal flexion and axial rotation, strain energy density results indicated that the L4-L5 implant substitute significantly lowered the trabecular bone in the upper L4 vertebra. In the case of axial rotation, the relative immobility of L4 may have reduced some loading effects of the antagonist L3-L4 and L4-L5 coupled rotations (Chap. 4). On one hand, under load-controlled flexion, L4 upper bony endplate was also affected, and peak load reduction in the upper bony components may result from the release of the posterior L3-L4 facet joint constraint (Section D.III) that could have locally limited anterior disc pressurization. On the other hand, load-controlled flexion was the only load-case where prosthesis-induced unloading effect extended up to the L4 mid-height trabecular and cortical areas. Under displacement-controlled pure flexion, peak load reduction from the intact to the treated model, was also predicted at the mid-height of the L4 cortical wall, but was completely suppressed in presence of the body weight-like load. This indicated that cortical load decrease in the L4 vertebra mid-height section could be due to shear stress variations induced by direction changes in the forces that exert on the upper and lower cortical shell in presence of the prosthesis. In absence of any bulging from the L4-L5 stiff disc substitute, lower forces remain mostly axial. However, under displacement-controlled flexion, the additional follower load acting on the highly tilted L3 vertebra increased the global transversal force component exerting on the L4 cortical wall. Moreover, under load-controlled flexion, absence of continuous contact between the L4-L5 disc substitute and the L4 vertebra may have made the global trabecular compressive load, away from the prosthesis, to be lower in the treated than in the intact model, for a given L3-L4 intersegmental rotation.

Whatever their origin, bone load reductions may induce weakened bony structures and possibly loss of bone mass could locally occur overtime. This may of course be highly problematic for patients suffering perturbations of the bone maintenance system, such as osteoporosis. Note also that such results may be highly affected by the load transfer described from the intact L3-L4 nucleus pulposus to the L4 vertebra (Chap. 2). Thus, as highlighted in Chapter 4, the constitutive model chosen for the nucleus pulposus can critically influence the predictions, and the hyperelastic behaviour described in this study may largely diverge from a natural nucleus-bone structure interaction. Actually, load transfers computed with a hyperelastic L3-L4 nucleus pulposus may be more representative of what could occur with degenerated intervertebral discs (Chap 4, (McNally and Adams, 1992; Adams *et al.*, 1996)).

2) Adjacent to the disc substitute

Close to the prosthesis, several significant reductions of peak strain energy density were also computed between the intact and the treated model. Most of them occurred during pure rotations only. As such, under axial rotation and sagittal extension, the L4-L5 disc substitute made the maximum energy stored into the lower L4 cortical wall and endplate to drop considerably. Under axial rotation, both the L5 upper endplate and cortical wall section were also affected. According to the load transfers discussed in

Chapter 2 between nucleus compression, annulus traction and vertebral cortex loading, under extension, posterior transversal traction of the bony endplate should occur by external annulus bulging and nucleus pressurization. Simultaneously, anterior annulus deformations transversally compress the surrounding endplate and highly stretch the convex lower cortical wall. Under axial rotation, co-action of annulus deformation, oblique fibre stretch through annulus thickness, and nucleus pressurization, should make the adjacent bony endplates to be approximately equibiaxially stretched. Moreover, axial annulus deformations generated by coupled motions should locally stretch the lower and upper L4 and L5 cortical walls, respectively (Chap. 4). Basically, as discussed in Section D.IV, under the simulated load cases, the modelled L4-L5 disc substitute was unable to lead to similar loadings as predicted with an intact intervertebral disc model. Failure of the prosthesis materials to deform adequately and reproduce the load distributions generated into the intact L4-L5 intervertebral disc is then responsible for the losses of bone strain energy density, computed nearby the device under pure extension and axial rotation. After implantation, such outcome is not desirable, as it may lead to prosthesis loosening. However, the existence of most of the load reductions in the bony areas surrounding the prosthesis was suppressed by including the additional body weight-like follower compressive load.

b. Overloaded areas

1) Away from the disc substitute

Displacement-controlled flexion was the only load-case where both L3 and upper L4 bony components were overloaded by the presence of the L4-L5 disc substitute. Truly, the stiff prosthesis of the treated model made the global rotation imposed on L3 to be mainly reported on the softest motion segment, i.e. the intact L3-L4 segment. Therefore, compared to the intact model, large deformations in the L3-L4 intervertebral disc of the treated model led to increased load transfers to the adjacent bone.

Under sagittal extension, unlike under other load-controlled load cases, prosthesis-induced overloading was predicted in the mid-transversal trabecular section of the L4 vertebra. Peak strain energy density in the surrounding cortical shell was also higher in presence of the implant, but only when additional body weight-like load was simulated. Such outcome could be explained by the reduction of load transfer through the L3-L4 zygapophysial joints. However, the loss of facet contact induced by the implant was not linked to any significant increase in L3-L4 intersegmental rotation. Thus, different combinations of vertebral translations in the intact and treated models (§D.III.b.2)), might explain the extra strain energy stored in the mid transversal bony sections of the treated model L4 vertebra, under extension. In such context, on one hand, under pure rotation, change of trabecular peak strain energy density with the implant could be associated to the change of transversal antero-posterior translations of L3 relative to L4. On the other hand, under extension with compressive load, the increased cortical shell strain energy in the treated model was due to the additional axial displacements generated by the body weight-like load.

2) *Adjacent to the disc substitute*

In the areas surrounding the prosthesis, peak values of trabecular bone strain energy density were increased for almost all load cases. If not destructive, extra loading brought by the prosthesis may locally favour bone remodelling, endochondral ossification of the invaded bone marrow, and contribute to the osteo-integration of the HAPEX[®] pegs beyond the perforated bony endplates. This could eventually compensate the effect of stress shielding discussed in Paragraph D.V.a.2). In many cases, the vertebral cortex adjacent to the L4-L5 disc substitute could be overloaded or not, mostly depending on whether the body weight-like load was simulated.

As such, under load-controlled flexion, the L4 lower cortical shell and endplate were locally subjected to significant increased mechanical work, only when pure rotations were applied. Conversely, under extension, the peak strain energy in the L4 lower cortex of the treated model appeared enlarged, only when the additional follower compressive force was present. Considering the deformed shapes predicted by the treated model under flexion and extension, it can be deduced that the lordosis of the lumbar spine bi-segment model had most likely a strong influence on the above results. Indeed, under flexion, the body weight-like follower force applied on L3 tended to become normal to the L4 mid transversal plane and reduced the shear forces exerted by the rotated L3 vertebra on the L4-L5 segment. On the contrary, under extension, the postero-anterior direction taken by the compressive follower force increased the internal shear forces on the subjacent L4-L5 segment, once L3 achieved equilibrium. Probably, a more flexible device allowing better distributions of the internal shear forces along the bi-segment model would reduce such load-dependency of the prosthesis effect.

At the caudal end of the prosthesis, device stiffness, increasing lordosis angle with respect to L3, and complete immobility of L5, all made that, both under flexion and extension, strain energy density peak values in the L5 upper cortex were largely increased, whenever the body weight-like load was added or not. Conversely, under axial rotation, the device increased maximum loadings of the L5 upper cortical shell and bony endplate, only when the follower compressive load was added to the rotational moment. As discussed in Chapter 4, the simulated axial rotation induced some coupled motions that were partly linked with the posterior zygapophysial joint contact and locally opened the intervertebral spaces. Obviously, at the L3-L4 level of the treated model, the body weight-like load limited such local coupled deformations. This contributed to reinforce the internal axial compressive force components over the bi-segment model and, either reduced the prosthesis-induced load relieve discussed in Paragraph D.V.a.2), or made the prosthesis to raise the mechanical energy, as predicted in the upper L5 cortex.

For all load cases, it should be highlighted that strain energy density increases predicted into the bony endplates adjacent to the L4-L5 disc substitute, from the intact to the treated model, always occurred on the trabecular bone side. Actually, on the bony endplate side facing the L4-L5 intervertebral joint, i.e. intact disc or prosthesis, peak values of strain energy density were nearly one order of magnitude smaller in the treated than in the intact model. This was evidently due to the high stiffness and insignificant deformations of the L4-L5 disc substitute, when compared to the intact disc model. Note that in both the treated and intact models, one element layer only represented bony endplates. Therefore strain energy density distribution through the endplate thickness

has to be cautiously considered and should be confirmed after further mesh refinement. Nevertheless, present results seem qualitatively reasonable and lead to question whether a prosthesis-induced long-term remodelling would not displace the bone mass toward the vertebra trabecular core. In such a case, loosening could occur at the base of the HAPEX[®] endplate pegs, while toward the tip of the pegs, bone could become stronger.

VI. Intact L3-L4 intervertebral disc

a. Pure rotations

1) Load- & displacement-controlled flexion

While under load-controlled flexion, the prosthesis had only little effect on the L3-L4 intact annulus fibrosus, under displacement-controlled flexion, L3-L4 annulus strain energy was significantly greater in the treated than in the intact model. Actually, in the intact model, geometrical differences between the L3-L4 and L4-L5 intervertebral discs, made the major part of imposed displacements to be reported on the L4-L5 segment, i.e. the most deformable one (Chap. 3). Conversely, in the treated model, the intact L3-L4 segment had to compensate the high stiffness of the L4-L5 implanted segment and mostly deformed, until the global rotation angle imposed on L3 was achieved. Thus, under displacement-controlled, the higher is the motion restriction at the treated level, the more the adjacent intact levels should be overloaded. At the treated level, the loss of load-controlled flexion motion, computed with the modelled prosthesis, was similar to simulation results obtained after virtual posterior interbody fusion simulated on a L1-L5 four-segment model (Chen *et al.*, 2008). From a kinematical point of view, a rough analogy between the evaluated composite device and a titanium cage, suggests that displacement-controlled predictions are in better agreement than load-controlled predictions with the long-term degeneration symptoms observed at spine levels adjacent to fused segments (Section A.). Overloading predicted in the L3-L4 intervertebral disc under displacement-control also agreed with *in vitro* intradiscal pressure measurements, performed on a fused cervical spine (Dmitriev *et al.*, 2005).

However, during *in vivo* motions, different muscle activations at different spine levels might locally induce a mix of displacement- and force-controlled external loadings. Displacement-controlled rotations may better represent voluntary trunk deformations than load-controlled motions do, but result accuracy depends on hardly identifiable instantaneous axes of rotation of the spine (Panjabi, 2007). In order to overcome such problem, a hybrid method, consisting in applying pure moments until a prescribed rotation angle is achieved, has been proposed by Panjabi *et al.* (Panjabi, 2007) for *in vitro* models, and applied *in silico* by Goel *et al.* (Goel *et al.*, 2005). The latter authors used a L3-S1 lumbo-sacral tri-segment model, and assessed the effect of replacing the L5-S1 disc with a SB CHARITÉ[™] device, by using both constant external moments and the above-cited hybrid method. Unfortunately, they did not report any internal load in the intact intervertebral discs adjacent to the treated level. Nevertheless, they found that facet load changes due to the device could only be predicted with the hybrid method. Moreover, similar to the displacement-control results

discussed in Paragraph D.III.b.1), facet contact force alterations at the adjacent levels corresponded to a compensation of the modified ranges of motion at the treated level. Thus, it can be concluded that under flexion, displacement-control results are probably more representative of the possible in vivo effect of the prosthesis than load-controlled results. Thus, like fusion cases, the high stiffness of the studied composite device could induce long-term degenerative changes in the adjacent intervertebral disc, if patients attempt to move their spine in a way similar to that before surgery.

Under displacement-controlled flexion, the presence of the L4-L5 disc substitute did not affect similarly all the L3-L4 intervertebral disc areas, but preferentially the outer and inner layers in the anterior and posterior annulus, respectively. Increased strain energy in the outer anterior annulus corresponded to the extra bulging induced by the large prosthesis-related L3-L4 ranges of motion. Also results were in good agreement with the coupling between annulus deformation and backward nucleus migration discussed in Chapter 4. In the treated model, pressure of the nucleus mass against the posterior inner annulus reduced somewhat the nucleus hydrostatic gradient index, although global intradiscal pressure was significantly increased by the simultaneous increment of anterior annulus axial compression. Disc replacement is generally recommended, either after serious disc injury, or for severe degenerations, when conservative treatments fail to ensure pain relieve. This raises then the question, whether the non-treated adjacent intervertebral discs are completely healthy. If not, the stiff composite device could highly accelerate the apparition or propagation of inner annulus cracks due to a pre-existing loss of proteoglycans / intradiscal pressure (Iatridis *et al.*, 2007).

2) Extension & axial rotation

Although extension and axial rotation motions were simulated under force-controlled conditions, unlike under load-controlled flexion, the L4-L5 disc substitute had significant effects on the L3-L4 intervertebral disc biomechanics. Under extension, the closer the anterior annulus layers were from the annulus, the more extra strain energy density was induced by the prosthesis. Based on the analysis of the RAD model reported in Chapter 4, such result suggests that, either the axial stretch of the anterior L3-L4 annulus, or the anterior L3-L4 nucleus mass migration, were increased by the presence of the implant. Nevertheless, the slight change of L3-L4 extension angle between the intact and treated models leads to think that nucleus pulposus effect was locally predominant. Similar results in the posterior annulus and small variation of $I_{\Delta h}$ between the intact and the treated model both indicated that the increased anterior nucleus mass migration was directly related to a posterior local increase of nucleus loading. As shown by the postero-lateral strain energy density relative differences generated by the prosthesis in the intact L3-L4 annulus, posterior nucleus loading might be due to enlarged local load transfers through the L3-L4 posterior disc areas. Greater posterior load transfers in the L3-L4 intervertebral disc of the treated model were most likely linked to the reduced capacity of the L3-L4 facets in locally limiting axial disc compression, because of the modified L3 transversal translation (§ D.III.b.2)).

Under axial rotation, the L4-L5 disc substitute induced a strong reduction of the maximum strain energy stored within the posterior and inner postero-lateral layers of the L3-L4 annulus. Both areas were actually under the influence of the main transversal shear deformations, and their local loading was most likely inversely correlated with the load transfer through the facet joints (Chap. 4). Therefore, present results agree with the fact that the prosthesis favoured the corresponding load transfer through the zygapophysial joints (§ D.III.a.). Note that implant-induced load transfer through the L3-L4 facets also contributed to reduce the nucleus maximum strain energy.

b. Body weight-like load effect

Under displacement-controlled flexion, the simulated additional follower compressive load considerably lowered the increase of L3-L4 annulus peak strain energy density from the intact to the treated model. Actually, as discussed in Section D.II., imposed rotation might generate significant internal shear loads in the treated model. Because of the difference of stiffness between the prosthesis and the intact L3-L4 disc substitute, these internal loads mostly concentrate in the L3-L4 segment. Similarly, the axial follower compressive load generated larger axial deformations in the intact L3-L4 intervertebral disc than in the prosthesis, stiffening much more the L3-L4 disc non-linear tissues than the implant materials. Such improved distribution of stiffness in the treated model stabilized the bi-segment model and limited the overloading effect of the prosthesis on the adjacent L3-L4 intervertebral disc.

Under extension, it was suggested that body weight-like load reinforced the preferentiality of the antero-posterior transversal shear between L3 and L4, induced by the prosthesis. Accordingly, the nucleus effects discussed in Paragraph D.IV.a.2) and mostly related to the posterior annulus axial loading were proportionally less notable. Thus, the influence of the prosthesis on the anterior and posterior inner areas of the L3-L4 annulus was reduced when both the intact and treated models were compared in presence of the additional follower compressive force. Such effect was sufficient to globally lower implant-induced L3-L4 overloading by about 10%. Nevertheless, increased influence of the antero-posterior transversal shear also made the L4-L5 disc substitute to further overload the L3-L4 lateral quadrants. Moreover, in most of the L3-L4 annulus outer and mid sections additional body weight-like load enlarged somewhat local overloading predicted under pure rotation after L4-L5 disc substitution. This was probably due to the further stiffening of the annulus non-linear materials under the influence of increasing combined loadings. Similarly, under axial rotation, additional follower force suppressed the strain energy reduction induced in the L3-L4 annulus posterior areas.

For all load-cases, $I_{\Delta h}$ values show that body weight-like follower forces reduced considerably the heterogeneity of the L3-L4 nucleus pulposus, both in the intact and treated models. According to experimental findings reported by Rohlmann et al (Rohlmann *et al.*, 2001), additional follower load allowed the intervertebral discs to work in a more physiological way. In both treated and intact models, body weight-like load should actually have contributed to segment stabilization through improved load transfers from the nucleus to the surrounding annulus (Chap. 1). From a modelling point

of view, combining pure rotations with axial compressive follower load has then a double implication. On one hand, it may better represent the prosthesis effect than pure rotations. On the other hand, it may limit the prediction errors of intradiscal pressure transfer, as induced by a hyperelastic nucleus model (Chap. 4).

VII. Comparison with other studies

As discussed in Paragraph VI.a.1), the disc substitute modelled in this study leads, at the treated level, to similar segment motion reduction as the posterior interbody fusion modelled by Chen et al (Chen *et al.*, 2008). The authors used a L1-L5 lumbar spine segment model and virtually implanted bi-lateral titanium cages with pedicle screws at the L3-L4 level. They evaluated the effect of the treatment by simulating 10 N.m pure moments with an axial compressive load of 150 N. According to the results obtained in the present study, under extension, posterior interbody fusion was found to significantly affect the annulus stress state at the superior adjacent level. However, unlike the composite prosthesis model, the fusion model also led to ranges of motion and facet contact forces increases. Moreover, even under load-controlled flexion, at the upper adjacent level, simulated fusion was reported to increase both ranges of motion and annulus stress, by nearly 20%. This did not occur with the composite disc substitute, neither under pure moment, nor with the additional body-weight load. Comparison with the present study has to be interpreted cautiously, as different geometric models may lead to different load transfers, even if the compared models both are able to reproduce macroscopic experimental data (Chap. 3). Nevertheless, improved results given by the composite prosthesis model, compared to the reported fusion model, could also come from less transversal shear constraints imposed by the fibre reinforced structure, than by screwed titanium cages. Therefore, in line with the idea that load sharing could be the real problem of spine instability (Mulholland, 2008), in terms of load transfer along multiple segments, the novel disc substitute seems to represent a better alternative than fusion, even if failing in restoring motions.

A comparison of the CHARITÉ[®] and the PRODISC[®]-L devices implanted in a L4-L5 lumbar spine segment suggested that the transversal shear stiffness of the PRODISC[®]-L device was actually responsible for facet joint overloading (Moumene and Geisler, 2007). Unfortunately, in this study, only one segment motion was modelled and adjacent level effects were consequently not available. However, besides differences between devices, reported results showed that misplacement of a disc substitute could substantially alter the efficiency of the implant in preserving functional load transfer through the facet joints of the treated segment. On this point, the manufacturing technique of the present composite device offers the great advantage that shape and size of the implant can be easily fitted to particular vertebra geometries (e.g. acquired by means of CT scans), reducing the risk of misplacement during surgery.

Truly, placement, size, shape, of intervertebral disc implants or mono segmental substitutes and surface contact with the adjacent vertebrae were showed by finite element simulations to largely affect the quality of load transfer through the vertebrae (Dooris *et al.*, 2001; Zander *et al.*, 2002; Noailly *et al.*, 2005; Lacroix *et al.*, 2006). Results and discussions reported in this chapter showed that failure of the composite

prosthesis to qualitatively preserve vertebral load distributions predicted in the intact model had a double origin. On one hand, it was due to stiffness of the HEMMA-PMMA matrix. On the other hand, it was also due to the load concentrations induced by the HAPEX[®] endplate pegs and to the irregular contact between prosthesis and vertebral endplates. A previous numerical analysis of a very similar device showed that prosthesis endplates perfectly fitting to the adjacent vertebra endplates improved considerably the quality of the stresses felt by the bone (Noailly *et al.*, 2005). Moreover, under load control, the absence of pegs on the prosthesis endplates limited the load increase in the vertebral endplate to less than 3%, compared to the almost 100%, occasionally computed in the present analysis. This strongly suggests that suppressing or reducing the amount of pegs, and filling the cavity between the disc substitute and the vertebra with osteo-integrable or reabsorbable porous cements, could already considerably improve the prosthesis effect. Problem of the stiff prosthesis matrix should also be solved. Another material, meeting minimum requirements of deformability and elasticity, should be designed to ensure appropriate load transfers to the different parts of the composite structure and to the surrounding tissues. For such task, this and former studies (Langrana *et al.*, 1991; Lee *et al.*, 1991b) showed that finite element spine models can be very valuable tools.

In the present study, displacement-controlled motion always returned one of the worst prosthesis adjacent effects, because the high stiffness of the treated segment was compensated by increased deformations in the rest of the bi-segment model. As discussed in Paragraph D.VI.a.1), by using the hybrid method in their L3-S1 tri-segment lumbar spine finite element model, Goel *et al.* (Goel *et al.*, 2005) also showed that the CHARITÉ[®] disc substitute had adjacent effects. However, unlike the present composite artificial disc, the CHARITÉ[®] implant increased intervertebral deformations at the treated level and therefore reduced adjacent level deformations and zygapophysial joint loads. Under flexion with a 400N follower compressive load, the lack of axial compliance of the CHARITÉ[®] metal-polythene assembly made the endplate normal forces adjacent to the prosthesis to be up to 90% relatively higher than with an intact disc. Such results is very similar to that found in the upper L5 endplate of the present treated model loaded under displacement-controlled flexion with the additional body weight-like load. Thus, comparison of Goel *et al.* (Goel *et al.*, 2005) finite element predictions with those hereby reported suggests that despite its limitations, the CHARITÉ[®] device still represents a better option than the novel composite disc substitute for total disc replacement. However, the prosthesis design evaluated in the present study is probably more promising than the CHARITÉ[®] or PRODISC[®] designs, since predicted limitations were more related to a modifiable choice of materials, rather than to the concept itself.

E. Conclusion

The L3-L5 finite element model presented in this chapter allowed studying the design of a novel composite artificial disc, modelled as a L4-L5 disc substitute. Several limitations were identified regarding the mechanical modelling of the device. However, because of the low deformations generally predicted in the implant inserted in the bi-

segment model, the influence of these limitations on the following conclusions should be minimal. The high stiffness of the nucleus-like and annulus-like matrices, were both responsible for a large stiffening of the treated level. This had a high propensity to affect the adjacent non-treated level if fixed rotations are imposed. Moreover, the low deformability of the matrix greatly limited the load transfers to the peripheral embedded fibre, which directly affected numerous bony areas. Such limitations of the device design are to be cautiously considered because of several limitations of the model (Chap. 4) and insufficient knowledge about the detailed spine mechanics (Chaps. 3,4). However, the present finite element study allowed asking for attention on several points of the design, such as how some materials may affect the whole functioning of the composite structure and lead to important biomechanical issues. The basic hypotheses suggested by the model can be further experimentally tested and finally assess the design process. Unfortunately, quantitative recommendations cannot be neither drawn *in silico*, nor tested *in vitro*, principally because of the diversity of the implant response with the type of applied external loads, and the lack of precise knowledge about the *in vivo* local forces. The access to such knowledge can very difficult to determine because of the influence of pain and/or psychological factors on the *in vivo* aware motions and muscle activation balance. Nevertheless, level of confidence of the general model can also be improved with the availability of prosthesis experimental data, not only on the component materials alone, or on the whole implant, but also at intermediate structural levels. Therefore, even if the lumbar spine L3-L5 bi-segment finite element model presented in this Thesis cannot be used for direct clinical applications, it would result very useful at the prosthesis device conception level.
